GAS-PHASE CHEMISTRY OF ATMOSPHERICALLY IMPORTANT COMPOUNDS

By

SUMANA SENGUPTA

Enrollment Number: CHEM01200604007

Bhabha Atomic Research Centre

A thesis submitted to the

Board of Studies in Chemical Science Discipline

In partial fulfillment of requirements

For the Degree of

DOCTOR OF PHILOSOPHY

of

HOMI BHABHA NATIONAL INSTITUTE

MARCH, 2012

Homi Bhabha National Institute

Recommendations of the Viva Voce Board

As members of the Viva Voce Board, we certify that we have read the dissertation prepared by **Sumana SenGupta** entitled **Gas Phase Chemistry of Atmospherically Important Molecules** and recommend that it may be accepted as fulfilling the dissertation requirement for the Degree of Doctor of Philosophy.

Chairman-
Dr. S. K. Sarkar
Date: 31/08/2012

Convener-
PNBajaj
Dr. P. N. Bajaj
Date: 31/08/2012

Co-guide-
PDNaik
Dr. P. D. Naik
Date: 31/08/2012

External Examiner-
Dr. S. Wategaonkar
Date: 31/08/2012

Member 1-
Awadhesh Kumar
Dr. Awadhesh Kumar
Date: 31/08/2012

Member 2-
RKVatsa
Dr. R. K. Vatsa
Date: 31/08/2012

Final approval and acceptance of this dissertation is contingent upon the candidate's submission of the final copies of the dissertation to HBNI. We hereby certify that we have read this dissertation prepared under our direction and recommend that it may be accepted as fulfilling the dissertation requirement.

Guide –
PNBajaj
Prof. P. N. Bajaj
Date: 31/08/2012

Co-guide –
PDNaik
Prof. P. D. Naik
Date: 31/08/2012

STATEMENT BY AUTHOR

This dissertation has been submitted in partial fulfillment of requirements for an advanced degree at Homi Bhabha National Institute (HBNI) and is deposited in the Library to be made available to borrowers under rules of the HBNI.

Brief quotations from this dissertation are allowable without special permission, provided that accurate acknowledgement of source is made. Requests for permission for extended quotation from or reproduction of this manuscript in whole or in part may be granted by the Competent Authority of HBNI when in his or her judgment the proposed use of the material is in the interests of scholarship. In all other instances, however, permission must be obtained from the author.

Sumana SenGupta

DECLARATION

I, hereby declare that the investigation presented in the thesis has been carried out by me. The work is original and has not been submitted earlier as a whole or in part for a degree / diploma at this or any other Institution / University.

Sumana SenGupta

This thesis is dedicated to…….

all who ever taught me anything.

Acknowledgement

I wish to record my most sincere gratitude towards my guide, Prof. P. N. Bajaj, and co-guide Prof. P. D. Naik of Bhabha Atomic Research Centre (BARC), for their guiding me with superior scientific knowledge and generous co-operation throughout the execution of this thesis. Their encouragement, interest, patience and good wishes will always be greatly cherished in my mind. Without their active contribution and detailed critical reviewing, this thesis would not have been what it is.

It is my great privilege to acknowledge Dr. Awadhesh Kumar, Dr. Dhanya Suresh and Dr. H. P. Upadhyaya, for their assistance and guidance throughout my research work. I am indebted to them for initiating me in the field of experimental chemistry and supporting through the journey therein.

Prof. S. K. Sarkar, Head of Radiation & Photochemistry Division, BARC has always shown kind interest and encouragement for my work. As the chairman of the doctoral committee, this thesis has benefitted substantially from his valuable suggestions. The members (Dr. P. D. Naik, Dr. Awadhesh Kumar, Dr. R. K. Vatsa, and Dr. V. Parthasarathy) of the doctoral committee are gratefully acknowledged for their critical review and suggestions during progress review and pre-synopsis viva-voce.

I thank my dear friends, Dr. Teena Goel, Dr. Nandita Maiti, and Ms. Payel Sarkar for being my pillars of support. They were always there when I most needed them. I wish to thank my younger colleagues, Ms. Asmita Sharma, Ms. Ridhima Chadha, Ms. Monali Kawade, Dr. Yogesh Indulkar, Mr. Ankur Saha and Mr. Hariprasad Alwe for making the laboratory such a nice place to be in. The very crucial help rendered by them at the right time solved many of my problems. Special thanks go to Ms. Asmita, and Dr. K. K. Pushpa, for helping out with the Gas Chromatography studies.

Dr. T. Mukherjee, Director of Chemistry Group, remains my source of inspiration in many ways. With his very positive and encouraging approach towards chemistry as well as life itself, his presence exerts a greatly supportive influence to many of the younger members of the chemistry group.

Dr. J. L. Goswami, my uncle, and his family deserve my heartfelt gratitude for providing me and many of my close friends with a “home away for home” in Mumbai.

The person, to whom I owe the largest acknowledgement, is, Mr. Tonmoy C. Das, my husband and best friend. Along with him, my mother, Ms. Lina SenGupta, and my sister, Ms. Sukanya SenGupta, CA, share the credit for constantly sustaining me with courage and perseverance.

The little footprints of my children, Adhyayan, and Abhilasha, are the deepest ones on my heart. I thank God for letting me have them in my life.

Finally, I take this opportunity to express my love and gratitude towards all the SenGuptas, the ones who brought me up, and the ones who were brought up with me, and all the Das’s, who took me as their own, for making me the person I am.

March, 2012 Sumana SenGupta

Contents

Chapter 4:Dynamic Study of Cyclic Ethers………………. 132

SYNOPSIS

Preamble

The chemical reactions have always been subject of great curiosity and fascination to the human mind, because these are responsible for the existence of naturally occurring compounds, various phenomena taking place in the nature, life in the universe, as well as many important scientific developments in the history of civilisation as well as the future of mankind. The study of chemistry has evolved through time, its journey starting from the laboratory of the alchemist, and arriving at today's femtosecond labs. Numerous approaches have been devised to tackle different aspects of chemistry, their aspects broad or minute, as per requirement. Thermodynamics and kinetics are two branches of science which are constantly being applied to chemical problems, in their respective fields. Thermodynamics predicts the feasibility of a process, which is often a chemical reaction, under given conditions, because it deals with the initial and the final states of the system. The mechanism by which the system goes from one state to another, and the time required to change are of no importance in thermodynamics, as time is not a thermodynamic variable. Kinetics deals with the details of a process by which the system goes from one state to another, and the time required for the transition, i.e., the rate of the process/reactions, and the factors that influence the rate of the process/reaction. Depending on whether the process is physical, or chemical, the kinetics is known as physical or chemical kinetics. Chemical kinetics is also known as reaction kinetics.

A chemical reaction may involve a number of elementary steps. The breaking of old bond/s, formation of new bond/s, electron, proton, or hydrogen atom transfer, inter- and intra-molecular energy transfer, etc., are some of the elementary steps involved in many reactions.

A photodissociation reaction taking place on a repulsive excited state is very fast (~100 fs), but a bimolecular reaction occurs in pico second, or longer time, depending on whether the chemical act is once-through (direct), or involves longer interaction between the reactants, and even transient intermediates, with lifetime varying from pico seconds to seconds. For a reaction,

a A + b B ......→ c C + d D,

Here a,b,c etc. are the coefficients in the balanced reaction, and A, B, C are the chemical species. The rate of the reaction is,

$$R = -\frac{1}{a}\left|\frac{dA}{dt}\right| = -\frac{1}{b}\left|\frac{dB}{dt}\right| = k\,|A|^{\alpha}.\,|B|^{\beta}$$

Here, k is the rate coefficients and α, β, γ are integers, or half integers, the sum of which gives the order of the reaction.

Arrhenius found an empirical relation for the temperature dependence of many reactions as

$$k(T) = A\, e^{-\frac{E_a}{RT}}$$

Where, A and E_a are Arrhenius A factor, or pre-exponential factor, and Arrhenius activation energy, respectively, which are constants characteristic of the reaction, and R is the universal gas constant.

Since the acceptance of kinetic theory of gases, it has been recognized that intermolecular collisions serve as the microscopic mechanism responsible for all the observed rate phenomena involving gases and liquids. The reactions in the gas phase are different from those taking place in the liquid phase, because the former are much more simple and free from the interference of the solvent molecules. The first theory of gas reactions, i.e., collision theory, postulated that, in order for the molecules to interact, they must approach each other so closely that these can be said to be in collision. Though it provided the first insight into a chemical reaction, it had limited success because of its inherent crudeness. Because of the inadequacies of the collision theory, H. Eyring and M. Polanyi proposed the Transition State theory, according to which, every chemical reaction goes through some transition state, or activated complex, and highlighted the role of the internal energies in the rate of the reactions. They also established the concept of potential energy surfaces, and used statistical mechanics and quantum chemistry methods, to provide firm theoretical base to chemical kinetics. Subsequently, other theories were developed to explain the rate of chemical reactions.

In simple chemical kinetics studies, the measurements are carried out on systems that are in thermal equilibrium, where both translational and internal energies are distributed among the molecules according to Boltzmann's distribution. The rate coefficients so obtained are the gross averages over a number of collisions, leading to the products. These results, which correspond to "bulk" reactions, i.e., a large number of molecules in thermal equilibrium, are dealt by "macroscopic kinetics", or simply "kinetics".

The first part of the thesis deals with studies on the kinetics of chemical reactions, with an aim to understand what influences the rates, and develop theories which can be used to predict them. The knowledge of reaction rates has many practical applications, for example, designing of industrial processes, understanding of the complex dynamics in the atmosphere, as well as the intricate interplay of the chemical reactions that are the basis of the life. We need to determine, by experiment, the form of the rate law, and hence, the associated rate coefficients, to extend our knowledge of the rates of chemical reactions, so that predictions can be made, and the measured rate coefficients can be compared with those predicted by theory. Chemical kinetics studies are also very helpful for understanding the mechanism of reactions, though other information also is required, like direct determination of intermediates, characterisation of the products, etc. However, using our chemical intuition and modelling techniques, a reasonable attempt can be made at deciphering the mechanism, using kinetic results. Apart from that, kinetic studies in the gas phase have acquired a heightened importance in the recent times because of their relevance in understanding the chemistry of atmospheric pollution. The extent of damage that can be caused by a polluting substance depends on its lifetime in the atmosphere, which, in turn, depends on the rate, or the rate coefficient, of its reaction with the important reactive species present therein. The present thesis includes kinetic studies of the reactions of some atmospherically important molecules with OH radicals, which is the most important reactive species present in the troposphere.

Though a lot of information on the mechanistic aspects and the technological potentials of the reactions have been derived from the kinetic studies, in recent years, the focus of the studies on the chemical reactions has shifted from the kinetics to the dynamics. Chemist of today wants to control reactions, rather than be a passive spectator. In order to achieve this, and develop new technologies, apart from knowing, “what are the various elementary steps involved in a reaction, and what is the detailed dynamics of each step, and how to eliminate, or reduce, unwanted products, a waste, by generating the desired products selectively”, an urge to “see” chemical reactions at the molecular level has emerged. Chemists have always cherished the vision of carrying out mode or bond selective reactions, eventually leading to chemical control of reactions. Chemical dynamics deals with the investigations of molecular/atomic mechanism of elementary chemical processes, both intermolecular and intramolecular. These fundamental processes are at the root of bulk rate phenomena. This microscopic approach has stimulated new experimental and theoretical developments, making chemical dynamics as one of the most active fields of physical chemistry. In order to investigate dynamics of a molecular process, physical or chemical, fast techniques are required. The development of lasers and molecular beams has greatly helped in this endeavour. One can prepare the reactants in well-defined quantum states, and monitor their journey from the reactant valley to the product valley, by taking snapshots from time zero, i.e., the time at which a chemical reaction starts. Now, it is possible to characterize the elusive transition state, which determines the course of reaction.

The second part of the thesis deals with the “Dynamics of Chemical Reactions”. Intermolecular collisions destroy the state selection of the reactants, as well as the quantum state distribution of the products, and hence, unless experiments are done under collisionless condition, no information can be gleaned about how the outcome of a chemical reaction depends on the pre-selection of the energy states in the reactants, or how the excess chemical energy is distributed in the products. Nowadays, “microscopic” investigations into the dynamics of a reaction can be made feasible by establishing single collision conditions, when the information sought is in the primary reaction quantities, like nascent product energy distribution, dependence of reaction cross-section on different types of internal energies, and impact parameters. These can be achieved by nanosecond pump-probe, or molecular beam experiments. In the present thesis, the dynamics studies carried out, to obtain a molecular level view of the product energy distribution of products in unimolecular photodissociation reactions, using nanosecond pump-probe technique, are described.

The thesis has been organized into six chapters, elaborating on the work carried out on the above-mentioned themes.

Chapter 1. Introduction

Volatile organic compounds (VOC) are being constantly released in the air through biogenic or anthropogenic means, and are also being removed by means of physical and chemical processes. During their lifetime in the atmosphere, these undergo a variety of reactions, by which various other chemical species are introduced in the atmosphere. Some of these are simply poisonous, while the others cause long-term environmental problems, such as ozone layer depletion, global warming, acid rain, etc. The knowledge of the basic chemical processes undergone by these compounds is essential, to evaluate their potential effects on the atmosphere, as well as the biosphere. Naturally, the extent of the harm caused by these compounds depends on their lifetime, as well as the different physical and chemical processes undergone by these in the atmosphere. In order to get an idea about these chemical processes, one has to identify the reactions by which these compounds are being removed, the products formed, the mechanism followed, and, of course, the rate of the reactions under atmospheric conditions. The major means of depletion of these compounds in the atmosphere can be divided into two types, viz., photochemical dissociation and chemical reactions with other compounds and radicals present therein. Since a large number of different radicals are present in the atmosphere, which are much more reactive than these molecules, the reactions with the radicals are the most important route by which the chemical compounds are removed. One of the most widespread, and also the most reactive radical present in the troposphere is the OH radical, and hence, oxidation by this radical is the most important removal channel for a large number of organic molecules. The atmospheric oxidation of these oxygenated compounds, initiated by the OH radical, could contribute to the formation of ozone and other components of photochemical smog in urban areas. Oxidation by OH radical is also an important step in the combustion process of the organic molecules. In order to model the chemistry in the atmosphere, as well as in the combustion process, accurate kinetic data are needed for the reactions of OH radicals with various organic compounds, together with mechanistic information on the overall oxidation process.

The processes undergone by the different chemical species in the atmosphere, or combustion environment, are very complex, and difficult to analyse as such. Unimolecular photodissociation reactions under collisionless condition are the most simple and clean chemical processes, which can be studied as models for the more complex processes. These reactions can be investigated in detail, by the currently available techniques. The advent of highly monochromatic lasers have given the experimentalist a powerful tool to prepare the reactants in well-defined states at very low pressure. Employing state-selective detection techniques, the distribution of energy in the different modes of the products can also be mapped. Unimolecular photodissociation can be studied in detail by using these techniques, and the potential energy surfaces can also be constructed with considerable accuracy. Once the knowledge about the dynamics and potential energy surface is obtained, more complex reactions of similar type can be simulated from it.

The investigations on atmospherically important molecules included in the thesis, can be broadly divided into two parts. The first part deals with the study of kinetics of the reactions of OH radical with several compounds, as described in Chapter 3. The second part deals with the studies of the photodissociation dynamics of polyatomic molecules, as discussed in Chapter 4, 5 and 6. Chapter 2 gives a concise account of the techniques employed in the course of investigations reported in the present research work.

Chapter 2. Techniques

This chapter gives a detailed account of the experimental and theoretical techniques that have been used in this work. Most of the important experiments described here have been carried out, using nanosecond Laser Photolysis- Laser Induced Fluorescence (LP-LIF) technique. LIF is a very sensitive ultrafast detection technique, where the level of detection can be as low as 10^9 molecules cm^{-3}. A flow system, with very low dynamic pressure, is used to attain collisionless condition[1-2]. In this set-up, the unimolecular dissociation of a compound is affected by a high power monochromatic pulsed laser, and the nascent products are detected and monitored, by recording their fluorescence excitation spectra, employing a tunable dye laser. In the case of the kinetic studies, laser photolysis was used, to generate one of the reactants, viz., OH radical, the decay of which due to the reaction with a molecule of interest was monitored by tunable laser induced fluorescence,[3] using a tunable dye laser. The other techniques that have been used as analytical tools are Gas Chromatography–Mass Spectrometry (GC-MS), Time-resolved Infrared and Visible Fluorescence Spectrometry and Fourier Transformation Infrared Red Spectrometry (FTIR).

The experimental results in the dynamics studies were supported by *ab initio* Molecular Orbital calculations, using Gaussian 92[4] package. In this method, the geometry and the relative potential energies of the molecules, as well as the transition states of the reactions, are optimized at different levels of theory, using suitable basis sets, to define molecular parameters. The calculations are completely based on the laws of quantum mechanics and some physical constants, like velocity of light (c), mass and charge of electron and nuclei, Planck's constant (h), etc. High quality quantitative data can be generated, using this method.

Chapter 3. Kinetic Studies

OH radical is one of the most reactive species present in the lower atmosphere, i.e., troposphere, and is responsible for the major removal channel for most of the organic molecules. OH radical is generated in the troposphere, by photodissociation of ozone molecules by solar radiation in the range of 300 - 320 nm, and subsequent reaction of the resultant $O(^1D)$ with the ambient water molecules. We, in our laboratory, have studied the reactions of different types of molecules with OH radical under nearly atmospheric condition, and measured the kinetic parameters by Laser induced fluorescence method.

In the experimental work, OH was generated in situ, by photolysis of H_2O_2 at 248 nm laser, and the LIF signal from the OH radical was used to monitor the reaction kinetics[5,6]. This is an absolute method for measuring the bimolecular rate coefficient for the reaction of OH radical with the molecule of interest, as the decay in OH concentration is directly monitored in real time. The bimolecular rate constant was measured at different temperatures, to obtain the Arrhenius frequency factor and the activation energy of the reaction. The kinetic studies described in the thesis led to some quite interesting results for the reactions of different types of compounds that have been studied.

3.1. Hydrofluoroether (Bis-trifluoroethyl ether)

Hydrofluoroethers (HFE) have been proposed recently as chlorofluorocarbon (CFC) alternatives, for usage as refrigerating and cleaning purpose, as these are benign to the ozone layer, and are expected to have comparatively shorter lifetime in the atmosphere. Bis-trifluoroethyl ether ($CF_3CH_2OCH_2CF_3$ (TFEE)) is one of the promising HFEs. The reaction rate, as well as the atmospheric lifetime of this compound, should be unambiguously estimated. Laser photolysis-laser induced fluorescence method, which is an absolute method, was used, for the first time, for measuring the kinetic parameters of the reaction of OH radicals with $CF_3CH_2OCH_2CF_3$ (TFEE), in the temperature range of 298 – 365 K. The bimolecular rate coefficient, at 298 K, $k_{II}(298)$, was measured to be $(1.47 \pm .03)\times10^{-13}$ $cm^3 molecule^{-1} s^{-1}$, and the temperature dependence of k_{II} was determined to be $(4.5 \pm 0.8) \times 10^{-12} \exp[-(1030 \pm 60)/T]$ $cm^3 molecule^{-1} s^{-1}$. (The error quoted is 1σ of the linear regression of the respective plots.) The positive value of the activation energy indicates that the reaction of OH radical with TFEE, which is actually an abstraction of H-atom, takes place directly, i.e., without any adduct formation. From the bimolecular rate coefficient at room temperature, the atmospheric lifetime of TFEE was calculated to be 0.35 years.

3.2. Polyfunctional Molecules: Morpholine

The rate coefficients of the reactions of OH radical with organic molecules are dependent their structure. Morpholine is a polyfunctional compound, a secondary amine, as well as an ether. A kinetic study of its reaction with OH radical is an interesting subject of investigation because the results are supposed to have the signature of both of these two classes of compounds. In fact, our study of the kinetics of the reaction of morpholine with OH radical has yielded significant results as described herein. The rate coefficient for this reaction at room temperature is measured to be $(8.0 \pm 0.03) \times 10^{-11}$ $\text{molecule}^{-1}\text{cm}^{3}\text{s}^{-1}$. Though the Arrhenius plot is not perfectly linear in the temperature range of 298 – 365, the approximate dependence of the rate coefficient on temperature is given by $(1.1 \pm 0.1) \times 10^{-11} \exp [(590 \pm 20)/T]$ $\text{cm}^{3}\text{molecule}^{-1}\text{s}^{-1}$. (The error quoted is 1σ of the linear regression of the respective plots.) The observed rate coefficients are very high, as compared to those of the equivalent heterocyclic molecules, with only O- atom. *Ab initio* molecular orbital (MO) calculations, using the Gaussian 92 programme, were used to investigate the potential energy surface (PES) for the H-abstraction reaction of OH radical. The theoretical calculations revealed that, prior to H-atom abstraction, OH radical forms pre-reactive complexes, by hydrogen bonding with the N- or O- atom of the morpholine molecule. The pre-reactive complexes are more stable than the reactant molecule, by 5-7 kcal mol^{-1} , and the one involving N-atom is more stable than that involving O-atom. The energies of the transition states for H- abstraction were found to be either negative, or very small, with respect to the reactants, which explains the observation of negative activation energy of the overall reaction, as well as the high value of the bimolecular rate coefficient.

Chapter 4. Photodissociation Dynamics of Cyclic Ethers

Cyclic ethers are a class of compounds which have interesting structural properties as well as important applications in various fields. These have at least one heteroatom, O, in the ring structure, and sometimes, can have more than one, as in case of morpholine, two heteroatoms, N and O, in the ring. Tetrahydrofuran (THF), tetrahydropyran (THP) and morpholine are a few of the cyclic ethers which are used in the industry as solvents, or precursors for synthesis of more complex molecules. All of these are confirmed environmental pollutants, which directly affect the health and the well being of the living species. When these molecules were photolyzed by a laser at 193 nm, OH radical was detected, among the products, for all of them[7-9]. This channel has not been reported by any previous researcher, for any of these compounds, by thermal or light induced dissociation. This is a very interesting reaction channel from the mechanism point of view, since none of these compounds contains an OH functional group in their structures. Detailed dynamics studies of this reaction channel revealed a complex reaction pathway, where the primary products of the photodissociation undergo intramolecular rearrangement, before the final products are formed.

In the case of these molecules, the first step is always the ring opening, by the scission of one of the two C—O bonds. Since both the bonds are chemically equivalent, this gives rise to one single biradical. This is always an endoergic step, wherein about 50 kcal mol^{-1} energy is consumed. The rest of the energy that has been supplied to the molecule, by absorption of

193 nm photon (147.8 kcal/ mol), is stored in the primary biradical as the available energy. This biradical, having high energy, can access different potential energy surfaces, and thus various reaction channels can open up, to generate an array of products. One of these channels is the migration of an H atom from one of the C-centres to the O-centre. This step involves a transition state that lies, in general, about 75-85 kcal/ mol above the ground state of the parent molecule. This process generates another biradical, which is stabler than the first biradical, by about 5 kcal mol^{-1}, and contains a OH moiety at the end of the carbon chain. In the next step, the C—OH bond is cleaved, forming the OH radical. The distribution of the available energy in the various degrees of freedom of the products, as obtained experimentally by Laser Induced Fluorescence Technique, indicates that, in all of these cyclic ethers, about 40% of the available energy goes to the relative translational motion of the products. The OH radical is formed in the vibrational ground state, and the average rotational energy is in the range of 2-3 kcal/ mol. The rest of the available energy goes to the internal energy states of the co-fragment. The high fraction of the translational energy indicates that the reaction channels should have an exit barrier. But, by theoretical calculations, either a very small exit barrier, or none, could be detected. The experimentally obtained energy distribution is explained, by invoking an earlier barrier in the reaction channel, i.e., the one encountered for the intramolecular rearrangement. Thus, it seems that in such multistep reaction channels, it is possible that the high translational energy present in the second biradical manifests itself in the high translational energy of the final products.

Chapter 5. Photodisociation Dynamics of the Epoxides

Epoxides are essentially cyclic ethers, with three-membered rings. This class of compounds was chosen, to understand as to how the effect of the higher strain energy present in the smaller ring compounds is manifested in the partitioning of the energy and overall dynamics of their photodissociation. The photodissociation dynamics of some asymmetrically substituted epoxides was studied, to gain advanced information about general photochemical behaviour of smaller ring compounds.

We have irradiated epoxides, with different susbstituents at the 3-memberd rings, such as ethylene oxide (EO), propylene oxide (PO), butadiene monoxide (BMO) and styrene oxide (SO), with 193 nm laser[10,11]. In the case of the first two, OH was not observed by photoexcitation, but in the case of the other two, OH radical was obtained. This is due to the fact that the absorption cross-sections (σ) at 193 nm for EO (0.44×10^{-20} cm^2) and PO (1.5×10^{-20} cm^2) are much smaller than that for BMO (1.2×10^{-17} cm^2) and SO (5.4×10^{-18} cm^2). Gas Chromatography-Mass Spectrometry (GC-MS) analyses of the products of photolyses of BMO and SO at 248 nm revealed the presence of some ketonic compounds. The OH formation channel in these compounds has multiple branches. Since the three-membered epoxide ring is unsymmetrically substituted, the ring opening by the cleavage of the two different C—O bonds generates two different biradicals, which can then have different fates. A certain fraction of these can undergo intramolecular H-atom migration from C-centre to O-centre, giving rise to the enolic forms of different ketones/ aldehydes. These enols, then can either tautomerise to their more stable keto forms, or undergo another C—O bond scission, producing the OH radical. By theoretical calculations, it has been seen that the OH formation channel is more energy demanding than all the others, and hence, the quantum yield of this channel is quite low, for both the compounds, 0.02 for SO, and 0.007 for BMO.

Chapter 6. Conclusion

The kinetic studies offer important data for the process of atmospheric removal of molecules in the atmosphere, which have significant applications. The study of TFEE showed that this compound has quite short lifetime in the troposphere, and hence reasonably small contribution to global warming. Morpholine showed an interesting property of having high bimolecular rate constant, combined with negative activation energy, which could be explained on the basis of pre-reactive adduct formation. These results are important for understanding of general chemical behavior of these compounds in the atmosphere.

Photodissociation dynamics of various classes of compounds was investigated, by mapping the energy partitioning in different states of OH radical. A reasonable amount of information about the photochemical behavior of these species was obtained, and it is observed that formation of OH radical by photodissociation is actually a minor, but very interesting reaction channel for cyclic compounds. The nature of the dissociative potential energy surface for OH formation was elucidated by theoretical studies, and compared with the experimental results.

References

1. P. D. Naik, H. P. Upadhyaya, A. Kumar, A.V. Sapre and J. P. Mittal, Chem. Phys. Lett. **340**, 116 (2001)
2. P. D. Naik, H. P. Upadhyaya, A. Kumar, A.V. Sapre and J. P. Mittal, J. Photochem. Photobiol. C **3**, 165 (2003)
3. A. Mellouki, S. Teton, and G. Le Bras, Int. J. Chem. Kinet. **27**, 791 (1995).
4. M. J. Frisch *et al.*, GAUSSIAN 92, Gaussian Inc., Pittsburgh, PA, 1992
5. S. SenGupta, Y. Indulkar, A. Kumar, S. Dhanya, P. D. Naik, and P. N. Bajaj, J. Phys. Chem. **114** (29) 7709
6. S. SenGupta, Y. Indulkar, A. Kumar, S. Dhanya, P. D. Naik, and P. N. Bajaj, Int. J. Chem. Kinet.s **42** (2010) 519 S. SenGupta, H. P. Upadhyaya, A. Kumar, P. D. Naik, and P. N. Bajaj, J. Chem. Phys. **122,** 124309 (2005)
7. S. SenGupta, H. P. Upadhyaya, A. Kumar, P. D. Naik, and P. N. Bajaj, J. Chem. Phys. **124,** 024305 (2006)

8. S. SenGupta, A. Kumar, P. D. Naik, and P. N. Bajaj, Chem. Phys. Lett. **465**, 197 (2008)
9. A. Kumar, S. SenGupta, K. K. Pushpa, P. D. Naik and P. N. Bajaj, Chem. Phys. Lett. **430**, 240 (2006)
10. S. SenGupta, Y. Indulkar, A. Kumar, P. D. Naik, and P. N. Bajaj, J. Chem. Phys. **128,** 024309 (2008)
11. G. Radhakrishnan, T. Parr, and C. Wittig, Chem. Phys. Lett. **111**, 25 (1984)
12. G. D. Greenblatt, H. Zuckermann, and Y. Haas, Chem. Phys. Lett. **134**, 593 (1986)
13. X. Yue, J. Sun, Q. Wei, H. Yin, and K. Han, Chin. J. Chem. Phys. **20,** 401 (2007)
14. L. J. Butler, D. Krajnovich, Y. T. Lee, G. Ondrey, and R. Bersohn, J. Chem. Phys. **79,** 1708 (1983)
15. E. A. Wade, K. E. Reak, S. L. Li, S. M. Clegg, P. Zou, and D. L. Osborn, J. Chem. Phys. A **110,** 4405 (2006)

List of Tables

List of Figures

Chapter 1

Introduction

The chemical reactions have always been subject of great curiosity and fascination to the human mind, because they are responsible for the existence of naturally occurring compounds, various phenomena taking place in the nature, life in the universe, many important scientific developments in the history of civilisation, as well as the future of mankind. The study of chemistry has evolved through time, its journey starting from the laboratory of the alchemist, and arriving at today's femtosecond labs. Numerous approaches have been devised, to tackle different aspects of chemistry, and their scopes, broad or minute, as per requirement. Thermodynamics and kinetics are the two branches of science which deal with study of the processes in general, and chemical reactions in particular. Thermodynamics predicts the feasibility of a reaction under given condition, because it deals with the initial and the final states of the system. The mechanism by which the system goes from one state to another, and the time required to change are of no importance in thermodynamics, as time is not a thermodynamic variable. Kinetics deals with the details of a process by which the system goes from one state to another, and the time required for the transition, i.e., the rate of the process/reaction, and the factors that influence the rate of the process/reaction. Depending on whether the process is physical or chemical, the kinetics is known as physical or chemical kinetics.

The first theory of gas reactions, i.e., collision theory, postulates that, for the molecules to interact, they must approach each other so closely that it can be said that they are in collision. Though it provided the first insight into a chemical reaction, it had limited success. Because of the inadequacies of the collision theory, H. Eyring and M.

Polanyi proposed the Transition State theory, according to which, every chemical reaction goes through some transition state, or activated complex, and highlighted the role of the internal energies in the rate of reactions. They also established the concept of potential energy surfaces, and used statistical mechanics and quantum chemistry methods, to provide firm theoretical base to chemical kinetics. Subsequently, other theories were proposed, to explain the rate of chemical reactions.

In simple chemical kinetics studies, the measurements are carried out on systems that are in thermal equilibrium, where both translational and internal energies are distributed among the molecules according to Boltzmann's distribution. The rate coefficients so obtained are the gross averages over a number of collisions, leading to the products. These results, which correspond to "bulk" reactions, i.e., a large number of molecules in thermal equilibrium, are dealt by "macroscopic kinetics", or simply "kinetics".

Upon photoexcitation, the molecules undergo various photophysical and photochemical processes. Several experimental and theoretical studies have been devoted to molecular dissociation process, as this is the initiation of many chemical reactions in the atmosphere, and has many applications in the other fields. Dynamics of photodissociation, following electronic excitation of small molecules, wherein dissociation occurs on a timescale comparable to those of molecular vibrations, is an area of current interest. Photodissociation of polyatomics may involve complex dynamics, resulting in dissociation at longer timescale. An excited state that undergoes dissociation at short time usually exhibits a broad absorption spectrum, which gives little or no information on the excited state. Information about the excited state of the parent molecule and the photodissociation dynamics can be obtained from the information of the photofragments. State-resolved measurements, probing the population of the individual states of the photofragments, provide microscopic details about the chemical reactions. Determination of energy disposal in the fragments reveals dynamical information about the dissociation pathways, and nature of the potential energy surface upon which fragmentation occurs. A non-statistical distribution in the energy partitioning indicates direct nature of the reaction, which occurs at a timescale shorter than the rotational period of the molecule. On the other hand, a statistical distribution indicates complex nature of the dissociation mechanism, with dissociation lifetime longer than the rotational period of the molecule. Detailed information about the unimolecular photodisociation obtained by study of its dynamics may also provide ways to control chemical reactions in future.

This chapter, which serves as the introduction to the later chapters of the present thesis, contains brief paragraphs describing the theories and concepts of chemical kinetics and dynamics, which are essential for understanding the advanced studies of chemical kinetics and dynamics. Starting from the very basic concept of the order and the molecularity, it spans over several important areas, like the inherent features of potential energy surfaces and the major physical and chemical properties of the earth's atmosphere.

1.1 Order and Molecularity

The concepts of the order and the molecularity of a reaction are preliminary for understanding chemical reactions.

For a reaction,

$$a\,\mathrm{A} + b\,\mathrm{B} \rightarrow c\,\mathrm{C} + d\,\mathrm{D} \qquad (1.1)$$

Where A, B, C, D are the chemical species and a, b, c, d are the coefficients in the balanced reaction. For most reactions, the rate *r* at time *t* is experimentally found to be related to the concentrations of the species present at that time *t* by an expression of the form,

$$\mathrm{r} = -\frac{1}{a}\left|\frac{dA}{dt}\right| = -\frac{1}{b}\left|\frac{dB}{dt}\right| = k\ |A|^{\alpha}.\,|B|^{\beta} \qquad (1.2)$$

Here, k is the rate coefficient, and α and β are integers, or half integers, the sum of which gives the order of the reaction.

In this case, the reaction is said to have an order of α with respect to A, and β with respect to B. The exponents α and β are called partial orders, and the sum $(\alpha + \beta) = n$ is the overall order, or simply the order of the reaction.

The number of molecules that react in an elementary step is the molecularity of the elementary reaction. Molecularity is defined only for elementary reactions, and should not be used to describe overall reactions which consist of more than one elementary step. The elementary reaction A → products is unimolecular. The elementary reactions, A + B → products and 2A → products, are bimolecular. The elementary reactions, A + B + C → products, 2A+B → products and 3A → products, are trimolecular (or termolecular). Most of the elementary reactions are bimolecular or unimolecular, trimolecular reactions are rare because of the low probability of three-body collisions. No elementary reaction with molecularity of more than three is known because of very low probability of near-simultaneous collision of more than three molecules.

1.2 Rate Determining Step Approximation and Steady State Approximation

Usually an exact deduction of the rate law from the differential equations of a multistep reaction is not possible, because of the mathematical difficulties in dealing with a system of several interrelated differential equations. Therefore, one of the two approximation methods are generally used, the rate determining step approximation and the steady state approximation.

1.2.1 Rate Determining Step Approximation

In the rate determining step approximation, alternatively called the equillibrium approximation, the reaction mechanism is assumed to be consisting of one or more reversible reactions, which remain close to equilibrium most of the time during the reaction, followed by one or more rapid reaction.

$$A + B \underset{k_{-1}}{\overset{k_1}{\rightleftharpoons}} C \qquad (1.3)$$

$$C \xrightarrow{k_2} D \qquad (1.4)$$

For the rate determining step approximation to hold good, $k_{-1} >> k_2$. The latter reaction is, therefore, rate determining.

At equilibrium,

$$k_1[A][B] = k_{-1}[C] \qquad (1.5)$$

Alternatively, the equilibrium constant will be,

$$K_{eq} = \frac{[A][B]}{[C]} \qquad (1.6)$$

Since step (2) is the rate determining step,

$$Rate = k_2[C] = k_2 \frac{[A][B]}{K_{eq}} = k_2 \frac{k_{-1}[A][B]}{k_1} \qquad (1.7)$$

This final form contains only the reacting species, and no intermediates. If the experimental rate law is found to be

$$\text{Rate} = k_{exp}[A][B], \qquad (1.8)$$

$$k_{exp} = \frac{k_2 k_{-1}}{k_1} \qquad (1.9)$$

In other words, the rate constant k_{exp} is really a composite of the rate constants of three elementary processes.

1.2.2 Steady State Approximation

In the case of sequential reactions,

$$\mathrm{A} \xrightarrow{k_1} \mathrm{B} \xrightarrow{k_2} \mathrm{C} \qquad (1.10)$$

it can be seen that, if $k_2 >>> k_1$, the intermediate B reacts the moment it is produced. In this situation, the concentration of B will always be low. It is also the case that once the reaction has got under way, the concentration of B will change very little during the reaction. During most of the time that the reaction is proceeding, we can assume that the concentration of B is constant. Mathematically, this condition is expressed as

$$\frac{d[B]}{dt} = 0 \qquad (1.11)$$

This approximation, that the concentration of an intermediate is not changing, is called the Steady State approximation. When the reaction is proceeding with an intermediate, or intermediates, at constant concentration, the reaction is said to be taking place "in the steady state".

The use of the steady state approximation greatly simplifies solving the differential equations, as it removes the time dependence. The rate of change of B has two terms;

$$\frac{d[B]}{dt} = k_1[A] - k_2[B] \qquad (1.12)$$

the first term is positive, as the first step leads to the production of B, whereas the second is negative, as the second step destroys B. If we assume that B is in the steady state, then,

$$\frac{d[B]}{dt} = k_1[A] - k_2[B] = 0 \tag{1.13}$$

$$[B] = \frac{k_1[A]}{k_2} \tag{1.14}$$

In the steady state, we can use this expression to calculate the rate of formation of products:

$$\frac{d[C]}{dt} = k_2[B] = k_2 \frac{k_1[A]}{k_2} = k_1[A] \tag{1.15}$$

The result is hardly a surprise. For B to be in the steady state, it must react the moment it is formed. In this situation, the first step is rate determining, and the reaction rate just depends on the rate of first step. Our final expression for the rate of formation of products says just this – the rate depends only on k_1.

1.3 Temperature Dependence of Rate Constants: Arrhenius Equation

Rate constants have a strong dependence on temperature, typically increasing rapidly with T. Generally, it has been seen that, for reactions in solution phase near room temperature, *k* doubles or triples, for each 10°C rise in the temperature depending on the activation energy of the reaction. The empirical relation between *k* and temperature was established by Arrhenius. Though in the case of most reactions, k increases with temperature, for some reactions, it has negative or zero temperature dependence. Such reactions generally have some pre-reactive complex, with stability higher than that of the reactants. Such a reaction is studied in details in section 3.4 of this thesis.

In 1889, Arrhenius noted that k(T) data for many reactions fitted the relation,

$$k = A\, e^{-\frac{E_a}{RT}} \tag{1.16}$$

where A and E_a are Arrhenius frequency factor, or pre-exponential factor, and Arrhenius activation energy, respectively, which are constants characteristic of the reaction, and R is the universal gas constant. This relation, which is known as the Arrhenius equation, holds good for nearly all homogeneous elementary reactions and for most composite reactions. A simple interpretation of this equation is that two colliding molecules require certain minimum kinetic energy of relative motion to initiate the breaking of the appropriate bonds, and allow new compounds to be formed. The Maxwell distribution law contains a factor $e^{-\varepsilon/kT}$, and the fraction of collisions in which the relative kinetic energy of the molecules along the line of collision exceeds the value ε_a is equal to $e^{-\frac{\varepsilon_a}{kT}} = e^{-\frac{E_a}{RT}}$, where $E_a = N_A\varepsilon_a$ is the molecular kinetic energy expressed on a per-mole basis.

From the Arrhenius equation, it is clear that a low activation energy means a fast reaction, and high activation energy means a slow reaction. The two theories of reaction rates, namely, Collision Theory and Transition State Theory, yield relations similar to Arrhenius equation, but with A and E_a both dependent on temperature. But, in case of experiments, when E_a>>RT (which is true for most chemical reactions), the temperature dependence of A and E_a are usually too small to be detected by experimental inadequacies unless a wide temperature range is studied.

The observed activation energies lie in the range of 0 to 80 kcal/mol, for most elementary chemical reactions, and tend to be lower for bimolecular than unimolecular reactions. Unimolecular decompositions of compounds, with strong bonds, have very high E_a values. For unimolecular reactions, A is typically 10^{12} to 10^{15} s^{-1}. For bimolecular reactions, A is typically 10^8 to 10^{12} $dm^3mol^{-1}s^{-1}$. Recombination of two radicals to form a polyatomic molecule does not require any bonds to be broken, and hence has zero activation energy, and temperature independent rate constant. The two prominent basic theories of reaction rate of ideal gases, namely, the Hard Sphere Collision Theory and the Transition State Theory, give different relations between the rate constant and temperature.

1.4 Theories of Reaction Rates

Researchers have tried to predict the rate of a reaction by theoretical method since long. In the course of that effort, two theories have emerged as the most prominent, the Hard-Sphere Collision Theory, which is rather crude, and the Transition State Theory, which is more refined. Accurate theoretical prediction of the reaction rates is a largely unsolved problem upon which much research is being carried out currently. This section discusses these two theories, in brief, and also the basic features of potential energy surface which is the most important concept of current day theoretical chemistry. Transition state theory is based on the idea of the potential energy surfaces. The dynamics of a reaction actually bears the signature of the different features on the potential energy surface of the reaction, hence the concept of potential energy surface needs to be understood well, before the importance of dynamics studies can be realized.

1.4.1 Hard-sphere Collision theory

The hard sphere collision theory, developed in the 1920s, uses the following assumptions, to arrive at an expression for the rate constant of an elementary bimolecular gas-phase reaction.

(I) The molecules are hard spheres. This is a very crude assumption, because polyatomic molecules are not spherical, and the hard sphere potential function completely lacks the real features of intermolecular interactions.

(II) For a reaction to occur between molecules B and C, the molecules must collide.

(III) Not all collisions result in reaction. Instead, reaction occurs, if and only if the relative translational kinetic energy along the line of center of the colliding molecules exceeds a threshold energy ε_{thr}. In most of the reactions, the threshold energy (or the experimental activation energy) is much greater than the mean molecular translational energy 1.5kT. Typical gas-phase bimolecular activation energies are 3 to 30 kcal/mol, compared with the value of 0.9 kcal/mol for 1.5kT at room temperature. Consequently, only a tiny fraction of the collisions produce reaction.

(IV) The Maxwell Boltzmann distribution of energy is maintained during the reaction. Since the collision rate is far greater than the depletion of high energy molecules, the redistribution of energy by the collisions is able to maintain the Maxwell Boltzmann energy distribution.

Using this theory, the calculation of reaction rate eventually boils down to the calculation of rate of collisions, for which the relative line-of-centres translational energy (ε_{lc}) exceeds threshold energy ε_{thr} for a reaction between molecules B and C. After detailed calculations, the final expression for rate constant is obtained as:

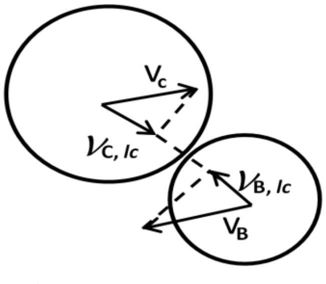

Fig.1.1: Line of centre components, $v_{C,lc}$ and $v_{B,lc}$ of the velocities of two colliding moleules

$$\mathrm{k}=\mathrm{N_A}\pi\,(\mathrm{r_B}+\mathrm{r_C})^2\left[\frac{8\mathrm{RT}}{\pi}\left(\frac{1}{\mathrm{M_B}}+\frac{1}{\mathrm{M_C}}\right)\right]^{1/2}\mathrm{e}^{-\mathrm{E_{thr}}/\mathrm{RT}} \qquad \text{(for B} \neq \text{C)} \qquad (1.17)$$

$$\mathrm{k}=\frac{1}{2^{\frac{1}{2}}}\,\mathrm{N_A}\pi\mathrm{d_B^2}\left(\frac{8\mathrm{RT}}{\pi\mathrm{M_B}}\right)^{\frac{1}{2}}\mathrm{e}^{-\mathrm{E_{thr}}/\mathrm{RT}} \qquad \text{(for B = C)} \qquad (1.18)$$

Where, r_B, r_C and M_B, M_C are the radii and mass of particles B and C respectively, d_B is the diameter of B, R is universal gas constant and N_A is the Avogadro’s number. Again, the activation energy for equations (1.17) and (1.18). is defined by,

$$E_a = RT^2\frac{d}{dt}(\ln k) = RT^2\left(\frac{1}{2T}+ E_{thr}/RT^2\right) \qquad (1.19)$$

$$\mathrm{E_a}=\mathrm{E_{thr}}+\mathrm{RT} \qquad (1.20)$$

The pre-exponential factor is

$$\mathrm{A}=\mathrm{N_A}\pi\,(\mathrm{r_B}+\mathrm{r_C})^2\left[\frac{8\mathrm{RT}}{\pi}\left(\frac{1}{\mathrm{M_B}}+\frac{1}{\mathrm{M_C}}\right)\right]^{1/2}\mathrm{e}^{1/2} \qquad \text{(for B=C)} \qquad (1.21)$$

Since ½ RT is small, the hard sphere activation energy is nearly the same as the threshold energy. The simple collision theory provides no means to calculate $E_{thr,}$ but gives only the value of A.

For most of the reactions, the calculated A values are much higher than the observed ones. Hence the right side of equation (1.21) is multiplied by a steric factor *p*, to match the calculated value with the measured value. *p* is supposed to denote the fraction of molecules which have the proper orientation for the collision to become reactive. The idea of proper orientation is valid, but *p* also includes contributions that arise from using hard sphere potential and from ignoring molecular vibrations and rotations. Typical *p* values vary from 1 to 10^{-6}, tending to be smaller for reactions involving bigger molecules, and vice versa.

The form of equation (1.17) is similar to that of Arrhenius equation, except for the fact that, the pre-exponential factor has a temperature dependence of $T^{1/2}$. But, because of the crudity of this theory, the temperature dependence should not be taken seriously.

1.4.2 Potential Energy Surfaces

The hard sphere collision theory does not give accurate rate constants, because it ignores the internal structures and the true intermolecular forces between the reacting molecules. During a molecular collision, the force on a given atom depends on both the internal and the external forces. Using Molecular Orbital Theory, the energy of a

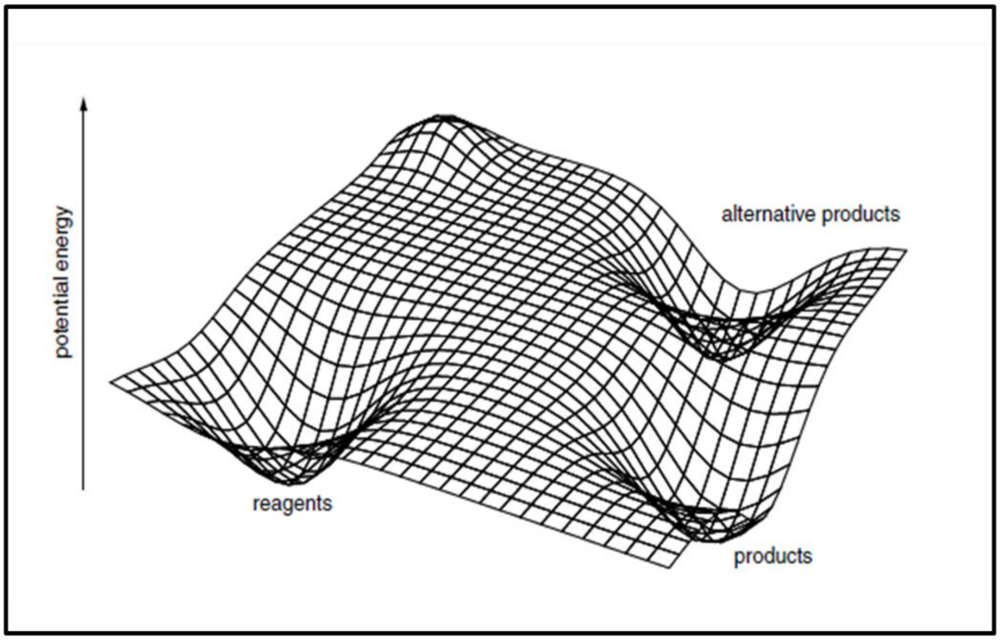

Fig. 1.2: A typical potential energy surface shown in 3 dimensions, with the reactants, the products, and alternative product wells. Generally, potential energy surfaces are in n-dimensional hyperspace, with multiple local minima for products and reactants.

molecule, or any arbitrary arrangement of nuclei, can be calculated, in principle. The energies of the individual MOs are found out, electrons are assigned to them, and hence, the overall electronic energy of the system is calculated.

As two molecules, B and C come together, and start to interact, the energy of the system can be calculated at each step. Initially, when the molecules are far apart, the energy of the system will simply be the sum of that of the two isolated molecules. However, as they approach each other, the total energy will depend on how the electrons and nuclei of the two molecules interact. Eventually, a transition state will be achieved, the energy of which can also be calculated. Finally, as the product molecules move apart, the energy will tend to be the sum of the energies of the products. Hence, we shall get an idea about how the total energy of the system varies continuously as a function of positions of all the atoms in the system. This is a potential energy surface (PES) of a system. For all, but the simplest molecules, potential energy surface is a function of very large number of angles and distances, i.e., it is a multidimensional surface in the hyperspace. The Potential Energy Surface (PES) is essential for the understanding of chemical reactions. The atoms can be imagined to start from a particular minimum on the surface, which corresponds to the reactants, move along some path over the surface, as these rearrange themselves, and end up in a minimum, which corresponds to the products. There can be several minima on a surface; some local minima and one global minimum (Fig. 1.2).

When the reactants and the products are stable species, i.e. they are at some potential energy minima, extra energy will always be required in order to traverse the path between them, the amount of which will depend on the features of the potential energy surface, and the pathway travelled. Of the many possible paths which lead from reactants to products, the one that requires minimum energy will be the most favoured pathway. The point of highest energy on this pathway is called the Transition State (TS). The reason for the reaction to take the minimum energy pathway lies in the way energy is distributed among the molecules. If E_a be the difference between the energies of the reactant and the transition state, the fraction of molecules which, at any instance, will have this amount of energy is given by Boltzmann's distribution as [exp($-E_a$/RT)]. Since this is an exponential function in energy, even a small increase in E_a greatly decreases the number of the molecules with the required extra energy. Thus, a very few molecules can afford to take a pathway other than the minimum energy route, and it can be safely assumed that all reactants which go to the products, do so via the minimum energy pathway. It is essential to understand the concept of potential energy surface, before going into the other major theory of reaction rate, i.e., the Transition State theory.

1.4.3 Transition State Theory for Ideal Gas Reactions

The rigorously correct way to theoretically calculate the rate constant (k) of a reaction is to solve the electronic (time-independent) Schrodinger's equation for a very large number of configurations of the nuclei, so as to generate the complete potential energy surface of the reaction, and then to use this surface to perform classical trajectory calculations for a wide variety of initial reactant states, and suitably average the results to obtain k. Alternately, one can deal with the collisions, using the time-dependent Schrodinger's equation, instead of the classical mechanics.

The difficulty and tediousness of this method can be modified to simpler and approximate theory of rate constants by using the Transition State Theory (TST), also called Activated-Complex Theory (ACT), developed by E. H. Eyring and M. Polanyi. TST eliminates the need of trajectory calculations, and requires the potential energy surface to be known only at the regions of the reactants and the transition state.

The TST chooses a boundary surface located between the reactant and the product regions, and assumes that all the supermolecules (which are assemblies of reacting molecules) which cross this boundary surface from the reactant side, become products. The boundary surface, called the critical dividing surface passes through the saddle point of the potential energy surface, and hence, it is a downhill path from there to the products. The second assumption of TST is that, during the reaction, the Boltzmann's distribution of energy is maintained for the reactant molecules. The third assumption is that the supermolecules crossing the critical surface from the reactant side have a Boltzmann's distribution of energy corresponding to the temperature of the system.

Let the elementary ideal gas equation be,

$$B + C \rightarrow E + F \qquad (1.22)$$

The reaction may have any molecularity, so B + C can also be considered as B.

An activated complex is any supermolecule whose nuclear configuration corresponds to any point on the dividing surface, or any point within a short distance δ beyond the dividing surface. We expect that most of the activated complexes will have configurations reasonably close to the saddle point configuration. The saddle point corresponds to the “equilibrium” structure of the activated complex, and the points on the dividing surface near the saddle point correspond to the “vibrations” about the equilibrium structure. A given activated complex exists only momentarily, and does not actually undergo repeated bending and stretching vibrations. Instead, since supermolecules cross the dividing surface at various points, any given activated complex is considered to be in a vibrational state that corresponds to the point at which the dividing surface is crossed. TST assumes these vibrational states to be populated according to the Boltzmann’s distribution. The term transition state is most commonly used for referring to the “equilibrium configuration” of the activated complex. Denoting the activated complex as $\{X_f^{\#}\}$, the elementary reaction can be written as,

$$B + C \rightarrow \{X_f^{\#}\} \rightarrow E + F \qquad (1.23)$$

The subscript “f” in $\{X_f^{\#}\}$ denotes that it is the activated complex for the forward reaction, and similarly, for the reverse reaction, the activated complex, which crosses the dividing barrier at the reverse direction, will be denoted as $\{X_b^{\#}\}$. $\{X_b^{\#}\}$ is of no concern to us, because we are considering only the forward reaction.

According to the postulate of TST, when all the reactants and activated complex are present, with each species distributed among its energy states according to the Boltzmann’s distribution law, then,

$$\frac{N_f^{\#}}{N_B.N_C} = \frac{Z_{\#}}{Z_B.Z_C} \exp\left(-\Delta\varepsilon_0^{\#}/kT\right) \qquad (1.24)$$

where, $N_f^{\#}$, N_B and N_C are the numbers of molecules of $X_f^{\#}$, B, and C respectively, and where $Z_{\#}$, Z_B and Z_C are the corresponding molecular partition functions of. In this case,

$$\Delta\varepsilon_0^{\#} \equiv \varepsilon_0(X_f^{\#}) - \varepsilon_0(B) - \varepsilon_0(C) \tag{1.25}$$

is the difference of the energy between $X_f^{\#}$, in its lowest state, and the energies of the reactants, in their lowest states. Dividing each N in equation (1.24) by N_AV, to convert it to a molar concentration, the equation can be written as,

$$K_f \equiv \frac{[X_f^{\#}]}{[B].[C]} = \frac{Z_{\#}/N_AV}{(Z_B/N_AV).(Z_C/N_AV)}\ exp\ (-\Delta\varepsilon_0^{\#}/kT) \tag{1.26}$$

From equation (1.26), it can be said that the activated complex is in equilibrium with the reactants, but it is actually not a true chemical reaction equilibrium. Instead, the activated complexes can be considered to be in thermal equilibrium with the reacting system, their energy states being populated according to Boltzmann’s distribution.

A nonlinear activated complex, with N number of atoms, has three rotational, three translational and 3N-6 vibrational degrees of freedom, the sum of which is equal to the number of co-ordinates for its potential energy surface. The saddle point, on which it lies, is a minimum point of potential energy on one particular co-ordinate and a point of maximum energy on all the others. Because the potential energy slopes downhill along both directions from the saddle point, nuclear motion or “vibration” along this co-ordinate breaks up the complex into the products, and hence a “normal” vibrational mode along this co-ordinate has no meaning. The partition function of the activated complex is given by $z_{\#} = z_{tr}^{\#}.\ z_{rot}^{\#}.\ z_{vib}^{\#}.\ z_{el}^{\#}$. Singling out the reaction co-ordinate, for special treatment, we can write $z_{vib}^{\#} = z_{rc}.\ z_{vib}^{\#'}$ where, z_{rc} is the partition function for the anomalous motion along the reaction co-ordinate and $z_{vib}^{\#'}$ is the partition function for the ordinary vibration modes. $z_{vib}^{\#'}$ is the product of partition functions of 3N-7 or 3N-6 number of co-ordinates, depending on whether the activated complex is linear or not. Therefore,

$$z_{\#} = z_{rc}.z'_{\#} \qquad (1.27)$$

$$z'_{\#} = z^{\#}_{tr}.z^{\#}_{rot}.z^{\#\prime}_{vib}.z^{\#}_{el} \qquad (1.28)$$

On the saddle point, which is a maxima, potential energy (V) does not change with displacement δ along reaction co-ordinate (Q_{rc}). Hence, the potential energy, is nearly constant over the distance δ that defines the region of activated complex. Since δ will cancel out in the final expression of the rate, it need not be specified with much detail, except for defining it as small enough, so that V does not vary significantly with $Q_{rc.}$ With V constant along the reaction co-ordinate, the force component ($F= - \partial V/\partial Q_{rc} \approx 0$) along the reaction co-ordinate is almost zero. The motion of the activated complexes along the reaction co-ordinate is hence considered as an one-dimensional translational motion of a free particle confined to a region marked by δ. Translational motion along the reaction co-ordinate is an internal motion of the activated complex nuclei relative to each other, and is not same as the ordinary translational motion of the activated complex as a whole through three dimensional space. The former motion corresponds to z_{rc}, whereas the later corresponds to $z_{tr}^{\#}$.

The partition function of a free particle moving in box of length a is given by, $(2\pi mkT)^{1/2}a/h$. Replacing a by δ, and m by m_{rc}, where m_{rc} is the effective mass for the motion along the reaction co-ordinate, we get, $(2\pi m_{rc}kT)^{1/2}\delta/h$. The partition function covers all the states, but since we are ignoring motion in the reverse direction along the reaction co-ordinate, half of the possible states are missing. We, therefore, have to consider a factor of ½, to get z_{rc} for $X_f^{\#}$. Thus,

$$z_{rc} = \frac{1}{2}(2\pi m_{rc}kT)^{1/2}\delta/h \tag{1.29}$$

$$z_{\#} = \frac{1}{2}(2\pi m_{rc}kT)^{1/2}\delta h^{-1}z_{\#}^{'} \tag{1.30}$$

Since TST assumes that all the molecules which cross the dividing surface, become products, the reaction rate is same as the rate at which they cross the surface. Let $v_{rc} = dQ_{rc}/dt$ be the velocity component of a given activated complex along the reaction co-ordinate. At a given time t_0, let there be $N_f^{\#}$ activated complex in the system, and τ be the average time needed for the activated complex to move a distance δ along Q_{rc}. At time $t_0 + \tau$, all the $N_f^{\#}$ activated complexes would cross the critical surface, and become products. The reaction rate is, therefore, $N_f^{\#} / \tau$. But $\tau = \delta / <v_{rc}>$ (where $<v_{rc}>$ is the average value of v_{rc}), so the reaction rate is $N_f^{\#}<v_{rc}>/ \delta$, in units of molecules per unit time. In kinetics, generally, moles per unit time is used as a unit, and in that case, dividing by N_A, to convert to moles, and by V, to get the rate per unit volume, we have,

$$r = N_f^{\#}<v_{rc}>/ N_A V \delta = [X_f^{\#}]<v_{rc}>/\delta \tag{1.31}$$

Using equation (1.26), we get

$$r = \frac{<v_{rc}>}{\delta}\frac{z_{\#}/N_AV}{\left(\frac{z_B}{N_AV}\right)\left(\frac{z_B}{N_AV}\right)\ldots\ldots\ldots\ldots}\exp(-\Delta\varepsilon_0^{\#}/kT)\,[B][C]\ldots\ldots\ldots \tag{1.32}$$

The motion along Q_{rc} is being treated as a translation. As with the other degrees of freedom of the activated complex, we assume Boltzmann distribution of energy along this translation. Hence, the fraction of complexes with speed along Q_{rc} in the range v_{rc} to v_{rc} + dv_{rc}, is $Be^{-m_{rc}v_{rc}^2/2kT}dv_{rc}$, where B is a constant. To find B, this expression is integrated from $v_{rc} = 0$ to ∞, and the total probability is set as 1. Hence,

$$B\int_o^\infty e^{-m_{rc}v_{rc}^2/2kT}dv_{rc} = 1 \tag{1.33}$$

which gives, $B=2(m_{rc}/2\pi kT)^{1/2}$. The probability density $g(v_{rc})$ for v_{rc} , is, therefore,

$$g(v_{rc}) = 2(m_{rc}/2\pi kT)^{1/2}e^{-m_{rc}v_{rc}^2/2kT} \tag{1.34}$$

The average value of v_{rc}, by the definition, is, $< v_{rc} >= \int_0^\infty v_{rc}g(v_{rc})\,dv_{rc}$, which gives,

$$< v_{rc} >= (2kT/\pi m_{rc})^{1/2} \tag{1.35}$$

Substitution of (1.30) and (1.34) into (1.32) gives,

$$r = \frac{1}{\delta}\left(\frac{2kT}{\pi m_{rc}}\right)^{1/2}\frac{(2\pi m_{rc}kT)^{1/2}\delta}{2h}\,\frac{z_{\#}^{'}/N_AV}{\left(\frac{z_B}{N_AV}\right)\left(\frac{z_C}{N_AV}\right)}exp\left(-\frac{\Delta\varepsilon_0^{\#}}{kT}\right)[B][C] \tag{1.36}$$

For the elementary reaction B + C →$\{X_f^{\#}\}$→ E + F, the reaction rate is $r = k_r[B][C]$. So,

$$k_r = \frac{kT}{h}\,\frac{z_{\#}^{'}/N_AV}{\left(\frac{z_B}{N_AV}\right)\left(\frac{z_C}{N_AV}\right)}exp\left(-\frac{\Delta\varepsilon_0^{\#}}{kT}\right) \tag{1.37}$$

This is the desired TST expression for the rate constant of an ideal gas elementary reaction.

The temperature dependence of the partition functions are given as,

$z_{tr}\,\alpha\,T^{\frac{3}{2}}$ (1.38a), $z_{rot,lin}\,\alpha\,T$ (1.38b)

$z_{rot,nonlin}\,\alpha\,T^{\frac{3}{2}}$ (1.38c), $z_{el}\,\alpha\,T^0$ (1.38d)

The temperature dependence of z_{vib} is not so simple. At temperatures such that $kT \ll h\nu_s$ for all ν_s, $z_{vib} \,\alpha\, T^{f_{vib}}$, where f_{vib} is the number of vibrational modes of a molecule. For an intermediate temperature, $z_{vib} \,\alpha\, T^b$, where b is between 0 and f_{vib} . For most of the vibrations, ν_s is sufficiently high for the condition $kT \gg h\nu_s$ to be reached only at quite high temperatures. For a moderate temperature, we can expect that,

$$z_{vib} \,\alpha\, T^a \qquad \text{Where } 0 \leq a \leq \frac{f_{vib}}{2} \tag{1.39}$$

Over a restricted temperature range, each z_{vib} will have its a value approximately constant, and we can write

$$k_r \approx CT^m \exp(-\Delta E_0^{\#}/RT) \tag{1.40}$$

Where C and m are constants, and where $\Delta E_0^{\#} = N_A \, \Delta\varepsilon_0^{\#}$

Using the temperature dependence of the partition functions, the value of m can be calculated. For a bimolecular gas phase reaction between a molecule and an atom, the value of m lies between -0.5 and 0.5. For a bimolecular gas phase reaction between two molecules, m lies between -2 and 0.5.

From equation (1.19) and (1.39), we get activation energy as,

$$E_a = \Delta E_0^{\#} + mRT \tag{1.41}$$

Since m can be negative, E_a can be less than, same, or greater than $\Delta E_0^{\#}$. The quantity $\Delta E_0^{\#}$ differs from the classical barrier height E_b by $\Delta ZPE^{\#}$, the change in zero point energy by formation of the complex. Since $\Delta ZPE^{\#}$ can be negative, zero, or positive, E_a can be less than, equal or greater than E_b.

1.4.4 The Relation Between Hard Sphere Collision Theory and Transition State Theory

For a bimolecular reaction, B + C → products, (with B ≠ C), if we ignore the internal structure of the colliding molecules, and treat them as hard spheres of radii r_B and r_C. Then, the reactant's partition functions are $z_B = z_{tr\ B}$ and $z_C = z_{tr,C}$.

$$\frac{z_B}{V} = (2\pi m_B kT/h^2)^{3/2} \tag{1.41a}$$

$$\frac{z_C}{V} = (2\pi m_C kT/h^2)^{3/2} \tag{1.41b}$$

If the transition state is considered as the two hard spheres in contact, the "diatomic" transition state will have zero vibrational modes, as the only vibrational mode is replaced by the reaction co-ordinate. If spheres of masses m_B and m_C are separated by centre-to-centre distance $r_B + r_C$ in the transition state, then the moment of inertia is $I = \mu\ (r_B + r_C)^2$. In that case, the partition function of the activated complex is:

$$\frac{z'_{\#}}{V} = \frac{z^{\#}_{tr}}{V} z^{\#}_{rot} = \left[\frac{2\pi(m_B + m_c)}{h^2}\right]^{\frac{3}{2}} 8\pi^2 \frac{m_B m_C}{m_B + m_C} (r_B + r_c)^2 \frac{kT}{h^2} \tag{1.42}$$

Substitution for z_B, z_C, and $z^{\#'}$ in equation (1.36) gives,

$$k = N_A \pi\ (r_A + r_B)^2 [\frac{8kT}{\pi M_B}\ (\frac{1}{M_B} + \frac{1}{M_C})]^{1/2} e^{-\Delta\varepsilon_0^{\#}/kT} \tag{1.43}$$

Which is identical to the hard sphere collision theory result for B ≠ C, if we take $\Delta\varepsilon_0^{\#}$ to be the threshold energy $\varepsilon_{thr} = E_{thr}/N_A$. Thus, the transition state reduces to the hard sphere collision theory when the structure of the molecules is ignored.

1.5 Molecular Reaction Dynamics

Molecular dynamics, which is a natural outgrowth of the long-standing attempts to explore the elementary chemical act, by now, has become a field in its own right, with chemical dynamics as its major sub-discipline. The latter serves as the foundation of macroscopic chemical kinetics, as well as a rich source of new knowledge of the basic phenomena involved in the elementary chemical act. When a reaction is studied in bulk phase, the products collide with other molecules, energy is transferred upon collisions (thus being effectively partitioned among all molecules), and the overall reaction exoergicity is finally liberated in its most degraded form, that is, heat. In macroscopic terms, the reaction is exothermic. The microscopic approach of molecular dynamics, however, is concerned with the outcomes of the individual reactive collisions. Thus, the techniques usually involve measurements at very low pressures, often employing fast flow arrangements for very short times. The newly formed products are, therefore, prevented from undergoing excessive collisional relaxation. Alternatively, rather than trying to prevent relaxation over the (comparatively long) timescale for spontaneous emission in the infrared, we can either induce emission, or determine the concentration of the molecules in different levels by light absorption.

The study of elementary processes has already proved to be of practical utility in many areas of physics and chemistry. One example is the development of chemical laser, where the specific energy release, found in many exoergic reactions, such as Cl + HI, and F + H_2, among others, is exploited to create population inversion. An understanding of elementary processes is also important for manipulation of a variety of the environmental phenomena, e.g., atmospheric and ionospheric chemistry, combustion and air pollution.

These involve a complex web of series and parallel elementary steps comprising the overall system of reactions. Many of the elementary processes are fast reactions, yielding products in a state of disequilibrium. The nascent products of such exoergic elementary reactions are often disproportionately energy rich. In particular, if one of the ‘slow steps’ in the overall scheme has an activation barrier, its rate may be very much enhanced, if one of the reactants has an abnormally large population of the excited states. In many cases, such reactions are highly selective in their energy requirements. Frequently, vibrational energy is more effective than relative translational energy in overcoming the barrier.

The realization that elementary reactive events can really be studied only under single-collision conditions, led to the development of modern molecular dynamics. It is another advanced step in the attempt to probe the molecular mechanism of chemical reactions. The dynamics of single molecular collisions are of interest not only for understanding chemical reactivity, but also because these are involved in all systems involving gases and fluids in a state of disequilibrium, whether chemical or physical. Just as reactive collisions can produce disequilibrium, nonreactive collisions provide the mechanism for bringing back the equilibrium condition.

A reaction path is defined as the line of minimal energy from the reactant to the product valley. For a simple atom-diatomic molecule elementary reaction, like A + BC → AB + C, if the barrier lies near the reactant valley on the reaction path, and the exoergicity is released early, then the potential energy surface of the reaction is called “attractive”, and the surface of the opposite kind, i.e., when the energy is released late along the reaction path, is called “repulsive”. Generally, along an attractive surface, the exoergicity is pumped into the vibration of the new emerging bond(s), whereas in the other case, it is mostly partitioned to the relative translational energy of the products. A useful, but not invariable, correlation is that exoergic reactions will have an early barrier. For reactions with a potential energy barrier, energy consumption is also highly selective. From the theories of Eyring, Polanyi, Evans and others, it can be seen that, for given reactant masses (and not too high energies), the efficiency of the conversion of the reaction exoergicity into product vibration will be greater for a more attractive potential

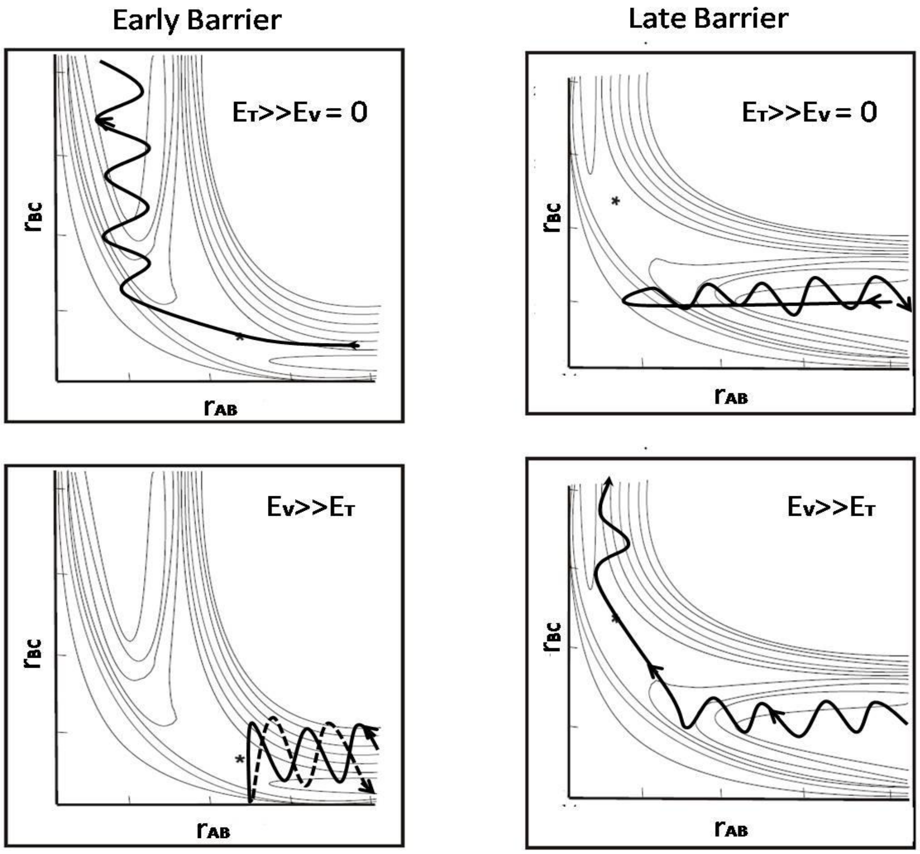

Fig.1.3: Influence of reactant energy on $A+BC \rightarrow AB+C$ reaction on a surface with a barrier (*). When the relative translational energy is high, (top row), there is ample kinetic energy for motion along R_{AB}. Reaction thus occurs for early barrier, but fails for late barrier. The opposite is true, when BC has high vibrational energy, but low kinetic energy (bottom row).

energy surface. In this case, there is a correlation between the position of the barrier on the reaction path and the initial energy most conducive to reaction. Translational energy is most effective for passage across an early barrier, whereas vibrational energy of the reactant molecules is more effective for surmounting a late barrier. These requirements can be interpreted by availability of kinetic energy along the proper co-ordinate. For an early barrier, one requires momentum along r_{AB}, whereas to overcome a late barrier, energy is required along r_{BC} co-ordinate. The energy requirements of the reaction becomes less restrictive at higher collisional energies, where an efficient interchange of vibrational and translational along the reaction path is more likely. Figure 1.3. is a pictorial representation of typical energy requirements, and disposal of the different types of potential energy surfaces with a barrier.

1.6 Study of Fast Reactions

Experiments for measuring kinetic and dynamic parameters of a reaction involves direct measurement of concentration of the reacting species or the products. Whatever method we choose for monitoring the concentration of the reacting species, we also have to consider how the reagents are going to be mixed, and the reaction initiated. This is a serious problem for fast reactions. Further, our method for measuring concentration should be fast enough for making measurements over the time scale of the reaction. Some of the methods which have been designed for tackling such problems are as follow.

1.6.1 Continuous Flow Method

In this method, the reagents in fluid state (liquid or gas) are flown together, and after mixing, they continue to flow down the reaction tube (Fig.1.4). The different distances along the tube correspond to different times after mixing and initiating the reaction. The mixing is generally completed under 1 ms, so reactions with half-lives in the ms timescale can be studied in this method. Usually, the detection techniques are spectroscopic, which are rapid technique. The main disadvantage of these techniques is that large amounts of reagents are required.

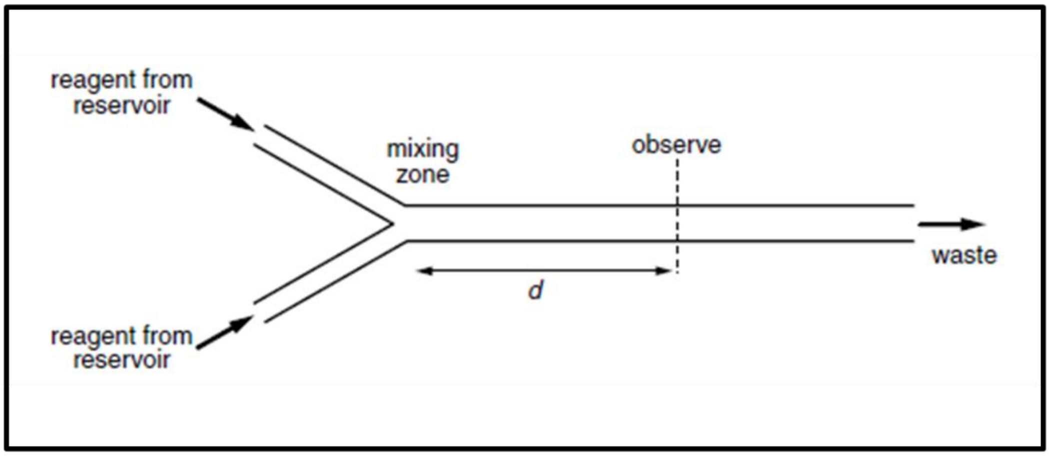

Fig. 1.4: Schematic diagram of a typical continuous flow set-up

1.6.2 Stopped Flow Method

This method, which is conceptually similar to continuous flow, allows rapid mixing of the reagents, but instead of continuous flow, in this case, the reacting mixture pushes a plunger back until it stops (Fig. 1.5). The measurements are made at this point with the halted flow where mixing is complete. This method allows measurements in real time, and large amounts of reagents are not required, unlike continuous flow method**.** Generally, the time resolution in stopped flow method is better than that in the continuous flow method, but this method can only be used in liquid phase.

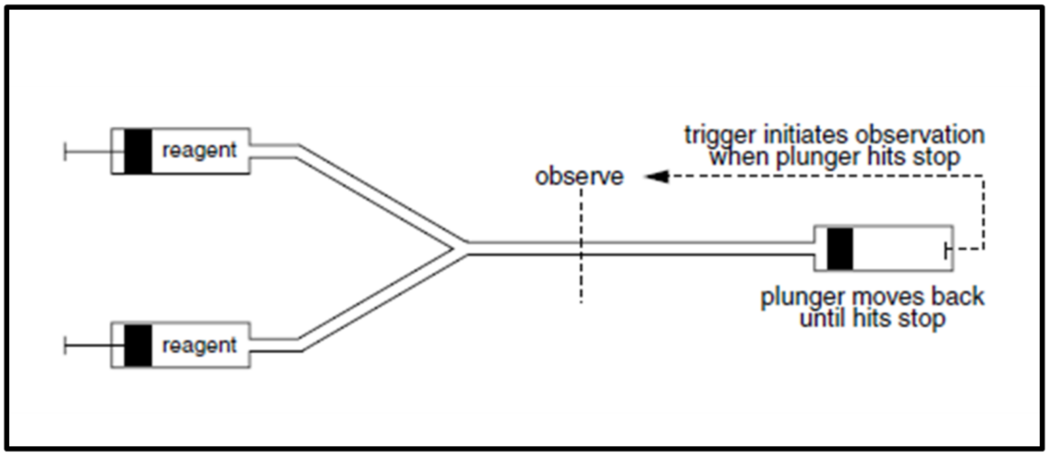

Fig. 1.5: Schematic diagram of a typical stopped flow set-up

1.6.3 Flash Photolysis

In this method, a short, intense flash of light (flashlamp or laser) is used to generate short-lived reacting species (generally free radicals) in situ, and hence, there is no problem of mixing. Then, the reaction of these species with other reactants present in the system is monitored, usually, spectrophotometrically. This method is very useful for studying fast reaction involving radicals. After the advent of sophisticated laser techniques, a lot of progress could be made in the studies of kinetics and dynamics of reactions in the gas phase, involving short-lived species, like free radicals. The method that has been used for all the experimental works described in this thesis, i.e., Laser Photolysis Laser–Induced Fluorescence (LP-LIF), falls under this category. In this method, a strong short pulse of UV laser is used to generate OH radical, and Laser Induced Fluorescence from the same OH radicals is detected, to monitor their reactions with other molecules.

1.7 Important Physical Processes in Electronically Excited Molecules

Since our work involves the excitation of molecules to higher energy states by absorption of photon energy from a laser source, prior to photodissociation, and then, again probing the products of the photodissociation, by absorption of photons from another laser source, we should have a clear idea about the basic properties of the electronically excited molecules. A molecule excited to a higher electronic state can either come back to the ground state, by some physical processes, or can get involved in a photochemical process from the initially excited state itself, or from a lower excited state, eventually losing its identity. The physical pathways of the transitions among the different electronic states are termed as photophysical processes. Some of these processes are intrinsic properties of the molecule, whereas some others depend on external perturbations, and involve bimolecular processes. All processes occur in a time period less than the natural radiative lifetime of the molecule, and priorities are based on their relative rate constants.

After the initial act of absorption,

$$A + h\nu \rightarrow A'^{*} \qquad (1.45)$$

where A'* is either an electronically excited molecule with excess vibrational energy in S_1 state, or a molecule excited to any of the higher singlet states, S_2, S_3 etc. The various photophysical processes that can take place, after the initial excitation, are listed as:

Unimolecular

$A'^{*} \rightarrow A^{*}$ + heat	Internal conversion (IC)	$S_n \rightsquigarrow S_1$	(1.46)
$A^{*} \rightarrow A$ + heat	Internal conversion (IC)	$S_1 \rightsquigarrow S_0$	(1.47)
$A^{*} \rightarrow A + h\nu_f$	Fluorescence emission	$S_1 \rightarrow S_0$	(1.48)
$A^{*} \rightarrow {}^{3}A$ + heat	Intersystem crossing (ISC)	$S_1 \rightsquigarrow T_1$	(1.49)
${}^{3}A \rightarrow A + h\nu_p$	Phosphorescence emission	$T_1 \rightarrow S_0$	(1.50)
${}^{3}A \rightarrow A$ + heat	Reverse intersystem crossing	$T_1 \rightsquigarrow S_0$	(1.51)

Bimolecular

$A^{*} + S \rightarrow A$ + heat	Solvent quenching	(1.52)
$A^{*} + A \rightarrow 2A$ + heat	Self quenching	(1.53)
$A^{*} + Q \rightarrow A + Q$ + heat	Impurity quenching	(1.54)
$A^{*} + B \rightarrow A + B^{*}$	Electronic Energy Transfer	(1.55)

A^*, ${}^3A$ and A are molecules in the first excited singlet state, the triplet state and the ground state, respectively. In radiationless processes, such as internal conversion and intersystem crossing, the excess energy is lost to the environment as thermal energy. Fig.1.6 shows a Jablonski diagram, which is a pictorial representation of most of these photophysical processes discussed above.

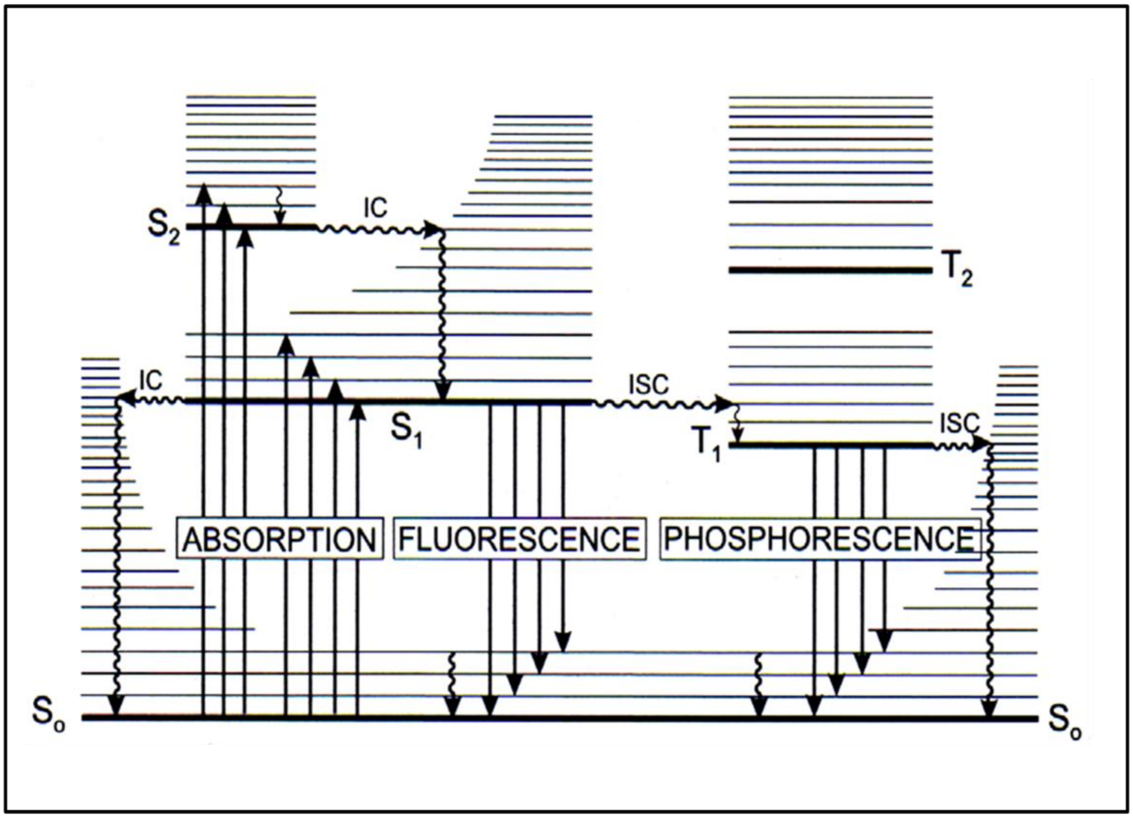

Fig. 1.6: Jablonski Diagram showing the important photophysical processes taking place, after absorption of photon by a molecule. Radiative processes are shown by straight arrows, whereas non-radiative processes are shown by curly arrows.

1.8 Electronic Spectrum of Diatomic Molecule

In a diatomic molecule, such as OH, the motion of electrons takes place in a field of cylindrical symmetry, unlike in an atomic system, where the field is spherically symmetrical. In this case, the electrostatic field of the two nuclei is directed along the internuclear axis. The precession of the orbital angular momentum vector about this field, which is aligned along the internuclear axis, gives the component, $M_L(h/2\pi)$, where M_L has values from -L to +L. Because of the electrostatic nature of the field, the states with same M_L values, but different signs, are degenerate, implying different states with same energy. These different values of M_L are represented by Λ, which is given by,

$$\Lambda = | M_L| \qquad (1.56)$$

Therefore, for a given value of L, there are L +1 values of Λ, representing L + 1 different energies. According to international nomenclature, Λ = 0,1,2,3…….are designated as **Σ, Π, Δ, Φ,** ….. states, respectively.

As in atoms, the spins of the individual electrons in the molecule give the resultant spin S, which refers to the orientation of the angular spin momentum. In the case of Λ = 0, i.e., Σ state, the resultant spin is oriented in a fixed space, as long as the molecule does not rotate. In other cases, (Λ ≠ 0), the internal magnetic field on the internal nuclear axis, resulting from the orbital angular motion, causes the precession of S around it. It is designated as Σ, and quantum theory allows (2S + 1) different values for it.

The algebraic addition of Λ, the orbital angular momentum along the internuclear axis, and Σ, electronic spin angular momentum along the internuclear axis, gives the total electronic angular momentum, Ω, about the internuclear axis:

$$\Omega = |\Lambda + \Sigma| \qquad (1.57)$$

The electronic term symbol of the diatomic species is designated as ${}^{2s+1}\mathbf{\Lambda}_{\Omega}$.

According to this nomenclature, the ground electronic state of OH is ${}^2\Pi$, and the first electronic excited state is ${}^2\Sigma$. The interaction of the electronic spin and the orbital angular momentum splits each rotational state, with Λ ≠ 0, into two spin orbit states. Thus, for the ground state of OH, the two spin-orbit states are $2\Pi_{1/2}$ and ${}^2\Pi_{3/2}$. At a high rotational quantum number, the rotational angular momentum interacts strongly with the electronic angular momentum, and lifts the degeneracy of the $\Lambda \neq 0$ states, which are doubly degenerate, giving the two components, Λ^+(A') and Λ^-(A"). The relative populations of these two spin-orbit states and Λ doublet states provide important information on dynamics of dissociation.

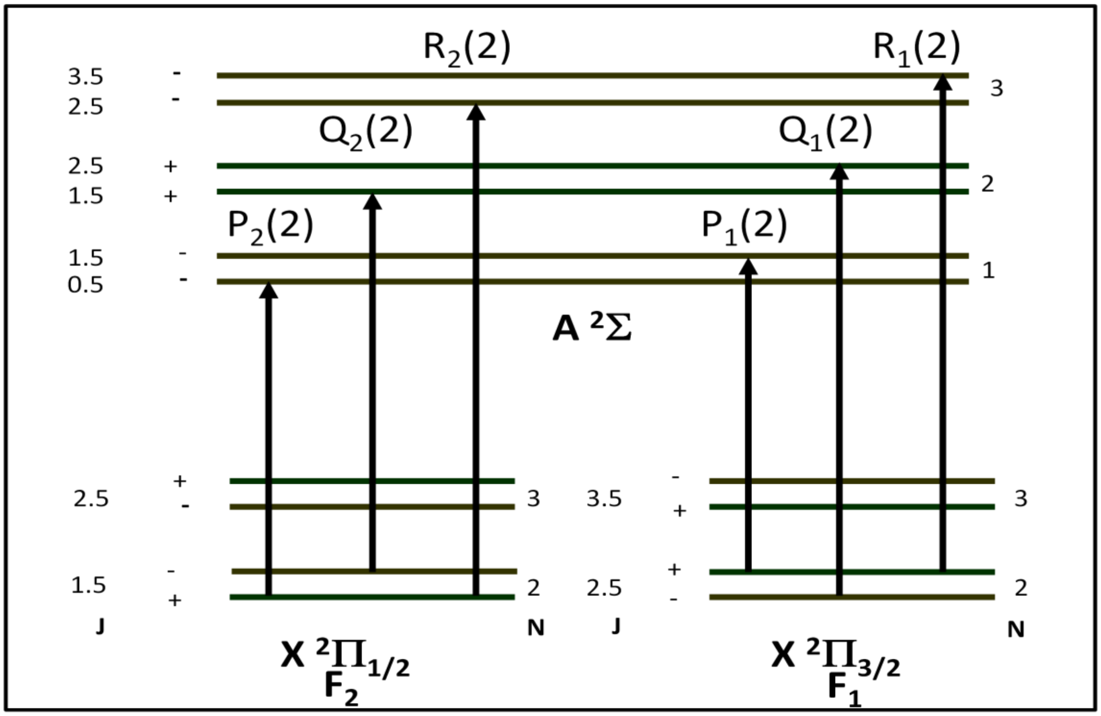

Fig. 1.7: Schematic representation of energy levels in OH Radical. The transitions shown are representative of their category.

Fig. 1.8 shows the energy states of OH radical involved in the relevant transitions. In all our experiments, the OH radical was detected by exciting (0,0) and (1,1) band of the $A^2\Sigma \leftarrow X^2\Pi$ transition, using a Nd:YAG-pumped frequency-doubled dye laser, tuned around 310 nm (probe beam), and collecting the broadband fluorescence. The fluorescence intensity was then plotted against the wavelength of the exciting laser, to construct the ro-vibrationally resolved LIF spectrum.

1.9 Atmospheric Chemistry

One of the main purpose for studying kinetics and dynamics of chemical reactions, as we have discussed earlier, is to understand the basic features of the complex reactions taking place in the atmosphere. Since the life and health of virtually all the living being on the Earth depend on the atmosphere, it is relevant to discuss the structure of the atmosphere and the important reactions occurring therein, before we go into the chapters which discuss the experiments.

1.9.1 Structure and Composition of the Atmosphere

The word "structure" is used in atmospheric physics to mean the vertical profile of particular variables of interest, such as temperature, density, pressure, etc. Atmospheric structure is divided into four thermal layers or "-spheres" that are separated by transition regions, or "-pauses". The nomenclature used dates back to the 1950's and is based on the measured temperature profile of the atmosphere. Figure 1.9 illustrates the temperature profile, and the names used for the different regions.

- **Troposphere**: (0-20 km):

This is the lowest region and contains 80% of the mass of the whole atmosphere. Almost all the weather is confined to the troposphere, in particular, it contains the clouds. The temperature falls linearly with height until at the top of the troposphere, where the temperature is approximately -50^0C.

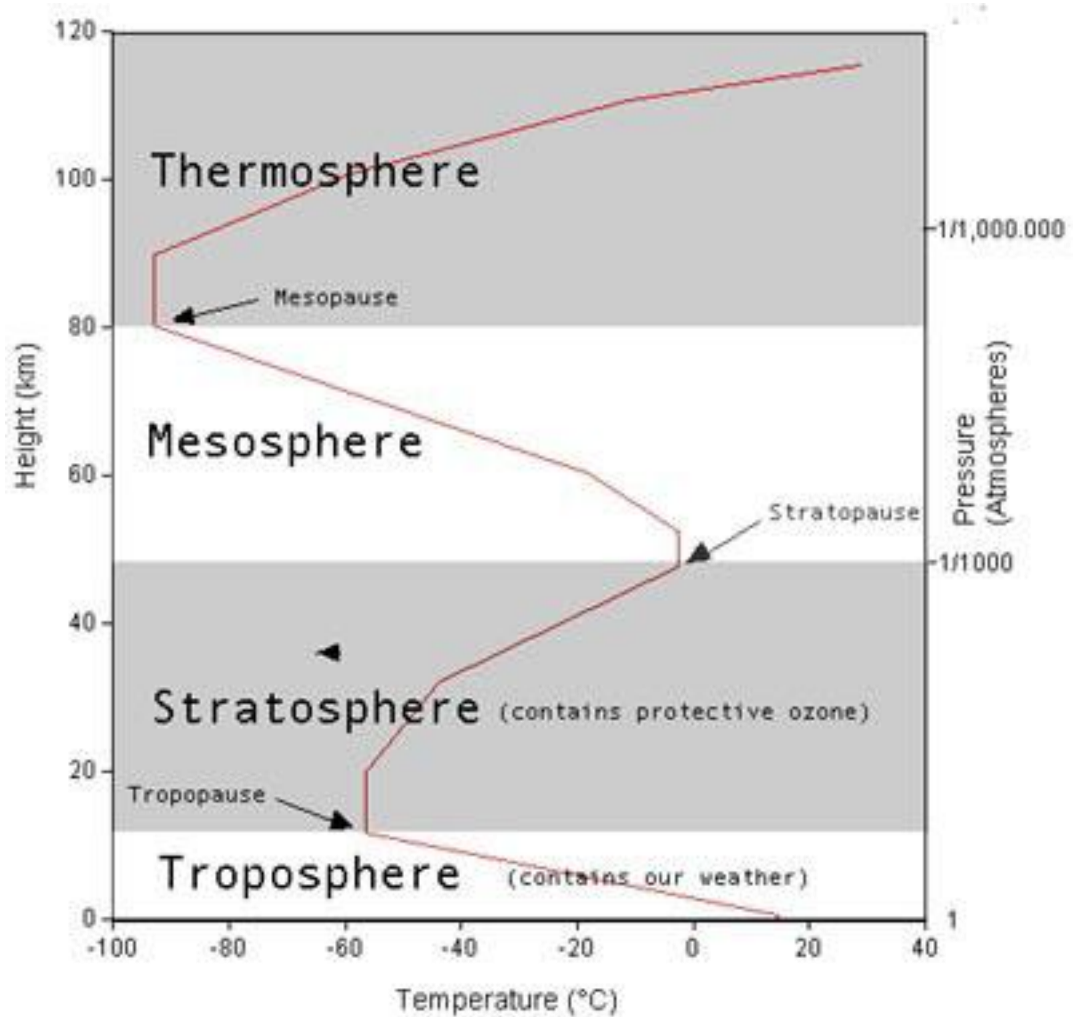

Fig. 1.8: Structure of atmosphere and the temperature profile. The "0" in the altitude co-ordinate lies at the sea level.

- **Stratosphere**: (20-50 km):

Above the *tropopause,* the temperature begins to rise again, until at about 50 km where the temperature is about 10^0C. The upper part of the stratosphere contains *ozone* , which creates a protective layer for life on earth, since it filters out harmful UV radiation.

- **Mesosphere**: (50-90 km):

The mesosphere extends from the stratopause to 85–90 km. It is the layer where most meteors burn up on entering the atmosphere. Temperature decreases with height in the mesosphere. The mesopause, the temperature minimum that marks the top of the mesosphere, is the coldest place on Earth, and has an average temperature around −85°C . At the mesopause, temperatures may drop to −100°C. Due to the cold temperature of the mesosphere, water vapor is frozen, forming ice clouds (or Noctilucent clouds). A type of lightning referred to as either sprites or ELVES, form many miles above thunderclouds in the troposphere.

- **Ionosphere:** (100-200 km):

This is an intensely ionised region of the atmosphere (upper mesosphere and lower thermosphere), where the temperature rises rapidly. Solar UV ionises the molecules of the atmosphere, like molecular oxygen and nitrogen (N_2 and O_2),

$$A + h\nu \rightarrow A^{+} + e^{-} \qquad (1.58)$$

A can be O_2, molecular oxygen, or N_2.The ionosphere reflects radio waves, and is also the region of the *aurorae* seen in high latitudes in the northern (*aurora borealis*) and southern (*aurora australis*) hemispheres. Intense visible and UV lines are caused by electron (or proton) collisions,

$$A + e^{-} \rightarrow A^{*}$$

$$A^{*} \rightarrow A + h\nu \qquad (1.59)$$

The energy given up by the electron excites the molecule to the A* state, which then decays back to the ground state, by radiating in the uv or visible range.

- **Thermosphere** (90-500 km):

Temperature increases with height in the thermosphere from the mesopause up to the thermopause, then is constant with height. Unlike in the stratosphere, where the inversion is caused by absorption of radiation by ozone, in the thermosphere the inversion is a result of the extremely low density of molecules. The temperature of this layer can rise to 1,500°C, though the gas molecules are so far apart that temperature in the usual sense is not well defined. The air is so rarefied, that an individual molecule (of oxygen, for example) travels an average of 1 kilometer between collisions with other molecules. The International Space Station orbits in this layer, between 320 and 380 km. Because of the relative infrequency of molecular collisions, the air above the mesopause is poorly mixed as compared to that below. While the composition from the troposphere to the mesosphere is fairly constant, above a certain point, air is poorly mixed, and becomes compositionally stratified. The point dividing these two regions is known as the turbopause. The region below is the homosphere, and the region above is the heterosphere. The top of the thermosphere is the bottom of the exosphere, called the exobase. Its height varies with solar activity, and ranges from about 350–800 km.

- **Magnetosphere** (Above 1000 km):

In this region, the Earth's magnetic field interacts with the solar wind, and traps the charged particles (electrons and protons) in the *Van Allen belts*.

The temperature profile of the atmosphere is a result of absorption of different portions of solar radiative output by different components in the atmosphere. In the visible region, the radiation intensity is fairly constant. N_2 absorbs radiation at less than 120 nm, and all the radiation below 100 nm is absorbed and converted to heat above 100 km. This is the reason for increase in temperature in the ionosphere and thermosphere with altitude. At lower heights, up to 60 km, O_2 absorbs wavelengths less than 220 nm, with a window at 121 nm, corresponding to Lyman α. So, all the photons less than 170 nm are removed at a height of about 85 km, with 121 nm penetrating up to 65 km. In the mesosphere and the stratosphere, absorption by O_2 and O_3 occurs. Absorption of 280 - 320 nm photons by ozone becomes important at lower stratosphere (< 33 km). At still lower heights, aerosol attenuation also becomes important. The troposphere temperature profile is due to absorption by earth's surface, leading to higher wavelength emission, which, in turn, is absorbed by the green house gases in the troposphere.

1.9.2 The Ozone Layer

Ozone, (O_3) is present throughout in the earth's atmosphere in varying concentrations (Fig. 1.11). Its concentration is highest (over 90% of the total ozone present in the atmosphere) in the altitudes between 15-35 km, and this region, which falls in the stratosphere, is popularly called the "Ozone Layer". This layer absorbs 97–99% of the sun's high frequency ultraviolet light (UVc, 200-280 nm), which is potentially damaging to the life on earth. The ozone layer was discovered in 1913 by the French physicists Charles Fabry and Henri Buisson. Its properties were explored in detail by the British meteorologist G. M. B. Dobson, who developed a simple spectrophotometer (the Dobsonmeter) that could be used to measure stratospheric ozone from the ground. Between 1928 and 1958, Dobson established a worldwide network of ozone monitoring stations, which continues to operate today. The "Dobson unit", a convenient measure of the columnar density of ozone overhead, is named in his honour. A Dobson Unit (DU) refers to a layer of ozone which will be 1μm thick under standard temperature and pressure. This correlates to a unit ozone concentration of around 2.7×10^{20} molecules m^{-2}. The thickness of the ozone layer, that is, the total amount of ozone in a column overhead, which is around 300 DUs, varies by a large factor worldwide, being, in general, smaller near the equator and larger towards the poles. It also varies with season, being, in general, thicker during the spring, and thinner during the autumn in the northern hemisphere. The reasons for this latitude and seasonal dependence are complex, involving atmospheric circulation patterns as well as solar intensity.

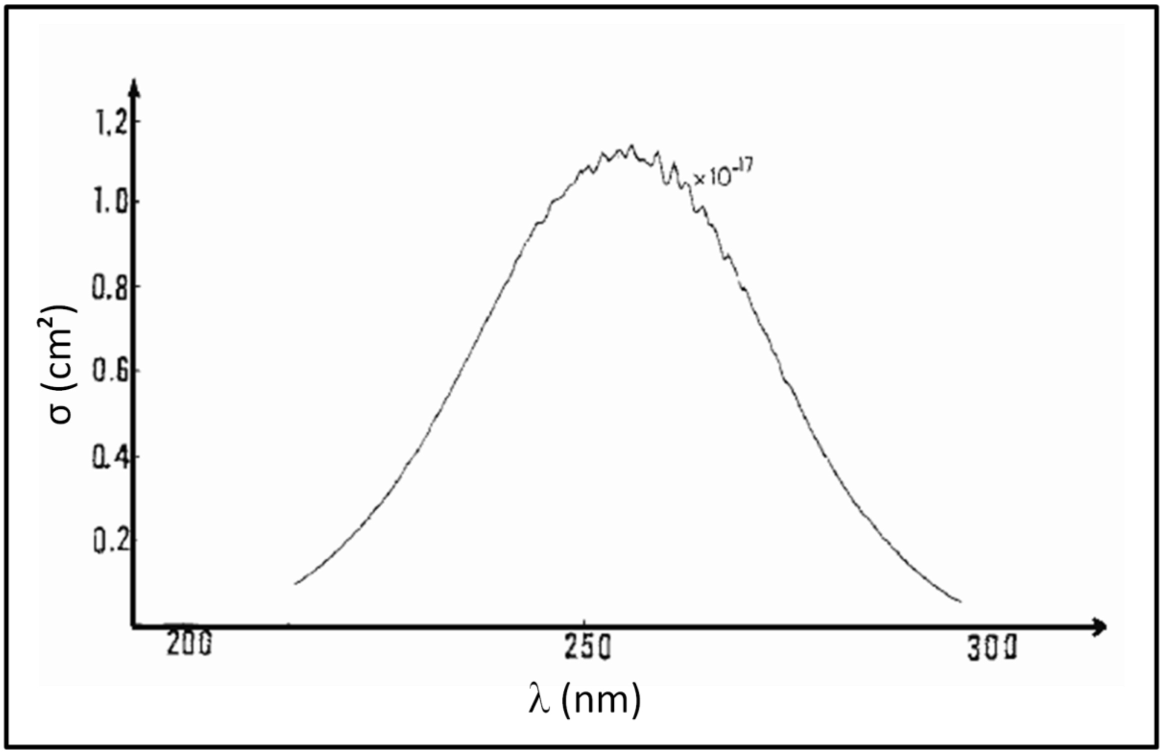

Fig. 1.9: Absorption cross-section of O_3 in the uv region. It effectively cuts off the intensity of radiation between 240-280 nm by 90%, before the solar radiation reaches the upper limit of the troposphere

The total column amount of ozone generally increases, as we move from the tropics to higher latitudes, in both the hemispheres. However, the overall column amounts are greater in the northern hemisphere high latitudes than in the southern hemisphere high latitudes. In addition, while the highest amounts of column ozone over the Arctic occur in the northern spring (March–April), the opposite is true over the Antarctic, where the lowest amounts of column ozone, occur in the southern spring (September–October). Indeed, the highest amounts of column ozone anywhere in the world, are found over the Arctic region during the northern spring period of March and April. The amounts then decrease over the course of the northern summer. Meanwhile, the lowest amounts of column ozone, anywhere in the world, are found over the Antarctic in the southern spring period of September and October, owing to the “Ozone Hole” phenomenon.

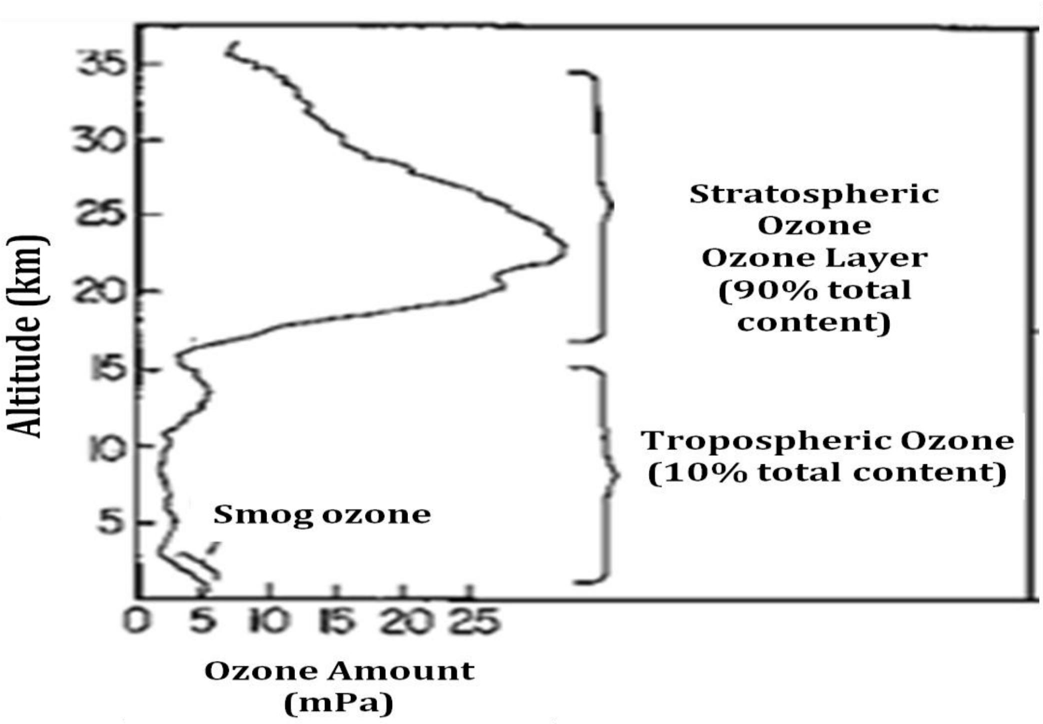

Fig. 1.10 Distribution of ozone over the altitude in the atmosphere. Maximum amount of ozone is confined between the altitudes of 15-35 km, which is generally called the “ozone layer”.

1.9.3 Ozone Formation and Decay in the Atmosphere

British scientist Sydney Chapman proposed that the ozone layer originates from the photolysis of atmospheric O_2 by photons of wavelength 240 nm, or less, (the bond energy of the O_2 molecule is 498 kJ mol^{-1}). The oxygen atom produced in the ground level triplet state (O^3P) reacts rapidly with O_2 in the presence of a third molecule, producing O_3.

$O_2 + h\nu\ (<240\ nm) \rightarrow\ O\ (^3P) + O(^1D)$ (1.60)

$O\ (^1D) + O_2 + M \rightarrow O_3 + M$ (1.61)

The O_3 molecules produced undergo photolysis at lower energy photons, because the bonds in the O_3 molecule are weaker than those in the O_2 molecule.

$O_3 + h\nu\ (220\text{-}320\ nm) \rightarrow O_2 + O(^1D)$ (1.62)

$O(^1D)$ is rapidly stabilized to $O(^3P)$, by collision with N_2, or O_2.

Alternatively, O atom may react with ozone,

$O_3 + O \rightarrow O_2 + O_2$ (1.63)

O and O_3 together are called odd oxygen, which are generated only by the reactions (1.60) and (1.61), and lost only by reaction (1.63). Considering the solar actinic flux, absorption cross-sections and reaction rates, the calculated steady state concentration of O_3, according to this mechanism, yielded a higher value than that measured, and hence, additional catalytic reactions with free radicals were proposed for scavenging of odd oxygen species (O and O_3).

$X + O_3 \rightarrow XO + O_2$ (1.64)

$XO + O \rightarrow X + O_2$ (1.65)

where X is a free radical catalyst, which can be H, OH, NO, Cl, or Br. OH can be formed by the reaction of $O(^1D)$ with stratospheric water vapour, and is found to be an important contributor in this catalytic cycle. The net reaction is

$$O + O_3 \rightarrow O_2 + O_2 \qquad (1.66)$$

1.9.4 Ozone Layer Depletion in the Antarctic Region ("Ozone Hole")

In 1985, a team of scientists from the British Antarctic Survey discovered that springtime stratospheric O_3 columns over the continent had decreased precipitously since the 1970s. The depletion was confined to the spring months (September-November); no depletion was observed in other seasons. The measured vertical profiles show that the depletion of O_3 is essentially total in the lowest region of the stratosphere between 10 and 20 km, which normally would contain most of the total O_3 column in polar spring.

In 1974, Mario Molina and Sherwood Rowland pointed out the potential for O_3 loss associated with rising atmospheric concentrations of chlorofluorocarbons (CFCs). CFCs are not found in nature; they were first manufactured, for industrial purposes, in the 1930s, and their use increased rapidly in the following decades. During the 1970s and 1980s, atmospheric concentrations of CFCs rose by 2-4% yr^{-1}. CFC molecules are inert in the troposphere, and have residence times more than 10 years; they are, therefore, transported to the stratosphere, where they photolyze to release Cl atoms. For example, in the case of CF_2Cl_2 (known by the trade name CFC-12),

$$CF_2Cl_2 + h\nu \rightarrow CF_2Cl + Cl \qquad (1.67)$$

The Cl atoms then trigger a catalytic loss mechanism for $O_{3,}$ involving cycling between Cl and ClO (the ClO_x family).

$$Cl + O_3 \rightarrow ClO + O_2 \qquad (1.68)$$

$$ClO + O \rightarrow Cl + O_2 \qquad (1.69)$$

The net reaction is,

$$O + O_3 \rightarrow O_2 + O_2 \qquad (1.70)$$

The rate-limiting step for O_3 loss in this cycle is reaction (1.68). The catalytic cycle is terminated by conversion of ClO_x to non-radical chlorine reservoirs, HCl and $ClNO_3$,

$$Cl + CH_4 \rightarrow HCl + CH_3 \qquad (1.71)$$

$$ClO + NO_2 + M \rightarrow ClNO_3 + M \qquad (1.72)$$

The lifetime of HCl is typically a few weeks, and the lifetime of $ClNO_3$ is of the order of a day. Eventually, these reservoirs return Cl/ClO_x.

$$HCl + OH \rightarrow Cl + H_2O \qquad (1.73)$$

$$ClNO_3 + h\nu \rightarrow Cl + NO_3 \qquad (1.74)$$

The “ozone hole” over Antarctica could not be explained by the established reactions of Chapman’s mechanism and catalytic cycles. The intense laboratory research and aircraft measurements in late 1980s showed the depletion of O_3 to be associated with exceptionally high concentration of ClO, a result confirmed by satellite data. The formation and decay of ClO in the atmosphere follow cyclic sequence of reactions,

$$Cl + O_3 \rightarrow ClO + O_2 \qquad (1.75)$$

$$ClO + ClO + M \rightarrow ClOOCl + M \qquad (1.76)$$

$$ClOOCl + h\nu \rightarrow ClOO + Cl \qquad (1.77)$$

$$ClOO + M \rightarrow Cl + O_2 + M \qquad (1.78)$$

Further research in the 1990s demonstrated the critical role of the reactions taking place in stratospheric aerosols at low temperature. Because of the lack of topography, or land-ocean contrast, the antarctic atmosphere is effectively isolated from the lower latitudes. This isolation is most pronounced during winter, and the isolated antarctic air mass in winter is called the antarctic vortex because of the strong circumpolar circulation. Temperatures in the wintertime antarctic vortex is sufficiently cold (-80°C), to cause formation of persistent ice-like clouds, called polar stratospheric clouds (PSCs), in the lower part of the stratosphere. The PSC particles provide surfaces for fast conversion of the ClO_x, reservoirs HCl, and $ClNO_3$, to Cl_2, which then rapidly photolyzes producing ClO_x,

$$ClNO_3 + HCl \rightarrow Cl_2 + HNO_3 \tag{1.79}$$

$$Cl_2 + h\nu \rightarrow 2Cl \tag{1.80}$$

In the winter, however, loss of O_3 is limited by the lack of solar radiation to photolyze the ClOOCl dimer. Significant depletion of O_3 begins only in September, when sufficient light is available for photolysis of ClOOCl to take place rapidly. Although temperatures rise sufficiently, to evaporate the PSCs by September, sedimentation of HNO_3-containing PSC particles occur over the course of the winter, and HNO_3 is not available for the competing reactions, which will lead to suppression of O_3 depletion.

$$HNO_3 + h\nu \rightarrow NO_2 + OH \tag{1.81}$$

followed by,

$$ClO + NO_2 + M \rightarrow ClNO_3 + M \tag{1.82}$$

There is much concern, at present, over the possibility of an ozone hole developing in the arctic, and the different factors are being closely watched by atmospheric chemists.

The chlorofluorocarbons (CFCs) and hydrochlorofluorocarbons (HCFCs) are, thus, notorious for the stratospheric ozone layer depletion, and global warming as well. One promising class of the proposed alternatives is the hydrofluoroethers[1]. Before any compound can be commercially used and produced, the total effect of it on the atmosphere, like the probable reactions, and their outcome, and the global warming potential, etc., must be thoroughly assessed. The lifetime, or residence time, of a molecule in the atmosphere is a very important parameter for the type and extent of the effect it has on the atmosphere. If the compound has very short residence time, significant variations in the concentration of the species will generally occur over very short spatial scales. They will be present close to the localised sources, and will lead to local effects, such as smog, acid rain, etc. Those with long residence time get distributed globally, leading to global effects, such as global warming and ozone hole formation. Temporal and spatial distribution of such species varies considerably. If there are different reactions for removal of the species represented as

$$M + X_i \underset{k_i}{\rightarrow} \text{products,} \qquad (1.83)$$

k_i, being the rate constant of the reaction. The total rate of removal will be given by the summation of the rates of the individual reactions.

$$dM/dt = M \times \Sigma\, k_i X_i \qquad (1.84)$$

So, the residence time (τ) = M/ dM/dt = 1/ $\Sigma\, k_i X_i$. $\qquad$ (1.85)

The total residence time, or the lifetime, of any molecule in the atmosphere is inversely proportional to the sum of rate constants for its removal channels.

1.9.5 Major Pathways of Removal from Earth's Atmosphere

a) **Photodissociation:**

The extent of photodissociation of a molecule is decided by the region of solar spectrum where the molecule absorbs, its absorption cross section and the intensity of light available at the required wavelength. Thus, it depends on the nature of the molecule, location, time of the day, etc.

b) Dissolution in the aqueous phase (ocean, rain, dew, and ice):

The rate of dissolution in the aqueous phase is decided by Henry's law constant K_H. The mass of a gas that dissolves in a given amount of liquid at a given temperature is directly proportional to the partial pressure of the gas above the liquid. Concentration in aqueous phase is given by the relation,

$$(M) = K_H \times p \tag{1.86}$$

where p is the partial pressure of the gas in equilibrium, and K_H is the Henry's law constant.

This law does not apply to gases that react with the liquid, or ionize in the liquid. The values for O_2, NO_2, CO_2, HNO_3 and H_2O_2 are: 1.3×10^{-2}, 1.0×10^{-2}, 3.4×10^{-2} , 2.1×10^{5} and 7.1×10^{4}, respectively. Note that, H_2O_2, HNO_3 are highly soluble in water, and are removed very fast from the troposphere.

c) Reactions with major reactants (OH, HO_2, NO_2 etc.):

The troposphere, which contains the maximum bulk of the atmospheric mass, is where most of the compounds are removed by the reactive species. OH, as we know, is the most reactive oxidizing species, and, alongwith $HO_{2,}$ it belongs to HO_x group, which are involved in the oxidation of molecular species, as well as different important catalytic cycles. $NO_{2,}$ which is another oxidant, belongs to the NOx group, alongwith NO, which participate in catalytic reaction to create reservoir molecules.

Thus, the major removal channel in the troposphere remains oxidation, and the rate of removal depends strongly upon the rate of reaction of these oxidising species, as well as their concentration. Photochemistry plays an indirect role in controlling the concentrations of the oxidising species.

1.9.6 Hydroxyl Radical - Major Reactant in Troposphere

OH, which is responsible for the major reaction channel for removal of any molecule from the troposphere, is produced by the reaction of water vapor with $O(^1D)$, produced photochemically:

$$O_3 + h\nu \rightarrow O(^1D) + O_2 \qquad (1.87)$$

$$O(^1D) + M \rightarrow O + M \qquad (1.88)$$

$$O(^1D) + H_2O \rightarrow 2\,OH \qquad (1.89)$$

Tropospheric production of $O(^1D)$ takes place in a narrow wavelength band, between 300 and 320 nm; radiation of shorter wavelengths does not penetrate into the troposphere, while radiation of longer wavelengths is not absorbed by O_3. Although the production of $O(^1D)$ in the troposphere is considerably slower than that in the stratosphere, this is compensated in terms of OH production by the larger H_2O mixing ratios in the troposphere (10^2-10^3 times higher than that in the stratosphere). Model calculations, in the 1970s, accounting for the penetration of UV radiation at 300-320 nm found tropospheric OH concentrations of the order of 10^6 molecules cm^{-3}.

Reactions with CO and other components decide the lifetime of OH, which is about 1 second in an unpolluted region.

$$CO + OH \rightarrow CO_2 + H \tag{1.90}$$

$$CH_4 + OH \rightarrow CH_3 + H_2O \tag{1.91}$$

Because of the short lifetime, atmospheric concentrations of OH are highly variable; they respond rapidly to changes in the sources or sinks. However, crude measurements of OH concentrations in the late 1970s, using industrial solvent methylchloroform (CH_3CCl_3), confirmed an average concentration of [OH] to be 1.2×10^6 molecules cm^{-3}. This value is highly variant with time and region. During summer days, concentration can be as high as $5\text{-}8 \times 10^6$ molecules cm^3, whereas in winter, it may be only $1\text{-}2 \times 10^6$ molecules cm^3 and during night time, it falls to less than 2×10^5 molecules cm^3.

This empirical estimate of [OH] is useful, because it can be used to estimate the lifetime t_i of any long-lived gas against oxidation by OH in the troposphere. For example, one infers a lifetime of 9 years for CH_4, and 2.0 years for CH_3Br.

1.10 Scope of the Thesis

The first part of the present thesis deals with studies on the kinetics of chemical reactions, with an aim to understand what influences these rates, and develop theories which can be used to predict them. The knowledge of reaction rates has many practical applications, for example, designing of industrial processes, understanding of the complex dynamics in the atmosphere, as well as the intricate interplay of the chemical reactions that are the basis of the life. We need to determine, by experiment, the form of the rate law, and hence, the associated rate coefficients, to extend our knowledge of the rates of chemical processes, so that predictions can be made, and the measured rate coefficients can be compared with those predicted by theory. Chemical kinetics studies are also very helpful for understanding the mechanism of reactions, though other information also is required, like direct determination of intermediates, characterisation of the products, etc. However, using our chemical intuition and modelling techniques, a reasonable attempt can be made at deciphering the mechanism, using kinetic results. Apart from that, kinetic studies in the gas phase have acquired a heightened importance in the recent times because of their relevance in understanding the chemistry of atmospheric pollution. The extent of damage that can be caused by a polluting substance depends on its lifetime in the atmosphere, which, in turn, depends on the rates, or the rate coefficients of its reactions with the important reactive species present therein. The present thesis includes kinetic studies of reactions of some atmospherically important molecules with OH radicals, which is the most important reactive species present in the troposphere.

Though a lot of information on the mechanistic aspects and the technological potentials of the reactions have been derived from kinetics studies, in recent years, the focus of the studies of the chemical reactions has shifted from the kinetics to dynamics. Chemist of today wants to control reactions, rather than be a passive spectator. In order to achieve this, and develop new technologies, it is essential to know, “what are the various elementary steps involved in a reaction, and what is the detailed dynamics of each step? How to eliminate, or reduce, unwanted products, a waste, by generating the desired products selectively?" Chemists have always cherished visions of carrying out mode, or bond selective reactions, eventually leading to chemical control of reactions. A chemical reaction may involve a number of elementary steps. The breaking of old bond(s), formation of new bond(s), electron, proton, or hydrogen atom transfer, inter- and intra-molecular energy transfer, etc., are some of the elementary steps involved in many reactions. A photodissociation reaction taking place on a repulsive excited state is very fast (~100 fs), but a bimolecular reaction occurs in pico second, or longer time, depending on whether the chemical act is once-through (direct), or involves longer interaction between the reactants, and even transient intermediates, with lifetime varying from pico seconds to seconds. Chemical dynamics deals with the investigations of molecular/atomic mechanism of elementary chemical processes, both intermolecular and intramolecular. These fundamental processes are at the root of the bulk rate phenomena. This microscopic approach has stimulated new experimental and theoretical developments, making chemical dynamics as one of the most active fields of physical chemistry. In order to investigate dynamics of a molecular process, physical or chemical, fast techniques are required. The development of lasers and molecular beams has greatly helped in this endeavour. One can prepare the reactants in well-defined quantum states, and monitor their journey from the reactant valley to the product valley, by taking snapshots from time zero, i.e., the time a chemical reaction starts. Now, it is possible to characterize the elusive transition state, which determines the course of reaction.

The second part of the thesis is concerned with the "Dynamics of Chemical Reactions". Intermolecular collisions destroy the state selection of the reactants, as well as the quantum state distribution of the products, and hence, unless experiments are done under collisionless condition, no information can be gleaned about how the outcome of a chemical reaction depends on the pre-selection of the energy states in the reactants, or how the excess chemical energy appears in the products. These two major questions are dealt with by chemical dynamics. Researches in chemical dynamics have been made very sophisticated, in recent times, mainly due to the advancement in spectroscopic techniques, using lasers. Nowadays, "microscopic" investigations into the dynamics of a reaction can be made feasible, by establishing single-collision conditions, when the information sought is in the primary reaction quantities, like nascent product energy distribution, dependence of the reaction cross-section on different types of internal energies, impact parameters, etc. These can be achieved by nanosecond pump-probe, or molecular beam, experiments. In the present thesis, the dynamic studies are carried out, to obtain a molecular level view of the product energy distribution in unimolecular photodissociation reactions, using nanosecond pump-probe technique.

The experimental work in this thesis has been organized into three chapters, elaborating on the work carried out on the above-mentioned themes.

In the first chapter, dealing with experimental results and discussions, i.e. Chapter 3, the study of the kinetics of reaction of OH radicals with $CF_3CH_2OCH_2CF_3$ (2,2,2 trifluoroethyl ether), in the temperature range of 298 – 365 K, using Laser photolysis-Laser Induced Fluorescence method, has been described. This is an absolute method for measuring the rate constant, i.e., the rate was measured in real time by following the decay of one of the reactants, namely, the OH radical. The bimolecular rate coefficient at 298 K, $k_{II}(298)$, for this reaction, was measured to be $(1.47 \pm 0.03)\times10^{-13}$ $cm^3molecule^{-1}s^{-1}$, and the temperature dependence of k_{II} was determined to be $(4.5 \pm 0.8) \times 10^{-12}exp[-(1030 \pm 60)/T]$ $cm^3molecule^{-1}s^{-1}$, by our experiments. Considering the atmospheric lifetime of methylchloroform, (which is a standard reference for lifetime measurement), with respect to OH radical reaction to be 6 years[1], the atmospheric life time of TFEE (τ_{TFEE}), due to its reaction with OH radicals in the atmosphere, is calculated to be 0.35 years. Apart from TFEE, we have also carried out kinetic study for the reaction of the OH radical with morpholine. The experimental results showed evidence of the involvement of a stable pre-reactive complex, due to hydrogen bond interaction between the OH radical and nitrogen/oxygen atom of morpholine, which was supported by theoretical studies. The rate constants for the reaction of the OH radical with morpholine, have been measured in the temperature range of 298 -365 K. The rate constant at room temperature (298 K) was measured to be $(8.0 \pm 0.1)\times10^{-11}$ $molecule^{-1}cm^3s^{-1}$. Though the Arrhenius plot was not perfectly linear in the temperature range studied, the approximate dependence of the rate constant on temperature is given by $(1.1 \pm 0.1) \times 10^{-11}exp[(590 \pm 20)/T]$ $cm^3molecule^{-1}s^{-1}$. Both the high rate constant and negative temperature dependence of rate constants could be attributed to the formation of the pre-reactive complex, with higher stability than the reactants.

In Chapter 4, the studies of photodissociation dynamics of cyclic ethers, namely, Tetrahydrofuran (THF), Tetrahydropyran (THP) and Morpholine are discussed. We have seen that all the three cyclic ethers, produce OH radical, when photolyzed by 193 nm laser, though all these compounds are rigid ring type, with no OH functional group present in their structure. Hence, OH must be formed as a secondary product, after some intramolecular rearrangement during photodissociation. All the dissociation processes most probably proceed from the energetic ground state molecule, having excess energy stored in its internal modes. This opens up energy expensive channels, producing unusual fragmentation products, such as OH. In most of the cases (THF, THP and triplet channel in morpholine), theoretical studies revealed that the first step of dissociation is the scission of the ring through C—O bond cleavage, which produces a biradical primary product. The initially formed biradical, then undergoes C atom to O atom intramolecular H-atom migration, to generate another biradical, which gives OH radical, after undergoing a final C—O bond scission. The results of the theoretical calculations, done to support the experimental observations, are discussed in details.

Chapter 5 includes the study of the dynamics of photodissociation of epoxides, which are essentially cyclic ethers, with three-membered rings. Due to smaller ring size, the strain is much higher in these rings. This class of compounds were chosen in order to understand how the effect of higher strain energy present in the smaller ring compounds is manifested in the energy partitioning and overall dynamics of their photodissociation. We irradiated epoxides with susbstituents at the 3-memberd rings, like ethylene oxide (EO), propylene oxide (PO), butadiene monoxide (BMO) and styrene oxide (SO), with 193 nm laser. In the case of the first two, there were no OH formation by photodissociation, but in the case of the other two, OH radical was obtained. This was due to the fact that the absorption cross-section (σ) at 193 nm for EO (0.44×10^{-20} cm^2) and PO (1.5×10^{-20} cm^2) are much smaller than that for BMO (1.2×10^{-17} cm^2), and SO (5.4×10^{-18} cm^2). Stable product analysis by Gas Chromatography-Mass Spectrometry

(GC-MS) of the products of photolysis of BMO and SO at 193 nm revealed the presence of some ketonic products. The OH formation channel in these compounds had multiple branches. Since the three-membered epoxide ring was unsymmetrically substituted, the ring opening could be caused by two different channels, involving $HC_{\alpha}—O$ and/or $H_2C_{\beta}—O$ bond scission, producing two different triplet biradicals. These biradicals, which were sufficiently energy rich, then could undergo intramolecular rearrangement, to generate the enolic form of the ketone products, which, in turn, could produce OH radical by C—O bond scission. Alternatively, these could tautomerise to their more stable ketone forms. All the reaction channels and their energetic are described in details, as obtained by *ab initio* molecular orbital calculations.

Chapter 2

Techniques

The work presented in this thesis is mainly experiment based with theoretical support obtained from computational chemistry. In the first part of the thesis (chapter 3), the kinetics of reaction of morpholine and 2,2,2 trifluorodiethylether with OH radical produced by uv-laser induced photodissociation of H_2O_2 are presented. In the second part, i.e., in chapters 4 and 5, the dynamics of unimolecular photodissocition reactions effected by uv laser of wavelength 193 or 248 nm are described in details. The major part of the experimental work deals with detection and monitoring of OH radical in its nascent state (for obtaining dynamics of photodissociation process), or observing the decay in its concentration in presence of the reactants (for measuring the rate coefficients). In the case of non adiabatic photodissociation reaction, the product may form in its ground state, and hence have no emission or chemiluminiscence that can be used for its detection. In these cases, only absorption or excitation-based techniques can be used for characterisation of the ground state product. In all the studies described in this thesis, Laser Induced Fluorescence (LIF), which is an advanced excitation spectra–based detection technique, has been coupled with laser photolysis, to investigate the dynamics and kinetics of the reactions involving OH radical product in its electronic ground state. The advantages of LIF as a diagnostic tool results from the fact that the intensity of the fluorescence signal, after normalizing with respect to laser intensity, I_{lif}, is proportional to the population of the species in the excited state, which is related to the initial ground state population that is being excited. LIF has been employed for both qualitative (i.e. flow visualization) and quantitative measurements of species concentration. Moreover, LIF can also be used for measurements of temperature (taking advantage of the dependence of rotational state population, in the ground vibrational state, on temperature), velocity along the beam propagation axis (by measuring the Doppler shift of the transition) and pressure (by examining pressure-dependent transition broadening). In our dynamics studies, the distribution of available energy among the fragments of photolysis reaction were determined by measuring the rotational and translational energy of the nascent OH fragment, by analysing its LIF spectrum. From the same spectrum, the distribution of population of the nascent OH radical among the different spin-orbit states and Λ-doublet states were also found out. The dynamics results obtained experimentally were compared with the different models for dissociation, and all these information, when used collectively, gave an insight into the nature of the dissociation reaction.

Apart from the laser-based techniques, Gas-Chromatography and FT-IR absorption techniques have also been used for different types of analyses, mainly the detection of the stable products of the reactions.

The experimental results were supported by theoretical calculations, where *ab initio* molecular orbital calculations were done using Gaussian 98[2] model. Calculations were done at different levels of theory, using different basis sets, depending on the necessity, to optimize the geometry, and calculate the energy of reactants, products, intermediate steps, and transition states. These theoretical studies, though used purely to support the experimental results, helped to understand the probable features of the potential energy surface of the reactions under study.

A detailed description of working principle, instrumentation of the experimental methods and basic theories of the models and theoretical calculations that are used in the present thesis, are presented in the following sections of this chapter, and the same can be referred to, as and when required, in the discussion of the experimental results in the subsequent chapters.

2.1 Laser Photolysis – Laser Induced Fluorescence

On photoexcitation of an atom, a molecule, or an ion, to a higher energy bound state, much lower than its dissociation level, the excited species can decay to a lower level, or the ground state of the same multiplicity, with emission of light. This phemenon is known as fluorescence, as discussed in section 1.7. When the upper and lower levels are of different multiplicity, the transition is forbidden, and the phenomenon is called phosphorescence. Consequently, the phosphorescence intensity is much less as compared to fluorescrence. In most of the cases, the fluorescence spectra are red shifted with respect to the absorption spectra. This makes fluorescence measurement an advantageous method for detection of suitable species, since the measurement of the shifted emission has less interference from the scattered photons. The fluorescence technique has two variants, dispersed fluorescence and excitation spectra. In the former, the species is excited by a light of suitable wavelength, where it has absorption. The emitted light from the excited species is dispersed by a suitable dispersing element, such as a grating. In the latter technique, the wavelength of the excitation source is tuned in steps, and at each step, the total fluorescence is collected. In both the techniques, fluorescence is collected at right angle to the excitation source, to minimize the contribution of the scattered light to the measured fluorescence signal. The two techniques are graphically depicted in Fig. 2.1.

The fluorescence technique is a very sensitive analytical tool, as compared to the absorption technique, as in the latter, the relative change in the photon intensity of light is measured, while in the former, the photon intensity is measured against an almost zero background. If the lifetime of the excited state is short, as compared to collisional deactivation, the intensity of the fluorescence is proportional to the concentration of chemical species in the state from which it is excited to the higher state. The excitation spectrum based technique of monitoring fluorescence, following excitation by laser source, coined Laser-Induced Fluorescence (LIF), has now become the most widely used laser diagnostic tool in many research fields. LIF technique involves absorption of radiation of a very precise wavelength by atomic/molecular species, and monitoring of the subsequent emission from the excited species, to obtain very specific probes of chemical species and their concentrations. Although, in principle, it can be used to detect single molecular species, in practice, for most of the systems, one might obtain the detection limit of 10^6 molecules/cc. This technique can be used for in situ monitoring, and is a well-established laboratory technique for obtaining the real-time concentration of many chemical species. In order to apply LIF technique to a given chemical species, for measuring its concentration, temperature, velocity, or pressure, it is necessary that the band system to be accessed by the LIF technique is spectroscopically well studied and analyzed. This requirement is very well satisfied by small diatomic species, but, for polyatomic species, the dissociation and radiationless transition contribute quite substantially, and, in many cases, dominate over the fluorescence. The third requirement is that the molecular band system should be accessible with a commercially available tuable laser. The last criterion can be bypassed by employing non-linear techniques, such as degenerate four-wave mixing. The excitation source generally used for LIF technique is a tunable dye laser, or an optical parametric oscillator (OPO). The LIF diagnostics is a highly selective and very sensitive technique. In combustion processes, it is employed for measurement of small radical species, such as OH, CH, NO, CN, NO_2, NCO, SO, S_2, CH_3O Cl, and so on.

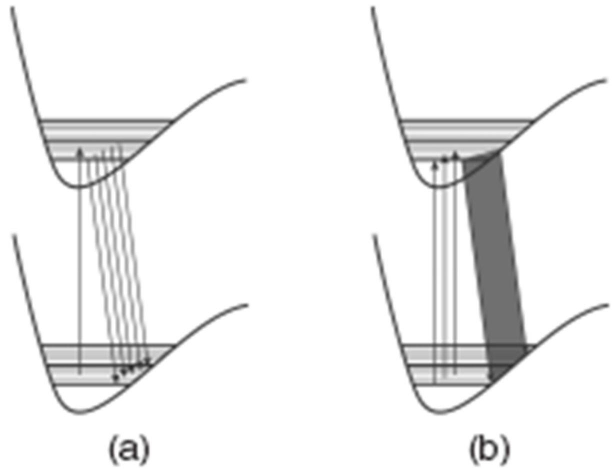

Fig. 2.1: Two variants of the fluorescence technique: (a) In the fluorescence spectrum, the excitation, source is tuned to specific transitions, and the dispersed fluorescence is obtained. (b) In the excitation spectrum, the wavelength of the excitation source is tuned in steps and the total fluorescence is obtained at each step: fluorescence background is obtained when the excitation wavelength matches with the particular transition.

2.1.1 Basic Principles of LIF

In the UV-visible LIF technique, the population of the molecules from a ro-vibrational state in the ground state is transferred to a ro-vibrational state in the excited electronic state, using a laser tuned to the requisite wavelength. It is possible to excite from only a particular ro-vibrational state in the ground state to a particular ro-vibrational state in the excited state in gaseous medium, provided the spectral bandwidth of the laser is smaller than the rotational state spacing.

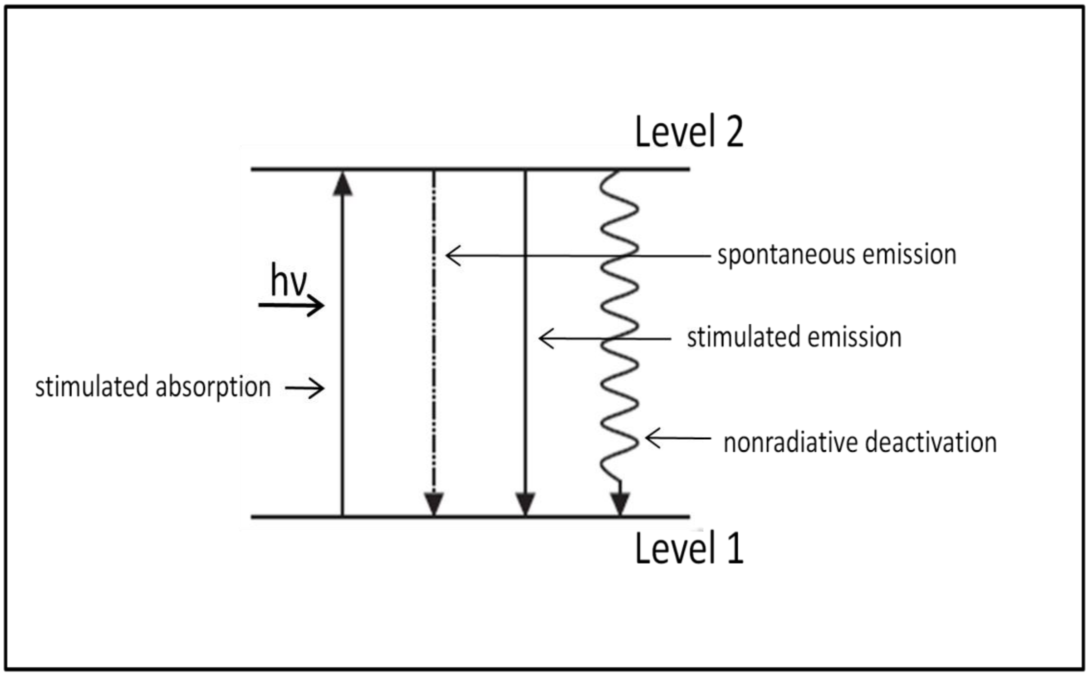

Fig. 2.2: The two energy level scheme for representing the excitation and de-excitation processes.

To understand the working principle of LIF, let us consider a system with two energy levels. Let the population density of the states 1 and 2 be N_1 and N_2, respectively, at any time t (Fig. 2.2). As the states 1 and 2 are the electronic ground and the excited states, for all practical purpose, we can consider that, in the beginning, all the population resides in the ground state, and let this initial population density, before laser irradiation, be $N_1(0)$, while $N_2(t=0) = 0$. If this system is irradiated with a laser tuned to $2 \leftarrow 1$ transition, and with laser intensity per unit frequency interval I_ν, then the rates of absorption, b_{12}, and stimulated emission, b_{21}, are related to I_ν by the expressions:

$b_{12}=B_{12}I\nu/c$ or $b_{12} = B_{12}\rho$ (2.1)

$b_{21}=B_{21}I\nu/c$ or $b_{21} = B_{21}\rho$ (2.2)

Where, Bs are the Einstein coefficients corresponding to bs, c is the speed of light, and ρ is the energy density per unit frequency interval. In addition to the stimulated emission, the population from the state 2 is transferred to the state 1 by spontaneous emission and non radiative processes influenced by collisions. The rate of spontaneous emission is given by Einstein's A coefficient. If A_2 is the rate constant for spontaneous emission and Q_{21} is the sum of rate constants for all non radiative deactivation processes, then the rates of change of the population densities of states 1 and 2 are given by,

$$\frac{dN_1}{dt} = -N_1 b_{12} + N_2(b_{21} + A_{21} + Q_{21}) \qquad (2.3)$$

$$\frac{dN_2}{dt} = N_1 b_{12} - N_2(b_{21} + A_{21} + Q_{21}) \qquad (2.4)$$

From the conservation of population,

$$N_1 + N_2 = N_1\,(0) \qquad (2.5)$$

On solving eqn. (2.4), the population density of state 2 at any time t is given by,

$$N_2(t) = \frac{b_{12}N_1(0)}{r}(1 - e^{-rt}) \qquad (2.6)$$

Where, $r = b_{12} + b_{21} + A_{21} + Q_{21}$. At the initial phase, t is very small, and hence $rt<<1$. In that case, the eqn. 2.6 simplifies to,

$$N_2(t) = b_{12}N_1(0)t \qquad (2.7)$$

The fluorescence signal may be expressed as,

$$S_{fl} = C\, n_{fl} = C\, N_2(t)\, A_{21}\, V_{fl} \tag{2.8}$$

Where n_{fl} (given by $N_2(t)\, A_{21}\, V_{fl}$), is the number of fluorescence photons emmitted per second from the source, V_{fl} is the fluorescence volume generated by the excitation laser and C is a constant factor for a given pair of fluorescence source and the detector system, which includes the solid angle subtended by the detector on the fluorescence source, and characteristics of the system. It is assumed that the excited molecules/atoms are uniformly distributed in the fluorescence volume.

Under the steady state condition, $dN_2/dt = 0$, and the time at which the steady-state value is reached depends on both the intensity of the excitation laser and nature of the LIF system. Whereas the former is related to the stimulated emission rate, the latter depends on the non-radiative rate. Let us consider some of the typical cases:

Case 1: Very low pressure (< 1Torr) and $N_1 \approx N_1(0)$

In this case, there is a very negligible change in the population of the ground state.

The population density of the excited state, N_2, under the steady state condition, is given by,

$$N_2 = \frac{b_{12} N_1}{(b_{21} + A_{21} + Q_{21})} \approx \frac{b_{12} N_1(0)}{(b_{21} + A_{21} + Q_{21})} \tag{2.9}$$

Here, the depopulation of the excited state, due to non radiative deactivation, is negligible, that is, $Q_{21} \approx 0$. On substituting the value of N_2 into the eqn. (2.8), we get,

$$S_{fl} = C N_1(0) A_{21} V_{fl} \frac{b_{12}}{(b_{21} + A_{21})} \tag{2.10}$$

The above equation, can be rearranged and expressred in terms of Einstein's B coefficients as,

$$S_{fl} = CN_1(0)V_{fl}\frac{B_{12}\rho}{(1+\frac{B_{21}\rho}{A_{21}})} \qquad (2.11)$$

Depending on the laser intensity, the limiting conditions can be considered as,

(a) at very low intensity, $B_{12}I_\nu/c = B_{12}\rho << A_{21}$ and

$$S_{fl} = C\,N_1(0)\;V_{fl}\,B_{12}\rho \qquad (2.12)$$

(b) at very high laser intensity, $A21 << B_{12}\,I_\nu\,/\,c$

$$S_{fl} = C\,N_1(0)\;V_{fl}\,A_{21} \qquad (2.13)$$

Case 2: Very high pressure, > 1bar:

The spontaneous emission rate, N_2A_{21}, is negligible, as compared to nonradiative deactivation rate, N_2Q_{21}, and rt>1 can be achieved, and a steady state value of population in state 2, from eqn. (2.6) is,

$$N_2(t) = b_{12}\ n_1(0)/r \qquad (2.14)$$

That is

$$N_2 = N_1(0)\frac{b_{12}}{(b_{12}+ b_{21}+ A_{21}+Q_{21})} \qquad (2.15)$$

Which can be rearranged to,

$$N_2 = N_1\,(0)\frac{b_{12}}{(b_{12}+b_{21})}\,\frac{1}{(1+\frac{A_{21}+Q_{21}}{b_{12}+ b_{21}})} \qquad (2.16)$$

On expressing the above equation in terms of Einstein B coefficients, and defining I_ν^{sat} as

$$I_\nu^{sat} = \frac{(A_{21}+Q_{21})c}{(B_{12}+ B_{21})} \qquad (2.17)$$

we have,

$$N_2 = N_1(0)\frac{B_{12}}{(B_{12}+B_{21})}\frac{1}{(1+\frac{I_{\vartheta}^{sat}}{I_{\vartheta}})} \tag{2.18}$$

Depending on the laser intensity, the limiting conditions can be given as,

(a) when laser intensity is very low, $I_v << I_v^{sat}$, and eqn. (2.18) becomes,

$$s_{fl} = C\, N_1(0) V_{fl}\frac{B_{12} I_{\vartheta}}{c} \cdot \frac{A_{21}}{(A_{21}+Q_{21})} \tag{2.19}$$

In this case, we have to take into account the rate of non-radiative deactivation processes, Q_{21}, which is not negligible. This will reduce the signal strength and, therefore, the sensitivity. Also, any error in the measurement of the rate of non-radiative deactivation processes will manifest as inaccuracy in the measurement of the concentration.

(b) When laser intensity is very high, $I_v >> I_v^{sat}$, we get a simple relation for fluorescence signal from eqn. (2.18),

$$S_{fl} = C N_1(0) V_{fl}\frac{B_{12}}{(B_{12}+B_{21})} A_{21} \tag{2.20}$$

In this case, the fluorescence signal is independent of both the laser intensity and quenching.

Case 3: Small pulse width, $\tau << 1/Q_{21}$

If pulse width, $\tau << 1/Q_{21}$, then at the initial build up time, $r\tau << 1$, and the fluorescence signal may be expressed as:

$$S_{fl} = C\, N_1(0)\, V_{fl}\, \tau\, B_{12}\, A_{21}\, \rho \tag{2.21}$$

Thus, in this case, the fluorescence signal is directly proportional to the laser intensity and population density of the absorbing states, and is independent of nonradiative deactivation processes. If fluorescence is collected at the time interval during the build up time, in this case, there is no need of correction for nonradiative processes.

The two-level model that we have used is valid for very low pressure and very short laser pulses. Under these conditions, the fluorescence signal is maximum, and, therefore, corresponds to lowest detection limit. At higher pressure, it is necessary to incorporate rotational relaxation.

2.1.2 Experimental Set-up

In all of the experiments included in the present thesis, the photolysis[3] of the molecule of interest was effected by an excimer laser (Lambda Physik, Model Compex-102, Fluorine version), operated in either ArF mode (for 193 nm) or KrF mode (for 248 nm). As shown in Fig. 2.2, here, the OH radical produced in electronic ground state by the photolysis is irradiated at a particular range of wavelength with the help of a tunable laser. Once the wavelength of the laser matches the energy gap between the ground state and the next higher electronic state of OH, a photon is absorbed, and the ground state species goes to the excited state. The excited state must not be dissociative, and a major fraction of the excited species must come back to the ground state by fluorescence. This fluorescence, when collected in broadband, and plotted against the exciting wavelength, gives the ro-vibrationally resolved Laser Induced Fluorescence (LIF) excitation spectrum of the OH radical. LIF is observed perpendicular to the direction of propagation of the laser beam, to minimize interference due to scattering. The emission may be at the same wavelength, as the exciting beam (on-resonance), or at a different wavelength (off-resonance). It is generally accepted that off-resonance laser induced fluorescence is more desirable since it allows the use of optical filters, to discriminate against the strong laser beam, while still detecting the LIF signal. This allows for greater signal to noise ratio, and hence a lower detection limit of OH radical. LIF is an excitation spectrum, as the intensity of different lines in the fluorescence spectrum is directly proportional to the number density in the *ground state* that absorbs, not the excited state, unlike a conventional emission spectrum.

The pump-probe set-up that has been used for Laser Photolysis Laser induced Fluorescence studies is represented in the Fig. 2.3. In the case of the dynamics studies, the flow cell was filled up with the sample at a few mTorr level of pressure. The average number density of the sample was always kept within the range of 10^{13} – 10^{15} molecules/cc, for the dynamics studies. The sample is photolysed, and the probe laser probes the reaction volume, before any collision can take place. In this case, the time delay between the pump and the probe lasers was kept 50 nsec. The reaction chamber was made of pyrex glass with crossed arms at right angles provided for the entrance of the pump and the probe laser beams, which intersect at the centre of the reaction chamber. The reaction volume had a diameter of around 5 mm, and the cell was continuously pumped at the flow velocity of 10 cm sec^{-1}. As the pump laser was operated at the repetition rate of 20 Hz, this ensured that every new pulse from the pump laser was absorbed by a fresh batch of molecules. The detection system was attached to the bottom window of the double-walled cell, to capture a view of the intersection volume of the photolysis and the probe lasers. This system consisted of a lens (focal length 500 mm, diameter 38 mm), to collect the fluorescence, a photomultiplier tube (Hamamatsu, model R 928P), to detect it, and a band pass filter (λ_{centre}=310 nm, FWHM=10 nm, $\%T_{310nm}$=10%) placed between them, to cut off the scattering from the photolysis laser light. The fluorescence signal was gate integrated by a boxcar (SRS 20), averaged over 30 laser shots, and fed into an interface (SRS 245), for A/D conversion. A Pentium II PC is used, to control the scan of the dye laser via an RS232 interface, and to collect data through a GPIB interface, using a control and data acquisition program.

In the case of the kinetics studies[4], as shown in Fig. (2.4), the temperature of the double-walled Pyrex glass cell was varied in the range of 298-365 K, by circulating water from a thermostated bath, through the outer jacket. The temperature and the pressure inside the reactor were continuously monitored, and kept constant during the experiments.

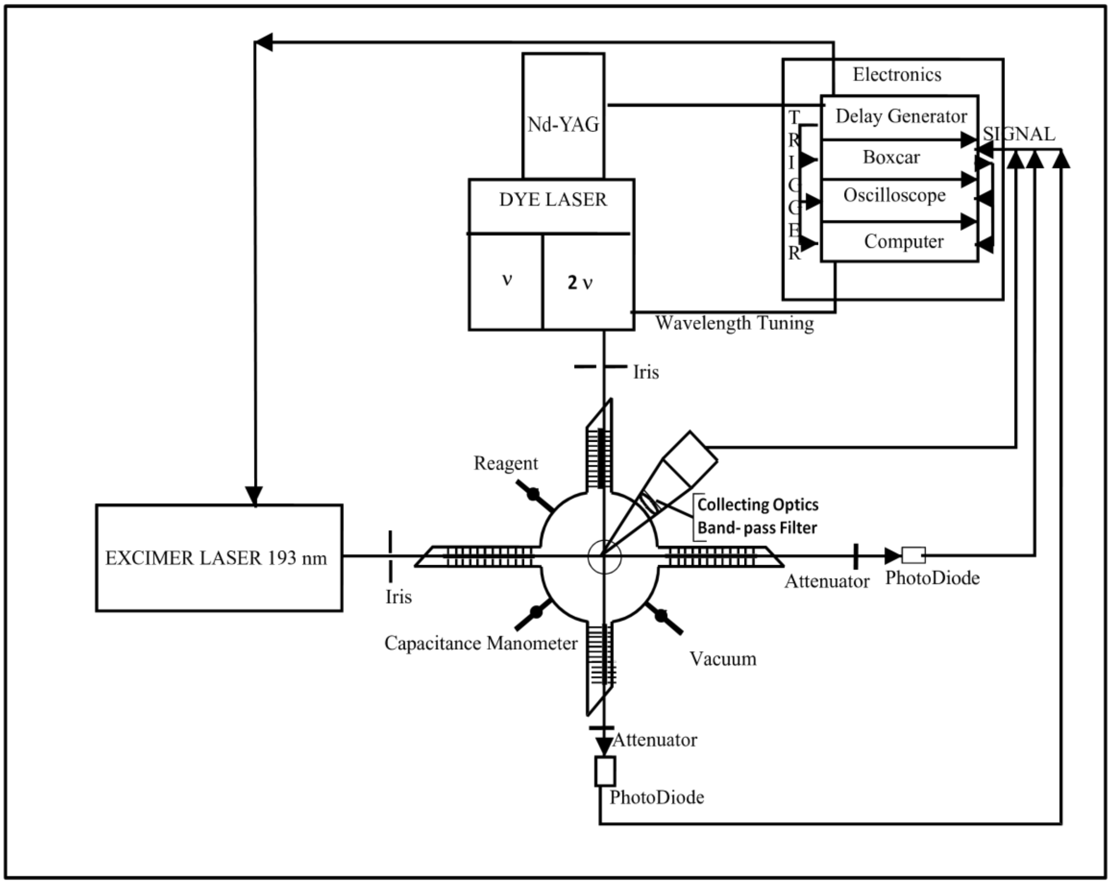

Fig. 2.3: Schematic diagram of the LP-LIF experimental set-up for dynamics experiments

OH radicals were generated by photolysis of H_2O_2 in the reaction cell, at 248 nm, using a KrF excimer laser (pump beam). LIF intensities were normalized with respect to both the pump and the probe laser energies, using suitable photodiodes, to correct for the laser intensity fluctuations. In the kinetics studies, the P1(2) line in the (0,0) band of the ($A^2\Sigma$, v′ = 0) ← ($X^2\Pi$, v″ = 0) transition (section 1.8) was excited, and fluorescence was collected at different delays between the pump and the probe lasers, varying in steps of a few microseconds. In all of the experiments, the laser beams were unfocussed and attenuated, to prevent any saturation effect, or multiphoton event.

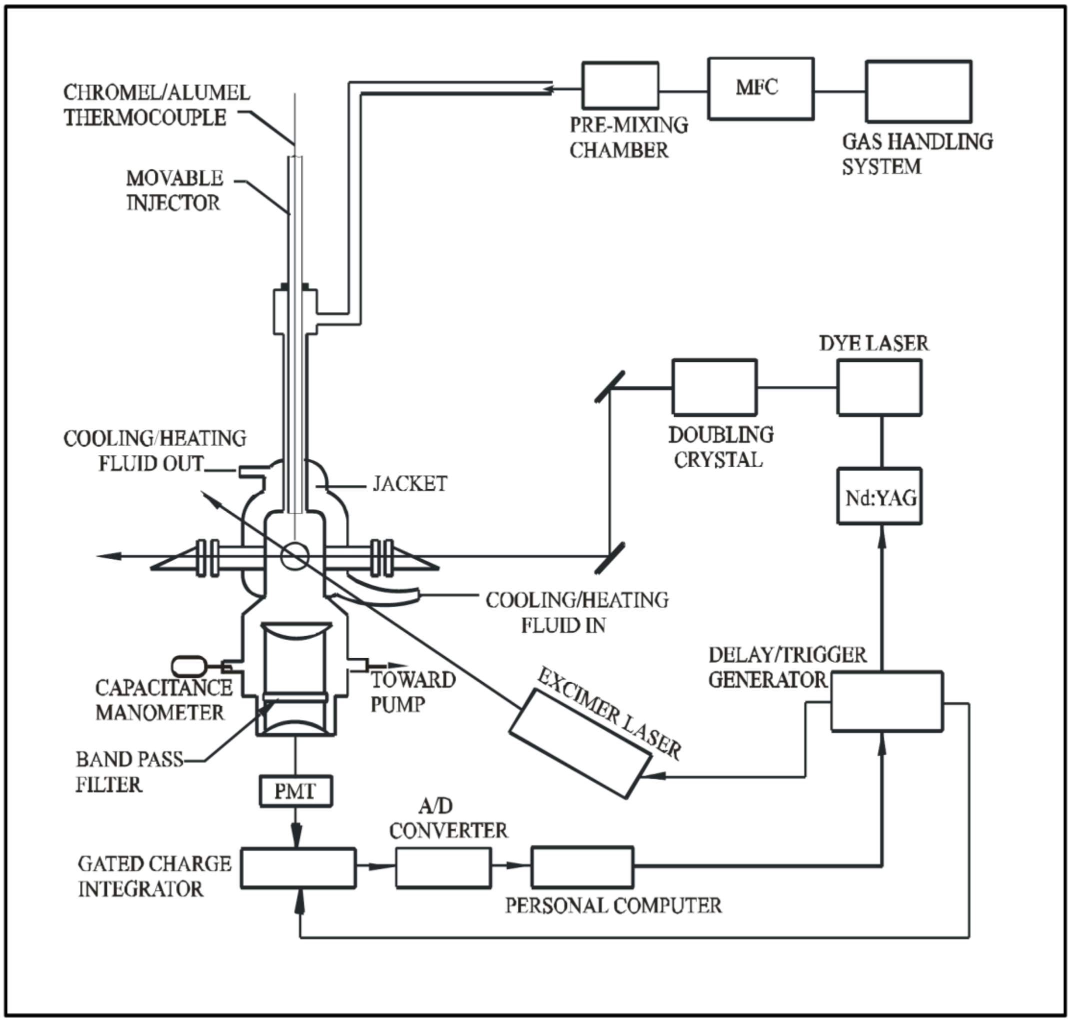

Fig. 2.4: Schematic diagram of the LP-LIF experimental set-up for kinetics experiments

2.2 Stable Product Detection

2.2.1 FTIR Spectrometry

In some of the works included in the present thesis, absorption in the IR region has been used for characterisation and quantification of certain samples and stable products. For this purpose, we have used a Bruker IFS 66s/V FTIR instrument in its steady state mode. The spectrometer basically consists of two parts, an optical system which uses an interferometer, and a dedicated computer. The computer controls the optical components, collects and stores data, performs computations on data and displays spectra. The real advantage of a FTIR spectrometer results from the use of an interferometer, instead of a grating, or a prism. A schematic diagram of a rapid scanning FT spectrometer is given in Fig. 2.5. The light from an IR source is collimated, and sent to the beam splitter of an interferometer. The beam is divided, a part going to the moving mirror, and the other part going to the fixed mirror. The reflected beams recombine at the beam splitter, and generate interference patterns. The reconstructed beam is then directed through the sample and focussed onto the detector. The motion of the mirror results in a signal at the detector, which, for a given wavelength, varies sinusoidally. A laser beam undergoing the same change in optical path, as the IR beam, is used to reference the position of the mirror during the scan, and initiates the collection of data points from the signal of the IR detector at uniform intervals of mirror travel. The data points are digitized by an analog-to-digital (A/D) converter, and stored in a computer memory. The result is an interferogram, i.e., a record of the signal of the IR detector as a function of the difference in path (retardation) for the two beams in the interferometer. Using an algorithm, Fourier transformation is performed on the interferogram, which generates the IR spectrum.

The instrument that was used, Bruker IFS 66s/V, is a flexible vacuum step-scan FT-IR spectrophotometer, with a water-cooled SiC globar source which covers the wavelength range of 7500-370 cm^{-1}. It has a multilayer Ge-coated KBr beamsplitter, and deuterated L-alanine doped triglycine sulfate (DLaTGS) detector, for the mid-IR range. The IR spectrum collected by this instrument, from an evacuated sample compartment (< 3 mbar), has a resolution of better than 0.25 cm^{-1}.

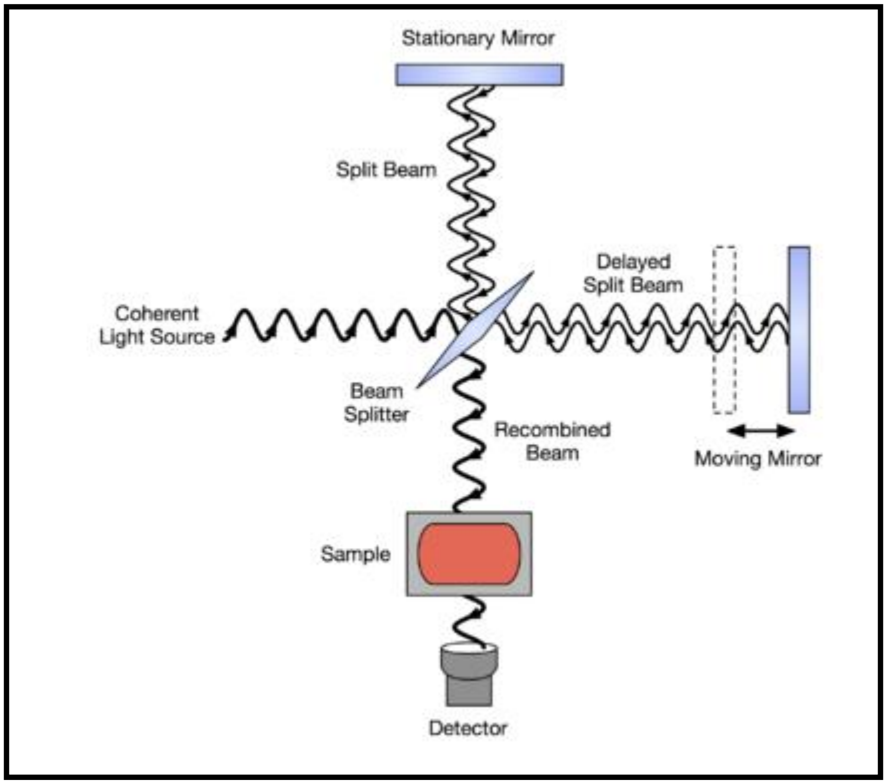

Fig. 2.5: Schematic diagram of FTIR spectrometer using Michelson's interferometer

A stainless steel cell, with crossed arms at right angles to each other fitted with suitable windows, for allowing UV and IR radiation, was used for identification of the stable products generated on photolysis at 193 nm. After irradiation for average 1000 pulses of the pump laser at low energy (~1 mJ/pulse), the stable products were analysed qualitatively, employing the FT-IR.

2.2.2 Gas-Chromatography

Chromatography is a physical process of separation, isolation, identification and quantification where the compounds to be isolated are distributed differently between two phases, one stationary phase, with large surface area, and the other is a mobile phase (gas or liquid), moving in contact with the stationary phase.

In the case of gas-chromatography, the gaseous mobile phase, which is called carrier gas should fulfil some particular requirements. It should primarily be an inert gas, which is easily available in high purity at a comparatively low cost. For different solute

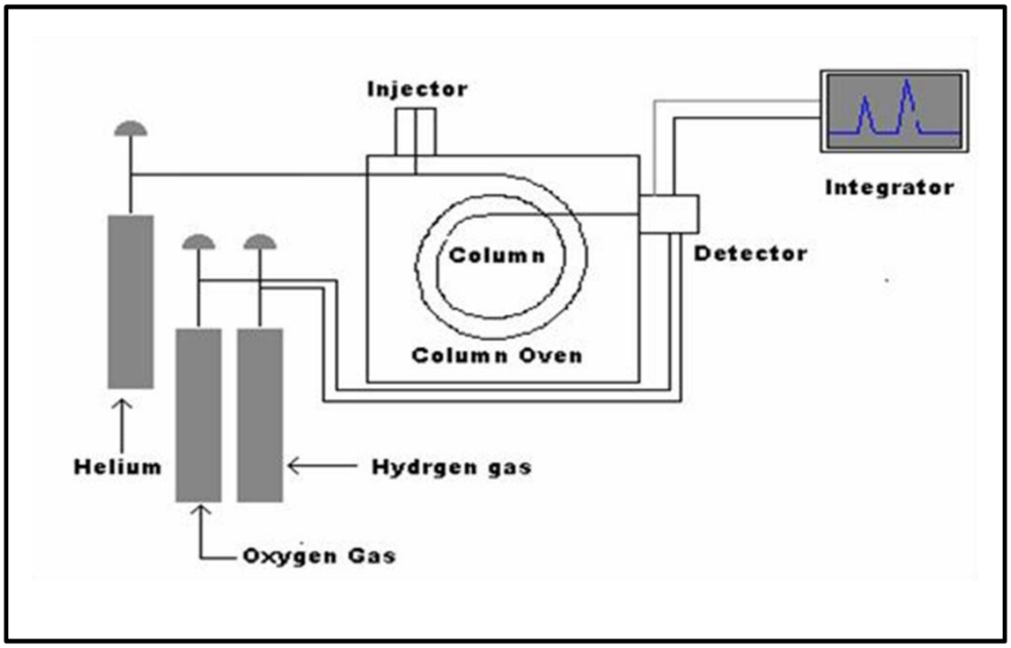

Fig. 2.6: Basic components of a Gas – Chromatography Instrument

characteristics and detection techniques, different carrier gases can be used, like He, Ar, N_2, or H_2. The stationary phase, which is commonly called the column, can either be capillary or packed type. Different types of column materials are used, depending on the solutes to be separated. In the case of gas chromatography, the mobile phase is a gas. The solutes are separated based on the value of their distribution coefficient between the two phases (K), which depends on temperature, the nature of solute, the mobile phase and the stationary phase.

$$K = \frac{\text{Concentration of solute in stationary phase}(C_S)}{\text{Concentration of solute in mobile phase }(C_M)} \qquad (2.22)$$

Depending on the value of K, the retention time of different solutes differ from each other, and they can be separated, based on the time required for their emergence from the column. A schematic of the GC is shown in Fig. 2.6.

The solutes, once separated, are characterized by a suitable detector. In most of the analyses described in this thesis, Flame Ionisation Detector (FID), or Thermal Conductivity Detector (TCD), has been used. In the case of TCD, the difference between the thermal conductivity of the sample and H_2 or He is detected by the deviation from the null condition in a balanced Wheatstone Bridge. In the case of FID, the ionisation current is recorded to distinguish the different compounds from the carrier gas. The identity of the compound is established by comparing the retention time with that of a standard compound. The choice of a detector depends on its sensitivity, capacity to operate linearly over a wide range of temperature, flow, and rapidity of its response to the presence of solute.

2.3 Absorption Cross-section and Quantum Yield Measurement

UV absorption spectroscopy has been employed for finding out the absorption cross-section of compounds at 193/248 nm, where it is not already reported in the literature. The value obtained has been used for determination of quantum yield of OH formation channel. For this purpose, a set-up[5] has been developed with sample-reference dual beam geometry. A beam-splitter is placed before the absorption cell, to bifurcate the beam. A part of it is directly sent to a photodiode, which measures the incident light intensity (I_0), and the other part is passed through the absorption cell of pathlength of 50 cm, before it falls on a photodiode which measures the emerging light intensity (I). As shown in Fig. 2.7, the normalized value of ln (I_0/I) is plotted against the concentration of the absorbing species. The linear plot obtained in this way is fitted to Lambert-Beer's law (eqn. 2.23), and from the slope of it, absorption cross section (σ) of the compound is determined.

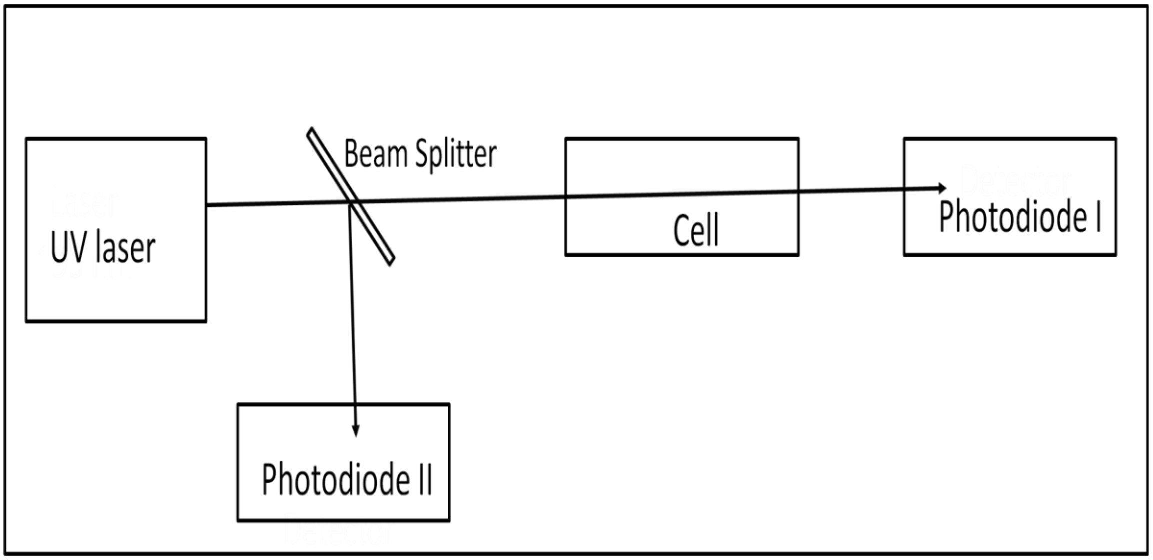

Fig. 2.7: Schematic representation of the dual beam set-up for absorption cross-section measurement

$$\ln(I_0/I) = \sigma.n.l \qquad (2.23)$$

where I_0 and I are the intensities of the incident light, and emergent light, respectively, and n is the number density of the absorbing species. The yield of the OH radical is related to the absorption cross-section of the parent molecule at that particular wavelength, photon intensity, no. density of the compound and the volume of the photolysis zone. Hence, the intensity of an OH rotational line, when normalized for the absorption cross section of the parent molecule, and photon intensity, and compared with a normalized reference, gives quantum yield of its generation channel. We calculated the quantum yield of OH generation from a relative method, using the relation:

$$\frac{(Q.Y.)_{sample}}{(Q.Y.)_{reference}} = \frac{\left(\frac{intensity}{\sigma}\right)_{sample}}{\left(\frac{intensity}{\sigma}\right)_{reference}} \qquad (2.24)$$

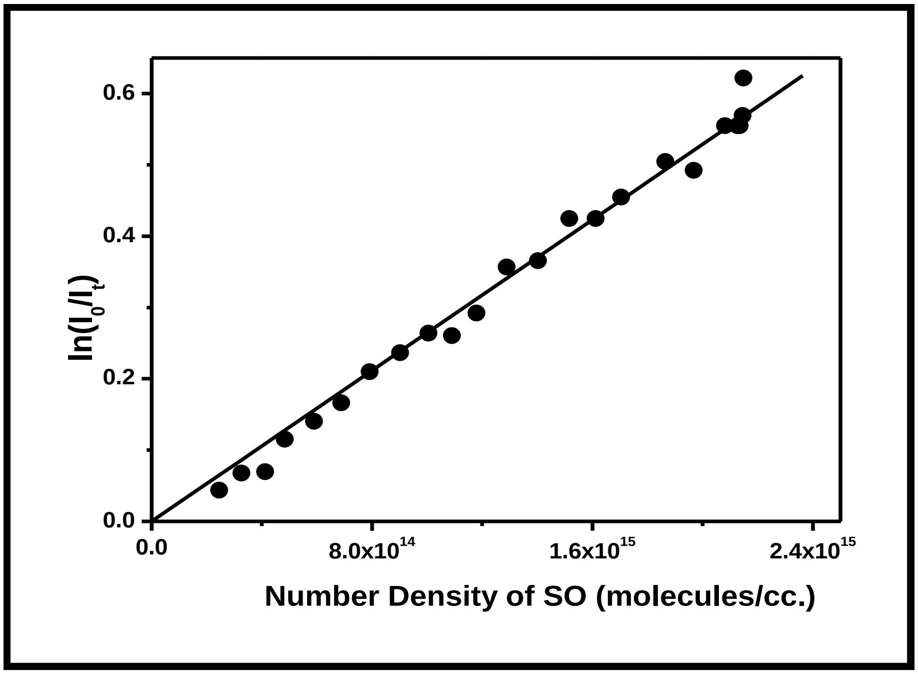

Fig. 2.8: A typical plot of Lambert- Beer's Law for the measurement of absorption cross-section of a compound

Acetic acid was taken as the reference compound, with the measured values of the absorption cross section (σ) and the quantum yield of OH generation channel to be 1.13×10^{-19} cm^2 $molecule^{-1}$ and 0.8, respectively. The areas under the curve of P1(2) line of the sample and acetic acid were compared for calculation of quantum yield.

2.4 Analysis of Experimental Results

The data obtained by LP-LIF are used for extracting important dynamic information of the photolysis reaction. The rotationally resolved electronic spectra collected under collisionless condition gives a reliable picture of the energy state distribution among the product species at their nascent states. The intensity of the different rotational lines is directly proportional to the population of the product in the different rotational levels. If higher vibrational states of the product molecules are found to be populated, the ratio of intensity of the same rotational line for transitions from two different vibrational states can give an idea about the vibrational temperature, too, i.e., vibrational energy of the products. Each of the rotational lines has some finite width due to Doppler effect. A Doppler broadened rotational line would have contributions from the different line broadening factors, like molecular velocity of the fragments, thermal motion of the parent molecule, and the spectral width of the probe laser. Hence, after correcting for the probe laser line width (0.07 cm^{-1} in the present work, measured by de-convolution of the line width of thermalized OH at high pressure and a longer pump-probe delay time of ~100 μs), the Doppler profile of a line in the spectrum shows the distribution of velocity component v_z of the absorbing species, i.e., the OH radical along the propagation direction of the probe laser beam. Thus, the LIF spectrum can be analyzed, and distribution of the energy among nascent products can be obtained.

2.4.1 Translational Energy in Products

LIF linewidth corresponds to the transition width between the two energy levels of the probe species. The width of the rotational lines is large; this has contributions from the natural, Doppler and pressure broadenings. The natural width is related to the lifetime of the excited state, and arises from the Heisenberg uncertainty principle. The Doppler broadening is due to the thermal motion of the probed species. The distribution of velocities at a thermodynamic temperature T can be determined from the Maxwell-Boltzmann distribution. Because of the different velocity components, (the projection of velocity of probed species on the propagation direction of probing light), each probed species has a slightly different transition frequency. The corresponding line shape function is given by the expression;

$$g(\nu) = \frac{c}{\nu_0}\sqrt{\frac{m}{2\pi kT}}\ \exp\ [-4ln2\frac{(\nu-\nu_0)^2}{\Delta\nu_D^2}] \qquad (2.25)$$

Where, $\Delta\nu_D$, the Doppler width at half maximum, is defined as,

$$\Delta\nu_D = \frac{2\alpha\nu_0}{c}\sqrt{2ln2} \qquad (2.26)$$

Here, α is the most probable velocity of the molecules, and ν_0 is the center frequency of the transition. In a flowing system at the temperature T, the Doppler width is the same as given by the above equation; however, the center frequency of the transition is shifted, which is given by the expression,

$$\nu - \nu_0 = \frac{\nu_0 . \mathrm{v}}{\mathrm{c}} \tag{2.27}$$

Where v is the velocity of the emitter towards the observer and c is the velocity of the probing light.

The collisional broadening is homogeneous in nature and hence generally results in a Lorentzian line shape, while the Doppler broadening, due to random thermal motion of the absorbing species, is inhomogeneous, resulting in a Gaussian line shape. The transition line broadening in LIF spectra contains information about the temperature, flow velocity and pressure, which can be extracted by suitable deconvolution method.

A typical measured Doppler profile of the $P_1(2)$ rotational line is depicted in (Fig. 2.9).

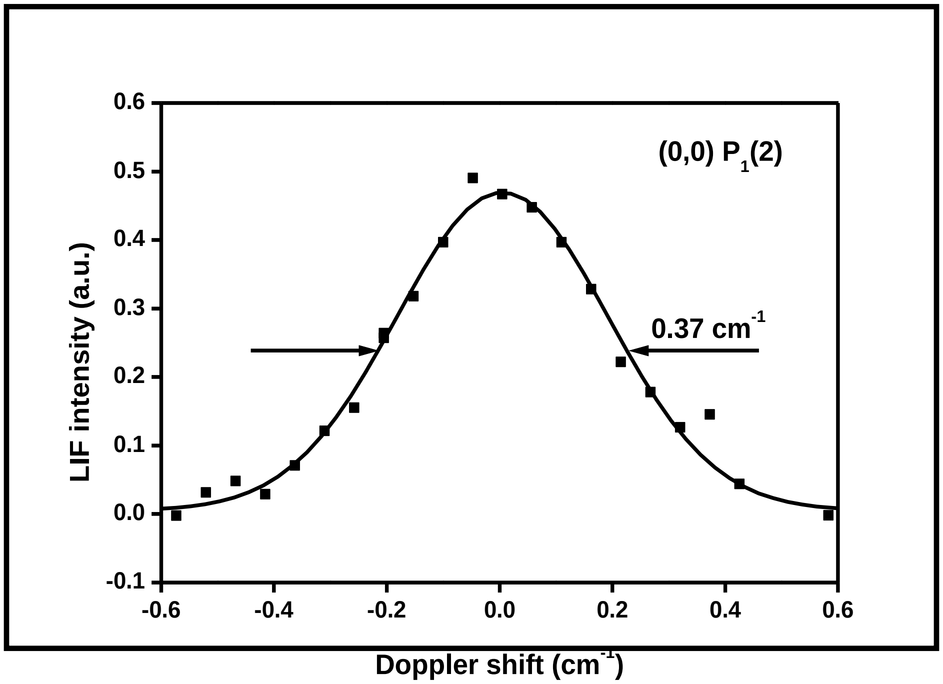

Fig. 2.9: A typical profile of a Dopplar broadened LIF peak. The width of the Gaussian type profile gives the value of average rotational energy.

If the velocity distribution f(v) is isotropic, i.e., $f(v_x)=f(v_y)=f(v_z)$, For a Gaussian Doppler profile, the one–dimensional distribution of velocity along any co-ordinate is given by,

$$f(v_z) = \frac{1}{\alpha\sqrt{\pi}} e^{\frac{-v^2}{\alpha^2}} \qquad (2.28)$$

Hence, $\langle v_z^2 \rangle_{OH}$, which represents the second moment of the laboratory velocity distribution of the OH radical in the direction of laser propagation, is given as,

$$\langle v_Z^2 \rangle_{OH} = \int_{-\infty}^{\infty} v_z^2 f(v_z) dv = \frac{1}{\alpha\sqrt{\pi}} \int_{-\infty}^{\infty} v_z^2 e^{-v^2/\alpha^2} dv \qquad (2.29)$$

By putting the value of the standard integral, and substituting the value of α from eqn. 2.26.,in eqn. 2.29, we get,

$$\langle v_Z^2 \rangle_{OH} = \frac{(\Delta\nu_D/2\nu_0)^2 c^2}{2 \ln 2}$$

ν_0 and $\Delta\nu_D$ are the position of the peak and width of the profile, respectively. The average translational energy in the laboratory frame is given by,

$$E_T^{lab}(OH) = \frac{3}{2} m_{OH} \langle v_Z^2 \rangle_{OH} \qquad (2.30)$$

About 15 rotational linewidths were estimated for each of $P_1(2)$ and $Q_1(4)$ lines, and using the above two equations, the kinetic energy of the OH fragment in laboratory frame, $E_T^{lab}(OH)$, was determined. The average translational energy in the centre-of-mass frame, E_{CM}, was calculated from $E_T^{lab}(OH)$, neglecting the translational energy of the parent molecule, by the use of the equation,

$$E_T^{CM} = E_T^{lab}(OH)\left[1 + \frac{m_{OH}}{m_{otherfragment}}\right] \qquad (2.31)$$

2.4.2 Rotational Temperature

The temperature of a system in thermodynamic equillibrium can be determined from the population distribution of the rotational levels, as populations of the different levels are related to the temperature by the Boltzmann's equation,

$$\frac{N_{J=m}}{N_{J=n}} = \frac{LIF_{signal\ at\ J=m}/(2m+1)}{LIF_{signal\ at\ J=n}/(2n+1)} = \exp\left(-\left[\frac{E^{R}_{J=m}-E^{R}_{J=n}}{kT}\right]\right) \tag{2.32}$$

Hence, from the relative populations of the different rotational levels, that is, from the relative LIF signal, the temperature of the system can be determined. Positions of all the rotational lines in the spectrum of the OH radical were marked, following the assignments made by Dieke and Crosswhite[6].

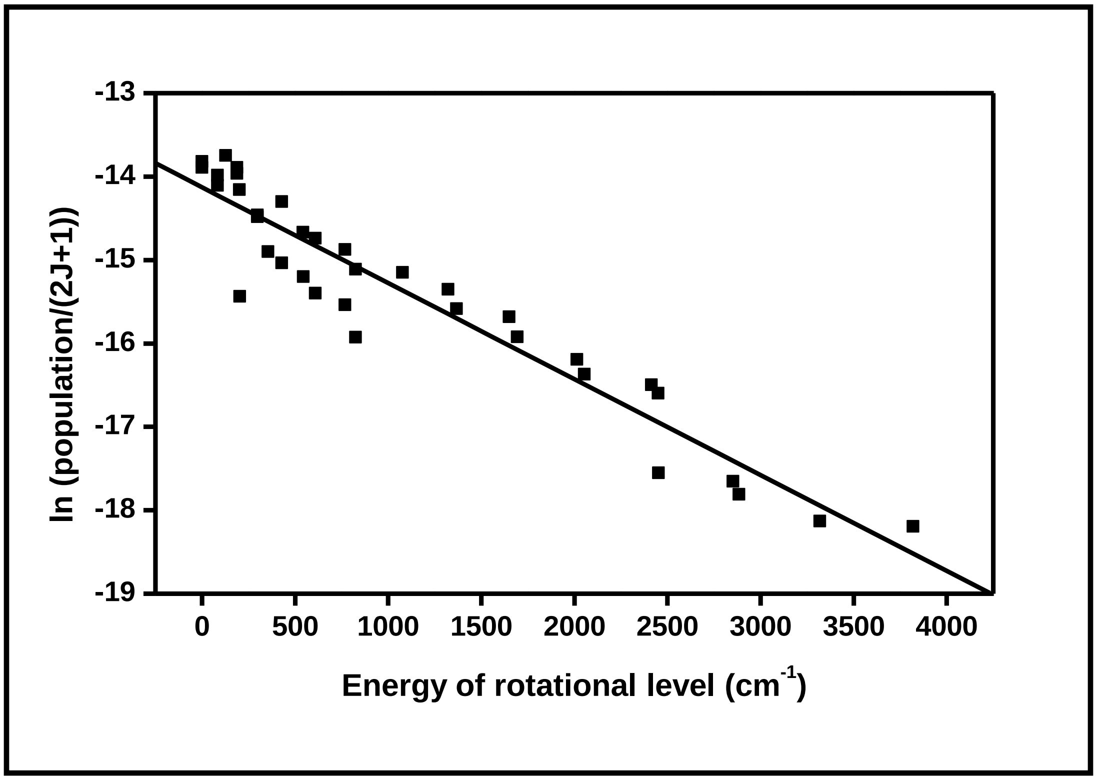

Fig. 2.10: A typical Boltzmann distribution of the population against energy of the rotational levels. The rotational temperature as well as rotational energy can be calculated from the slope of the straight line.

The respective LIF intensities were normalized with respect to the photolysis and the probe laser intensities, pressure of the sample in the cell, and Einstein's absorption coefficients B_{ij} (taken from the work of Chidsey and Crossley[7]), to calculate the relative population of each rotational level. The populations P(J), obtained in this fashion, of the nascent OH fragment generated by photodissociation, were plotted against energy of rotational levels (ε), to construct a Boltzmann plot given by the equation

$$\ln\frac{P(J^{"})}{(2J^{"}+1)} = \frac{-\varepsilon hc}{kT_R} + constant \qquad (2.33)$$

The rotational temperature (T_R) of OH is determined from the slope of this plot (depicted in Fig.2.10).

2.4.3 Spin-orbit and Λ Doublet State Distribution

The spin-orbit ratio, generally known as the F_1/F_2 ratio, which gives the relative population in the $\Pi_{3/2}$ and $\Pi_{1/2}$ states, was obtained from the ratio of populations, $P_1(N)/P_2(N)$, $Q_1(N)/Q_2(N)$, and so on. For $F_1(N)$ and $F_2(N)$, since the J values are not the same, the populations were normalized with a statistical weighing factor, (2J+1). The ratios of the populations of $\Pi_{3/2}$ and $\Pi_{1/2}$ states, after normalization, were plotted against the respective rotational quantum numbers (N). If the plot (Fig.2.11 is one typical representative) shows that the ratio is close to unity, for all values of N, it can be concluded that the distribution of OH population between these two states is statistical, and there is no preference for either of these spin-orbit states, or vice versa. Sometimes, non-statistical distribution of the spin-orbit states is observed due to reasons[8, 9], like interaction of the initially excited state with nearby triplet states, or inelastic scattering between the recoiling fragments, etc.

The difference in the orientation of π lobes with respect to the plane of rotation of the molecule gives rise to Λ doublets. In $^2\Pi^+(A')$ state of OH, the π lobe lies in the plane of rotation, while in $^2\Pi^-(A'')$ state, the π lobe lies perpendicular to the plane of rotation. The Λ doublet ratio ($^2\Pi^-(A'')/^2\Pi^+(A'')$) was obtained from $(Q_1(N)/P_1(N))$ or $(Q_1(N)/R_1(N))$. For $Q_1(N)$, $P_1(N)$, and $R_1(N)$, since J values are same, normalization of population is not required. From the ratio of populations of these two states (as shown in Fig.2.12), it can be found out whether both the levels are equally populated, or there is some preference for one particular level, for all the values of N.

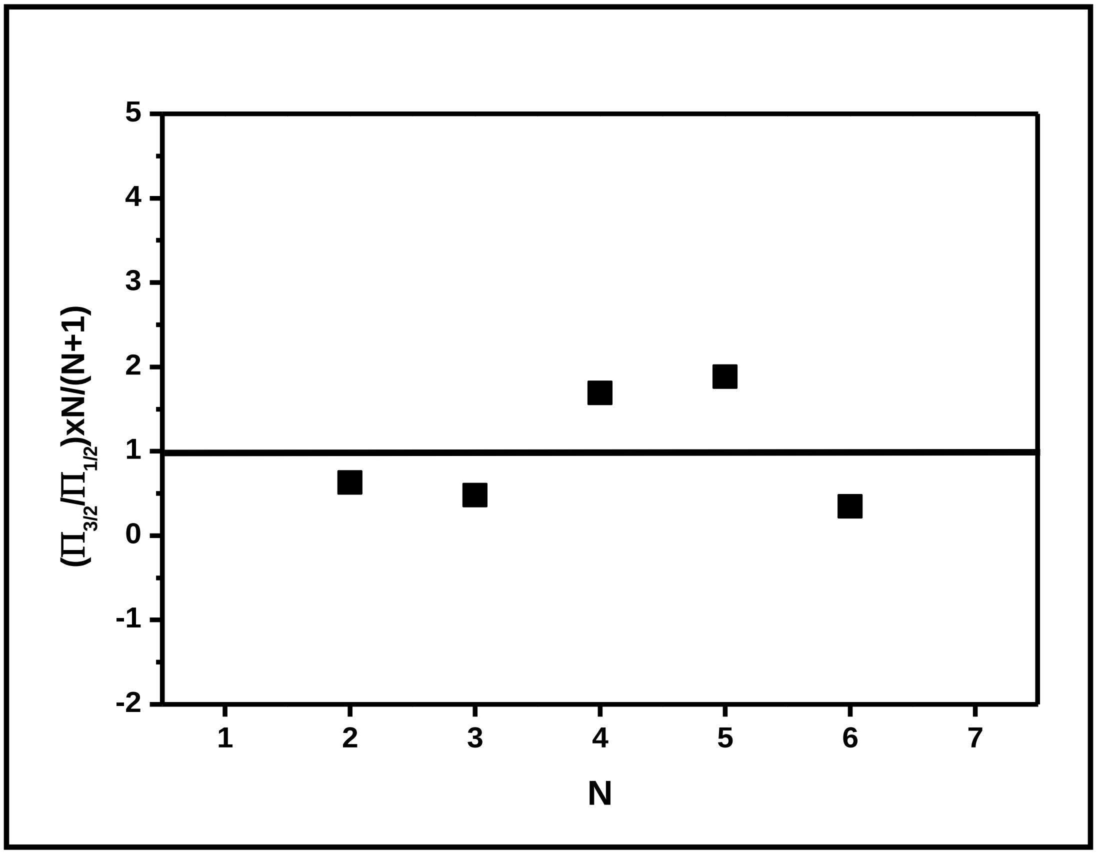

Fig 2.11: A typical plot of the ratio of the population s in the two different spin-orbit states ($\Pi_{3/2}$ and $\Pi_{1/2}$) against rotational quantum number (N). Here, the ratio is nearly one for all values of N, i.e., there is no preference for any particular spin-orbit state.

In a diatomic molecule, with a singly occupied p_Π orbital, such as OH, the coupling between the electronic angular momentum and the nuclear rotation splits the two degenerate states of $\Lambda = \pm 1$, which originates from the different orientations of the orbital angular momentum projection on the internuclear axis. In the limit of high rotation, the p_Π orbital is approximated as a lobe aligned perpendicular to the plane of rotation (Π^-, the lower Λ state) or a lobe in the plane of rotation (Π^+, the upper Λ state).

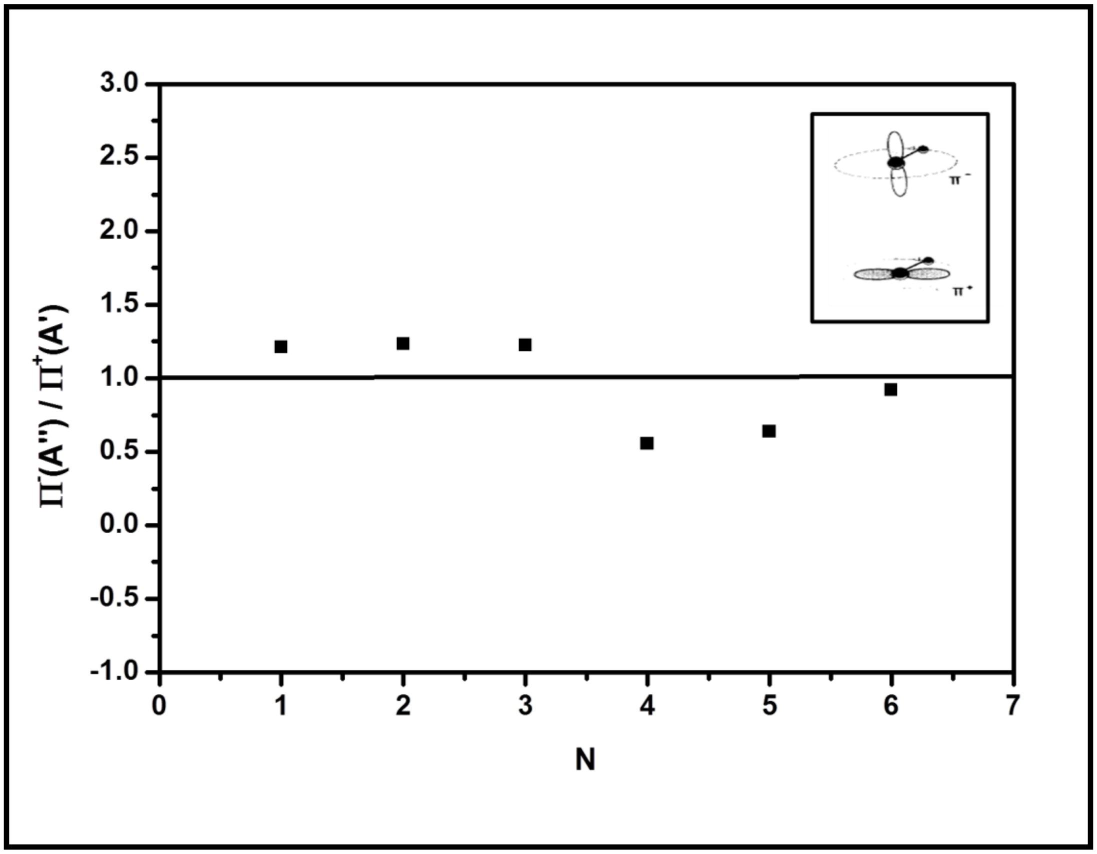

Fig. 2.12: A typical plot of distribution of the ratio of populations in the two different Λ doublet states ($^2\Pi^+(A')$ and $^2\Pi^-(A'')$) against the rotational quantum number (N). Here, the ratio is nearly zero for all values of N, i.e., there is no preference for any particular Λ doublet state.

Inset: orientation of Π lobes with respect to the plane of rotation of the molecule, for different Λ doublet states.

According to the parity selection rule, the Q-branch rotational transition is induced from the Π^- state, whereas the R- and P-branches transitions from the Π^+ state in the electronic transition. Thus, the specific Λ-doublet population can be measured experimentally in the spectra. The distribution between the two Λ-doublet states of OH produced in the photodissociation depends on the correlation of the p_Π orbital of the OH fragment with the orbitals of the parent molecule, and how the p_Π orbital is generated upon dissociation, that is, the mechanism of the dissociation process. In other words, OH rotating in the plane containing the dissociating C—O bond axis, would be expected as a result of in-plane dissociation, if the rotation of OH originates solely from the impulse upon dissociation. Conversely, out-of-plane dissociation would be expected if the parent torsional motion plays a role upon dissociation. If the measured Λ-doublet distribution in this experiment shows no propensity in the two Λ-doublet states, it is possible that both the impulse and the parent torsion should be transformed into product rotational motion. On the other hand, a non-statistical population of Λ doublets is observed, when the torque responsible for the rotational excitation of the fragment lies in a preferred plane[10].

2.5 Dynamic Models: Distribution of Available Energy among the Products

For any chemical reaction, the total energy E of the colliding molecules is a conserved quantity (constant throughout the collision), and a very important variable. It thus determines which states of the products are allowed to be populated. The total available energy E_{avl} is usually defined with respect to the lowest possible energy state (of either the reactants or the products). For a particular initial reactant state, the total available energy is the sum of the internal energy of the reactants, the relative translational energy, and the zero-point to zero-point exoergicity, ($-\Delta E_0$), of the reaction. After the reactive collision, the energy is partitioned between the products' internal energy and translational energy. The internal energy consists of the vibrational and the rotational energy of the products. In the case of photodisociation reaction, the partitioning of this excess energy, which we shall call as the available energy, is mainly governed by the nature of the transition state on the dissociative potential energy surface. It can be examined quantitatively in terms of two limiting models, the Impulsive Model[11] and the Statistical Model[12-15]. We have applied both of these models, to calculate partitioning of available energy among the various degrees of freedom of the photofragments.

2.5.1. Statistical Model

The statistical model for distribution of the available energy is based on ideas developed from prior distribution[16], Phase Space Theory (PST)[17, 18], or Separate Statistical Ensembles theory (SSE)[19]. While the first two rely solely on the information about the product states to partition energy, the third attempts to correct these deficiencies by using some of the information about energy partitioning in the parent molecule, to obtain product state partitioning, but, below the vibrational threshold, SSE and PST do not differ at all.

The basic assumption for prior distribution model of partitioning of energy is that all the possible combinations of product states that conserve energy and linear momentum, are equally probable. This approach completely ignores any angular momentum constraint, and hence is equivalent to the simplest calculation of the *a priori* distribution in the information theory analysis of energy disposal by Levine and

Bernstein[20]. The breaking of the bond is viewed as an instantaneous event, which prevents any further redistribution of energy. Following this reasoning, it makes sense to partition the statistical energy into translational (T), rotational (R), and vibrational (V) degrees of freedom using information only from the parent, and not information from the products as in PST and the prior distribution. This statistical prior distribution is convenient for understanding any dissociating event, and usually, provides a better description of partitioning of available energy for photodissociation reactions without any barrier.

The statistical model predicts the energy partitioning to the rotational degrees of freedom in the following manner

$$\langle E_R \rangle = \frac{\int_o^{Eavl} dE_v \int_0^{Eavl-Ev} dE_t \int_0^{Eavl-Ev-Et} dE_R \rho_P(E_v)\rho_R(E_R)\rho_t(E_t)\delta(E_{avl}-E_v-E_t-E_R)E_R}{\int_o^{Eavl} dE_v \int_0^{Eavl-Ev} dE_t \int_0^{Eavl-Ev-Et} dE_R \rho_P(E_v)\rho_R(E_R)\rho_t(E_t)\delta(E_{avl}-E_v-E_t-E_R)}$$

(2.34)

where ρ_P , ρ_R , and ρ_T are the densities of states for the P (parent), R, and T ensembles of the parent vibrational modes. The P ensemble is made up of all the vibrational modes of the parent molecule. Partitioning of the available energy is made with a number of important assumptions. We use vibrational densities of states by using the rigid rotor harmonic oscillator (RRHO) approximation, and we assume that both the fragments can be well approximated by totally symmetric tops. The harmonic approximation to the vibrational density of states does moderately well, due, in part, to fortuitous cancellation of the effects of coupling and anharmonicity. Anharmonicity tends to raise the density of states at energies near the dissociation limit, and coupling between the modes tends to separate the nearly degenerate vibrational levels. The cancellation of the two effects makes the harmonic approximation to the density of states a reasonable approximation. In the rigid rotor harmonic approximation, the densities of states can be computed easily, using the Beyer-Swinehart algorithm. The expressions for $\langle E_v \rangle$ and $\langle E_T \rangle$ are similar to the one for the rotational energy that is given above.

Essentially, it is assumed that the total available energy is going to be distributed statistically between the three ensembles, where the ensemble for vibrations can sample from the other two ensembles. The statistics (and hence the energy distribution) are governed by the vibrational frequencies of the parent as well as a judicious choice of modes for membership in each ensemble.

Dividing $\langle E_T \rangle$ between the two fragments is easily accomplished by conserving linear momentum:

$$E_t^A = \frac{m_B}{m_A + m_B} E_{avl} \tag{2.35}$$

$$E_t^B = \frac{m_A}{m_A + m_B} E_{avl} \tag{2.36}$$

$\langle E_R \rangle$ is similarly partitioned by requiring conservation of angular momentum:

$$E_R^A = \frac{I_B}{I_A + I_B} E_{avl} \tag{2.37}$$

$$E_R^B = \frac{I_A}{I_A + I_B} E_{avl} \tag{2.38}$$

In these equations, the moments of inertia, I_A and I_B, are calculated by approximating that both the fragments are spherical tops, with moments of inertia which are the averages of the real moments of inertia for that fragment. The approximation of both the fragments as spherically symmetric tops is a necessary approximation for satisfying conservation of angular momentum, while being subject to the constraint of having minimal information about the geometry of the transition state. An additional approximation is that the parent is assumed to have no rotational motion prior to the dissociation.

The only remaining difficulty is to divide the vibrational energy from the statistical reservoir between the two fragments. It seems reasonable to view the impulse as an instantaneous event, so that the energy is frozen in the parent modes. The energy in the modes that develop into fragment vibrations should then be assigned to the appropriate fragment. Identifying these modes and obtaining their frequencies seems to be impossible for all, but the simplest of the molecules. By approximating the frequencies of these modes by the frequencies of the fragment modes themselves, one obtains the following expression for the vibrational energy partitioned into fragment A from the statistical model:

$$\left\langle E_V(A)\right\rangle = \frac{\int_o^{Ev} dE_v \int_0^{Ev-EA} dE_B \rho_A(E_A)\rho_B(E_B)\delta(E_v - E_A - E_B)E_A}{\int_o^{Ev} dE_v \int_0^{Ev-EA} dE_B \rho_A(E_A)\rho_B(E_B)\delta(E_v - E_A - E_B)} \tag{2.39}$$

where ρ_A and ρ_B are the vibrational densities of states of fragments A and B, respectively.

A significant problem with these methods is that they tend to overestimate product rotational excitation above the vibrational threshold[21], while underestimating product vibrations[22]. This has been understood in terms of the vibrational modes of the parent molecule that can develop asymptotically into both product rotations and vibrations.

2.5.2. Impulsive Model

In the impulsive model, distribution of the available energy among the product states is governed by the dissociation event. In the present study, the soft radical model of A.F. Tuck[11] was used for calculating the impulsive energy for the photofragments. In this model, it is assumed that excitation of a molecule creates a stiff repulsive potential between the two atoms in a molecule which, at the moment of dissociation, are assumed to be independent of the other atoms present in the structure. Due to this repulsive potential, the bond between the concerned atoms breaks rapidly, and because of the suddenness of the rupture, all the available energy E_{avl} goes initially to the kinetic energy of the recoiling atoms. Generally, the impulse is not along the centre of mass of the photofragments, and hence imparts rotational angular momentum to them. Once cleaved, the recoiling atoms collide with the other atoms in the respective photofragments, and their initial translational energies get partitioned into translational, rotational and vibrational energies of the respective photofragments. The translational energy of the individual photofragments can be calculated, applying the conservation of momentum, as the recoiling atom in each is slowed down by the remainder of the fragment. Similarly, rotational energy can be calculated from the rotational angular momentum, using conservation of angular momentum in the whole process. No assumptions are made about the stiffness of any of the vibrations, which means no restrictions are placed on the amount of energy which may appear as fragment vibrational excitation. From the conservation of energy, the remaining available energy is assumed to be partitioned in the vibrational mode.

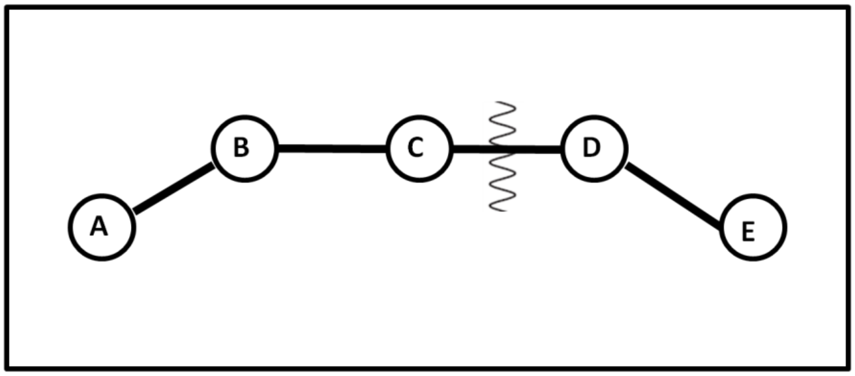

Fig. 2.13: A hypothetical model of a pentatomic molecule, where the C—D bond breaks impulsively.

The above considerations lead to the following formulae for a pentatomic molecule ABCDE (as in Fig. 2.13), in which, the bond between atom D and atom C is breaking impulsively. The initial translational energy of the recoiling atoms, using the conservation of linear momentum, can be calculated as:

$$E_t^D = \frac{m_D}{m_C + m_D} E_{avl} \tag{2.40}$$

$$E_t^C = \frac{m_C}{m_C + m_D} E_{avl} \tag{2.41}$$

Where m_i denotes the mass of the identity i. Conservation of linear momentum applied to the fragments gives the relations:

$$E_t^{DE} = \frac{m_{ABC}}{M} \frac{\mu_a}{\mu_f} E_{avl} \tag{2.42}$$

$$E_t^{ABC} = \frac{m_{DE}}{M} \frac{\mu_a}{\mu_f} E_{avl} \tag{2.43}$$

Here, E_t^i is the translational energy of the fragment i, m_i is the mass of the fragment i, μ_a is the reduced mass of atoms C and D, μ_f is the reduced mass of the fragments and M is the mass of the parent molecule. The angular momenta of atoms C and D about the centres of mass of DE and ABC are given by

$$J_C = (2m_C E_t^C)^{1/2} r_C \sin\chi \tag{2.44}$$

$$J_D = (2m_D E_t^D)^{1/2} r_D \sin\chi \tag{2.45}$$

Where r_i is the distance between the the centre of mass of the fragment i from atom i, and χ is the bond angle between the dissociating atoms. Assuming now that the angular momenta J_C and J_D are conserved, the energies of rotation E_t^{ABC} and E_t^{DE} may be calculated from the formulae

$$E_t^{DE} = \frac{J_D^2}{2I_{DE}} = \frac{m_D m_C}{m_D + m_C} . \frac{r_D^2 \sin^2\chi}{I_{DE}} E_{avl} \tag{2.46}$$

$$E_t^{ABC} = \frac{J_C^2}{2I_{ABC}} = \frac{m_D m_C}{m_D + m_C} . \frac{r_C^2 \sin^2 \chi}{I_{ABC}} E_{avl} \tag{2.47}$$

Where I_t is the moment of inertia of fragment i.

It is now further assumed that the fragment vibrational excitation may be calculated by applying the conservation of energy to the fragment. At this point, their translational and rotational energies have been computed and it has been assumed that there is no electronic excitation of either fragment. The appropriate formulae are,

$$E_v^{DE} = E_t^D - E_t^{DE} - E_r^{DE} \tag{2.48}$$

When both the statistical and the impulsive models fail to explain the experimental results on partitioning of the available energy, a hybrid model, which is a combination of both statistical and impulsive models, can be used for predicting energy partitioning in good agreement with the experimental results.

2.5.3 Hybrid Model

This hybrid model is usually applicable for the reactions with considerable energy barrier in the exit channel. In this model[12, 15], which is known as "barrier impulsive model", the total E_{avl} of the products is divided into two energy reservoirs. One is the statistical energy reservoir, which consists of excess energy above the transition state, E_{stat}(total), and the other is the impulsive energy reservoir, which consists of energy released by exit barrier, E_{imp}(total). The apportioning of the available energy to the different energy reservoirs is shown in Fig. 2.14.

The total available energy can be expressed as

$$E_{avl}(total) = E_{stat}(total) + E_{imp}(total) \tag{2.49}$$

E_{imp}(total) is distributed among the rotational, vibrational, and translational degrees of freedom of each fragment, following the laws of energy and angular momentum conservation, and E_{stat}(total) is partitioned into the same modes according to simple statistical calculations. The total energy partitioned into all the individual degrees of freedom of each fragment is obtained by adding contributions from each of these two models, each applicable to a specific proportion of the available energy.

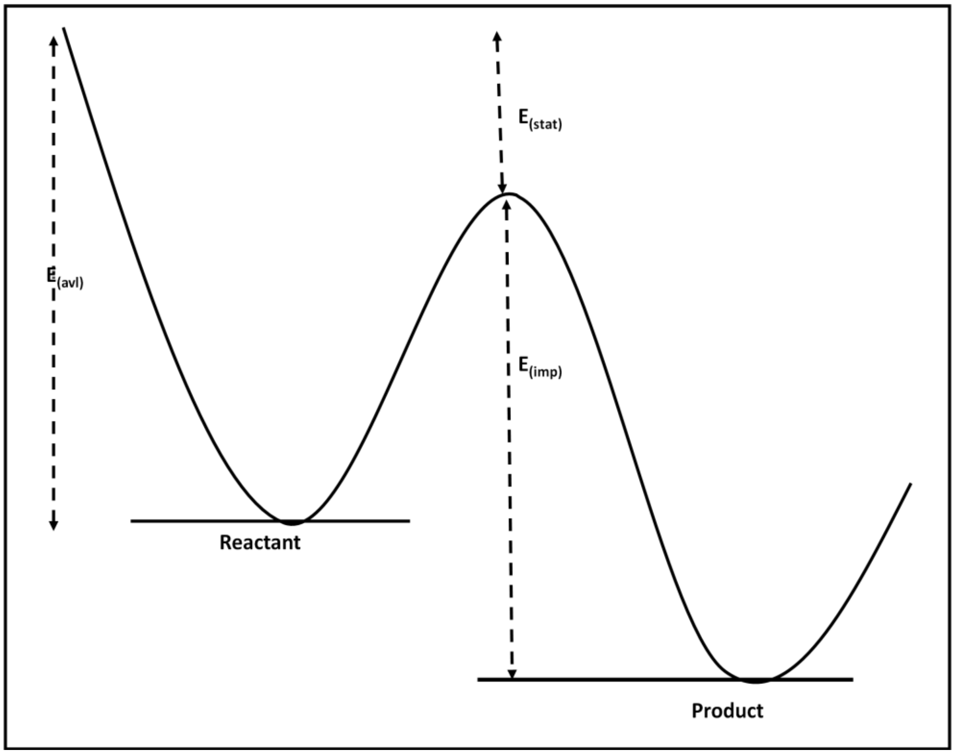

Fig 2.14: Apportioning of the available energy in the different reservoirs in the barrier impulsive model. The energy excess to the exit barrier is distributed according to statistical model, and the energy released by the barrier height is distributed according to the impulsive model.

2.6. Ab initio Molecular Orbital Calculations

In computational chemistry, theoretical models are a very important approach for solving the Schrodinger's equation, by first clearly defining a level of theory, and then, applying it uniformly to molecular systems of all sizes upto a maximum defined by available computational resources. A theoretical model can be applied uniquely for any configuration of nuclei and any number of electrons, to explore all the structures, energies, and other physical properties of the systems, once the mathematical procedure is established through a computer programme. In the Molecular Orbital (MO) method[23], the geometry and the relative potential energy of the molecules, as well as the transition states, are optimized at different levels of the theory, using suitable basis sets, to define molecular parameters. Gaussian 92[2] package was used for *ab initio* molecular orbital calculations, which are completely based on laws of quantum mechanics and some physical constants, like velocity of light (c), mass and charge of electron and nuclei, Planck's constant (h), etc. In the Molecular Orbital theory, individual electrons are assigned to one-electron functions called spin orbitals, which are products of spatial functions, called molecular orbitals, (MO), denoted as $\Psi_i(x,y,z)$, and α or β spin components. The MOs are further restricted to be the linear combinations of n no. of known one-electron functions, $\varphi_i\,(x,y,z)$,

$$\Psi_i = \sum_{\mu=1}^{N} c_{\mu i}\phi_\mu \qquad (2.50)$$

All the $\varphi_i\,(x,y,z)$ together, which are known simply as basis functions, constitute the basis set. For a given basis set, the unknown coefficients, $c_{\mu i}$, are determined, so that the total electronic energy calculated is minimized, and according to the *variational theorem*, is as close as possible to the exact solution of the Schrodinger's equation. This energy and the corresponding wave functions represent the best that can be obtained within the limitations of Hartree-Fock approximations. Atomic basis sets of Gaussian type functions have been used for energy calculation and geometry optimisation. As the size of the basis set increases, the accuracy of the results increases, but the cost of computation also increases. Therefore, the ultimate choice of the basis set size depends on a compromise between the accuracy and the efficiency. Different types of basis sets have different attributes, and they can be classified as follows, with increasing sophistication:

1. Minimal Basis Sets:

These basis sets, which contain the minimum number of basis functions needed for each atom, use fixed-size atomic type orbitals. For example,

H: 1s

C: 1s, 2s, $2p_x$, $2p_y$, $2p_z$

The STO-3G basis set is an example of minimal basis set (Slater Type Orbitals) which uses three Gaussian primitives per basis function (3G).

2. Split Valence Basis Sets:

These basis sets have two or more sizes of basis functions for each valence orbital. For example,

H: 1s, 1s'

C: 1s, 1s', 2s, 2s', $2p_x$, $2p_x'$, $2p_y$, $2p_y'$, $2p_z$, $2p_z'$

Where the primed and the unprimed orbitals differ in size. 6-311G uses three sizes of contracted functions for each orbital type.

3. Polarized Basis Sets:

These basis sets add orbitals with angular momentum, which are beyond what is required for the description of ground state of each atom. For example, 6-31G(d,p) adds d functions to C atom, and p functions to H atom.

4. Diffuse functions:

These are large size versions of s and p orbitals, which allow orbitals to occupy a larger region of space. These functions are applicable for systems where electrons are relatively far away from the molecules, e.g., the molecules with lone pairs, anions and other systems with significant negative charge, systems in their excited state, systems with low ionization potentials, description of absolute acidities, etc. For example, 6-31++G(d) basis set adds diffuse functions to H and heavier atoms as well. Table 2.1 summarizes the most popular basis sets, and provides some recommendations about when they are applicable. Simple Hartree-Fock (HF) models are the most basic to be used for chemical applications, where the number of basis functions of each atom is as small as possible, i.e., only large enough to accommodate all the electrons, and yet maintain spherical symmetry. The main deficiency in Hatree-Fock models is incomplete description of the correlation between the motions of the electrons. To correct for such deficiency, it is necessary to go beyond Hatree-Fock level, and include contributions from more than one electron configuration. The two directions in which a

Table 2.1: Commonly used basis functions with their basic criteria and field of usefulness

Basis set	Description	No. of basis functions	
		heavy atoms*	hydrogen
STO-3G	Minimal basis set: Use for more qualitative results for big systems	5	1
3-21G	2 sets of functions in the valence region: Use when 6-31G is too expensive	9	2
6-31G(d)	Adds polarisation functions to atoms: Use for most jobs upto medium size systems.	15	2
6-31G(d,p)	Adds polarisation function to hydrogens as well: Use when hydrogens are the site of interest.	15	5
6-31+G(d)	Adds diffuse functions: Most important for systems with lone pairs, anions, excited states.	19	2
6-31+G(d,p)	Adds p functions to hydrogen as Well: Use when diffuse functions are needed over 6-31G(d,p)	19	5
6-311+G(d,p)	Adds extra valence functions (3 sizes of s and p functions) 31+G(d,p)	22	6
6-311+G(2d,2p)	Puts 2d functions (and diffuse functions) on heavy atoms and 2p functions on hydrogens.	27	9
6-311++G(2df,2pd)	Puts 2d and 1f functions (and diffuse functions) on heavy atoms and 2p and 1d functions on hydrogens	34	14
6-311++G(3df,3pd)	Puts 3d and 1f functions (and diffuse functions) on heavy atoms and 3p and 1d functions on hydrogens	39	18

*Lithium through Neon

theoretical model can be improved are shown as a two dimensional chart, as in Fig. 2.15. Progression in the horizontal direction (Improvement of Correlation Treatment) corresponds to improved flexibility by taking the sum of an increasing number of multiple electron functions, and progress in the vertical direction (Improvement of Basis Sets) corresponds to increasing flexibility of the one-electron spin orbital.

The perturbation theory of Moller and Plesset (MP) is an alternative approach to the correlation problem. Within a given basis set, its aim is to find the lowest eigenvalue and the corresponding eigenvector of the full Hamiltonian. MP models are formulated by first introducing a generalized electronic Hamiltonian, $\hat{H}_\lambda$, according to which,

$$\hat{H}_\lambda = \hat{H}_0 + \lambda \hat{V} \tag{2.51}$$

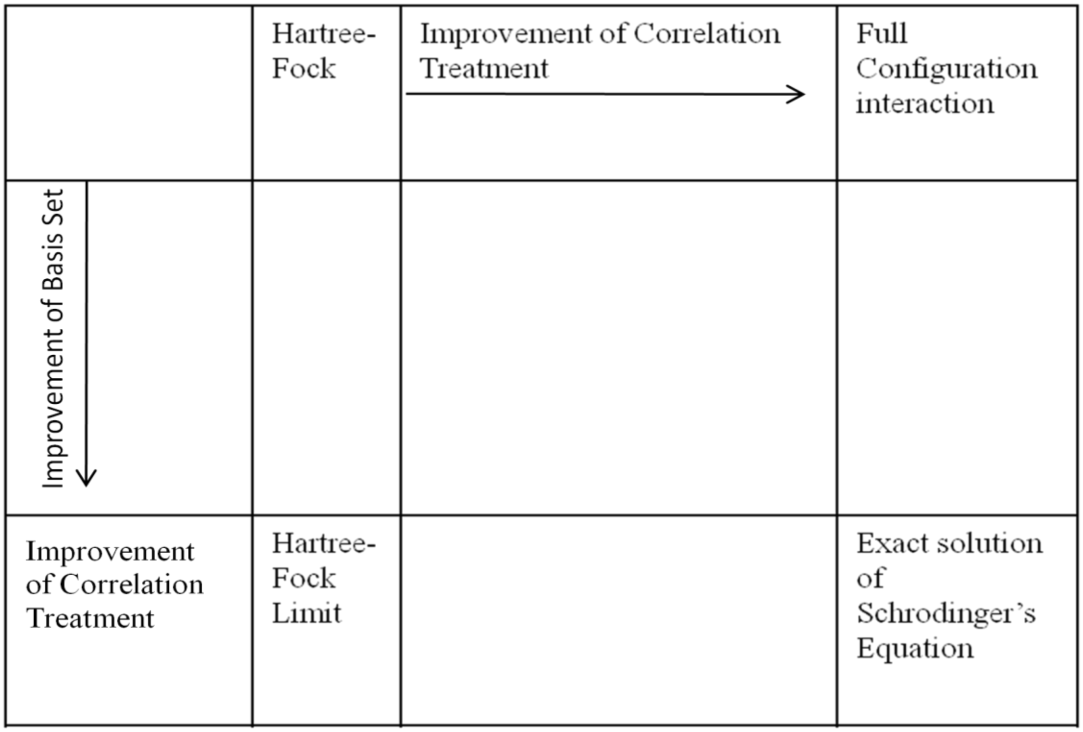

	Hartree-Fock	Improvement of Correlation Treatment →	Full Configuration interaction
Improvement of Basis Set ↓			
Improvement of Correlation Treatment	Hartree-Fock Limit		Exact solution of Schrodinger's Equation

Fig. 2.15: Schematic representation of the theoretical models, showing basis set improvement vertically and correlation improvement horizontally

Where the perturbation, $\lambda\hat{V}$, is defined by,

$$\lambda\hat{V} = \lambda(\hat{H} - \hat{H}_0) \tag{2.52}$$

Where Ĥ is the correct Hamiltonian and λ is an dimensionless parameter. In MP theory, the zero order Hamiltonian, $\hat{H}_0$, is taken to be the sum of one-electron Fock operators. The ground state wavefunction, Ψ_λ, and energy, E_λ, of a system, can now be expanded in powers of λ as

$$\Psi_\lambda = \Psi^{(0)} + \lambda\Psi^{(1)} + \lambda^2\Psi^{(2)} + ... \tag{2.53}$$

$$E_\lambda = E^{(0)} + \lambda E^{(1)} + \lambda^2 E^{(2)} + ... \tag{2.54}$$

Practical correlation methods are formulated by setting λ=1, and truncation of the series at various orders. We refer to the methods by the highest order energy term allowed, that is truncation after second order as MP2, after third order as MP3, and so forth.

The basis of Density functional Theory (DFT) is the proof by Hohenberg and Kohn[24] that the ground state electronic energy is determined completely by the electron density ρ. In other words, there exists a one-to-one correspondence between the electron density of the system and the energy. While the complexity of a wave function increase with the number of electrons, the electron density has the same number of variables. The goal of DFT methods is to design functional connecting the electron density with the energy. From the wave mechanics approach, it seems clear that the energy functional can be divided into three parts, kinetic energy, T(ρ), attraction between the electrons and nuclei, E_{ne}(ρ), and electron–electron repulsion E_{ee}(ρ); the nuclear–nuclear repulsion is a constant under Born-Openheimer approximation. Furthermore, with reference to Hartree-

Fock theory, the $E_{ee}(\rho)$ term can be divided into a Coulomb and an exchange part, $J(\rho)$ and $K(\rho)$, implicitly including correlation energy in all parts.

Models which include exact exchange are often called Hybrid Methods, where the correlation energy may be taken as the Local Spin Density Approximation (LSDA) expression plus a gradient correlation term,

$$E_{xc}^{B3} = (1-a)E_x^{LSDA} + \ a\,E_x^{Exact} + b\Delta E_x^{B88} + E_c^{LSDA} + cE_c^{CGA} \qquad (2.55)$$

The Adiabatic Connection Model (ACM) and Becke 3 parameter functional (B3) are examples of such hybrid models. Associated acronyms are BLYP, BP86, BPW91, B3LYP, B3P86 and B3PW91.

The way the energy of a molecular system varies with small changes in its structure is specified by its potential energy surface. Potential Energy Surface (PES) can be defined as the mathematical relation, linking the molecular structure and the corresponding energy. For a diatomic molecule, it is a two-dimensional plot, with the internuclear separation on the X-axis, and the energy at that bond distance at the Y-axis, producing a curve. For larger systems, the surface has as many dimensions as there are degrees of freedom within the molecule. On the potential energy surface, there are minima which correspond to the equilibrium structures. A minimum can be a local minimum, or a global minimum, the lowest energy point anywhere on the potential energy surface. A point which is a maximum in one direction and a minimum in all others is called a saddle point, and it corresponds to a transition structure connecting two equilibrium structures. The harmonic vibrational frequencies and force constants are calculated at the stationary points on the potential energy surfaces, to ensure that they are true saddle points. All transition state structures are characterized by only one imaginary frequency and one negative eigenvalue of the force constant matrix.

Chapter 3
Kinetics studies

There are many complex chemical reactions continuously taking place in the atmosphere, almost all of them essentially oxidation, leading to their comparison with a low temperature flame. Though complex and cyclic mechanisms are involved, most of the organic molecules in this environment eventually get oxidised (burnt) to CO_2 and water. In the process, however, many intermediates and side products are formed. Though the ultimate chemistry is similar, the order of the lifetimes of the species in flame and atmosphere are very different. The key difference is the difference in the oxidising radical concentration, which, in the atmosphere, is much lower than that in a flame. The reactions are most brisk at the troposphere, since it contains majority of the bulk of atmospheric mass (85%) and gases are generally emitted at the surface, which makes the concentration of the trace species and reactive radicals maximum in this level.

The most abundant oxidants in the earth's atmosphere are O_2 and O_3. These oxidants have large bond energies, and hence are relatively unreactive, except towards radicals (O_2 only toward highly unstable radicals). With a few exceptions, oxidation of non-radical species by O_2, or O_3, is extremely slow. Work in the 1950s first identified the OH radical as the strongest oxidant in the atmosphere. OH reacts rapidly with most non-radical species, and is particularly reactive with H-containing molecules, due to H-abstraction reactions, converting OH to H_2O. OH radical is generated in the troposphere from photodissociation of ozone (O_3) molecules by solar radiation in the range of 300-320 nm, and subsequent reaction of the resultant $O(^1D)$ with ambient water molecules.

Apart from OH radical, an organic molecule may also react in the atmosphere with Cl atom, another oxidising species, (found mainly in the polluted urban atmosphere and marine boundary layer), or may undergo photolysis. But, the role of these degradation processes is negligible, as compared to that of the reactions of OH in most of the troposphere. The kinetic parameters of the reaction of any molecule with OH radical are, therefore, very important, because their values are the major factors in determining the lifetime and other related properties of that molecule in the atmosphere.

In this chapter, the study of the reaction kinetics of OH radical with different types of molecules is presented. Bis-2,2,2 trifluoroethyl ether (TFEE) is a potential chlorofluorocarbon (CFC) alternative, and before it is commercially produced and used, its reactions in the atmosphere must be thoroughly studied. Morpholine, on the other hand, is a polyfunctional compound, which is a cyclic ether as well as a secondary amine. The kinetics of the reaction of this compound with OH radical showed some interesting traits, like high rate coefficient and negative temperature dependence. Theoretical studies indicated the involvement of pre-reactive complex in the reaction mechanism of H-abstraction.

In the kinetics experiments, OH radical was generated in the laboratory by photolysis of H_2O_2 by 248 nm laser, and LIF signal from the OH radical was used for monitoring the reaction kinetics under near atmospheric conditions. This is an absolute method for measuring the bimolecular rate constant for the reaction of OH radical with the molecule of interest, as the decay in OH concentration is directly monitored against real time. An absolute method for measurement of reaction rate constant is preferable than the relative methods, where the rate of reaction of the sample is compared with that of a reference molecule. By absolute measurement, one is capable of avoiding the errors generated from the error in the measurement of values for the reference compound.

3.1 Working Principle for Kinetic Study using LP-LIF System

The set-up described in section 2.1.2. (Fig. 2.4) was used to measure the bimolecular rate constants of the reactions of OH with different molecules in the temperature range of 298-365 K. To minimize the catalytic dissociation of H_2O_2, teflon tubings and glass joints were used throughout the gas handling system. The gas mixture was introduced to the reaction cell, after pre-mixing. The temperature of the reaction cell was varied in the range of 298-365 K, by circulating water from a thermostated bath through the outer jacket. The temperature and the pressure inside the reactor were continuously monitored, and kept constant during the experiments. The reservoir bulb was passivated with H_2O_2, and the H_2O_2 / He gas mixture was flown through the reaction cell, without the reactant (blank), till the LIF intensity, as well as decay kinetics of the hydroxyl radical were reproducible. The absence of any dark reaction between the sample and H_2O_2 was confirmed by gas chromatography measurements. All the kinetics measurements were carried out at nearly constant total pressure of ~ 55 Torr. The flow velocity of the experimental mixture was kept to be 15 cm/s, to make sure that a fresh gaseous reaction mixture was seen by each pulse of the photolysis laser operating at 20 Hz.

At a given temperature and composition of the reaction mixture, the variation of intensity of the fluorescence signal, which was proportional to the concentration of OH, with time, i.e., the pump-probe delay, was recorded for obtaining kinetics of the reaction of OH with the sample. In these experiments, concentration of sample was much higher than that of OH, maintaining the pseudo-first order condition. Thus, the decay followed a first-order exponential relation. The reactions that were expected to take place, once OH radical is formed, are:

$$H_2O_2 + h\nu\ (\lambda=248\ \text{nm}) \rightarrow 2OH \qquad (3.1)$$

$$OH + H_2O_2 \rightarrow HO_2 + H_2O \qquad (k_2) \qquad (3.2)$$

$$OH \rightarrow \text{diffusion out of the detection zone} \qquad (k_3) \qquad (3.3)$$

$$OH + \text{sample} \rightarrow \text{pdt.} + H_2O \qquad (k_4) \qquad (3.4)$$

where k_2, k_3, and k_4 are the rate constants for reactions (3.2), (3.3) and (3.4), respectively. The LIF intensity, and hence, the concentration of OH radicals, generated by photolysis of H_2O_2 at 248 nm, decreased with time due to their diffusion from the detection zone, as well as their reactions with the sample and undissociated H_2O_2 molecules. Therefore, the time dependent decay can be represented by the mathematical relation:

$$-d[OH]/dt = [OH]\,(k_2[H_2O_2] + k_3 + k_4\,[\text{sample}]) \qquad (3.5)$$

Since $[H_2O_2]$ and [sample] remained almost constant during the decay of OH, the concentration of OH radicals at any time, $[OH]_t$, is given by the first-order kinetics equation,

$$[OH]_t = [OH]_0 \exp\,[-\,(k' + k_4\,[\text{sample}])\,t] \qquad (3.6)$$

where k' is the rate constant for loss of OH radicals due to diffusion and all other reactions, except for that with the sample. This is a sum of the rate of reaction of OH radical with H_2O_2 molecules, as well as any impurities present in the gas mixture of H_2O_2 and helium, and the rate of diffusion of OH from the detection zone.

This relation can also be written as,

$$[OH]_t = [OH]_0 \exp[-k_I t] \tag{3.7}$$

The pseudo first-order rate constant (k_1) for decay of OH radical has the value of the bimolecular rate constant k_4 embedded in it. k_1 can be determined by monitoring the decay of OH radical concentration in real time.

As the LIF intensity is proportional to OH concentration, the above relation may be written in terms of LIF intensity at time t=0 and time t=t as,

$$S_t = S_0 \exp[-k_I t] \tag{3.8}$$

Where S_t and S_0 are the LIF intensities from the OH radical at time t=0 and t=t, respectively.

The pseudo first-order rate constant (k_I) was obtained from the linear least square fit of the signal intensity, in logarithmic scale, with time, as shown in Fig. 3.1. k_I can be written in terms of the bimolecular rate coefficient k_4, as

$$k_I = k_4 [\text{sample}] + k' \tag{3.9}$$

where [sample] is the number density of the sample (TFEE) and k' is the rate constant for decay of OH concentration in the absence of TFEE. At a particular temperature, the concentration of the sample was varied, and the same set of experiments were performed at each value of the concentration. When k_I is plotted against sample concentration, a straight line is obtained, which obeyed equation (3.9), as shown in Fig. 3.3. The slope of the straight line gave the value of the bimolecular rate constant $k_{4,}$ at a particular temperature. The bimolecular rate constant k_4(T) for the reaction of OH radical with any compound, at that temperature, is generally referred to as k_{II}(T), and for the rest of the chapter and the thesis, the same convention will be followed.

The values of (T) at different temperatures were obtained, and the values of ln k_{II} were plotted against temperature (T). The points were fitted to the semilog expression for the Arrhenius equation for variation of rate constant with temperature (Equation 1.16).

$$lnk = lnA - \frac{E_a}{RT} \tag{3.10}$$

From this linear relation, the value of activation energy (Ea) and pre-exponential factor A were determined.

3.2 Kinetic Study of Hydrofluoroether: (Bis-2,2,2 trifluoroethyl ether)

Hydrofluoroethers[25, 26] are a class of compounds which have shown promising possibility for being used as a CFC alternative, for various kinds of uses, like blowing and cleaning agents, etc. These compounds have the advantage of being completely benign to the ozone layer, due to the absence of any Cl atom in their structure. In addition, because of their higher reactivity with the oxidizing species present in the troposphere, these compounds are expected to have a lower atmospheric lifetime, which reduces their possible contribution to the global warming effect. The presence of abstractable H atom/(s) in hydrofluoroethers indicates that the major pathway of removal of these compounds from troposphere is through their reaction with OH radical. In this context, the kinetics of the reactions of various members of the hydrofluoroether family with OH has already been studied by employing various experimental methods[27-33]. The data obtained from these studies, using different methodologies, are fairly consistent for some of the molecules, but, for many molecules, there is a substantial variation. In the case of bis-2,2,2 trifluoroethyl ether, $CF_3CH_2OCH_2CF_3$, the earliest reported rate coefficient for the reaction with OH radical at 298 K($k_{II}(298)$) is $(1.01 \pm 0.15) \times 10^{-13}$ $cm^3 molecule^{-1} s^{-1}$ [27] whereas it was measured to be 1.64×10^{-13} $cm^3 molecule^{-1} s^{-1}$, using flash photolysis resonance fluorescence technique[29], which is an absolute method. A marginally lower value, $(1.51 \pm 0.24) \times 10^{-13}$ $cm^3 molecule^{-1} s^{-1}$, was obtained later, by using relative rate method[31]. However, the value of $k_{II}(298)$ obtained recently, using relative rate measurement[33], is still lower, 1.3×10^{-13} $cm^3 molecule^{-1} s^{-1}$. There is a difference in the reported activation energy (E_a/R) values also, which are 790 ± 47 K[29] and 962 ± 19 K[33]. In view of these differences, the need for further work on the kinetics of the reaction of this compound with OH radical was pointed out[33].

The difference in the kinetics parameters obtained from these studies might arise due to systematic errors involved in the techniques employed, and in such cases, more independent studies, using different standards in the relative rate method, or by different techniques of generation and detection of free radicals in the absolute method, are required. Laser Photolysis-Laser Induced Fluorescence (LP-LIF) is a standard absolute technique, used in kinetic studies. This technique has been used, for the first time, to determine the bimolecular rate constant k_{II}, as well as E_a/R, for the reaction of OH with

$CF_3CH_2OCH_2CF_3$ in this study. Here, the concentration of OH radicals generated and monitored can be as low as 10^7- 10^{11} molecules cm^{-3}, and hence, any secondary reaction and mutual reactions of OH radicals are avoided. The experimentally obtained results are compared with the reported values, and also compared with the structure activity relationships.

3.2.1 Experimental Results and Discussion

For the experiment, 50% H_2O_2 was concentrated further, by bubbling N_2 gas through it, for several days. TFEE, 99% from Aldrich, Germany, was used, after several freeze-pump-thaw cycles. The helium, used as the buffer gas, was of 99.9% purity, from Praxair, India. Our gas chromatography analysis with an FID detector, as well as Mass Spectrometry, using different columns, showed the presence CF_3CH_2OH as the major impurity, along with two minor (< 0.1%) unidentified impurities. The rate of flow of the H_2O_2/He mixture into the reaction cell was kept constant at 25 SCCM in all the cases. The rates of flow of TFEE - He mixture and pure helium were adjusted at different ratios, keeping the total flow rate of these two together always at 25 SCCM, to obtain different sample concentrations in the reaction cell.

The number density of the H_2O_2 molecule in the reaction cell was kept at $\sim 1\times10^{14}$ molecules cm^{-3}. From the laser fluence used for the experiments and the absorption cross-section of H_2O_2, the concentration of OH generated was estimated to be of the order of 10^{10}-10^{11} molecules cm^{-3}. In the absence of any other reactant, OH radical reacts with unreacted H_2O_2 according to reaction (3.2), with a bimolecular rate coefficient of 1.8×10^{-12} $cm^3 molecule^{-1} s^{-1}$, independent of temperature over the range of 200-400K[3]. The reactant, TFEE, does not absorb at 248 nm, and hence, there were no complications due to reaction of OH with the photolysis products. The number density of the reactant, TFEE, was varied in the range of 10^{14}-10^{15} molecules cm^{-3}, in order to observe appreciable change in the OH concentration due to reaction with TFEE. The concentration of TFEE in the reaction cell in each experiment was determined from the flow rates and the total pressure in the cell. The concentration was also cross-checked by taking the FTIR spectrum of the mixture, collected downstream of the reaction cell, and comparing it with a previously created calibration curve. The calibration was done by preparing different concentrations of TFEE in He, in the concentration range employed in the kinetic studies. The integrated area of the IR band in the range 1070 – 1250 cm^{-1}, with

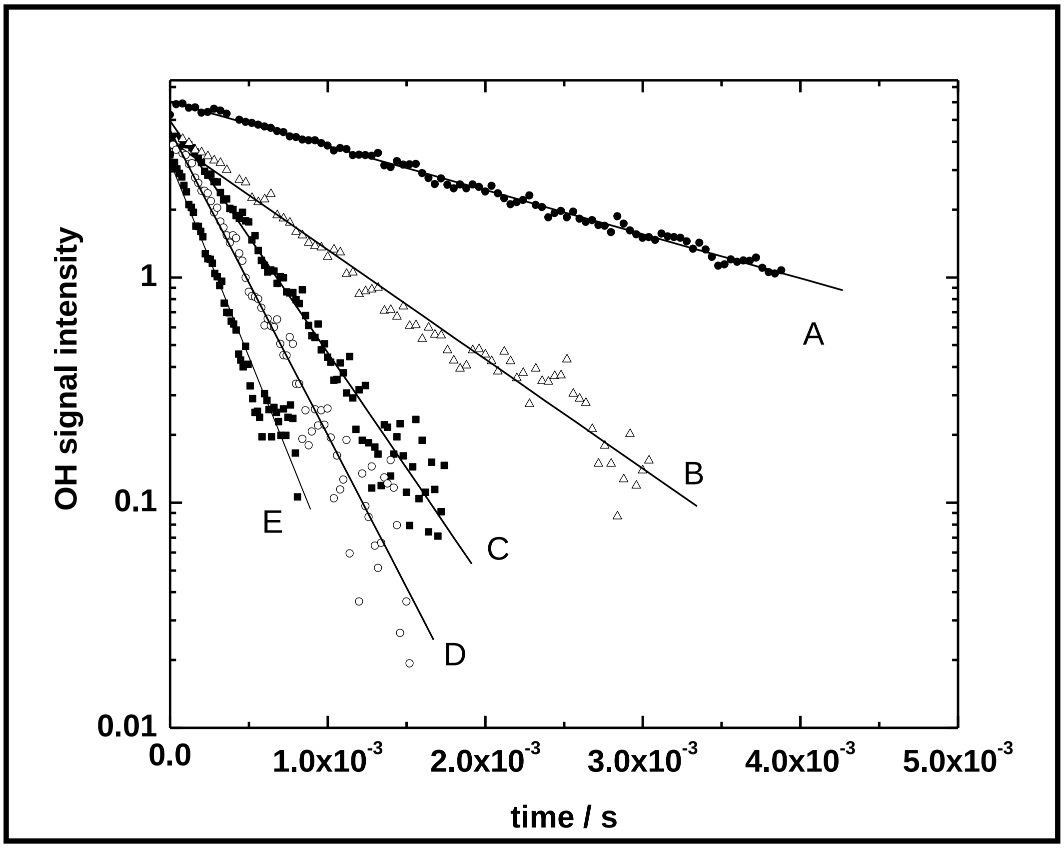

Fig. 3.1: Typical profiles of OH radical decay with time, at a particular temperature, with increasing concentration of TFEE as follows. A: 0; B: 5.5×10^{15} ; C:1.2×10^{16}; D :1.5×10^{16} and E: 2.3×10^{16} molecules cm^{-3} . Time for reaching maximum concentration of OH (formation time) is neglected. The curves fit into first-order kinetics equation, shown as solid lines.

peak at 1187 cm^{-1}, was used for the measurements. A set of typical profiles for the decay of OH radical with time at different sample concentrations, at a particular temperature, is shown in Fig. 3.1.

The ratio, [TFEE]/[OH], was kept in the order of 10^5 during the course of the experiment, so that contributions from the reactions of OH with the products of the primary reaction was negligible. This was verified by the fact that variations in the photolysis laser intensity did not affect the results. At each concentration of TFEE, at least four measurements were taken, to ensure consistency, and the values of $k_{II}(T)$, obtained at different concentrations of TFEE at a particular temperature T, were plotted against [TFEE]. A typical plot at 308 K is shown in Fig.3.2. The slope and the intercept

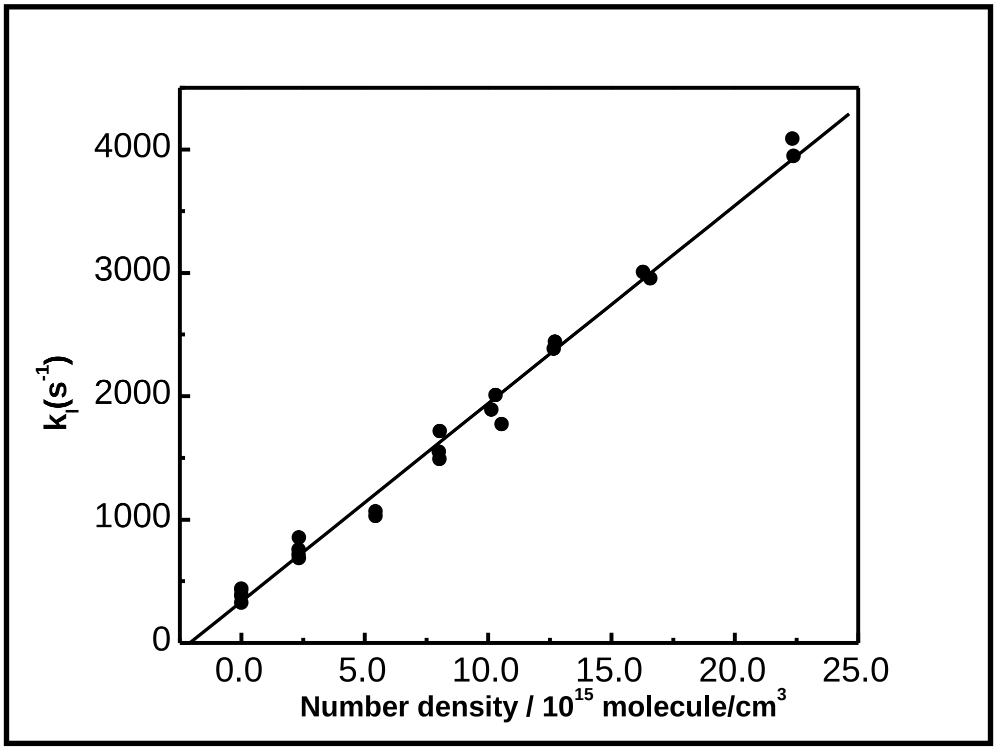

Fig. 3.2. Variation of the pseudo first-order decay coefficients (k_I) with the concentration of TFEE at 308 K. slope of the straight line gives the bimolecular rate constant (k_{II}).

of the linear graph give the values of the bimolecular rate constant $k_{II}(T)$ for the reaction of OH radical with TFEE, at that temperature, and k', respectively. From the temperature dependence of $k_{II}(T)$, the activation energy was determined. By our methods, at room temperature, the value of the bimolecular rate coefficient $k_{II}(298)$ was found to be $(1.47 \pm 0.03) \times 10^{-13}$ cm^3 molecule^{-1} s^{-1}. The values of $k_{II}(T)$ obtained at different temperatures are presented in Table 3.1. The Arrhenius plot, where ln ($k_{II}(T)$) is plotted against the inverse

Table 3.1: Summary of the experimental conditions and rate coefficients for the reaction of OH with TFEE at different temperatures. Laser fluence ~2.5 mJ cm^{-2} pulse^{-1}. [H_2O_2]~10^{14} molecules cm^{-3}, [OH] ~ 10^{11} molecules cm^{-3}.

Temperature	Pressure (torr)	[TFEE] (molecule cm^{-3})	k_{II} (cm^3 molecule^{-1} s^{-1})
298 K	56	$5.0 \times 10^{15} – 1.7 \times 10^{16}$	$(1.47\pm 0.03) \times 10^{-13}$
308 K	58	$2.9 \times 10^{15} – 2.4 \times 10^{16}$	$(1.60\pm 0.03) \times 10^{-13}$
318 K	57	$2.5 \times 10^{15} – 1.7 \times 10^{16}$	$(1.73\pm 0.05) \times 10^{-13}$
333 K	58	$4.7 \times 10^{15} – 1.2 \times 10^{16}$	$(1.96\pm 0.16) \times 10^{-13}$
349 K	58	$4.6 \times 10^{15} – 2.0 \times 10^{16}$	$(2.33 \pm 0.08) \times 10^{-13}$
355 K	57	$2.4 \times 10^{15} – 1.5 \times 10^{16}$	$(2.49\pm 0.07) \times 10^{-13}$
365 K	58	$4.5 \times 10^{15} – 1.5 \times 10^{16}$	$(2.81\pm 0.10) \times 10^{-13}$

of the respective temperature, is shown in Fig. 3.3. From the linear regression of this plot, E_a/R and A-factor are found to be 1030 ± 60 K and $(4.5 \pm 0.8) \times 10^{-12}$ $cm^3molecule^{-1}s^{-1}$, respectively. The errors quoted here are 1 σ of the linear regression.

The previously reported values of room temperature rate coefficients and other kinetic parameters are listed in Table 3.2, along with the current data. The two previous measurements of activation energies are also shown in Fig. 3.3, for comparison. The rate coefficient that we measured at room temperature was very close to the average of the three previous measurements in Refs. 4, 6 and 7. The value of E_a/R, 1030 K, was higher than the two previously reported values[29-33], but very close to 962 K, reported in ref.28.

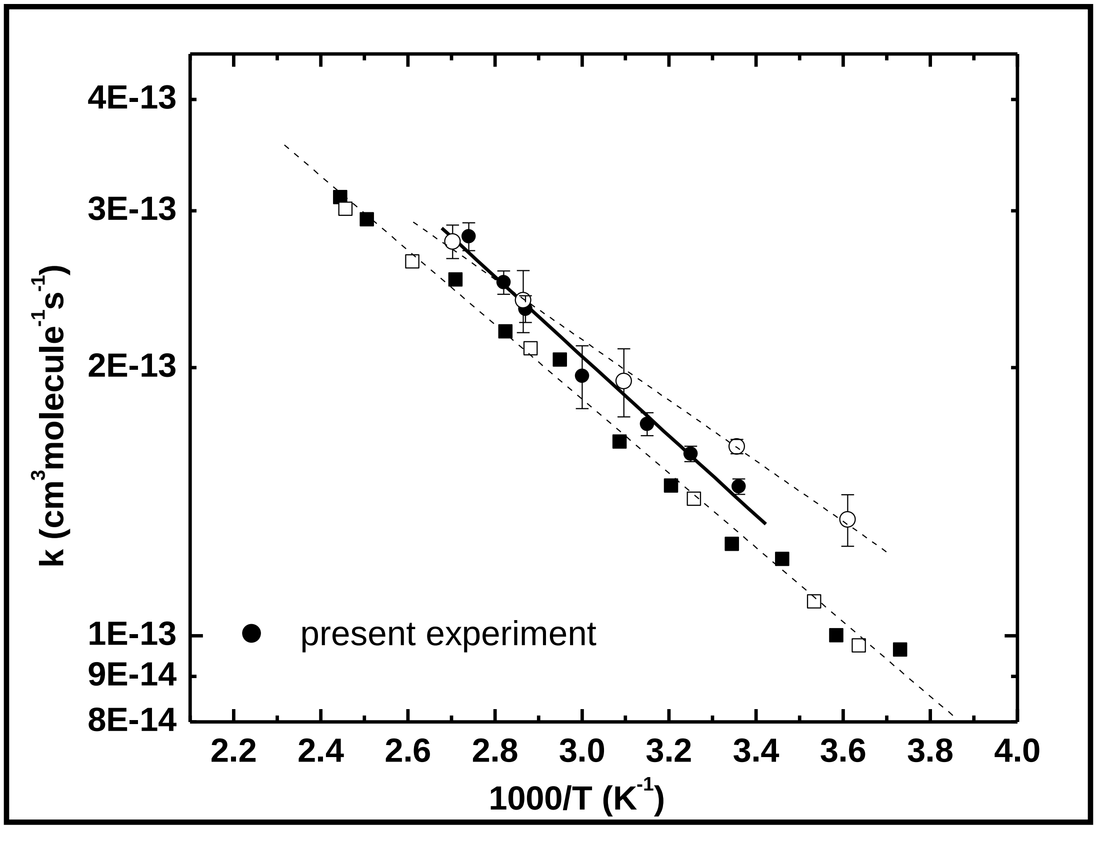

Fig. 3.3: Arrhenius plot of the rate coefficients (k_{II}) of reaction of OH radical with TFEE at different temperatures and comparison with previous studies.

•:- This work; ○:- ref. 28; □ and ■:- Ref. 31 with different reference molecules.

The reference molecules used for relative rate measurement by Wilson et al.[33] had a complex temperature dependence according to the latest recommendation[27], and thus the E_a/R obtained by them may be modified to a lower value. The A-factor is also higher than the previous values, ($2.32^{+0.46}_{-0.41}$) × 10^{-12} and (3.28 ± 0.19) × 10^{-12}, reported in refs. 28 and 31, respectively.

Many empirical and theoretical calculations are reported in the literature, for predicting the values of $k_{II}(298)$ and E_a/R, for different classes of organic molecules. Demore[34] has suggested a Structure Activity Relationship for H abstraction reactions of fluorocompounds, in which both E_a/R and Arrhenius factor are empirically related with rate constants at room temperature by the equations:

$$\frac{E_a}{R}(K) = -509\log\left(\frac{k_{II}(298)}{n}\right) - 5771 \tag{3.11}$$

$$\log_{10}\left(\frac{A}{n}\right) = 0.258\log\left(\frac{k_{II}(298)}{n}\right) - 8.411 \tag{3.12}$$

where n is the number of H atoms in the fluorocompounds. The observed temperature dependence for fluoroethers, which contain a single type of C—H bond, as in the case of TFEE, are shown to be accurately predictable by this method. The two parameters E_a/R and A-factor calculated, using the presently measured room temperature rate coefficient, are 1067 K and 5.3 × 10^{-12} $cm^3 molecule^{-1} s^{-1}$. There is a good agreement between these calculated values and the presently measured values of E_a/R and A-factor. The present room temperature rate coefficient value, 1.47 × 10^{-12} $cm^3 molecule^{-1} s^{-1}$, is very close to 1.54 × 10^{-12} $cm^3 molecule^{-1} s^{-1}$, calculated by Urata et al[35], based on an empirical correlation of the rate coefficients of the reactions of OH radical with hydrofluorocarbons and hydrofluoroethers with the calculated bond dissociation enthalpies.

The atmospheric lifetimes of TFEE, with respect to OH radical reaction, could be calculated relative to the atmospheric lifetime of CH_3CCl_3 (MC), and the rate coefficients (k_{II}) of MC and TFEE at 272 K[36]. Due to limitations of the present experimental set-up, measurement of rate coefficient at this temperature was not possible. However, the present data in 298 – 365 K range can be extrapolated to 272 K, because the Arrhenius plot is linear in 270 – 400 K range, for all the fluoroethers reported so far[29, 31, 33]. The rate coefficient of TFEE at 272 K, calculated from this work is found to be 1.02×10^{-13} $cm^3 molecule^{-1} s^{-1}$, very close to 9.55×10^{-14} $cm^3 molecule^{-1} s^{-1}$, calculated using the

Table 3.2: Summary of measurements of rate coefficient of reaction of OH with TFEE. The quoted errors in ref.30 include estimated systematic errors of 4%. The error in ref.30 represents the 3σ statistical error and includes the uncertainty in the reference reaction rate coefficients, but not any possible systematic errors. The errors in ref.31 are 1σ of the least square fit, and do not reflect uncertainties in the reference rate constant, or other possible systematic errors. The error in the present work is 1σ of the least square fit, and does not include systematic errors.

Method k	k_{II} (298) (cm^3 $molecule^{-1}$ s^{-1})	E_a/R (K)	A(cm^3 $molecule^{-1}$ s^{-1})	Ref.
Relative rate i	$(1.01 \pm 0.15) \times 10^{-13}$			26
FP / RF n	$(1.63 \pm 0.09) \times 10^{-13}$	790 ± 47	$(2.32^{+0.46}_{-0.41}) \times 10^{-12}$	28
Relative rate e Reference- $CHCl_3$ t	$(1.51 \pm 0.24) \times 10^{-13}$			30
Relative rate Reference- i HFC-152a, HFC-161 c	1.3×10^{-13}	962 ± 19	$(3.28 \pm 0.19) \times 10^{-12}$	31
LP / LIF	$(1.47 \pm 0.03) \times 10^{-13}$	1030 ± 60	$(4.5 \pm 0.8) \times 10^{-12}$	Present work

kinetic parameters of ref. 31. Considering the atmospheric lifetime of MC with respect to OH radical reaction to be 6 years[1], the atmospheric life time of TFEE (τ_{TFEE}) due to reaction with OH radicals in the atmosphere was calculated to be 0.35 years. Though this is marginally higher than 0.294 years calculated by Orkin et al.[29], this value also implies a low global warming potential for TFEE, as estimated by them.

3.3. Kinetic Study of a Polyfunctional Molecule: Morpholine

Morpholine is a versatile industrial chemical used as a solvent, catalyst, corrosion inhibitor, crop protection agent, and also as a chemical intermediate in rubber industry, synthesis of optical brighteners, etc[37]. Human and environmental exposure arises from both gaseous and aqueous emissions, and directly from some of its uses, such as rubber chemicals, cosmetic formulations, waxes and polishes, which lead to the release of morpholine into the environment through volatilization. Under environmental and physiological conditions, *N*-nitrosomorpholine (NMOR), a proven animal carcinogen, is formed by the reaction of solutions of nitrite, or gaseous nitrogen oxides, with dilute solution of morpholine[37]. However, there are not many reports on gas phase reactions and the vapour phase degradation of this molecule in the troposphere. In the tropospheric conditions, many organic molecules undergo addition or abstraction reaction with OH radical, the key oxidative species present therein. The rate constants of these reactions, which are the major sinks for these molecules, depend on their structures[38]. Structurally, morpholine is a polyfunctional compound, a secondary amine as well as an ether. The ether linkage increases the reactivity with OH radical in comparison with the corresponding hydrocarbons. Many ethers[39], diethers[40] and cyclic ethers[41] are known to have very high rate coefficients for their reactions with OH radical. In some of these reactions, the rate constants exhibit slight negative temperature dependence. This behaviour has been correlated to hydrogen bonded pre-reactive complex formation[40]. The present study aims at measuring the kinetic parameters of the reaction of OH radical with morpholine in the gas phase, and to understand the effect of additional heteroatom, nitrogen, on the reactivity of cyclic ethers. The kinetics measurements were carried out in the temperature range 298 – 365 K. The possibility of formation of hydrogen bonded prereactive complexes of morpholine with OH radical, and nature of the transition states for the H abstraction reactions were investigated, using *ab initio* molecular orbital calculations.

3.3.1 Experimental Results

The helium, used as the buffer gas, was of 99.9% purity, from Praxair, India.

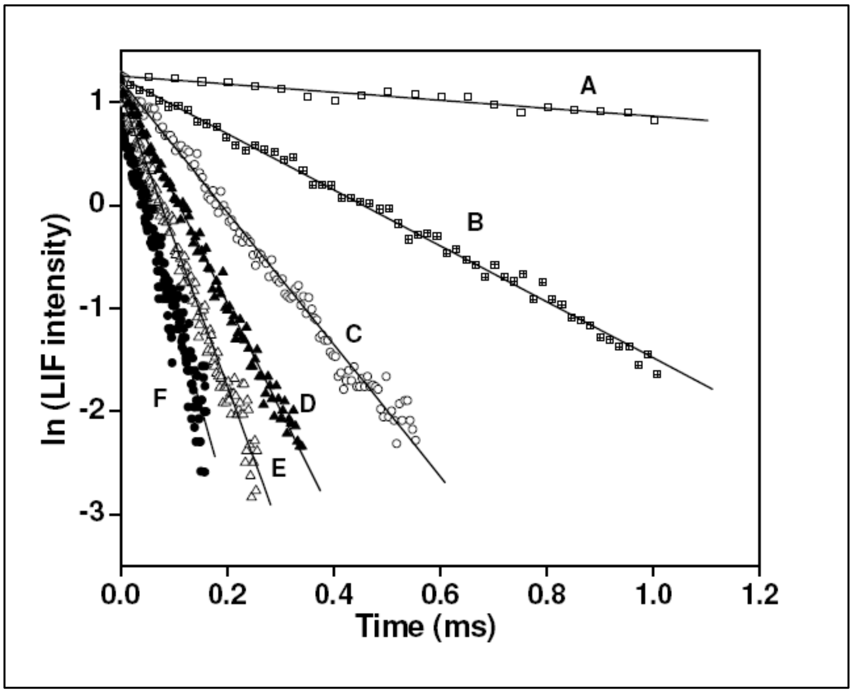

Fig. 3.4: Typical profiles of OH radical decay with time, at room temperature, with increasing concentration of morpholine as follows. A: 0; B: 3.2×10^{13}; C: 8.1×10^{13}; D: 1.3×10^{14}; E: 1.8×10^{14} and F: 2.3×10^{14} molecules cm^{-3}. Time for reaching maximum concentration of OH (formation time) is neglected. The least square linear fits are shown as solid lines.

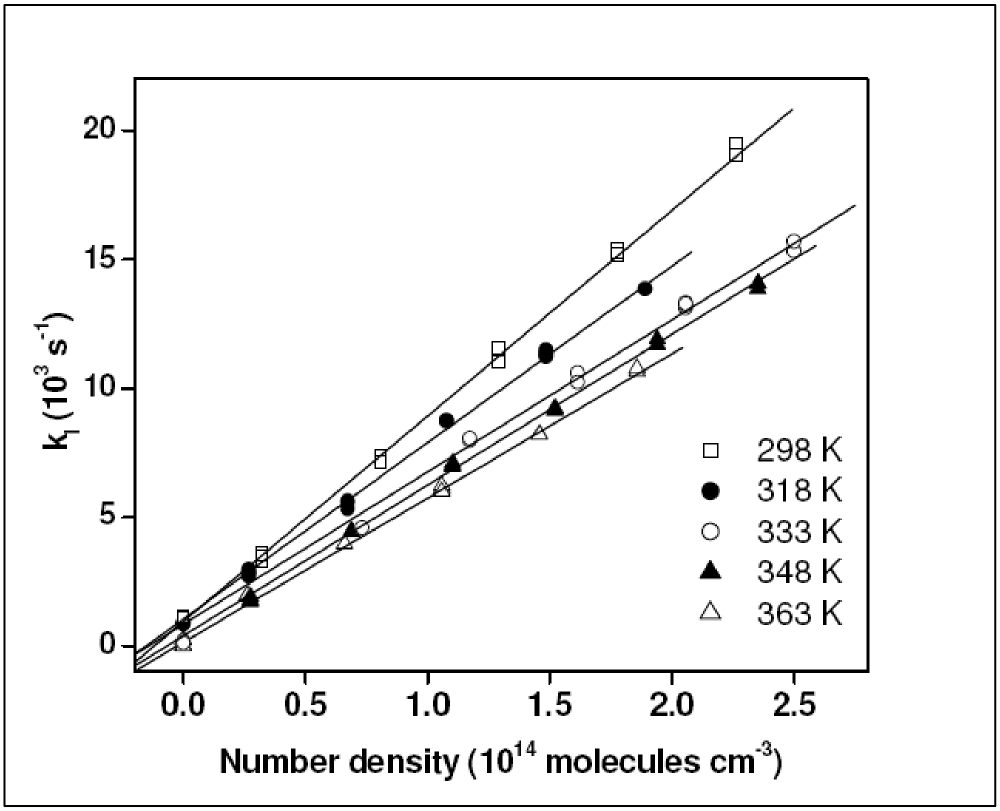

Fig. 3.5: Variation of the pseudo first-order decay constants with the concentration of morpholine at different temperatures. Slope of the line gives the value of the bimolecular rate constant, k_4(T).

H_2O_2 (50%) was concentrated further by bubbling N_2 gas, for several days. Morpholine, (99%, Aldrich), was used, after degassing, employing several freeze-pump-thaw cycles. The gaseous reaction mixture consisted of a precursor molecule H_2O_2, the reactant morpholine and the buffer gas helium, flowing from reservoir flasks with Teflon stopcocks (5 liters). The total pressure inside the reaction cell was kept nearly constant (55 Torr), and the concentrations were varied, by changing the flow rates. The flow velocity of the experimental mixture was kept to be 15 cm/s, to make sure that a fresh gas mixture was seen by each photolysis laser pulse (20 Hz). The number densities of the H_2O_2, OH generated and morpholine inside the reaction cell were kept to be about 10^{14},

10^{10} and 10^{14} molecules cm^{-3}, respectively, to maintain a pseudo first-order condition, with [reactant] >> [OH].

Typical decay profiles, obtained at different concentrations of morpholine at room temperature, where the logarithmic LIF intensities exhibit good linearity with time, are shown in Fig. 3.4. Using the same calculations, as discussed in section 3.1.2., we obtained the bimolecular rate constant for reaction of morpholine with OH radical, reaction (3.4), at room temperature, $k_{II}(298K)$, to be, $(8.0\pm 0.1) \times 10^{-11}$ cm^3 $molecule^{-1}$ s^{-1}. This value was arrived at, by plotting the slopes of these decay profiles against the concentration of morpholine, as shown in Fig. 3.5, according to the equation (3.9).

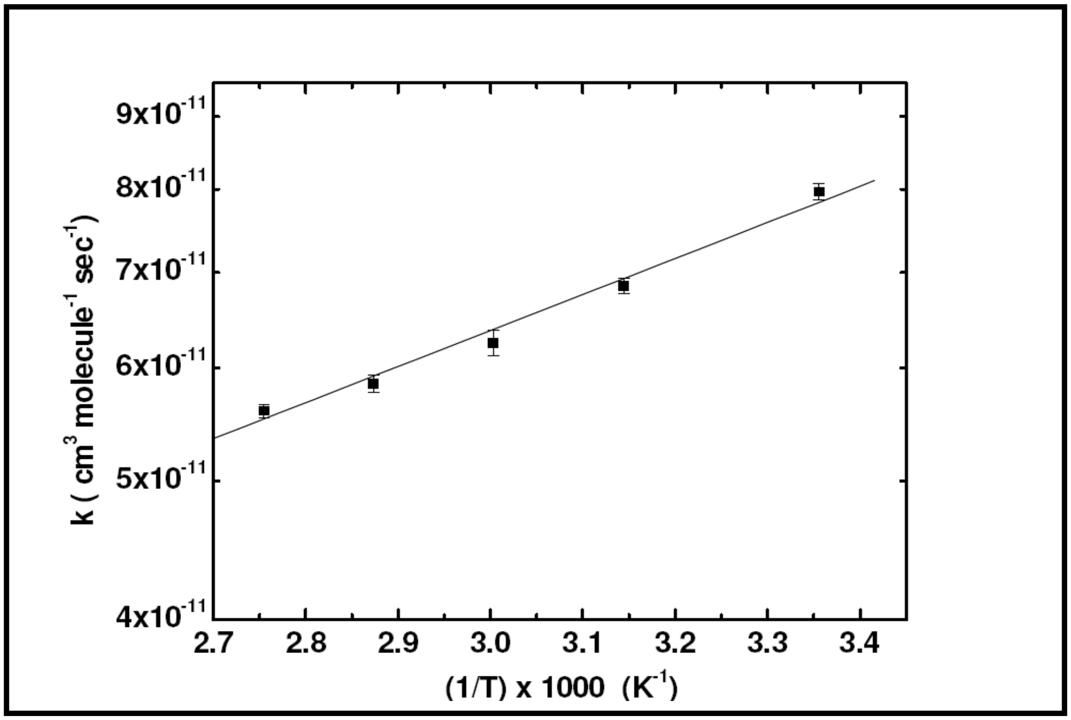

Fig. 3.6. Arrhenius plot of the average value of rate constants $k_{II}(T)$ of the reaction of OH radical with morpholine molecule.

Table 3.3: Summary of the experimental conditions and the rate coefficients for the reaction of OH with morpholine, at different temperatures. Laser fluence ~2.5 mJ cm^{-2} pulse^{-1}. [H_2O_2]~10^{14} molecules cm^{-3} and [OH] ~ 10^{11} molecules cm^{-3}.

Temperatur (K)	**Pressure (torr)**	**[Morpholine] (molecule cm^{-3})**	**k_{II} (cm^3 molecule^{-1} s^{-1})**
298	54	$3.2 \times 10^{13} – 2.3 \times 10^{14}$	$(7.97\pm 0.11) \times 10^{-11}$
318	48	$2.7 \times 10^{13} – 1.9\times 10^{14}$	$(6.85\pm 0.08) \times 10^{-11}$
333	55	$2.9 \times 10^{13} – 2.5\times 10^{14}$	$(6.25\pm 0.13) \times 10^{-11}$
348	54	$2.7 \times 10^{13} – 2.4 \times 10^{14}$	$(5.85\pm 0.08) \times 10^{-11}$
363	56	$2.6 \times 10^{13} – 1.9\times 10^{14}$	$(5.6 \pm 0.06) \times 10^{-11}$

The value of the bimolecular rate constants, $k_{II}(T)$ at different temperatures and experimental conditions are given in Table 3.3. The Arrhenius plot, where variation of $\ln(k_{II}(T)$ is plotted with inverse of temperature, is shown in Fig. 3.6. The plot shows negative temperature dependence, with a slight curvature. The points can be still reasonably fitted to a straight line, with a pre-exponential factor of $(1.1 \pm 0.1) \times 10^{-11}$ cm^3 molecule^{-1}s^{-1} and activation energy (Ea/R) of (-590 ± 20) K in the temperature range studied.

3.3.2 Theoretical Calculations and Discussion

Ab initio molecular orbital (MO) calculations were performed, using Gaussian 92 program[2], to investigate the potential energy surface (PES) of the reaction of morpholine with OH. The geometries of the ground electronic states of morpholine, prereactive complexes with OH, and the products, including the transition state structures, were optimized at MP2 / 6-311+G(d,p) level. The harmonic vibrational frequencies and the force constants were calculated, to ensure the stationary points on the potential energy surfaces, to be true saddle points. All the transition state (TS) structures calculated have only one imaginary frequency and one negative eigenvalue of the force constant matrix. Electronic energies corresponding to the optimized geometries were calculated at the MP2 level, using the same basis sets. With the inclusion of thermal energies, derived from the vibrational frequencies, the reaction energies and the activation barriers at 298 K were evaluated. For the radical species, the energies were also calculated at the projected MP2 (PMP2) level, to correct for spin contamination, if any.

The reaction of OH radical with saturated molecules, like, morpholine, is expected to be dominated by hydrogen atom abstraction. There are three different types of hydrogen atoms in this molecule, namely, H attached to nitrogen atom (N-H), to carbon atoms adjacent (α to) to nitrogen atom (C-H(N)), and to carbon atoms α to O atom (C-H(O)), and, therefore, different reaction channels, involving abstraction of these H atoms, can be possible in morpholine. Reaction of OH radical with morpholine in aqueous solution has been studied, using pulse radiolysis technique, and the major site of abstraction reaction is considered to be the nitrogen atom[42] .

Normally, the hydrogen atom, which is having the lowest bond strength, is preferentially abstracted. The presence of heteroatoms, like oxygen and nitrogen, as in an ether linkage, a hydroxyl group, an amino group, etc., is known to affect the C-H bond strength and the rate coefficient of H abstraction reaction of the OH radical, with a significant deviation from simple structure activity relationships, due to long range activating effects[41]. In the case of saturated cyclic molecules, like morpholine, in addition to the weakening of the C-H bond strengths due to the presence of heteroatoms, steric hindrance due to ring structure also can be an important factor deciding the H abstraction channels. The formation of a pre-reactive complex, suggested by the observation of negative activation energy, adds to the complexity. Detailed *ab initio* studies on the structures and energies of morpholine, pre-reactive complexes and transition states involved in the different hydrogen abstraction channels, are useful in understanding the potential energy surfaces of these reactions, and can help in understanding the reaction mechanism. Even though direct abstraction channels can't be ruled out, only the channels through pre-reactive complexes are considered here, because the observation of negative activation energy implies the prominence of these channels.

Ab initio molecular orbital calculations have been carried out for the ground state morpholine molecule, and the pathways leading to the formation of the OH radical upon photodissociation at 193 nm have been discussed in Section 4.3.3 of this thesis. Theoretical studies on the morpholine radical also have been carried out[43], to determine the C-H bond dissociation energies. Our calculations on the ground state morpholine molecule show that the eclipsed chair form of morpholine, with H atom on nitrogen in the equatorial position, is the most stable form. This result is in agreement with the previous studies[43,44]. The ground state structure, with the geometrical parameters, is shown in Fig. 3.8.

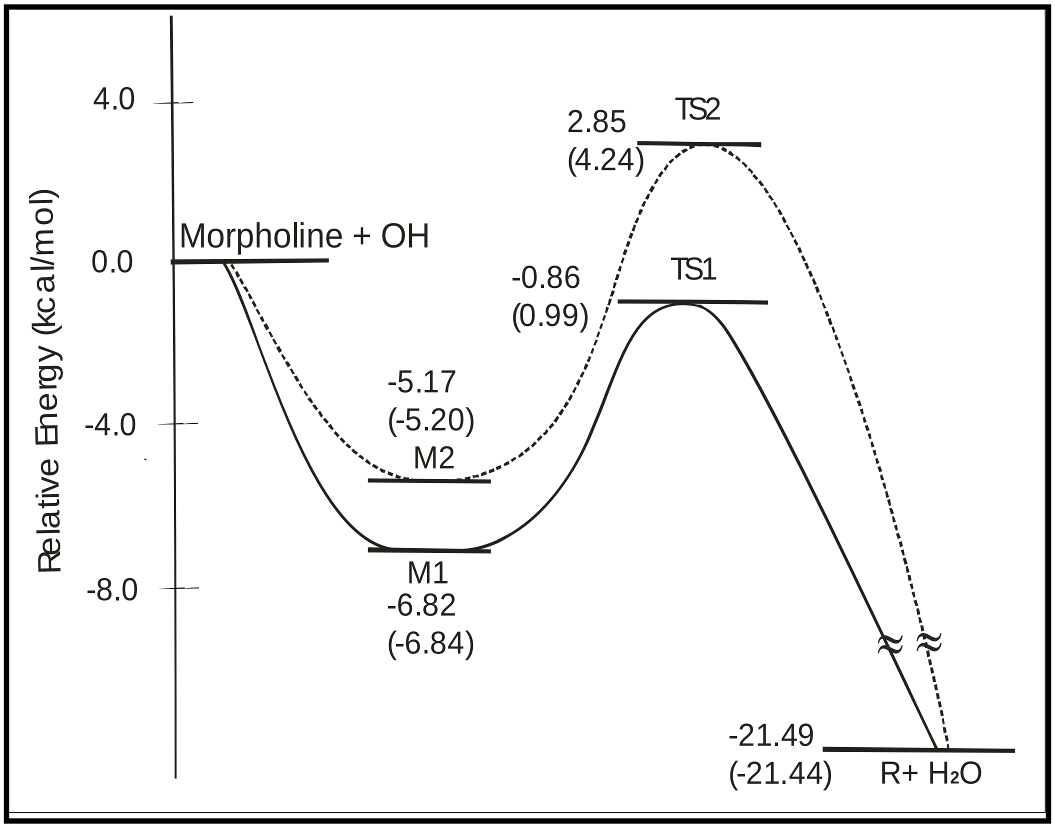

Fig. 3.7. Schematic energy diagram of H abstraction in the reaction of OH radical with morpholine. The geometry optimization and calculation of energies are done at PMP2 (MP2) / 6-311+G(d,p) level. The MP2 energies are shown in parentheses.

The observation of negative activation energy suggests the involvement of pre-reactive complex in the reaction. Although formation of these complexes with OH has been proposed in the case of ethers[40], there are not many theoretical studies on such complexes. The electronic structure and energetics of the reactants, the products, the transition states and the associated complexes involved in the reaction of dimethylether (DME) with OH radical have been investigated at the MP2(FC) and DFT levels of theory, using different basis sets[45]. They obtained a pre-reactive complex of this molecule with OH, which is more stable than the reactants by about 5 kcal mol^{-1}. Formation of such complexes is also reported in the case of nitrogen compounds, as calculated for many aminoacids, like β-alanine[46], serine[47], etc. In these molecules, the pre-reactive complexes are found to be 4 - 5 kcal mol^{-1} more stable than the isolated reactants.

Our calculations on morpholine molecule show the existence of two types of pre-reactive complexes, namely, M1 (N-adduct) and M2 (O-adduct). The fully optimized geometries of these complexes are shown in Fig. 3.8. In M1, the H atom of OH interacts with the N atom, and in M2, the H atom interacts with the O atom of the molecule. Though the geometry of the parent molecule is maintained in both the complexes, the O atom of the OH moiety is away from the ring in the case of M2, whereas it is towards the ring, and placed symmetrically above the ring, in the case of M1. The bond length of O—H is elongated marginally to 0.98 Å, from 0.97 Å, in M1 as well as the M2. The angle ∠ O-H-N is 165° in M1, and the corresponding angle, ∠ O-H-O is 179° in M2. In M1, the distance between the H atom of OH and the N atom of the ring is 1.89 Å, whereas in M2, the corresponding distance to the O atom of the ring is 1.86 Å. These distances suggest a hydrogen bond interaction. The N- adduct is found to be more stable. The stabilization energies in both these complexes are of the order of 5-7 kcal mol^{-1}, almost similar to the earlier calculations in the case of aminoacids. Attempts made to locate pre-reactive complexes, in which the orientation of the OH moiety facilitates an H-bonding interaction between H atom of OH and O/N atom of morpholine as well as between O atom of the OH moiety and the nearest H atom of morpholine were unsuccessful. Such complexes with five-membered or six-membered rings are expected to be more stable, as suggested in the case of ethers[41]. The restriction due to rigidity of the ring and steric hindrance may be responsible for not observing this type of complexes.

The pre-reactive complexes, M1 and M2, can subsequently undergo H abstraction reaction. Hence, the structural features of the transition states for H abstraction from morpholine by OH, in both these adducts, were also investigated. H abstraction is possible from the carbon atom which is α to N or O atoms, resulting in two different radicals. In the present transition state optimizations, both types of abstractions were considered for each pre-reactive complex.

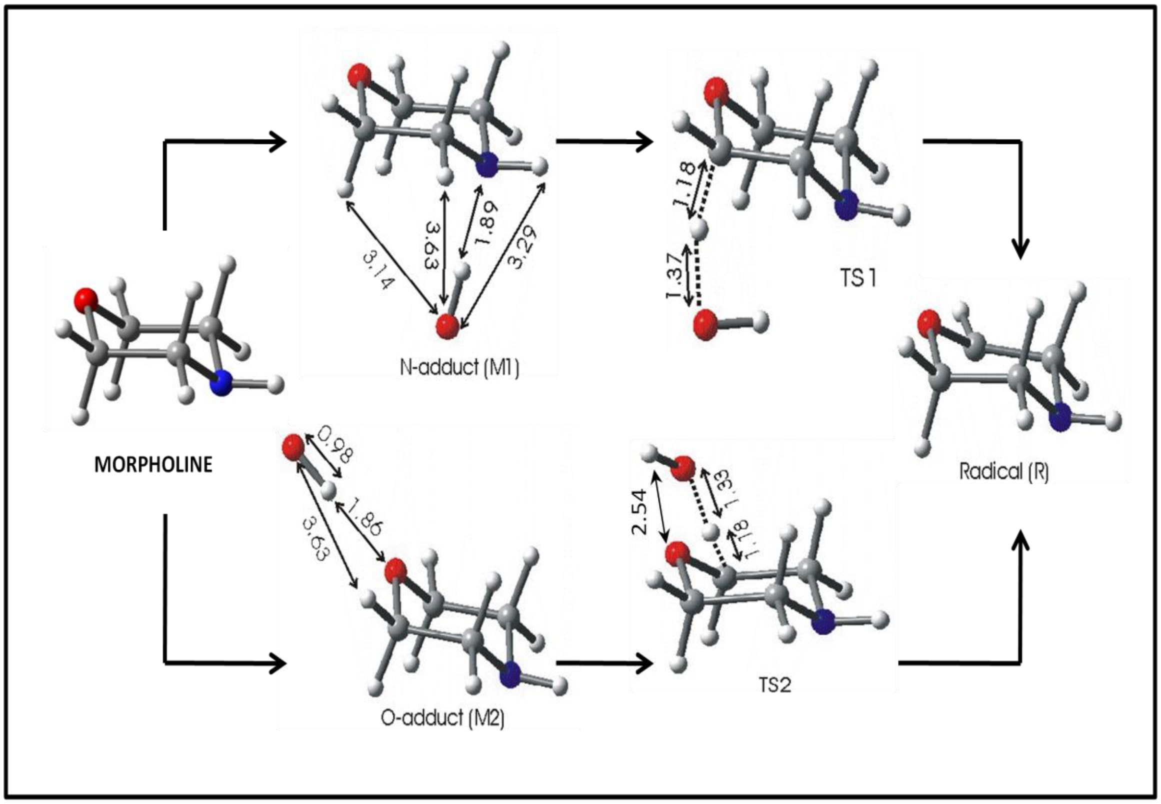

Fig. 3.8: Optimized structures of morpholine, pre-reactive complexes formed by hydrogen bond interaction between OH and N / O atom of morpholine (M1 and M2), transition states (TS1 and TS2), and product radical (R) for the H abstraction reaction of morpholine with OH radical.

However, in both the complexes, we could optimize the TS structures involving the abstraction of the hydrogen atom attached to a carbon atom α to only O atom, and not N atom. This selective abstraction of hydrogen atom can be explained based on the structures of the complexes, M1 and M2. In M1, the distance from O atom of OH to H atom, α to nitrogen, is 3.63 Å, whereas the distance to H atom α to O atom is 3.14 Å. The H atom attached to N atom is 3.29 Å away from O atom of OH. Thus, the proximity of the O atom of the OH moiety to the morpholine H atom attached to the C atom in the α position to the oxygen atom is responsible for selective H atom abstraction seen in the transition state optimization. Geometries of the two transition states, which could be optimized, are shown in Fig.3.8, as TS1 and TS2, for the pre-reactive complexes M1 and M2, respectively.

TS1 is the transition state for H atom abstraction in the case of pre-reactive complex M1. Here, the OH moiety, which was closer to N atom in the pre-reactive complex, moves away, and its O atom comes closer to the H atom, α to morpholine O atom. The OH moiety in M2 rotates in TS2, so that the O atom is closer to the H atom, α to O atom. Thus, it is observed that, in both the transition states, the O atom of the O-H group is closer to the H atom, α to the O atom of the ring, axial H atom in case of TS1, and equatorial H atom in case of TS2. The distance between the abstracted H atom and the O atom of OH is 1.37 Å in TS1, and 1.33 Å in TS2.

Both these transition states are found to lead to the same radical, R, with the optimized structure given in Fig. 3.8, even though the axial H atom is removed from TS1, and the equatorial H atom is removed from TS2. The products state is 21 kcal mol^{-1} lower in energy, as compared to the reactants. Earlier calculations on morpholine radicals have shown that, the radical formed by abstraction of H, □α to N atom, is more stable (by 4.0 kcal mol^{-1}) than the one formed by abstraction of H atom, α to the O atom[43]. The theoretically calculated dissociation energy of C—H bond, □α to N atom, is found to be 92.0 kcal mol^{-1} [43], close to the experimental value of 93.0 kcal mol^{-1} [48]. The dissociation energy of N—H bond is also considered to be similar to that of the C—H bond, α to N atom, in the case of secondary amines[37]. Thus, it is difficult to differentiate energetically H abstraction from nitrogen and carbon α □to nitrogen, though the latter is considered to be dominating[49]. However, as mentioned earlier, all the attempts to optimize TS, by appropriately orienting OH, to abstract an H atom, α to N, or H atom on N, were unsuccessful, from any of the pre-reactive complexes. As discussed above, the proximity of O atom of OH to H atom, α to O atom, in both the pre-reactive complexes, and steric hindrance for formation of any other complexes may be responsible for this.

Based on the above transition state geometries, the L parameter, which denotes whether a transition state structure is reactant-like ($L < 1$), or product-like ($L > 1$), is calculated. The value of L is given by,

$$L = \delta r\,(\text{C-H}) / \delta r(\text{H-O}_{\text{OH}}), \qquad (3.13)$$

where δr (C-H) is the variation in the breaking bond distance between the transition states and the reactants, and $\delta r(\text{H-O}_{\text{OH}})$ is the variation in the forming bond distance between the transition states and the products. In the case of H abstraction through TS1 and TS2, L value is calculated to be 0.23 and 0.25, respectively. Thus, in both the complexes, the H abstraction reaction involves reactant-like TS. A direct relation between L parameter and heat of reaction has also been established[50, 51]. For a L-value of 0.3, exothermicity of 20 kcal mol^{-1} is reported for serine[47], which is very similar to our calculated value of 21 kcal mol^{-1}.

The steps involved in the hydrogen abstraction reaction from morpholine are (3.14A), a fast pre-equilibrium between the reactants and the pre-reactive complex C_4H_9NO—OH (M1 or M2), followed by (3.14B), the elimination of a water molecule.

$$C_4H_9NO + OH \underset{k_{14A'}}{\overset{k_{14A}}{\rightleftharpoons}} C_4H_9NO{-}{-}{-}OH \qquad (3.14A)$$

$$C_4H_9NO{-}{-}{-}OH \xrightarrow{k_{14B}} C_4H_8NO + H_2O \qquad (3.14B)$$

Based on a steady state analysis, the overall rate constant can be written as

$$k_{14} = \frac{k_{14A}k_{14B}}{k_{14A'}} = \left(\frac{A_{14A}A_{14B}}{A_{14A'}}\right) exp\left(\frac{-(E_{14A} + E_{14B} - E_{14A'})}{RT}\right) \qquad (3.15)$$

Since the reaction (3.14A) is barrierless, the temperature dependence of the overall rate constant will depend on the relative barriers for the reaction (3.14B) and the reverse reaction (3.14A′). The PMP2 (MP2) energies of the relevant stationary points, the pre-reactive complexes M1 and M2, the transition states TS1 and TS2, and the isolated products, with respect to the reactants, are shown in the energy level diagram (Fig. 3.7). The stability of the pre-reactive complex is significant, 6.82 and 5.17 kcal mol^{-1}, for M1 and M2, respectively. From the theoretical calculations (Fig. 3.7), it can be seen that the back reaction of the pre-reactive complex M1 has a higher activation barrier than the H abstraction reaction, i.e., $E_{14A'} > E_{14B}$, which makes the term within the exponential, ($-(E_{14A} + E_{14B} - E_{14A'})/_{RT}$), a positive quantity. Hence the overall rate and the rate constant will decrease with increase in temperature. Hence, the apparent activation energy for the pathway through M1 is negative (-0.8 kcal mol^{-1}), whereas the pathway through M2 has a small activation barrier of about 2.25 kcal mol^{-1}. The experimentally observed negative activation energy of 1.17 kcal mol^{-1} suggests the predominance of the pathway through M1, though the second pathway can't be completely ruled out. In addition to these pathways through pre-reactive complexes, direct abstraction pathways, with higher activation energies, are also possible, especially at higher temperatures. These different possibilities are probably responsible for the "negative activation energy" as found in Fig. 3.7.

The results of these theoretical calculations explain the experimentally observed negative activation energy. However, the rate constant for the reaction of morpholine with OH radical is found to be high, higher than that for the ethers, diethers and cyclic ethers. In 1,4 dioxane, where the N atom of morpholine is replaced by O atom, the rate constant for the reaction with OH at the room temperature is only 1 x 10^{-11} cm^{3} molecule^{-1} s^{-1}, eight times lower than the presently measured value for the reaction of morpholine. Theoretical calculations on the pre-reactive complex and transition states are not available for this molecule, to compare with the present study. In another oxygen containing compound, hydroxy acetone, the order of stabilization of the pre-reactive complex with OH is calculated[41] to be in the range 4.0 – 5.7 kcal mol^{-1}, depending on the level of the theory, and the transition state energies, with respect to the reactants, are calculated to be in the range of 1.0 to –1.0 kcal mol^{-1}, very similar to that observed in the present work. However, at a pressure of 2-5 torr, the rate constant for OH reaction at room temperature is (3.02 ±0.28) × 10^{-12} cm^{3} molecule^{-1} s^{-1}, and positive temperature dependence of the rate constants is observed. The rate constant reported at room temperature and atmospheric pressure is 1.5 x 10^{-11} cm^3 $molecule^{-1}$ s^{-1} [52], almost five times lower than that observed for morpholine. In the case of cyclic ethers, like tetrahydrofuran, 1,3 dioxane, 1,3,5 trioxane, oxepane, etc, the experimentally observed pre-exponential factors are very close to that for morpholine, but the activation energies are less negative (positive in the case of trioxane), as compared to that for morpholine, observed in this work. Thus, the presence of an N atom in morpholine is found to have a profound effect on the activation energy and the rate constant for the reaction with the OH radical. Morpholine is a secondary amine. Only two experimental studies on the kinetics of the reaction of OH radical with amines are available[53, 54], and both report high rate constants. The rate constant of the reaction of OH with dimethyl amine at room temperature is reported to be around 6.5 x 10^{-11} cm^3 $molecule^{-1}$ s^{-1}, in both the studies, whereas there is a difference in the rate constant reported for trimethyl amine, 3.5 x 10^{-11} cm^3 $molecule^{-1}$ s^{-1} by Atkinson et al[53] and 6.1 x 10^{-11} cm^3 $molecule^{-1}$ s^{-1} by Carl and Crowley[54]. Activation energy is also reported to be negative in the case of CH_3NH_2, $(CH_3)_2NH$, $(CH_3)_3N$, $C_2H_5NH_2$[53], in the range of -375 to -500 cal mol^{-1}. The observation of negative activation energies of these molecules were assigned to a zero, or near zero, activation energy, combined with a temperature dependent pre-exponential factor. However, the present results on morpholine and the previous calculations on aminoacids[46, 47], suggest that formation of a stable pre-reactive complex may be responsible for the observed negative activation energies in the case of amines also. The respective pre-exponential factors for the above amines are: 1.02, 2.89, 2.62 and 1.47 x 10^{-11} cm^3 $molecule^{-1}$ s^{-1}, higher than that observed for morpholine, in the present study.

The rate constant observed for morpholine is marginally higher than that observed for these amines, and the activation energy is more negative (-1170 cal mol^{-1}). The theoretically computed overall rate constant at room temperature, for all possible pathways, in the case of aminoacids, like serine[47], is very close to that observed here for morpholine. As mentioned earlier, the relative energy of pre-reactive complex and transition states computed for the aminoacids were found to be similar to that of morpholine. Thus, it can be seen that formation of pre-reactive complexes, negative activation energy and very high rate constants are common features of the reactions of OH radical with amines, more prominent than that in the case of oxygen compounds.

3.4 Summary

Laser Photolysis-Laser Induced Fluorescence method has been used for measuring the kinetic parameters of the reaction of OH radicals with $CF_3CH_2OCH_2CF_3$ (bis-2,2,2 trifluoroethyl ether) and morpholine, in the temperature range of 298 – 365 K. The bimolecular rate coefficient of reaction of OH radical with bis-2,2,2 trifluoroethyl ether at 298 K, $k_{II}(298)$, has been measured to be $(1.47 \pm 0.03)\times10^{-13}$ $cm^3molecule^{-1}s^{-1}$, and the temperature dependence of k_{II} has been determined to be $(4.5 \pm 0.8) \times 10^{-12}exp[-(1030 \pm 60)/T]$ $cm^3molecule^{-1}s^{-1}$. The error quoted is 1σ of the linear regression of the respective plots. The rate coefficient at room temperature is very close to the average of the three previous measurements, whereas the values of E_a/R and A-factor are higher than the two previously reported values.

Kinetics studies and theoretical computations on the reaction of the OH radical with morpholine show evidence of the involvement of a stable pre-reactive complex, due to hydrogen bond interaction between the OH radical and nitrogen/oxygen atom of morpholine. The rate constant at room temperature (298 K) has been measured to be (8.0 ± 0.1)×10^{-11} molecule^{-1}cm^{3}s^{-1}. Though the Arrhenius plot is not perfectly linear in the temperature range studied, the approximate dependence of the rate constant on temperature is given by (1.1 ± 0.1) × 10^{-11}exp [(590 ± 20)/T] cm^{3}molecule^{-1}s^{-1}. The rate constants are observed to be high as compared to those for the reactions of similar heterocyclic molecules with oxygen atom. *Ab initio* molecular orbital calculations show that pre-reactive complexes are formed due to hydrogen bond interaction between OH and the N / O atom of morpholine. The energies of these pre-reactive complexes are lower as compared to that of the reactants, by 5–7 kcal mol^{-1}, the pre-reactive complex involving N atom being more stable than that with O atom. The energies of the transition states for H abstraction from these pre-reactive complexes are found to be either negative, or very small, with respect to the reactants, which explains the observation of negative activation energy.

Chapter 4

Dynamic Study of Cyclic Ethers

Dynamics, i.e., the relation between the distribution of energy among the parent, and product molecules in a reaction bear direct signatures of the actual features present in the potential energy surface. Unimolecular photodisociation is the simplest reaction whose dynamics can be studied quite authentically with the advanced spectral and diagnostic tools available to the modern researcher. The dynamics of photodissociation of various classes of compounds, with different structural peculiarities, are already studied and reported in the literature. Understanding the effect of structural features of a molecule on the dynamics of its photodissociation reaction also helps in interpreteing its behaviour in more complex bulk systems, like in combustion, or atmospheric reactions[2, 5-8, 10, 12-17, 20-23]. Cyclic ethers belong to a class of compounds which have interesting structural properties, as well as importance applications in different fields. They have at least one heteroatom, O, in the ring structure like tetrahydrofuran and tetrahydropyran, and sometimes, can have more than one, like in the case of morpholine, where there are two heteroatoms, N and O, present in the ring. The photodissociation reactions of these three compounds, namely, tetrahydrofuran, tetrahydropyran, and morpholine have been studied in order to understand some basic features of the photochemical behavior of cyclic compounds.

Tetrahydrofuran (THF), the completely hydrogenated form of furan, is an extensively used chemical compound, with biological, chemical and environmental importance. THF molecule is the structural unit of DNA, many carbohydrates and other biological molecules. Being one of the most polar ethers, THF, the cyclic analogue of diethyl ether, is widely used as a polar solvent and polar reagent in chemical laboratories and industries. Due to its high solubility in water (100%), quite low boiling point (66^{o}C) and low degradability, THF gets released into the environment very easily. When introduced into living systems through inhalation, or any other pathway, THF can cause severe physical disorders, by attacking mainly the skin, the eyes and the central nervous system. It can also affect the liver and the kidney in a minor way. Consequently, it has been identified as an environmental pollutant. The knowledge of photochemistry of this compound is essential to understand its fate in the atmosphere, as well as in the other parts of the environment. Moreover, understanding of the thermal and photochemical dissociation of THF is important to get an insight into cell damage and cell death caused by DNA damage. The spectroscopy and photochemistry of THF have been already studied to some extent. THF is an ideally suited five-membered cyclic molecule for investigation of pseudorotation, and has actually shown direct spectroscopic observation of pseudorotation, for the first time[55]. Since last four decades, pseudorotation of THF has been investigated, and considerable knowledge has been acquired on spectroscopic data and potential energy surface[55]. Even *ab initio* molecular orbital (MO) calculations have been employed, to investigate vibrational spectra and properties of the various conformers of the ground state of THF[56]. Experiments on the unimolecular dissociation of THF, are of considerable significance, since they provide an insight into the general ring opening mechanism of heterocyclic molecules.

Tetrahydropyran (THP), a saturated 6-membered cyclic ether, has been studied, for its structure and conformations, in both its ground and excited states, for quite a long time. The techniques used so far are NMR[57], electron diffraction[58, 59], vacuum-ultraviolet[60], microwave[61] and vibrational[62] spectroscopy. This compound is the main structural unit of pyranose sugars, a few marine monotarpenes[63], peptidomimetics and foldamers[64], and hence, is biologically important. Recently, some of the optically active THP derivatives have gained technological importance as components of ferroelectric[65] and antiferroelectric[66] liquid crystals. THP ring is also a structural part of a newly developed highly effective anti-tumor agent, called mucocin[67]. As this immediate higher homologue of tetrahydrofuran (THF) gains increased implicational importance, it is necessary to study its chemistry, particularly photochemistry and kinetics, with more advanced techniques. Investigation of unimolecular reactions of molecules in collision-free conditions is one of the best tools for understanding their environmental and combustion reactions. Unimolecular reactions can be studied by both thermochemical and photochemical means, of which the latter offers additional advantages, such as collision-free environment, selective excitation, etc. Studies of the photochemical dissociation of THP in uv-visible region, apart from providing better understanding of the unimolecular ring opening process of cyclic ethers, can throw some light on the environmental behaviour and combustion reactions of this compound.

Morpholine (C_4H_9NO) is similar to tetrahydropyran in having a six-membered ring, but differs from the latter (at the γ-position with respect to the O atom in the ring) by replacement of the CH_2 group, by an NH group. Morpholine and its derivatives are used in the synthesis of numerous pesticides, chemicals and drugs, as solvents and as anticorrosive agents in boiler water, particularly in nuclear power reactors[68]. Morpholine itself is used widely in medical field to treat pain, inflammation, migraine, emesis and fungal infection. This group of compounds, nonetheless, is toxic and mutagenic, which is readily absorbed through skin. Morpholine is introduced in the biosphere as a pollutant through its use as a fungicide[69, 70]. In spite of being a biologically important molecule, the photochemistry of morpholine is not studied well. Dowherty et al.[71] has reported the removal of morpholine in the aqueous phase by TiO_2 mediated photocatalytic degradation. However, the gas-phase photochemistry is largely unstudied. There are some spectroscopic studies of the morpholine molecule reported in the literature. Friedel et al.[72] studied its infrared absorption spectrum, whereas Indris et al.[73] and Alekseev[74] investigated the ground state molecular structure. In the present work, we investigated photodissociation of morpholine molecule, to understand its dynamics and mechanism, and to compare it with that of the other cyclic ethers. The photodissociation dynamics of morpholine will offer further insight into the laser-induced photochemistry of heterocyclic ring, with more than one heteroatom.

In this chapter, photodissociation of THF, THP, and morpholine by 193 nm laser was found to produce OH radical. This channel, which has yet not been reported, is an extremely interesting from the mechanism point of view, since none of these compounds contains an OH functional group in their structure. Detailed dynamic studies of this reaction channel reveal an involved reaction pathway, where the primary products of the photodissociation undergo intramolecular rearrangement, before the OH radical is formed as the final product.

4.1 Experimental results

4.1.1 Absorption Cross-section Measurement

The uv-visible absorption spectra of THF and THP are already reported[60] in the literature, but not that of morpholine. We measured morpholine's absorption cross-section (σ) at 193 nm by the set-up described in section 2.3. Plotting the $\ln(I_0/I)$, I_0 and I being the intensities of the incident and the transmitted beam, respectively, against the number density of morpholine molecules in the absorption cell, we got a straight-line graph (Fig. 4.1.), which obeys the Lambert–Beer's law, given by eqn.(2.23). The measured slope of the line is 2.4×10^{-15} cm^3 molecule^{-1}, which gives the value of σ as 4.8×10^{-17} cm^2 molecule^{-1}.

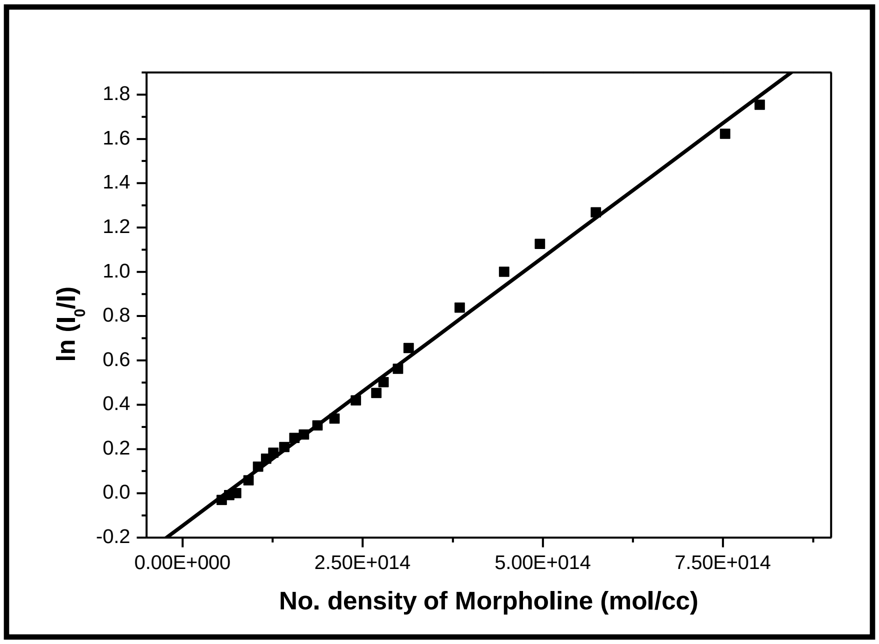

Fig. 4.1: A plot of $\ln(I_0/I)$ vs. the number density of morpholine gives the value of its absorption cross-sectiont to be 4.8×10^{-17} cm^2 molecule^{-1}

4.1.2 Detection of OH among the Products of Photodissociation at 193 nm

We detected transient OH radical by its characteristic LIF spectrum as a product of photolysis of all the three molecules, namely, THF, THP and morpholine, after irradiation at 193 nm by ArF excimer laser. Fig. 4.2 shows the characteristic LIF spectrum of the OH radical introduced in the case of the three compounds respectively. In assigning the line positions of OH, we used the standard notation **Δ**J (N) for the transition, and denote transitions associated with the spin–orbit states $X^2\Pi_{3/2}$ and $X^2\Pi_{1/2}$, with subscripts '1' and '2', respectively as discussed in section 1.8. The observation of OH was extremely significant, because none of the earlier reports about the dissociation of these compounds, by any means, reported the generation of OH radical among the products. Moreover, the O atom in these molecules is bonded to two carbon atoms that are at the two ends of a rigid ring. Therefore, there is no chance of OH being formed as a primary photoproduct. The mechanism of OH formation on photoexcitation of THF, THP, or morpholine, hence, is not, therefore, intuitively obvious. The molecules must be undergoing a high energy multistep reaction channel, involving at least one intramolecular rearrangement step, in order to generate this unusual product. The dynamics of this very interesting OH generation channel was studied, to understand the actual properties of the potential energy surface of the photodissociation reaction of these cyclic compounds.

The state selective distribution of the nascent OH radicals was probed by measuring fluorescence of the (0,0) and (1,1) bands of the $(A^2\Sigma)\leftarrow(X^2\Pi)$ transition, after exciting the same system with a Nd:YAG pumped frequency-doubled tunable dye laser. The data were collected at 50 mTorr sample pressure, with 50 ns time delay between the photolysis and the probe beams. In all the three cases, the OH generated was found to be in the ground vibrational level, i.e., it was vibrationally cold. Several rotational lines were measured (shown in Fig.4.2), to obtain dynamic information about the OH radical formed. When we compared the intensities of the rotational lines of the LIF spectrum

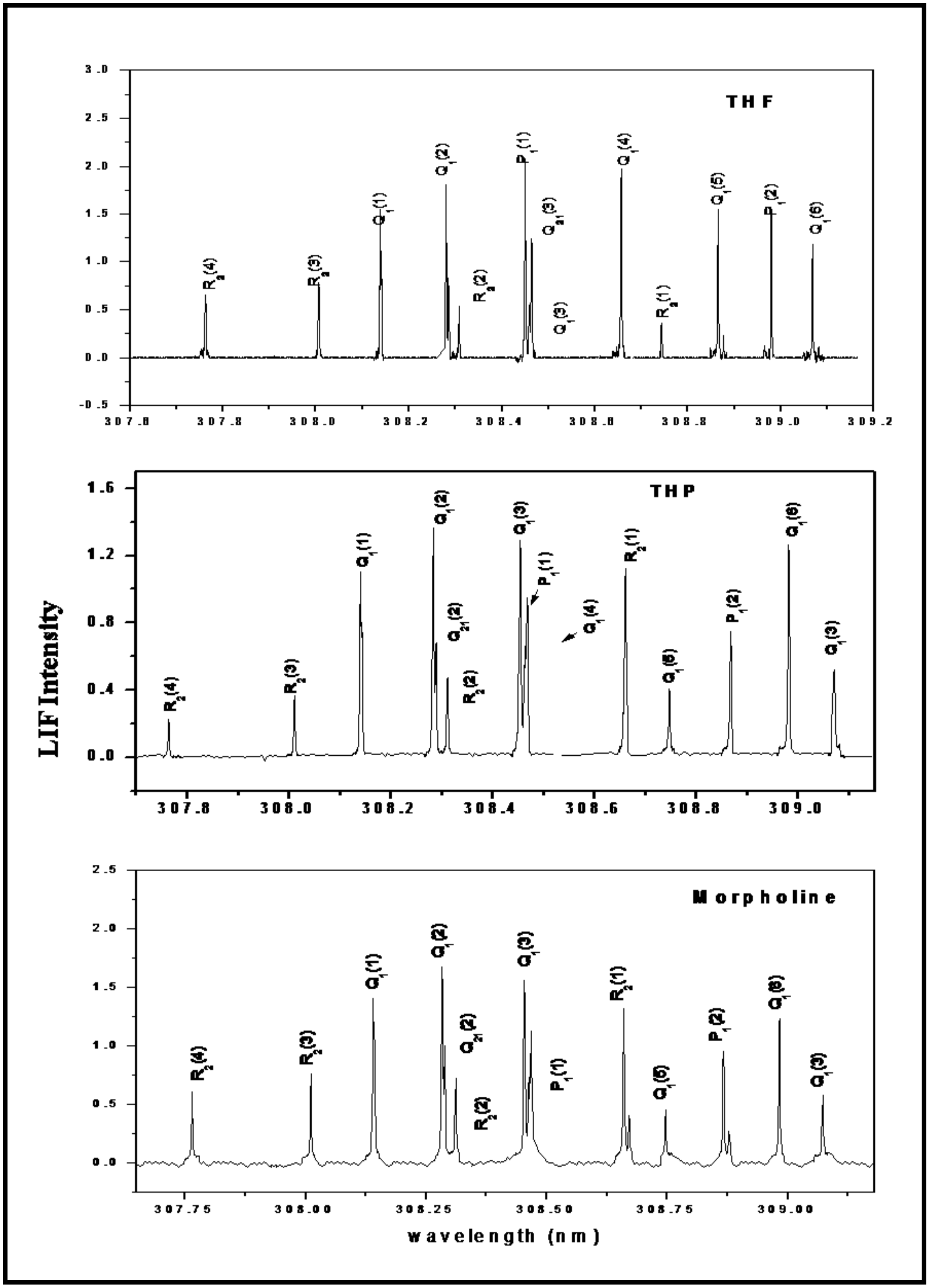

Fig. 4.2: LIF Excitation spectra of the (0,0) band of $A^2\Sigma \leftarrow X^2\Pi$ transition for THF, THP and morpholine respectively. Rotational lines are marked in the figure.

obtained by using unpolarized laser beam with that obtained by using laser beam polarized with a stack of quartz plates, no noticeable change was observed under otherwise identical experimental condition. This fact, which was applicable for all the three molecules, indicated that the OH generating channel is probably operative from the ground states of the parent molecules.

4.1.3 Dynamics of OH Formation Channel

The rotational lines obtained by LIF are analyzed for obtaining the dynamics data of the photodissociation process, as discussed in section 2.5. The relative populations of the different ground state rotational levels can be obtained by comparing the intensities of the LIF lines originating from them. The relative populations are indicative of the rotational energy of OH radical. From the Doppler width of the individual lines, translational energy can also be deduced. Since in none of these molecules, any signal was obtained for the (1,1) transition, it can safely be assumed that, in all the three cases, the OH radical is formed in the vibrational ground state. The experimentally obtained energy state distribution of OH radicals formed by photodissociation of each compound is tabulated in Table 4.1.

Translational Energy

All the rotational lines, in the case of each molecule, were observed to have similar linewidth, within the range of experimental error. After correcting for the probe laser linewidth, the Doppler profile of the peaks were analyzed, for the measurement of translational energy of the photofragments (section 2.4.1). Fig. 4.3 shows the typical Doppler profiles for the $P_1(2)$ line for the (0,0) transition, in the case of THF, THP and morpholine, respectively. From the individual Doppler widths, the average translational energy in the centre of mass frame, E_{CM}, was calculated to be 17.4 ± 2.2, 21.9 ± 3.2 and 19.6 ± 0.28 kcal mol^{-1}, for THF, THP and morpholine, respectively.

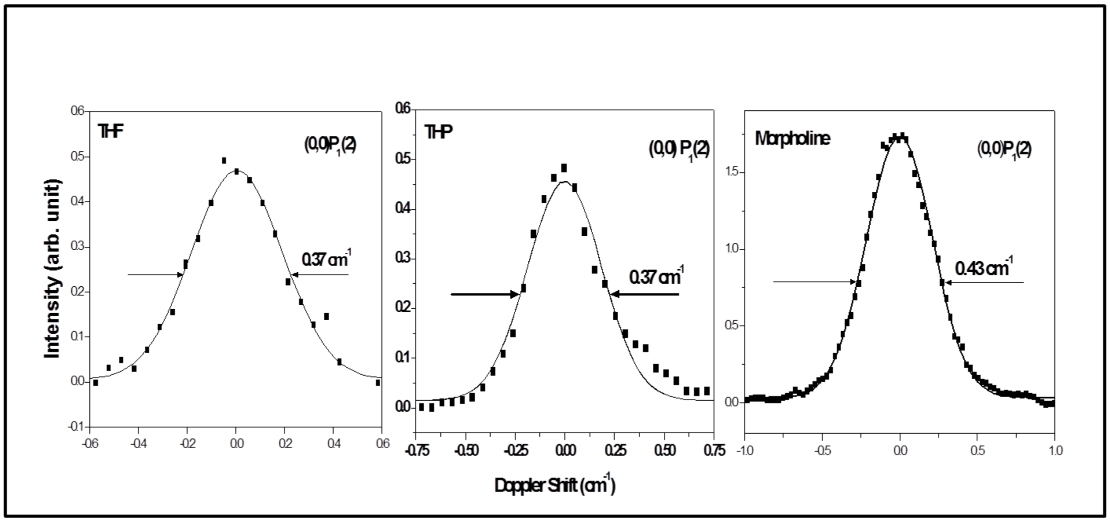

Fig. 4.3: Doppler broadened $P_1(2)$ line of the (0,0) band of the ($A^2\Sigma$, v′ = 0) ← ($X^2\Pi$, v″ = 0) system of OH radical, produced by photodissociation of THF, THP and Morpholine molecule respectively

Rotational Energy

The positions of all the rotational lines in the OH spectrum were marked following the assignments made by Dieke and Crosswhite[6]. The log of the intensity of the respective LIF lines, after normalization with respect to required parameters (section 2.4.2), were plotted against the energy of the rotational levels. In the case of all the three compounds, the data fitted a straight line, within reasonable limit of scattering, which indicates that the rotational levels are equilibrated among themselves in all the cases. By fitting the data to Boltzmann's equation (eqn. (2.33)), the rotational energy of OH radical was found to be 3.7 ± 0.4, 0.86 ± 0.06 and 1.0 ± 0.2 kcal mol^{-1} , for THF, THP and morpholine, respectively. Fig. 4.4 shows the Boltzmann plots.

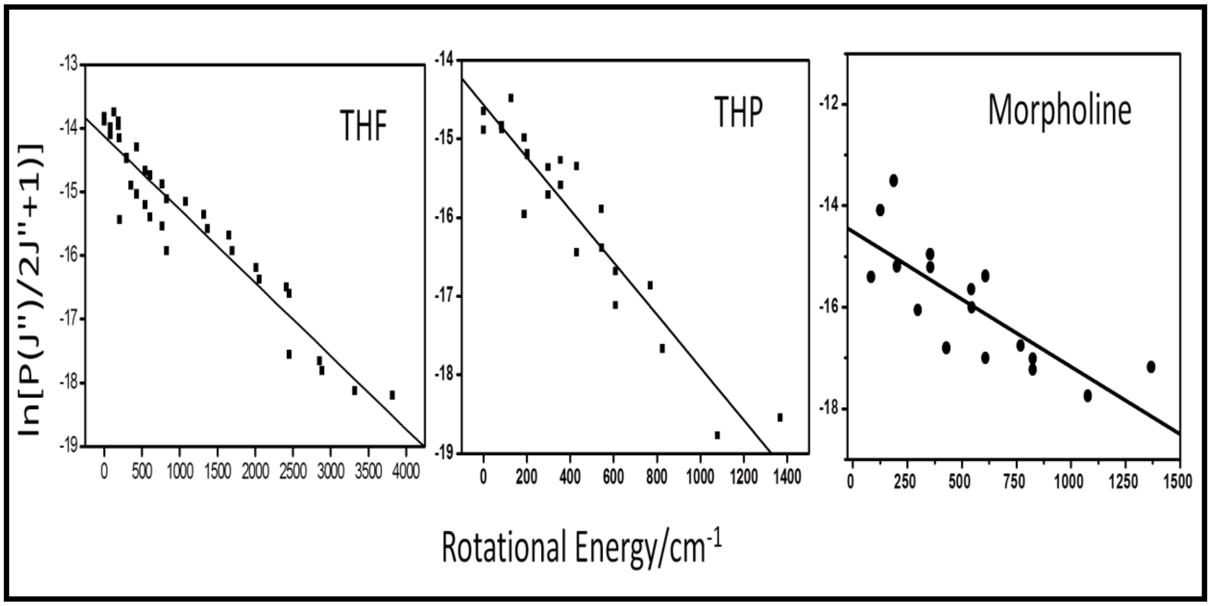

Fig. 4.4. The figure depicts Boltzmann plots of the rotational state populations of OH (v=0), generated in dissociation of THF, THP and Morpholine, at 193 nm.

Λ-doublet and Spin-orbit State distribution

The OH radicals formed by photolysis of the parent compounds can be distributed among the two spin orbit states ($\Pi_{3/2}$/ $\Pi_{1/2}$) and two Λ-doublet states ($^2\Pi^-(A^{''})/^2\Pi^+(A^{''})$) as well. The population distribution between these two states is indicative of some important aspects of the photodissociation process, as discussed in section 2.4.3. From fig.4.5, which shows the spin orbit and Λ-doublet state population distribution of OH (*v*=0), generated by dissociation of THF, THP and morpholine at 193 nm, it can be seen that, the spin orbit states are statistically populated, except in the case of morpholine, where $^2\Pi_{1/2}$ state is preferentially populated. This indicates that, in the case of morpholine, an interaction of the initially excited state with nearby triplet states may occur along the reaction pathway. Alternatively, this effect can also be created by inelastic scattering between the recoiling fragments. Any such effect may be absent in the OH generation channel in the case of THF and THP.

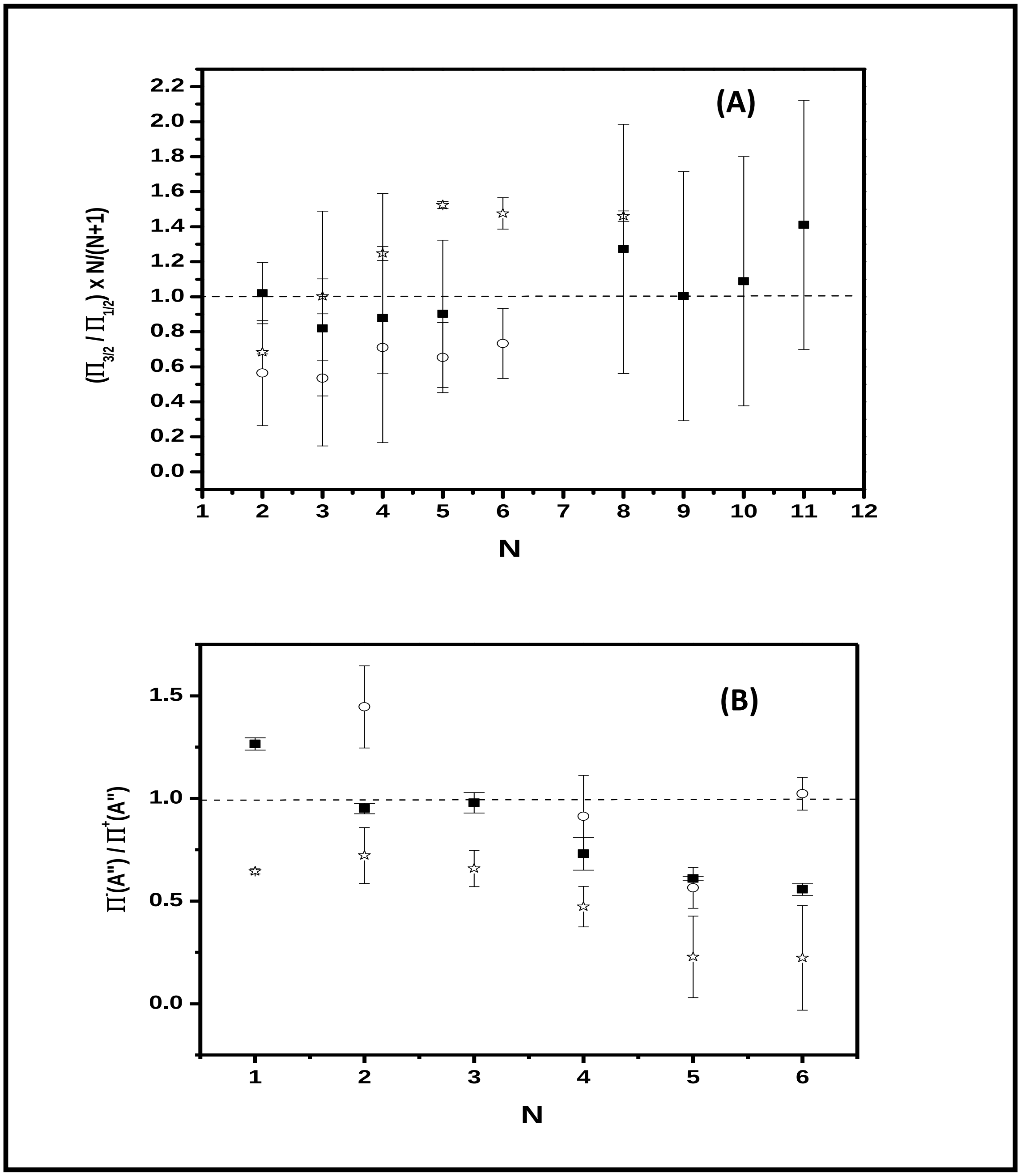

Fig. 4.5: (A) The spin orbit state population distribution of OH (v=0), generated by dissociation of THF, THP and morpholine at 193 nm.

(B) The Λ-doublet state population distribution of OH (v=0), generated by dissociation of THF, THP and morpholine at 193 nm.

☆ :- THF, ■ :- THP, O :- Morpholine

On the other hand, in the case of the Λ-doublet states, the population is distributed statistically in case of THP and Morpholine, but, for THF, $^2\Pi^+(A'')$ is populated preferentially. This observation indicates that, in the case of five-membered THF ring, the rotation of OH originates majorly from the impulse upon dissociation, whereas for six-membered rings in THP and morpholine, both the impulse and the parent torsion probably are transformed into product rotational motion. The difference in the size of the ring, and the strain associated with that, is probably responsible for this difference in Λ-doublet state distribution.

4.2 Energy Distribution among the Fragments and Dynamic Models

The distribution of the energy among the different modes in the photoproducts follows an overall similar pattern in the three molecules. A large amount of the energy is partitioned to the relative translational motion of the products. According to Table 4.1, it is clear that the percentage of the available energy partitioned as translational energy varies between 35%-45%, for all the three cyclic ethers. As discussed in section 2.5, a quantitative examination of the available energy can be done by two limiting models, the impulsive and the statistical models. The former is applicable in the case of dissociation over a repulsive surface. The latter is applicable in the case where no barrier exists.

The comparison between the experimentally obtained values and those calculated by using these limiting models clearly shows that, none of the models can successfully explain the experimental results. This is expected, because OH cannot be formed by a primary process, and at least one intermediate step must be present between the reactants and the products. Hence, a hybrid model was used, which is actually a combination of both the statistical and the impulsive models. The hybrid model could explain the energy distribution in the case of Tetrahydropyran and Tetrahydrofuran, but no suitable hybrid model could be proposed for morpholine. This can be due to the presence of more than one reaction channels, with different characteristics, leading to formation of OH radical in the case of morpholine. The applicability of the hybrid model in the case of THF and THP suggests that there is an energy barrier in the exit channel. In the case of THF, the exit barrier which matches the experimental data is 16 kcal/ mol, and that for THP is 40 kcal/mol. However, much significance can not be attached to the exact value of the barrier, as it only signifies an appreciable exit barrier in the OH formation channel. Since none of the cyclic ethers have any OH moiety in their structure, it is not possible to expect the OH radical as a primary product, after its photodissociation. Thus, OH being a secondary product, the dynamics is expected to be more compatible with the statistical model of energy partitioning among the different modes of the products. The nonstatistical nature of the energy partitioning, explained by a hybrid model, suggests that the OH generating channel from the ground state of the molecules involves a transition state. Ab initio molecular orbital calculations are done, to find out the possible reaction mechanism and potential energy surface of the OH generation channel in the photodissociation of THF, THP and morpholine.

Table 4.1: Experimentally obtained energy distribution of the OH channel in the photodissociation of THF, THP and morpholine at 193 nm, and its comparison with that obtained by employing statistical, impulsive and hybrid models. All the energies are given in kcal/ mol unit. In the case of morpholine, energies for both the triplet and the singlet channels are given, the latter within parentheses.

	E_T(CM)	E_R(OH)	E_{vib}(OH)	E_{int}(cofrag)
		THF [$E_{available}$ = 49.2 kcal/mol]		
Experimental	17.4 ± 2.2	3.7 ± 0.4	0	28.1 ± 4.7
Impulsive	25.9	1.3	0	22.0
Statistical	4.7	1.1	0.2	43.1
Hybrid	17.8	1.2	0.1	30.1
		THP [$E_{available}$ = 50.3 kcal/mol]		
Experimental	21.9 ± 3.2	0.86 ± 0.06	0	27.5 ± 4.3
Impulsive	25.3	1.4	0	23.6
Statistical	3.7	2.2	0	44.0
Hybrid	22.0	2.4	0	26.1
		Morpholine [$E_{available}$ = 52.4 (58.1) kcal/mol]		
Experimental	19.6 ± 0.8	1.0 ± 0.2	0	31.8 ± 1.3
	(19.6 ± 0.8)	(1.0 ± 0.02)		(37.5 ± 1.7)
Impulsive	4.1 (4.4)	2.5 (2.8)	0.2 (0.1)	45.6 (50.8)
Statistical	26.3 (29.1)	1.3 (1.5)	0 (0)	24.8 (27.5)

4.3 Theoretical Studies and Discussions

4.3.1 Tetrahydrofuran

4.3.1.1 Nature of the Dissociative State

Various researchers recorded the uv-visible absorption spectra of THF in different regions, between 105 and 250 nm, i.e., 11.8–5.0 eV, and from these reports, the nature of the ground state, as well as that of the excited state, accessed by absorption at 193 nm (6.4 eV) can be ascertained. Pickette *et al*[60] found bands for THF in the region of 166–200 nm, due to excitation of an unshared electron of oxygen. G. Z. Hernandez[61] found the low-lying electronically excited states to be Rydberg in nature. Electronic spectra of THF were reported in the 180–210 nm[75] and 120–200 nm[76] regions. The transition in the former region takes place between the nonplanar ground state and a planar excited state. Bremner *et al.*[77] studied the electronic states of THF, along with those of other simple ethers. They, too, found the low-lying excited states to be Rydberg in nature, but selectively mixed with the valence electronic states.The three lowest absorption bands in THF were assigned to excitation of the Rydberg states, $n_o \rightarrow 3s$, $n_o \rightarrow 3p$ and $n_o \rightarrow 3d$, at about 6.6, 7.2 and 7.8 eV, respectively[77]. There remained some disagreement for the first band at 6.6 eV, with respect to a few features, including the origin of the band. Fine structures, originating from valence bands were observed, starting at 6.4 eV (encompassing the $n_o \rightarrow 3s$ state) and 6.9 eV (running into the $n_o \rightarrow 3p$ state). However, it is not understood whether the Rydberg and the valence states are co-existing as two distinct independent states, or there is a single Rydberg/valence composite state in each band.

4.3.1.2 *Ab Initio* Molecular Orbital Calculations

In order to determine the mechanism of formation of OH radical on photodissociation of THP at 193 nm, it is necessary to correlate the experimentally obtained results with the theoretically calculated parameters. *Ab initio* molecular orbital (MO) calculations were performed with Gaussian 92[2]. The geometries of the ground electronic state of THF, the various intermediate products and the transition state structures were optimized with the B3LYP level of theory, using 6-311++G(d,p) basis sets. The energies corresponding to the optimized geometries were further calculated at the second-order Moller-Plesset (MP2) and/or MP4(SDQ) level of theories, using the same basis sets. For radical species, PMP2 levels were sometimes used, as they gave more accurate energy for spin contamination in open-shell systems. Harmonic vibrational frequencies and the force constants were calculated, to ensure that the stationary points on the potential energy surface are true saddle points. All transition states were characterized by only one imaginary frequency and one negative eigenvalue of the force constant matrix. The results are described in detail in the following paragraph.

The structures of THF, the intermediates and the transition states, along with their relative energetics for the proposed OH channel (vide infra), are depicted in Fig.4.6. The first step in the formation of OH is the C—O bond cleavage, leading to the formation of a triplet biradical, with calculated ΔH^0 of 84.1 and 74.8 kcal mol^{-1}, respectively, at MP2 and MP4(SDQ) levels, the latter value is in good agreement with the reported value[78] of 74.6 kcal mol^{-1}. Subsequently, the dissociation channel from the ring opening to the final products follows a triplet pathway. This biradical undergoes isomerisation to alkylhydroxy radical, after abstraction of one β-H atom by the O atom. The four-centered

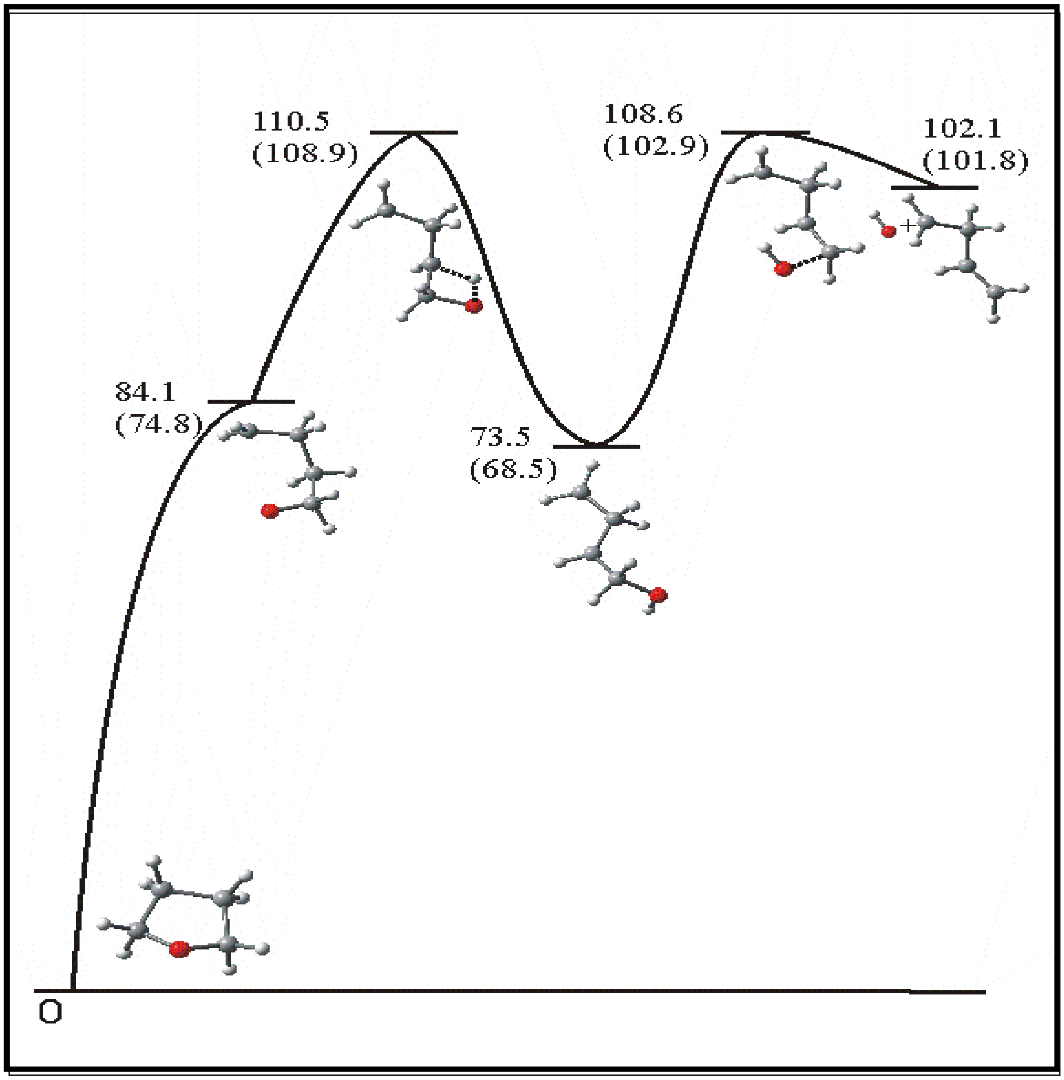

Fig. 4.6: Potential energy curves of the OH formation channel from the electronic ground state of THF, with geometry optimization at B3LYP/6-311++G(*d*, *p*) level, and energy calculations at MP2/6-311++G(*d*, *p*) level of theory. Calculation of the last step of the reaction scheme is at lower level of theories (please see the text). Values in parentheses are at MP4(SDQ) level. All the values of energies are in kcal mol^{-1}.

TS structure of this isomerization reaction has all the three C—C bond lengths equal (1.50 Å), with almost planar geometry for the cyclic structure. For this concerted isomerisation reaction, E_a and ΔH^0 were found to be 26.4 (34.1) and -10.6(-6.3)kcal mol^{-1}, respectively, at the MP2 (MP4(SDQ)) level. We were not able to obtain the TS structure of the C—OH bond cleavage reaction from the isomerised radical at the B3LYP level, but it was obtained at the MP2 level, with 6-311+G(d) basis sets. This TS structure, with a negative frequency of 530 cm^{-1}, was further confirmed, employing optimization criterion of tight convergence. Hence, for this reaction channel, geometries were optimized at MP2 level of theory with 6-311+G(d) basis sets. The TS structure suggests that, after the C—OH bond cleavage, OH emerges out perpendicular to the plane containing the C atom, attached to the dissociating bond, and two other neighbouring C atoms of THF. The structure of the other fragment in the TS is almost similar to that of the isolated fragment, implying that the C—OH bond cleavage reaction has a late barrier. The energies of the optimized structure were calculated at MP2 and MP4(SDQ) levels of theories, with 6-311+G(d,p) basis sets. For the C—OH bond cleavage reaction, E_a and ΔH^0 were estimated to be 35.4 (31.0) and 28.3 (24.9) kcal mol^{-1}, respectively, at the MP2 (MP4(SDQ)) level of theory.

4.3.1.3 The OH Generating Channel

Dissociation of THF in the gas phase induced by heat[79], reflected shocks[80], pulsed CO_2 laser[81, 82], UV mercury arc[83, 84], and UV resonance lamps[85] has been reported in literature. In most of these studies, the emphasis was on investigation of the dissociation mechanism of THF based on characterization of the stable products. In the infrared multiphoton dissociation (IRMPD)[81, 82], the focus was on the measurement of isotope selectivity for ^{16}O and ^{18}O in the dissociation product CO. The major stable products in the low pressure photolysis of THF are: ethylene (C_2H_4), propylene (C_3H_6), and formaldehyde (HCHO). However, HCHO could not be detected in UV photodissociation[85], because of its polymerization. Several other minor products, such as methane (CH_4), ethane (C_2H_6), acetylene (C_2H_2), cyclopropane (c-C_3H_6), 1-butene (C_4H_8), carbon monoxide (CO), and H_2, are also reported. The product distribution and the reaction mechanism are sensitive to the pressure[78, 83-85], temperature[79, 80], and its wavelength of the photolysis light[78, 85]. Although mechanisms of formation of these products have been explained, there exist some differences in the details of these mechanisms proposed under different experimental conditions. In the pyrolytic study[79], at a temperature near 820 K, the major channel is formation of ethylene and acetaldehyde [reaction (4.1)], of which, the latter subsequently dissociates into CH_4 and CO [reaction (4.2)],

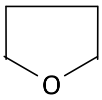

$$\longrightarrow C_2H_4 + CH_3CHO \qquad (4.1)$$

$$CH_3CHO \rightarrow CH4 + CO \qquad (4.2)$$

The minor reaction channel [reaction (4.3)] is the formation of propylene and formaldehyde. Formaldehyde then breaks up into H_2 and CO [reaction (4.4)],

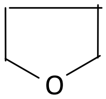

$$\longrightarrow CH2 = CH\ CH3 + HCHO \qquad (4.3)$$

$$HCHO \rightarrow H_2 + CO \qquad (4.4)$$

At high temperatures (1070–1530 K) in shock tube experiments[80], acetaldehyde is not observed; instead, there are two major primary channels, reactions (4.3) and (4.5), producing several intermediates and stable products,

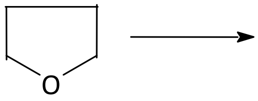

$$2C_2H_4 + (CH_2)_2O \tag{4.5}$$

In the IRMPD[82], as well as in the UV photodissociation [85] of THF, the first step proposed is the C–O bond cleavage, leading to the formation of the $CH_2CH_2CH_2CH_2O$ biradical [reaction (4.6)], which further decomposes via mainly two different pathways [reactions (4.7) and (4.8)],

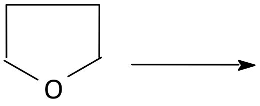

$$CH_2CH_2CH_2CH_2O \tag{4.6}$$

$$CH_2CH_2CH_2CH_2O \rightarrow C_2H_4 + CH_2CH_2O \tag{4.7}$$

$$\rightarrow HCHO + CH_2CH_2CH_2 \tag{4.8}$$

In IRMPD[82], one pathway generates C_2H_4 as a stable product, along with the CH_2CH_2O radical [reaction (4.7)], which eventually leads to CH_3 and CHO radicals. The second pathway leads to the formation of HCHO and the trimethylene biradical $CH_2CH_2CH_2$ [reaction (4.8)], which re-arranges to C_3H_6.

The suggested mechanism of UV photodissociation[85] of THF differs from that of IRMPD[82], with respect to both the reactions (4.7) and (4.8). Instead of CH_2CH_2O in reaction (4.7), two radical products CH_3 and CHO are co-generated [reaction (4.9)]. Similarly, in contrast to the reaction (4.8), the second pathway produces HCO, C_3H_6 and H [reaction (4.10)]. In addition, another major channel opens up, yielding HCO, C_3H_5 and H_2 [reaction (4.11)].

$$CH_2CH_2CH_2CH_2O \rightarrow C_2H_4 + CH_3 + CHO \qquad (4.9)$$

$$\rightarrow HCO + C_3H_6 + H \qquad (4.10)$$

$$\rightarrow HCO + C_3H_5 + H_2 \qquad (4.11)$$

All the intermediates, such as $(CH_2)_2O$, CH_2CH_2O, HCO, etc., undergo subsequent reactions, giving various other stable products, such as C_2H_4, C_2H_6, CH_4, CO, etc.

The stable products of THF were analysed by gas chromatography and FTIR[86]. In the FTIR absorption spectrum of the irradiated THF, the characteristic peaks for ethylene (C_2H_4), propylene (C_3H_6), and formaldehyde (HCHO) were found. In the gas chromatographic analysis, we confirmed these major products, and also detected C_2H_2 and CO as minor products. In addition, CH_4, C_2H_6, C_3H_8, and H_2 were detected in trace amounts. These products were similar to those observed in high temperature pyrolytic[79, 80], IRMPD[82] and UV dissociation[85] studies of THF. This implies that, on excitation at 193 nm, probably the initially electronically excited THF molecule undergoes fast internal conversion to the ground electronic state, from which dissociation occurs, generating the observed stable products. The two major products, ethylene and propylene, detected in both gas chromatographic and FTIR studies, can be explained by various proposed reaction channels (4.3) and (4.6-4.11) by earlier researchers. The other observed products can be explained by secondary reactions, involving transient species, such as $(CH_2)_2O$, $CH_2CH_2CH_2$, etc. If OH were produced from the ground electronic state of THF, on excitation at 193 nm, as our calculations suggest, signature of it would have been obtained in its thermal dissociation and IRMPD too. However, OH was detected neither in these studies nor in UV photodissociation, probably, because of its formation being a minor channel. On the other hand, even a small yield of OH could be detected in our work due to the high sensitivity of LIF technique. Moreover, the C—OH bond cleavage is a high energy channel, which requires, according to the present calculations, more than 100 kcal mol^{-1} of energy to yield OH. This supports the fact that OH formation is a minor channel, and could not be observed in dissociation of THF reported so far. Thus, it can be concluded that, THF can dissociate from its ground electronic state, excited state, or both the states.

4.3.2 Tetrahydropyran

4.3.2.1 Nature of the Dissociative State

There exists sufficient literature on the spectroscopy of both the ground and the excited states of tetrahydropyran (THP). The ground state conformations of THP, a molecule with a saturated six-membered ring, which is a subject of interest for a long time, was probed with a number of different techniques. In general, a stable molecule of six-membered ring can exist as chair, boat, or twist conformer. Rao and Kewley[62] studied the equilibrium structure of THP by using microwave spectroscopy, and established the most stable ground state equilibrium conformation of THP to be the non-planar chair form, which was further confirmed by electron diffraction studies[59]. Even for the ground state THP radical cation also, the most stable conformer is the chair form. In addition to the microwave spectra, vibrational spectra of THP have also been measured and reviewed[62].

The earliest spectroscopic data on THP in vacuum-ultraviolet (VUV) region, reported by Pickett *et al.*[60], in the vapour phase, reveal absorption bands between 50,000 and 60,000 cm^{-1}, due to the excitation of the unshared electrons of oxygen. Subsequently, Hernandez[61] reported the VUV spectra of THP at higher resolution. These transitions have Rydberg character, and they found that the Rydberg series converges at 74,630 cm^{-1} (9.25 eV). This agreed quite well with the value obtained by Watanabe *et al.*[87], using photoionization method (9.26±0.03 eV), and that obtained by Planckaert *et al.*[88], using photoelectron spectroscopy (9.46 eV). The band system of THP accessed by 193 nm was analysed, in detail, by Gray *et al.*[89] They found that the excitation at 193 nm leads to the lowest allowed transition in this molecule, showing extensive vibrational structure, with the origin of the system at 51,908 cm^{-1}. Analyzing the vibrational structure, they predicted the first excited state of THP to be nonplanar, with chair configuration, like the ground state. This first, highly structured band system was characterized as an $n \rightarrow 3s$ Rydberg transition[90]. The second band system of THP is broad, starting at 54,437 cm^{-1}, and contains two electronic transitions belonging to the 3*p* manifold[88]. But, the strong band at 68,000 cm^{-1} was assigned to the 3*d* and 4*s* Rydberg transitions. The lowest electronic state transition is also investigated by 2+1 resonance-enhanced multiphoton ionization (REMPI) studies[91] of jet-cooled THP. These studies showed that the Rydberg state consists mainly of 3*s* atomic-orbital contributions from the ring carbon atoms in THP, in conformity with the earlier assignment of the lowest transition as n_o→3*s*.

4.3.2.2 *Ab Initio* Molecular Orbital Calculations

Ab initio molecular orbital calculations for the OH formation channel from THP were performed, using the same basis set and the same level of theory, as in the case of THF. The geometries of the ground electronic state of THP, as well as those of the intermediate products and the transition state structures (TS), were optimized with B3LYP theory, using 6-311+G(d,p) basis sets. The energies corresponding to the optimized geometries were calculated at the second order Moiller–plasset (MP2) and the projected MP2 (PMP2) level of theories, using the same basis sets. The PMP2 values are the corrected energies for spin contamination in the open-shell systems, and, therefore, there are small differences between MP2 and PMP2 energies. Thus, for the radical species, PMP2 energies are more accurate. For the C**—**OH bond cleavage, the TS structure could not be optimized at the B3LYP/6-311+G(d,p) level of theory, and, therefore, optimizations of both the geometries and the energy calculations for this step were carried out at the MP2/6-31+G(d) level of theory. The structures of THP, the intermediate products, and the transition states, along with their relative energetic for the possible OH generating channels, are depicted in Fig.4.7.

Between the chair and the boat conformers of THP in the ground electronic state, the former was calculated to be more stable by 6.7 kcal mol^{-1}, in agreement with the reported results[59, 60]. The boat is somewhat twisted, and the four opposite C atoms, which are planar in ideal boat conformation, lie at a dihedral angle of 53.7° in this structure. In the proposed mechanism, both the conformers lead to OH formation in a sequence of reactions. The species generated in different steps from the two forms of THP are different conformers, with overall similar energetics for OH formation (shown in Fig. 4.7). This implies that, on excitation of THP at 193 nm, the chair conformer of the excited state can relax to the more stable chair or the boat conformer of the ground electronic state, which subsequently undergoes a series of reactions, generating OH. The first step in the mechanism of OH formation is the C—O bond cleavage (ring opening), leading to the formation of a triplet biradical (Fr1 in Fig. 4.7.), with enthalpy change (ΔH^o) of 73.9 (71.9) kcal mol^{-1}, calculated at MP2(PMP2) level. All efforts to optimize the geometry of a corresponding singlet biradical proved futile, as calculations led to the geometry of the parent molecule, THP. The singlet biradical is expected to be relatively less stable, and thus, all the subsequent processes, leading to the final products are proposed to follow a triplet pathway. After the first step, theory predicts that the biradical may undergo isomerisation to a different alkylhydroxy radical through a β-H atom migration to the O atom via a transition state, as shown in Fig. 4.7. For this concerted isomerisation reaction, the activation energy, E_a and ΔH^0 are found out to be 34.4 (31.9) and –2.0(-2.1) kcal mol^{-1}, respectively, at the MP2 (PMP2) level. The four-membered transition state (TS1 in Fig. 4.7.) structure is planar (dihedral angle HO1C6C5 = 0.4°), and all the four C—C bond lengths are almost equal (~1.50 Å). The C—H bond in the TS is stretched to 1.35 Å, bringing the migrating H atom closer to O, with O—H bond length of 1.28 Å. The isomerised alkylhydroxy radical (Fr2 in fig. 4.7.) then undergoes C—OH bond scission, giving OH radical. For this C—OH bond cleavage reaction, E_a and ΔH^0 are 33.8 (28.6) and –5.7 (-1.0) kcal mol^{-1}, respectively, at the MP2(PMP2)/6-31+G(d) level of theory. For this C—OH bond cleavage step. Transition state could not be optimized at the B3LYP/6-311+ G(d,p) level of theory.

Thus, our theoretical calculations predicts TS for OH formation from the ground electronic state of THP. The TS structure (marked as TS2 in Fig 4.7.) suggests that, after

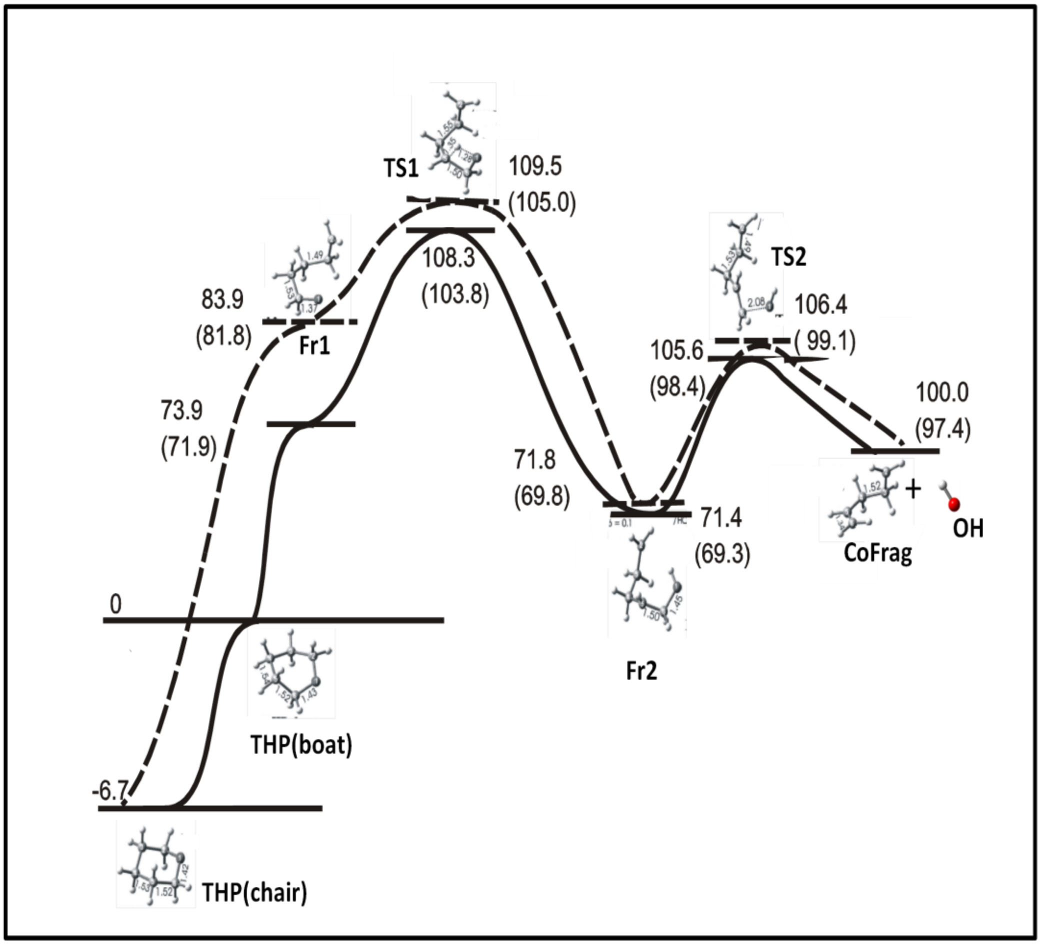

Fig. 4.7: Potential energy curves for the OH channel from the electronic ground state of THP with geometry optimization at B3LYP/6-311+G(d,p) level, and energies of the optimized geometries at MP2/6-311+G(d,p) level of theory. For the last step, both the geometries and the energies were calculated at MP2/6-31+G(d) level of theory. All the values of energy are in kcal/mol unit.

the C—OH bond cleavage, OH emerges out perpendicular (∠ HO1C6=101.7°) to the C atom, attached to the dissociating bond, and with dihedral angle 49.2° with respect to the plane containing the next two C atoms attached to it. The C-OH bond (2.08 Å) is almost completely broken. The isolated C_5H_9 (other fragment) retains its structure in the TS, as in case of THF. Identification of the TS structure for the C—OH bond cleavage implies the existence of an exit barrier. Thus, our theoretical calculations supports the experimental results, which suggests the presence of an exit barrier in the C-OH bond cleavage, based on a considerable portion of the available energy being partitioned to the translational degrees of freedom of the products.

4.3.2.3 The OH Generating Channel

Although spectroscopy of THP is well studied, its dissociation dynamics is not well understood. Its pulse radiolysis in aqueous solution[92] and γ radiolysis[93] in frozen aqueous solution have been reported. Scala *et al.*[94] studied its photodissociation at 147 nm, and suggested a two-step mechanism for dissociation [reaction (4.12)],

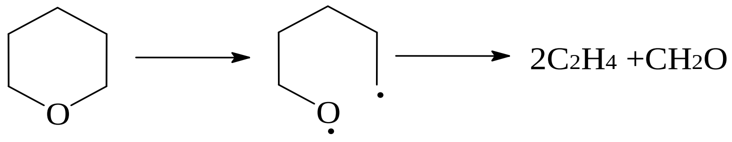

(4.12)

The upper state achieved by THP by the weak absorption at 193 nm, due to the *n*→3*s* Rydberg transition, is nonplanar, with chair conformation and very high barrier for inversion[89]. After excitation at 193 nm, THP undergoes a series of reactions to generate OH from its ground electronic state, like as in the case of THF discussed earlier [86]. Even furan, on excitation at 193 nm to a Rydberg level, was proposed to undergo dissociation, generating $CO+C_3H_4$ and C_2H_2 $+H_2C_2O$, from the ground electronic state, after fast internal conversion had taken place[95]. However, the radical dissociation channel, generating $HCO+C_3H_3$, was proposed to occur at the Rydberg excited state. Similar to furan, THP, after excitation at 193 nm, can dissociate directly from the excited state, and can compete with internal conversion to the ground state. Both these paths involving the ground and the excited states of THP may generate OH, but it is not possible to establish unequivocally from the present study whether OH is also formed from the excited state. Also, in an earlier vacuum-uv photoexcitation study of THP at 147 nm, the dissociation mechanism, as reported by Scala *et al.*[94], consists of an initial bond breaking to form $\cdot O–(CH_2)_4–CH_2\cdot$ biradical. Subsequently, this biradical was proposed to undergo cleavages, generating two C_2H_4 and one CH_2O molecules (reaction 4.12). However, the electronic state from which THP dissociates, after excitation at 147 nm was not investigated, and the OH radical was not monitored, although it was also expected to be a product at 147 nm. From the extensive similarity between the dissociation mechanisms of THF and THP, it is expected that all cyclic ethers, on excitation at 193 nm, may undergo dissociation, leading to OH formation from the ground, as well as, probably, from the excited states.

4.3.3 Morpholine

4.3.3.1 Nature of the Dissociative State

In the case of morpholine, the nature of the excited state achieved by absorption of one 193 nm photon could not be ascertained due to lack of spectroscopic data in the literature. But, our experimental and theoretical studies suggest that, in this case also, the molecule is initially excited to a higher electronic state by absorption of a photon of 193 nm, and, prior to the dissociation, it crosses over to the ground electronic state by a non-radiative pathway. All the dissociation processes, like in cyclic ethers THF and THP, proceed from the energetic ground state molecule, having excess energy stored in its internal modes. This opens up energy expensive channels, producing unusual fragmentation products, such as OH.

4.3.3.2 *Ab Initio* Molecular Orbital Calculations

Theoretical calculations for the formation of OH radical from morpholine were carried out, using Gaussian 92 package[2]. All the geometries were optimized at B3LYP level of theory, using 6-311+G(d,p) basis sets, whereas potential energy of each molecular species was calculated at MP4(SDQ) and B3LYP level of theories, using the same basis sets. In Fig. 4.8, the potential energy surface is schematically represented by indicating energy of each species. The energy values outside parantheses were obtained, using MP4(SDQ)/6-311+G(d,p)level of theory, and that within the parantheses were obtained at B3LYP/6-311+gG(d,p) level.

Both the boat and the chair conformations of the morpholine molecule were found to be stable, with the latter being more stable by 7.6 (7.4) kcal/mol, as expected for cyclic saturated compounds. This calculated structure of morpholine molecule is in good agreement with that measured by FT-microwave spectroscopy[74], which shows the ground state structure to be the chair one, with the N-atom in the equatorial position. Theoretical studies indicate that the first step of dissociation of morpholine can be cleavage of either a C—O bond or a C—N bond. The cleavage of the C—O bond leads to formation of a triplet biradical, represented as Rad1 in Fig.4.9. This biradical undergoes intramolecular rearrangement, involving the transfer of an H atom from a C atom to the O atom,

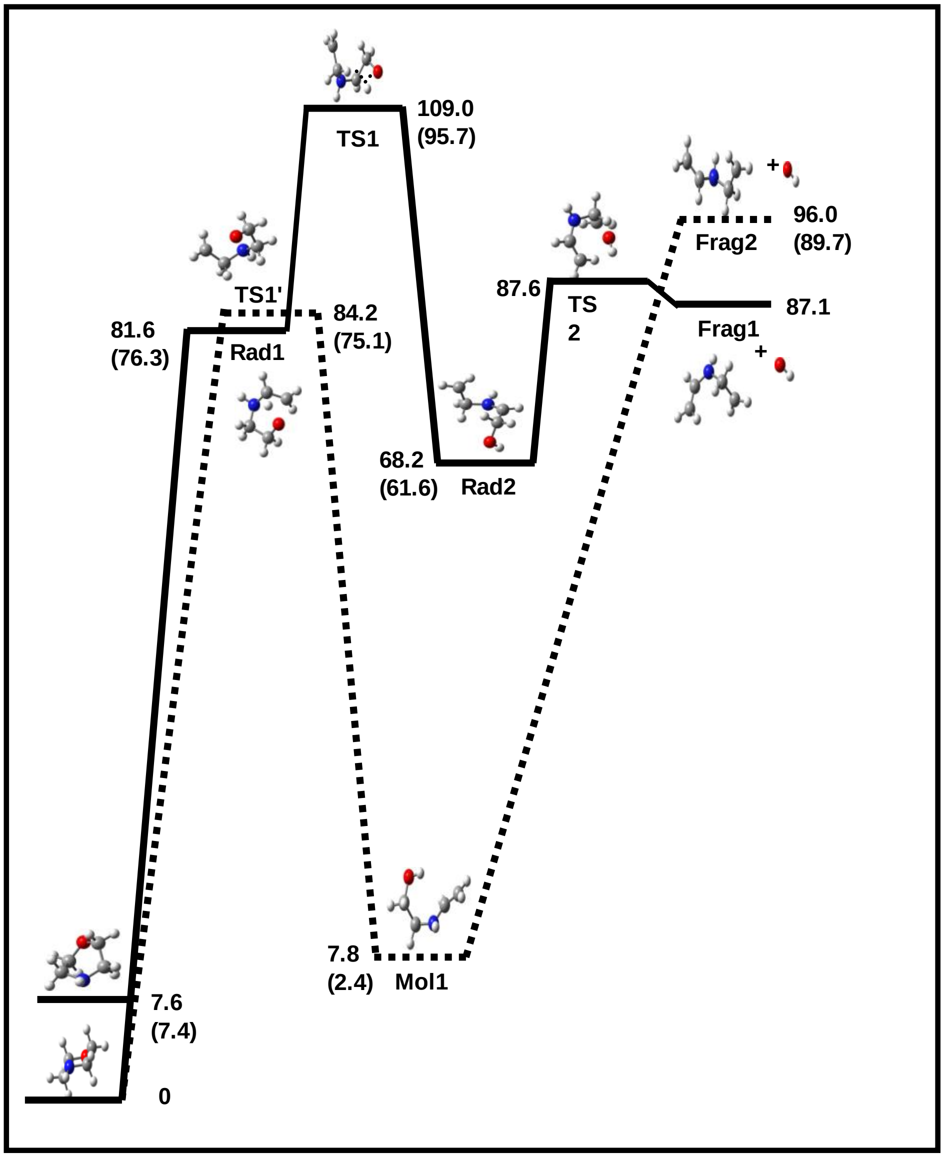

Fig. 4.8: Potential energy curves of the different OH formation channels from the ground electronic state of morpholine. The geometry is optimized at B3LYP/6-311+G(d,p) level of theory and the energies are calculated at MP4(SDQ)and B3LYP level of theory using the same basis sets. The last step of the triplet channel is optimized at HF/6-311+G(d,p) level. All energies are given in kcal/mol unit. The solid curve represents the triplet biradical pathway and the dashed curve represents the singlet biradical pathway.

followed by C—O bond scission. All the intermediates and the products involved in this pathway are triplets; hence, this pathway is referred as the triplet pathway, and represented by the solid lines in Fig.4.8. In an alternative pathway, the C—O bond breaking and H migration from a C atom to the O atom are concerted. This step generates a stable molecule, which is an open-chain alcoholic isomer of morpholine, marked as Mol1 in Fig.4.8. This stable molecule is in singlet spin state, and hence, this pathway is referred as the singlet pathway, in our discussions. Energised Mol1 can lead to OH formation by a direct scission of the C—OH bond. This singlet pathway is shown by the broken lines in the Fig.4.9. The C—N bond is weaker than the C—O bond by about 4kcal/mol, but, to generate OH radical, the C—O bond has to be broken only after C—N bond is cleaved. Hence, the energy requirement of the OH pathway, which starts with C—N bond scission to the overall OH formation, must be negligible. The major channels are those which start with C—O bond cleavage.

(I) Triplet biradical pathway

The first step in the formation of OH involves a C—O bond cleavage, leading to a triplet biradical that is depicted as Rad1 in Fig. 4.8. This triplet radical lies at an energy level of 81.6(76.3) kcal/mol higher than the chair conformation of the ground state morpholine molecule. Theoretical calculations suggest that, in the next step, a H atom attached to the β carbon (in reference to the unruptured morpholine ring) undergoes an 1,3 shift to the O atom. This lead to the formation of another triplet biradical (Rad2). This step involves a four-membered transition state (TS1), which is almost planar, with the dihedral angle OCCH of 0.5°, and lies at about 27.4 kcal/mol above Rad1. The resultant triplet biradical (Rad2), having an OH group, lies at 68.2(61.6) kcal/mol with respect to the parent molecule. Thus, Rad2 is considerably more stable (by 13-15 kcal/mol) than Rad1, and the migration of the H atom is a thermodynamically favourable step. In the subsequent step, the C—OH bond breaks, forming the OH radical and another photofragment (Frag1). At MP4(SDQ) or B3LYP level, no TS could be identified for this step, but at a lower level of theory, i.e., HF/6-311+G(d,p), a transition state (TS2), with a very small exit barrier of 0.5 kcal/mol, could be located. The combined potential energy of the products, i.e., OH radical and the cofragment (Frag 1), lies at 87.1 kcal/mol above that of the morpholine molecule. This reaction channel, leading to OH generation by photolysis of morpholine molecule by absorption at 193 nm, is qualitatively similar to OH generation channel of THF and THP, as discussed in the sections 4.3.1. and 4.3.2.

(II) Singlet pathway

Unlike THF and THP, theoretical calculations revealed the possibility of another, entirely different reaction channel that may lead to formation of OH radical by photolysis of morpholine molecule. In this pathway, the first step is a concerted process, involving a C—O bond cleavage, with a simultaneous intramolecular migration of H atom to the O atom (1,5 shift), from the C atom at δ position with respect to the dissociating C—O bond, forming a stable alcohol molecule (Mol 1 in Fig. 4.8), with singlet spin multiplicity. Thus, we coin this pathway as the “singlet pathway”. This concerted step involves a six-membered transition state TS1', as shown in Fig. 4.8, with an activation barrier of 84.2(75.1) kcal/mol, in which the dihedral angle OHCC is 2.85°. The energy of the stable molecule (Mol1 in Fig. 4.8), which already contains an OH group, has been calculated as

7.8(2.4) kcal/mol with respect to the parent molecule. In the next step, the C—OH bond breaks to free the OH radical, and co-fragment (Frag2 in Fig. 4.8). Our theoretical studies suggest that this last step is a simple C—O bond cleavage, without any transition state. The combined energy of the photofragments lies 96.0(89.7) kcal/mol above that of the ground state chair conformation of the parent molecule.

4.3.3.3 The OH Generating Channel

By comparing the results obtained from the experimental and theoretical studies, a plausible mechanism for the unique channel of OH formation in photodissociation of morpholine molecule at 193 nm could be suggested. The possibility is that the initially excited higher electronic state, formed by absorption of a photon of 193 nm crosses over to the ground electronic state by a non-radiative pathway, before any dissociation takes place. Then, the dissociation processes proceed from the energetic ground state molecule, having excess energy stored in its internal modes. This explains the formation of unusual fragmentation products, such as OH. One possible pathway for OH formation is fragmentation of the energy-rich ground state molecule by cleavage of a C–O bond, to initiate a reaction channel that proceeds through the involvement of intermediates in triplet spin state, eventually releasing the OH radical. This pathway was discussed in detail as the Triplet pathway in the previous paragraphs. The other possible OH formation mechanism can be via a stable alcohol molecule, formed by a concerted step that involves a C–O bond cleavage and simultaneous migration of H atom from the C atom to the O atom. OH radical is produced by dissociation of this energized stable molecule. The pathway is designated as the Singlet pathway, as described in previous paragraphs. The experimental results show that a large fraction of the available energy (~35%) is partitioned to the relative kinetic energy of the fragments, which suggests the presence of a considerable exit barrier in the reaction channel. In our theoretical calculations, a small energy barrier (0.5 kcal/mol) could be located in the Triplet pathway, but none in the Singlet pathway. Since the reaction channels involve multiple steps, some of which require high-activation energy, the effect of those barriers are manifested in the overall energy distribution of the reaction, even though the last product-forming step itself might not have a high-activation barrier. Though the contribution of the two different reaction channels in the actual OH production could not be ascertained from our studies, the fact that $^2\Pi_{1/2}$ spin state of OH radical is preferentially populated in the case of morpholine (section 4.1.3) indicates that the singlet channel is more dominant, assuming the reaction pathway to be adiabatic.

4.4 Summary

It is seen that all the three cyclic ethers, namely, THF, THP and Morpholine, produce OH radical when photolyzed by 193 nm laser. The dissociation, most likely takes place from the ground state of the molecules, though no confirmatory conclusion can actually be drawn, without further experimental support, like anisotropy studies, etc. All these compounds are rigid ring type, with no OH functional group present in their structure. Hence, OH must be formed as a secondary product, after some internal rearrangement during the photodissociation. All the dissociation processes most probably proceed from the energetic ground state molecule, having excess energy stored in its internal modes. This opens up energy expensive channels, producing unusual fragmentation products, such as OH. In most of the cases (THF, THP and triplet channel in morpholine), theoretical studies reveal that, the first step of dissociation is the scission of the ring through C—O bond cleavage, which produces a biradical primary product. This step takes place without any barrier. This biradical, then, undergoes internal rearrangement, involving migration of an H-atom from a C-atom in the chain to the O-atom. This step, which involves an energy barrier and a transition state, produces another biradical, which has one OH group at an end. In the next step, OH radical is separated from the rest of the photofragment through another C—O bond cleavage. The TS structure for the last C—OH bond cleavage, with the bond completely cleaved and the two fragments almost acquiring structures of isolated product molecules, suggests that the reaction has late barrier. This barrier controls the dissociation dynamics significantly, with about 35-45% of the available energy going into the relative translation of the products. The hybrid model of energy partitioning predicts a higher barrier for this step in case of THF and THP, about 16 kcal/ mol for THF, and 40 kcal/ mol for THP, though *ab initio* calculation reveals very small barrier in both the cases, about 5 kcal/ mol. In the case of morpholine, a very small exit barrier (0.5 kcal/ mol) is seen in the last step. The dynamic studies reveal that in all the cases, a major part of the available energy goes to the relative translational mode of the photofragments, which, again, indicates the presence of an exit barrier in the potential energy surface. Much importance should, however, not be attached to the size of the actual exit barrier, since the effect of the earlier, bigger energy barrier (about 35 kcal/ mol) of the rearrangement step in this multiple-step reaction channel is expected to be manifested in the final results. In the case of morpholine, there is an alternative reaction channel (singlet channel), where the reaction proceeds through a concerted rearrangement- C—O bond cleavage step, which produces another stable, alcoholic isotope of morpholine, which later dissociates, producing the OH radical. In this channel, in the first step, there is an energy barrier, but none in the second step. The possibility of an alternative reaction channel for OH generation in the case of morpholine, which could not be established in the case of THF, or THP is probably the effect of having another heteroatom, i.e., the N-atom in the ring structure. Overall, these studied could successfully establish a pattern for formation of OH radical by photolysing at 193 nm, for different types of heterocycles.

Chapter 5: Photodissociation Dynamics of Epoxides

Epoxides are essentially cyclic ethers, with three-membered rings that contain an O-atom. After studying photodisociation dynamics of cycloethers, with 5-6 membered O-containing rings, epoxides was chosen to understand how the higher amount of strain energy present in the smaller, 3-membered rings influences the overall outcome of their photodissociation, especially the distribution of the energy among the products. Epoxide molecules with different kinds of substituents, like aromatic ring, e.g., styrene oxide, saturated aliphatic chain, e.g., ethelyne oxide and propylene oxide, and unsaturated aliphatic chain, e.g., butadiene monoxide, were studied to understand the effect of the substituent group on the photon induced ring opening mechanism of the highly strained epoxide molecules. The difference results for these different epoxide molecules were explained on the basis of information obtained theoretically and experimentally.

Aromatic epoxides comprise an important class of organic molecules, with significant applications in synthetic processes. Styrene oxide (SO), the simplest unsymmetrical aromatic oxide, with two stereoisomers R(+)- and S(-), plays an important role in many asymmetric synthetic processes, as well as in inducing mutations and cancer in humans[96]. Optically active SO and its derivatives serve as chiral building blocks, and are used extensively in the synthesis of pharmaceutical products[97]. These are employed as key intermediates, to synthesize complex chiral organic compounds[98]. Aromatic epoxides are causative factors for mutagenic and carcinogenic activity of polycyclic arenes. SO has been employed as a model carcinogen, and its role in causing damage to DNA has been studied, using fluorescence-based methods[99]. Importance of SO has encouraged several recent investigations on its formation and the reactivity, which are mainly associated with the ring opening process. Oxidation of styrene with oxygen in radio-frequency (rf) plasma takes place predominantly at the olefinic double bond, producing SO[100]. Facile synthesis of optically active derivatives of SO is reported by asymmetric reduction[101]. IR spectroscopic measurements on SO have been carried out in various solutions, to understand interaction of the epoxy group with the solvent system[102].

There is not much work reported on photochemistry of Butadiene monoxide (BMO). The mechanism of ring cleavage of BMO, as well as that of SO, caused by nucleophillic attack, has been studied for a very long time for conjugative effect[103]. Biologists studied BMO extensively because of its carcinogenicity and mutagenicity[104] towards human and other animals. This molecule is generated inside the body as a reactive metabolite of butadiene gas in the bone marrow[105]. Once generated, it binds with DNA and hemoglobin, and can lead to leukemia or lymphoma[106]. Furthermore, it can undergo *in vivo* tautomerization to another carcinogen, crotonaldehyde. Tautomerization of BMO and similar terminal epoxides to aldehydes has applications in chemical synthesis. Catalytic methods for converting epoxides to aldehydes have been reported[107] and patented[108].

5.1 Experimental Results

5.1.1 Detection of OH Radicals and Quantum Yield

As in the case of the cyclic ethers (Chapter 4), ethylene oxide (EO), propylene oxide (PO), butadiene monoxide (BMO) and styrene oxide (SO), were irradiated with 193 nm laser. OH radical was detected as a product of photolysis of SO and BMO at 193 nm by its characteristic LIF spectrum, but in case of the other two, OH radical could not be obtained. There could be various cause of for this difference in photochemical behavior, like, difference in the absorption cross-section (σ) at 193 nm, or some peculiarity in the mecahnism of photodissociation of these compounds. The experimental studies of photodissociation dynamics of SO and BMO were taken up, to resolve these queries and to get a better understanding of the unusual OH generation channel by photodissociation of smaller, heterocyclic compounds, as these compounds also do not have any OH radical inherent in their structure. The reaction pathway is expected to follow a multistep mechanism involving intramolecular rearrangement.

This was the first time when formation of OH radical by photiodissociation of SO[109] and BMO[110] was detected and reported in literature. Fig. 5.1 shows partial LIF excitation spectra of the (0,0) band of the $A^2\Sigma$– $X^2\Pi$ system of OH generated from the respective compounds. In assigning the line positions of OH, we used the standard notation **Δ**J (N) for the transition, and denote transitions associated with the spin–orbit states $X^2\Pi_{3/2}$ and $X^2\Pi_{1/2}$, with subscripts ‘1’ and ‘2’, respectively, as discussed in section 1.8. However, during irradiation of neat SO, even at 20 mTorr of steady pressure,

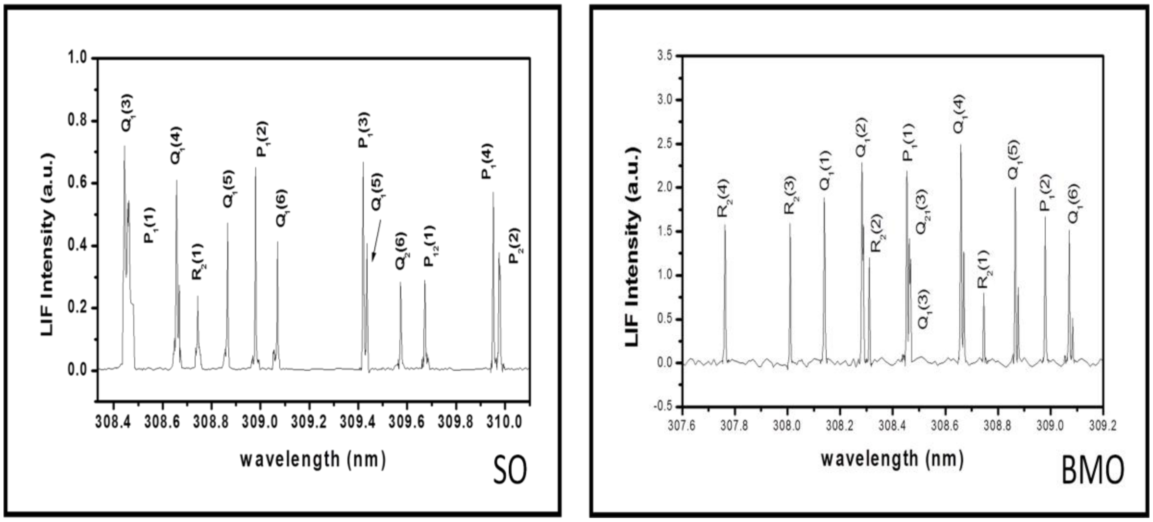

Fig. 5.1: LIF Excitation spectra of the (0,0) band of $A^2\Sigma \leftarrow X^2\Pi$ transition for SO and BMO, respectively. Rotational lines are marked in the figure.

windows for the photolysis laser developed rapidly a thick coating of some photoproducts, which drastically attenuated the laser energy and, therefore, it was not possible to collect data quantitatively. The studies were carried on the mixture of SO (97% purity, Aldrich) in Ar (99% purity, BOC, India, used as supplied) at a relatively higher pressure (~3.0 Torr), with a time delay of ~50 ns, and hence collisional relaxation of OH could not be avoided. Thus, the measured rotational state distribution of OH is partially relaxed.

To understand the factors responsible for not observing OH from EO and PO, on excitation at 193 nm, the absorption cross-sections of EO, PO, BMO and SO were estimated by measuring attenuation of 193 nm laser upon passing through vapour of these compounds. The detailed description of the method is discussed in section 2.3. Typical plots of ln (I_0/I_t), where I_0 and I_t are, respectively, the initial and the transmitted

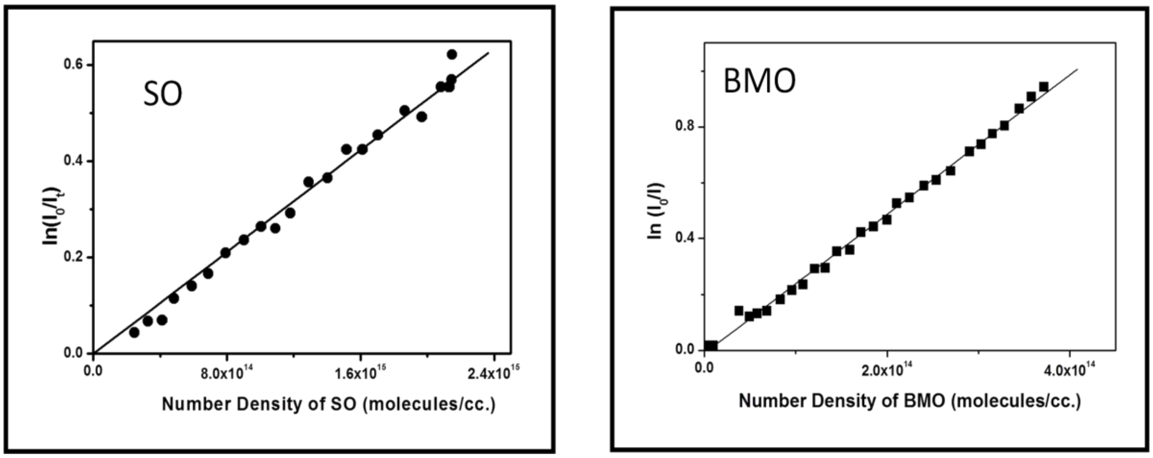

Fig. 5.2: A plot of $\ln(I_0/I)$ vs. the number density of SO and BMO, respectively. Absorption cross-section can be calculated from the slope of the straight line.

intensities at 193 nm, as a function of number density of SO/BMO are depicted in Fig. 5.2. from the slopes of the straight lines, absorption cross-sections of SO, BMO, EO and PO at 193 nm were estimated to be 1.13×10^{-19}, 5.4×10^{-18} , 1.5×10^{-20} and 4.4×10^{-21} cm^2 molecule $^{-1}$, respectively.

These results showed that absorption cross-sections of EO and PO are lower than that of SO and BMO by one or two orders of magnitude, which can be responsible for OH not being detected on excitation of EO and PO at 193 nm. We measured the quantum yield of OH formation in SO and BMO, by comparing its LIF intensity in them with that in acetic acid, after excitation at 193 nm, under identical experimental conditions. Taking absorption cross-section of acetic acid at 193 nm, and the quantum yield for OH formation, as 1.1×10^{-19} cm^2 molecule^{-1} and 0.8[5], respectively, we estimated quantum yield of OH in the case of SO and BMO to be ~0.02 and 0.007 respectively. Thus, the low absorption cross-sections of EO and PO at 193 nm could be one reason responsible for non-observation of OH from these molecules.

5.1.2 Stable Product Analysis

Known amount of neat Butadiene Monoxide (~5 Torr pressure, 98% purity, Aldrich), or Styrene Oxide (~500 mTorr pressure, 97% purity, Aldrich), as the case may be, after degassing by several freeze-pump-thaw cycles, were filled in a stainless steel cell, fitted with a pair of CaF_2 windows. After photolysing by ~3000 pulses of 193 nm laser, the reaction mixture was analysed, using GC (Chemito, model 8610), equipped with a capillary column (25 m x 0.22 mm, make: SGE, model: HT8) and a flame ionisation detector. Temperature of the column was maintained at 100°C, with N_2 as a carrier gas. In the case of SO, two stable products, phenylacetaldehyde (PA) and acetophenone (AP), were detected, the former having higher abundance than the latter (Fig. 5.3). An attempt to detect IR fluorescence from these products by an InSb detector, to determine whether they are formed in vibrationally excited state, did not give any result, probably because of the low yield. The stable products formed in the photolysis of BMO at 193 nm, as detected by Gas-Chromatography (Fig. 5.3) are, H_2, CH_4, CO, methylvinylketone (MVK) and crotonaldehyde (CA). The relative abundance of CA was found to be considerably higher than that of MVK. One additional peak was observed near CA peak, which we suspect to be due to vinylacetaldehyde (VAA), but could not confirm. The samples, phenylacetaldehyde (>90%), acetophenone (99%), methyl vinyl ketone (90% purity, Aldrich) and crotonaldehyde (98% purity, Aldrich) were used as standards for gas-chromatography, after degassing.

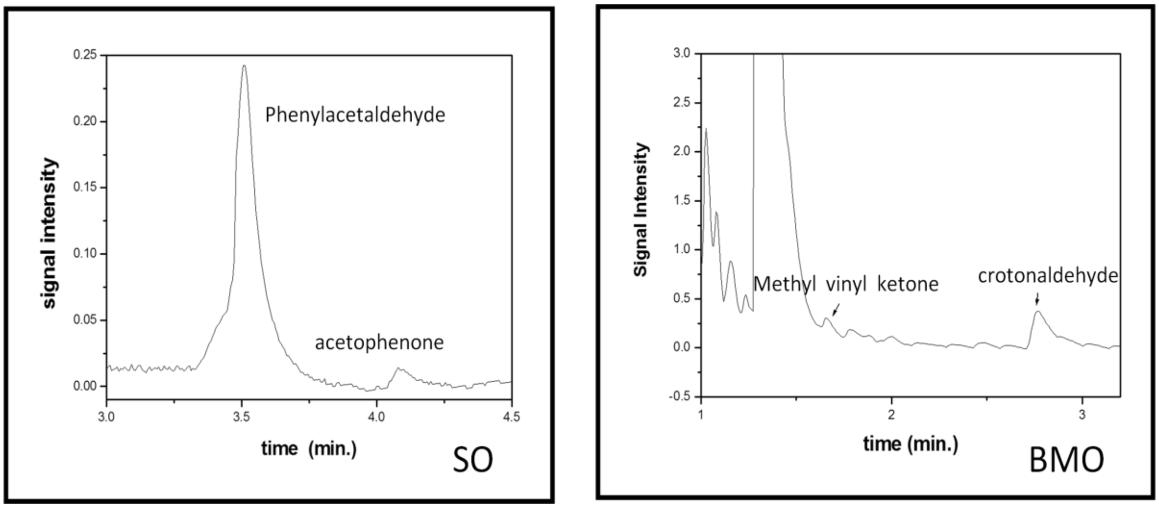

Fig. 5.3: Gas-chroamatograms showing the characteristic peaks of ketonic stable products obtained by photolysis of SO and BMO by 193 nm laser.

To make sure that OH is generated from SO itself, and not from any other stable product, such as PA and AP, we photolyzed these compounds at 193 nm, under similar experimental conditions, and searched carefully for OH, but all of them gave negative result. This establishes unambiguously that OH is formed only from SO, on excitation at 193 nm. For similar reasons, in the case of BMO, the stable products, CA and MVK were irradiated at 193 nm under similar experimental conditions, but again, no OH radical was detected.

5.1.3 Dynamics of OH Radical Channel

As mentioned earlier, in section 5.1.1, SO was diluted with argon gas, and taken with higher pressure, for all the measurements, to avoid the deposit formation on the window by irradiation of the neat sample. The rotational states of OH formed in this case, was partially relaxed and hence no dynamics information could be obtained from the spectrum.

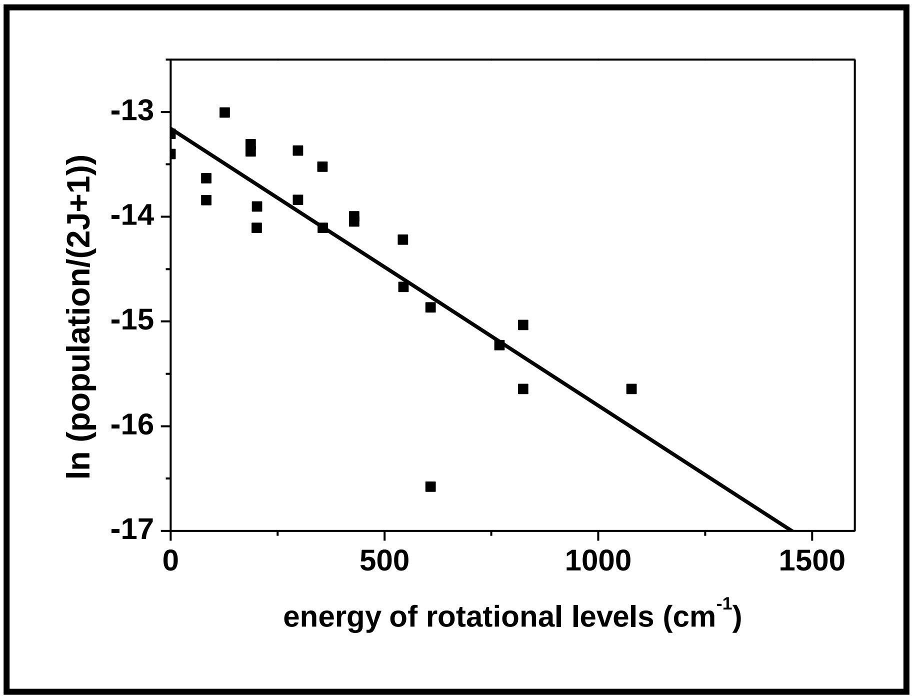

Fig. 5.4: Boltzmann plot of the rotational state population of OH (v=0), generated in dissociation of BMO at 193 nm.

The degassed BMO sample, taken at 50 mTorr pressure, was photolysed by 193 nm laser, and the fluorescence of the A-X system was measured, after exciting the same system with frequency-doubled tunable dye laser. The data were collected at and 50 ns time delay between the photolysis and probe laser beams. Both the (0,0) and (1,1) vibronic transitions were studied. Though rotationally resolved LIF lines could be easily measured for the first transition, there was no signal for the second transition. This indicates that the OH radical is generated mainly in the ground vibrational level, and the yields of other higher vibrational levels are negligible. Several rotational lines were measured for the (0,0) transition, (shown in Fig. 5.1), to obtain dynamic information about the OH radical formed. The translational and rotational temperature were determined from the Boltzmann distribution of the intensity (Fig. 5.4) and the Doppler

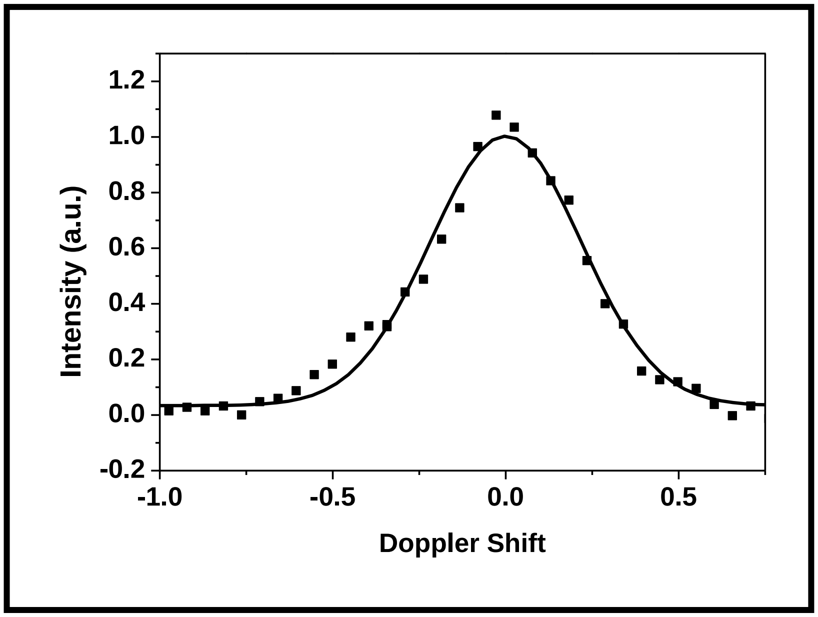

Fig. 5.5: Doppler broadened $P_1(2)$ line of the (0,0) band of the $(A^2\Sigma, v' = 0) \leftarrow (X^2\Pi, v'' = 0)$ system of OH radical, produced by photodissociation of BMO.

profile (Fig. 5.5) of these rotational lines, using the methods described in the section 2.4. The measured value of rotational temperature of the OH fragment is 456±70 K, which corresponds to the rotational energy of 0.9±0.1 kcal mol^{-1}, and the translational energy is determined to be 17.9±2.2 kcal mol^{-1}.

When the population distribution in the two Λ- doublet states and spin orbit states are plotted against rotational number (N) in the case of BMO, in both cases, it is found that the two levels are statistically populated upto N=6 (Fig.5.6).

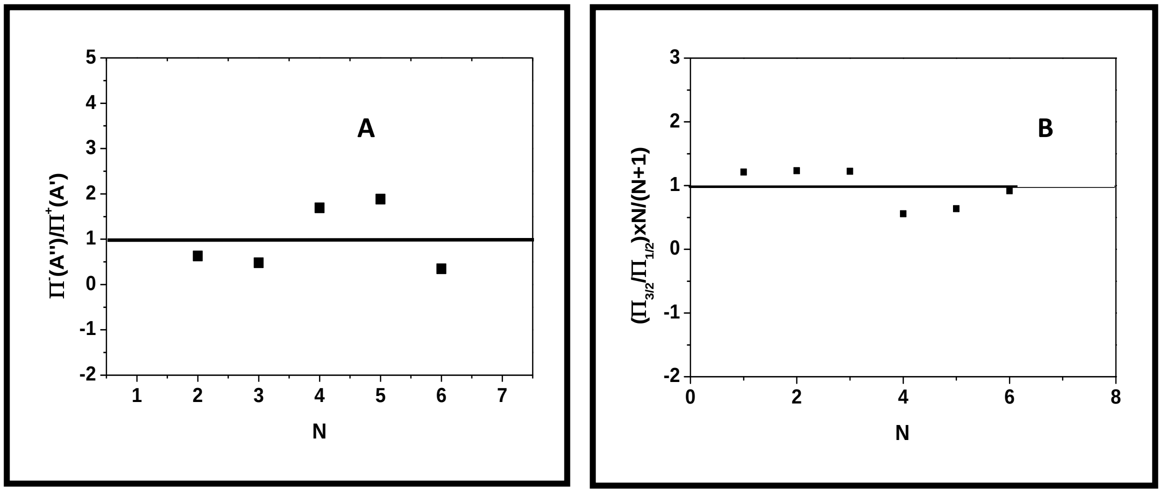

Fig. 5.6: The figures (A) and (B), respectively, depict the spin orbit and Λ-doublet state population distribution of OH (v=0) generated by dissociation of BMO at 193 nm.

5.1.4 Formation Time of OH from BMO

We measured the formation time of the OH radical, formed by photodissociation of BMO at 193 nm, by selecting excitation wavelength for a particular ro-vibrational line, and scanning the time delay between the photolysis and the probe lasers. The LIF signal at λ_{max} of the different rotational lines was measured, to investigate N dependence of the formation kinetics of OH radical. A few plots of the LIF intensity against time delay, for different rotational lines, are presented in Fig. 5.7. Each delay scan has two components, the fast one, with the rise time of ~100 ns is almost independent of the pressure of BMO and the rotational quantum number N. This gives the formation time of OH in a particular N to be ~100 ns. The second slow component, which is strongly dependent on both N and pressures of BMO, is due to the formation of OH in a particular N from higher levels by rotational relaxation. With decreasing N, the rise time becomes slower because of increase in the contributions from the relaxation of OH in higher rotational levels. The rise time of ~800 ns, observed for N=7, has less contributions from the relaxation of higher OH(N). Thus, the relaxation of higher levels to lower levels delays the observed formation of OH from BMO.

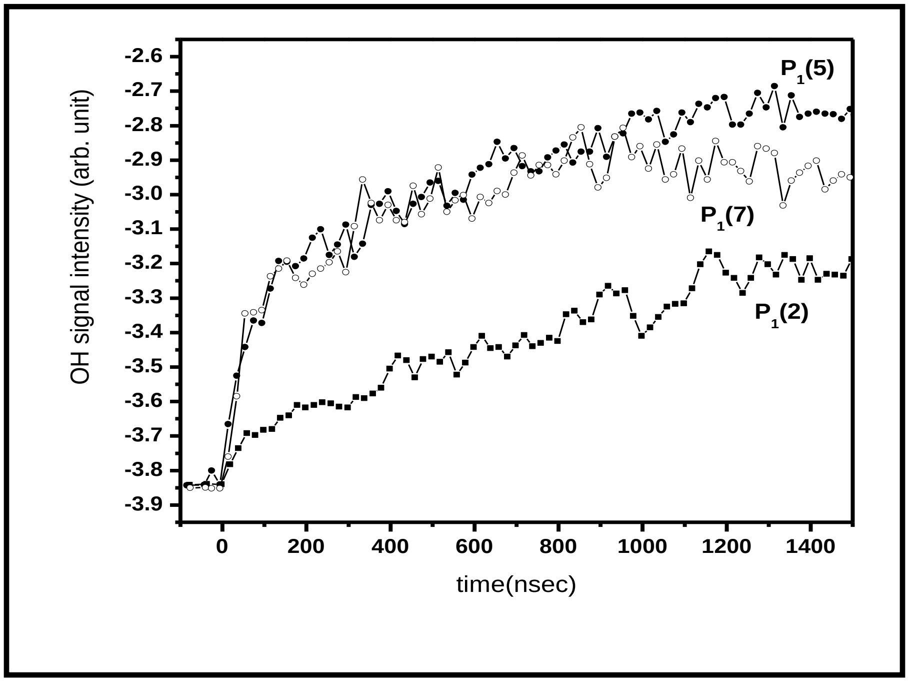

Fig. 5.7: Formation of OH in different rotational levels (N=2,5 and 7), based on the measurement of time evolution of (0,0) band of p1(N) lines. The figure shows faster formation of OH with increased N.

5.2 Theoretical Studies and Discussions

Unlike in EO and PO, in SO and BMO, on excitation at 193 nm, OH was observed. But, these epoxides, like the cyclic ethers discussed in chapter 4, are devoid of any OH group. Hence, to generate OH, it should undergo the epoxy ring-opening, followed by some molecular re-arrangements, leading to a species which contains OH group. The proposed mechanism is based on detection of these stable products from the biradicals, following hydrogen migration.

It has long been well-known that a nucleophile may attack at both primary α and secondary β carbon atoms of a nonsymmetrical terminal epoxide ring, cleaving it, to produce two different reaction channels[103]. The orientation of the ring opening, and, hence, the relative yield of the products from these two channels depend on three main effects of the substituent groups present in the epoxide molecule, steric, polar (inductive), and conjugative. The steric effects promote attack of neucleophiles at the less substituted carbon atom, i.e., the β carbon atom, whereas the other two effects can go either way. The reactions of butadiene monoxide as well as styrene oxide with different nucleophiles have been extensively studied and tabulated by Isaacs and Parker[103]. They observed that, for smaller nucleophiles, with no steric effect, the attack preferably takes place on the α carbon atom, due to conjugative effect of the phenyl or the ethylenic group. However, for bulkier nucleophiles, the relative abundance of the two products is reversed due to steric effect. Photolysis of SO in solution[111-113], using conventional lamps, proceeds with initial cleavage of the HC_α—O bond of the ring, producing a biradical. These studies, along with photolysis of 1,2-dihydronaphthalene[114], indene[115] and trans-β-methylstyrene[116] oxides, suggest that these epoxides undergo cleavage of the benzylic HC_α—O bond, followed by re-arrangement, to generate stable products, aldehydes, or ketones. Similarly, photoexcitation of SO and BMO at 193 nm can lead to dissociation of either, or both, of the HC_{α}—O and H_2C_{β}—O bonds (designated α and β with respect to the phenyl group or the ethylenic double bond as the case may be). Detection of the different stable products in the photolysis of both SO and BMO by 193 nm suggests that more than one major reaction channels are operating in the photolysis of these epoxides. The first step for both these channels is, of course, opening of the epoxide ring.

5.2.1 Styrene Oxide

5.2.1.1 Nature of Dissociative State

We carried out the excited electronic state calculations og SO at the configuration interaction with single electronic excitation (CIS) level. Time dependent density functional theory (TD-DFT), with 6-311+G(d,p) basis sets, was employed to calculate vertical excitation energies, and understand the nature of the excitation at 193 nm. MO's were analyzed to assign each electronic transition. Theoretical calculations for the excited state predicts that the strongest transition to be $S_0 \rightarrow S_2$ (oscillator strength = 0.112), which is predominantly HOMO→LUMO π–π* transition of the benzene ring, with some contribution from the n–π* transition, having vertical excitation energy (VE) of 5.71 eV. Other strong transitions, in the decreasing order, are $S_0 \rightarrow S_5$ (n/π–π*, oscillator strength = 0.089, VE = 6.37 eV) and $S_0 \rightarrow S_4$ (mainly n_O–π* transition, oscillator strength = 0.016, VE = 6.22 eV). This implies that at 193 nm, both π and n electrons of SO are excited to π* orbitals.

5.2.1.2 Ab initio Molecular Orbital Calculations: The Photodissociation Channels

We performed ab initio molecular orbital (MO) calculations, using GAUSSIAN 92[2] program, to investigate the potential energy surface for the OH channel from the ground electronic state of SO. The geometries of the ground electronic state of SO, the various possible products and the transition state structures were subjected to optimization with the B3LYP theory, using 6-311+G(d,p) basis sets. The harmonic vibrational frequencies and the force constants were calculated, to ensure the stationary points on the potential energy surfaces to be true saddle points. All the transition state (TS) structures have only one imaginary frequency and one negative eigenvalue of the force constant matrix. Electronic energies corresponding to the optimized geometries were calculated at the MP2 level, with the same basis sets. With the inclusion of thermal energies, derived from vibrational frequencies, obtained at the B3LYP/6-311+G(d,p) level, reaction energies and activation barriers at 298 K were evaluated. For the radical species, the energies were also estimated at the projected MP2 (PMP2) level, to correct for severe spin contamination. All the calculated energies mentioned in this work are at PMP2/6-311+G(d,p) level.

Step 1: C—O Bond Cleavage

Either of the two C—O bonds of SO can undergo cleavage, generating biradical $C_6H_5CHCH_2O$ or $C_6H_5CHOCH_2$, on opening the ring at the α or β position, respectively, i.e., cleavage of the HC_α—O or H_2C_β—O bond. The transition state (TS) structures were calculated for better understanding of the mechanism and the energetics of the experimentally observed ring-opening channel of SO, leading to formation of OH and the stable products. The optimized structures of SO (marked as SO), biradicals (Birad) and the transition states, TS1(1) and TS1(2), for the proposed channels, generating OH from the ground electronic state, are depicted in Fig. 5.8. This figure also shows the various elementary steps leading to formation of OH, and the stable products phenylacetaldehyde

(PA) and acetophenone (AP), which are marked as Keto (1) and Keto (2), respectively. The epoxide ring-opening, involving HCα—O and H_2C_β—O bonds, is shown in the figure as two channels, namely, Phenyl/(1) and Aceto/(2), respectively, which, apart from generating OH, lead to the final stable products, phenylacetaldehyde and acetophenone, respectively. The benzene ring of SO remained planar, or nearly planar, in all these structures.

Step 2: Formation of Enol Structures

SO was found to undergo cleavage of either the HC_α—O or H_2C_β—O bond, generating two different triplet 1,3-biradicals (shown as Birad), which undergo 1,2 H-migration via transition state, TS1, producing enols of phenylacetaldehyde and acetophenone, Enol(1) and Enol(2), respectively, shown in Fig.5.8, with activation barriers of 88.5 and 93.9 kcal mol^{-1}, respectively. The relative energetics for OH formation via enols of phenylacetaldehyde (solid curves) and acetophenone (dashed curves) are depicted in Fig. 5.9. The lower activation barrier for the enol of phenylacetaldehyde suggests preference for the phenylacetaldehyde channel over the acetophenone channel, and thus explains the observed higher yield of phenylacetaldehyde than that of acetophenone as a stable product. The activation barrier was lower mainly because of more stability of the corresponding transition state, TS1(1) in Fig. 5.8, imparted by delocalization of the unpaired electron on the C_α atom by the benzene ring. This delocalization results in different C—C bond lengths of the benzene ring in the transition state structure. The delocalization of the unpaired electron in the case of the transition state for the enol of acetophenone, TS1(2), is absent as it is located on the C_β atom, and hence the C—C bond lengths of the benzene ring in the transition state remain unaffected. The same explanation hold good for higher stability of the biradical Birad(1) than that of Birad(2).

Both the syn (the dihedral angle H—O—C—C ~ 0°) and anti (the dihedral angle H—O—C—C ~ 180°) conformers of these enols are identified, with the former, in both the cases, being lower in energy. The syn conformers of enols of phenylacetaldehyde and acetophenone are more stable than the anti ones, by 2.0 and 0.7 kcal mol^{-1}, respectively. The calculated energy difference between the two conformers is in good agreement with that in other enols[117].

Step 3: Formation of OH

The energized enols formed, after molecular re-arrangement of the biradical, produced on excitation of SO at 193 nm, could generate the observed OH radical by the C—OH bond cleavage. This OH channel could involve either simple C—OH bond cleavage, or a transition state, implying presence of an exit barrier. Since the corresponding TS could not be located, it implies that the enols of phenylacetaldehyde and acetophenone, marked as Enol(1) and Enol(2), respectively, in Figs. 5.8 and 5.9, undergo simple C—OH bond rupture, generating OH, without any exit barrier. But, the relative contributions to the OH channel from these two enols were difficult to ascertain from our studies. According to our calculations, activation barriers of 88.5 and 93.9 kcal mol^{-1}, for formation of the enols of phenylacetaldehyde and acetophenone, respectively, suggested that the former should contribute more to the OH channel, assuming that both the channels have similar frequency factor. We calculated the reaction energies for OH channel from the more stable enol conformer to be 110.2 and 100.8 kcal mol^{-1} for the

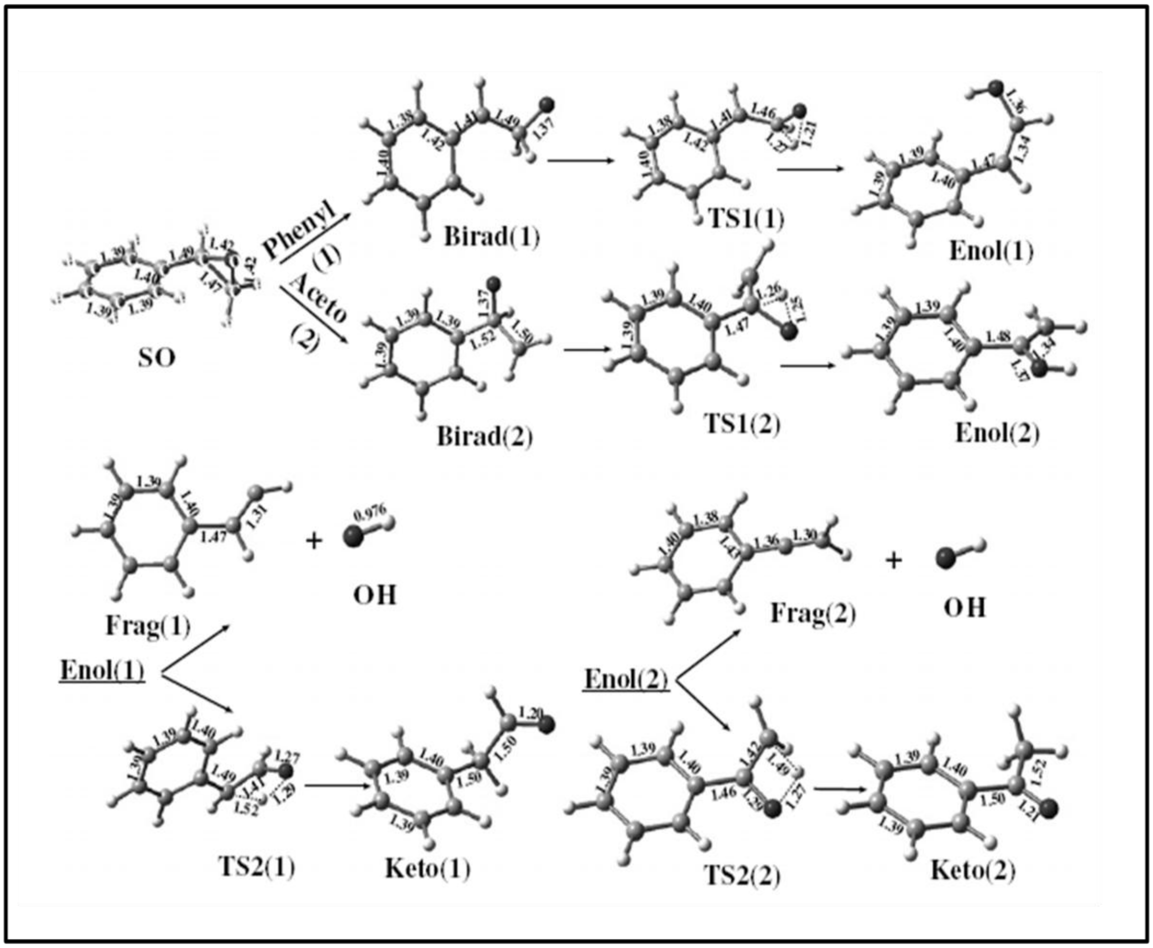

Fig. 5.8: The optimized structures of the transition states and products of the two reaction pathways for ring opening and subsequent generation of OH from the ground electronic state of SO.

phenylacetaldehyde and the acetophenone channels, respectively. This difference in reaction energies is primarily due to different stabilities of the co-fragments of OH, marked as Frag(1) and Frag(2) in Fig.5.8, for phenylacetaldehyde and acetophenone channels. Frag(2) is more stable because of delocalization of electron on the C_α atom by the benzene ring. This delocalization leads to different lengths of C—C bonds in the benzene ring of the Frag(2), which are not changed in Frag(1), as seen in the optimized structures of Frag(1) and Frag(2) in Fig.5.8.

Step 4: Formation of Keto Structures

In addition to the OH pathway, the enols produced on photo-excitation of SO, undergo tautomerization, producing keto products, phenylacetaldehyde and acetophenone, shown as Keto(1) and Keto(2), respectively, in Fig. 5.8, which were detected as stable products, using GC. These keto tautomers are expected to be more stable than their corresponding enols[118-120]. With respect to the more stable conformer of the corresponding enol, phenylacetaldehyde and acetophenone were calculated to be

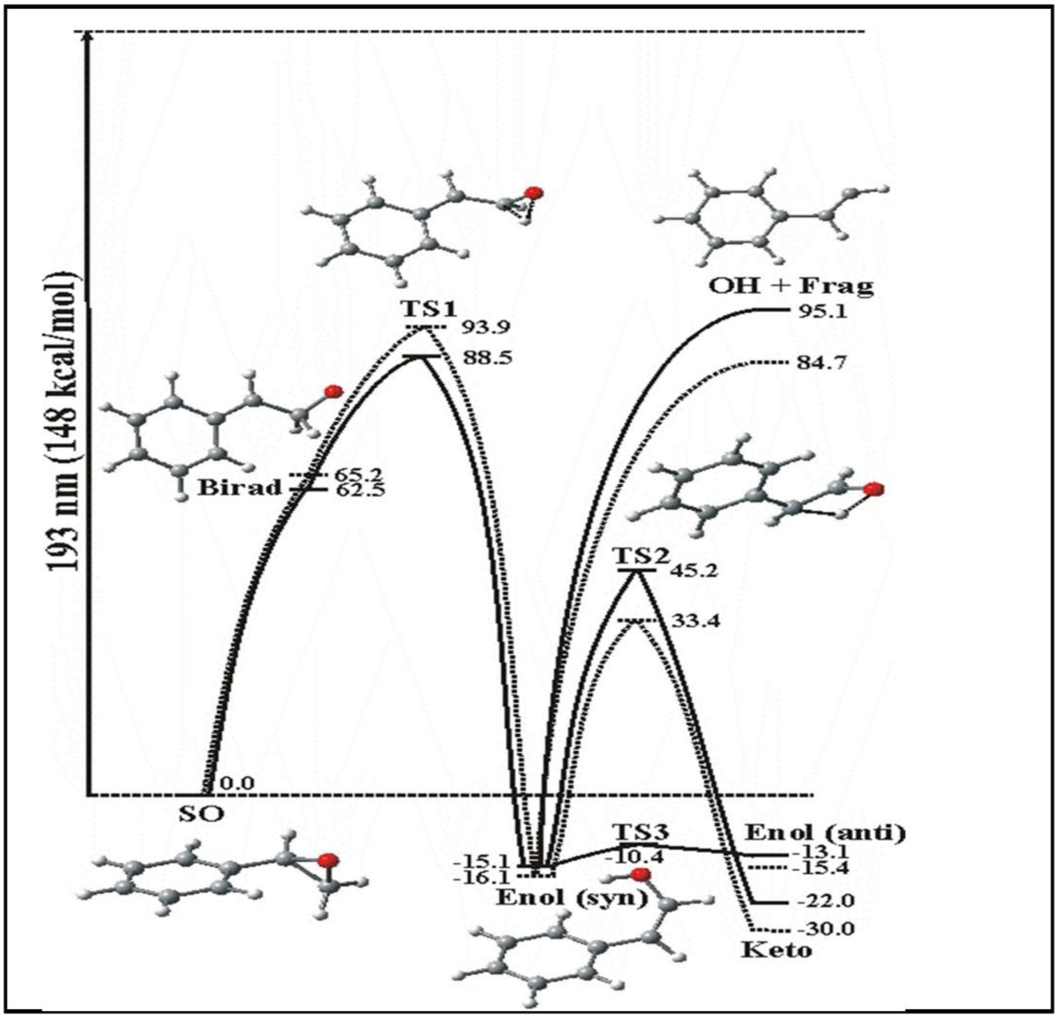

Fig. 5.9: Potential energy diagram for formation of OH from the ground electronic state of SO on excitation at 193 nm.

more stable by 6.9 and 13.9 kcal mol^{-1}, respectively, in agreement with literature values. The four-centred TS structures for tautomerization, (TS2(1) and TS2(2) in Fig. 5.8), were optimized, and their energies calculated, and the activation barriers for enol to keto conversion were estimated to be 60.3 and 49.5 kcal mol^{-1}, respectively, for phenylacetaldehyde and acetophenone. This barrier for acetophenone at the MP2(Full)/6-31G(d) level was reported to be 49.3 kcal mol^{-1} [118], which has good agreement with our calculations.

5.2.2 Butadiene Monoxide

5.2.2.1 Nature of the Dissociative State

Like SO, we carried out the excited electronic state calculations at the configuration interaction with single electronic excitation level, for BMO. Time dependent density functional theory, with 6-311+G(*d*, *p*) basis sets, was employed, to calculate vertical excitation energies, and understand the nature of the excitation at 193 nm. MOs were analyzed to assign each electronic transition. Theoretical calculations predict that BMO undergoes the $S_0 \rightarrow S_1$ transition, on excitation at 193 nm. This excitation involves mainly n_O-π^* C=C transition, with some contribution from HOMO→LUMO π-π^* transition of the ethylenic double bond, having vertical excitation energy of 6.28 eV and oscillator strength of 0.051. This implies that at 193 nm, similar to SO, both *n* and π electrons of BMO are excited to π^* orbital. A relatively slow formation time of OH (as shown in Fig. 5.7) in the case of BMO, i.e., ~100 ns, suggests that BMO does not dissociate from a repulsive state and, hence, most probably, not from an excited electronic state. All the reaction channels studied theoretically originated from the ground electronic state of BMO molecule. Still, the possibility of a reaction channel from the excited electronic state, which contributed to the observed OH product, can not be completely ruled out from our studies.

5.2.2.2 Ab initio Molecular Orbital Calculations: The Photodissociation Channels

The geometries of the ground electronic state of BMO, the various possible products, and the transition state structures were subjected to optimization with the B3LYP theory, using 6-311+G(*d*, *p*) basis sets. Electronic energies corresponding to the optimized geometries were calculated, using the Moller-Plesset, MP2, MP3, MP4(D), and MP4(SDQ) levels of theory, with the same basis sets. Energies were also calculated at the quadratic configuration interaction (single, doubles, and triples), QCISD(T), level, with the same basis sets. With the inclusion of thermal energies, derived from the vibrational frequencies obtained at the B3LYP/6-311+G(*d*, *p*) level, reaction energies and activation barriers at 298 K were calculated. All the calculated energies, mentioned in this work, are at QCISD(T) /6-311+G(*d*, *p*) level.

Step 1: C—O Bond Cleavage

In the case of OH generation channel in photodissociation of BMO by 193 nm laser, the first step is ring cleavage, involving HC_{α}—O or/and H_2C_{β}—O bond scission, producing two different triplet biradicals (shown as Birad in Figs. 5.10 and 5.11), with dissociation energies of 45.3 and 57.7 kcal mol^{-1}. Thus, these calculations suggest

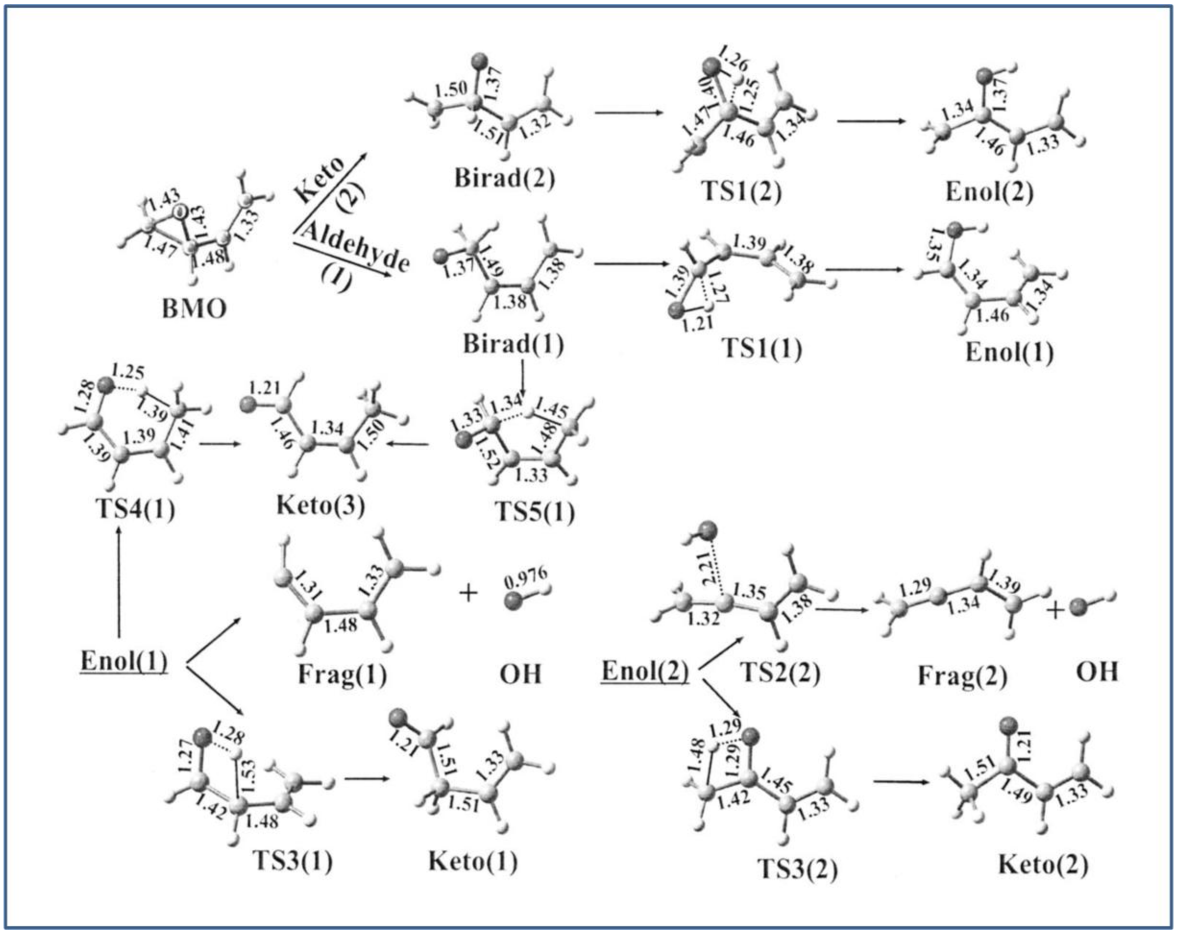

Fig. 5.10: The optimized structures of the transition states and products of the two reaction pathways for ring opening and subsequent generation of OH from the ground electronic state of SO.

preference for the HC_α—O to the H_2C_β—O bond scission in the ring opening of BMO, similar to that in SO. Both of these radicals can undergo further intramolecular rearrangements by two different reaction channels, eventually leading to generation of the OH radical and other stable products. The TS structures were calculated for better understanding of the mechanism and the energetics of the experimentally observed ring-opening channel of BMO, leading to formation of OH and stable products.

The epoxide ring openings, involving HC_α—O and H_2C_β—O bonds, are shown in the Figs. 5.10 and 5.11 as two channels, namely, Aldehyde (1) and Keto (2), respectively, which, apart from generating OH, lead to the final stable products, VAA, CA and MVK, respectively. The optimized structures of BMO (marked as BMO), biradicals, Birad (1) and Birad (2), and the transition states, TS1 (1) and TS1 (2), for the proposed channels, generating OH from the ground electronic state, are depicted in Fig. 5.10. This figure also shows the various elementary steps leading to formation of OH and the stable products VAA, MVK, and CA, which are marked as Keto (1), Keto (2), and Keto (3), respectively.

Step 2: Enol Formation

The triplet 1,3- biradicals (shown as Birad in Fig. 5.10), formed in the first step of ring opening, undergo 1,2 H migration via the transition state, TS1, producing enols of VAA and MVK, Enol (1) and Enol (2) (in Fig. 5.10), respectively, with corresponding activation barriers of 30.6 and 24.4 kcal mol^{-1} (in Fig. 5.11). The relative energetics for OH formation via enols of VAA (dotted curves) and MVK (solid curves) are depicted in Fig. 5.11. Both the C—O bond cleavage and subsequent rearrangement to the enol form are more energetically favorable for the Aldehyde (1) channel, mainly because of the ethylenic double bond. The delocalization of the electron results in slight lengthening of the ethylenic double bond and appreciable shortening of the adjacent C—C bond, making lengths of both bonds to be equal (1.38 Å) in Birad (1) as well as TS1 (1), as shown in Fig. 5.10. In addition, all the four C atoms in the two molecules, Birad (1) and TS1 (1), lie nearly in the same plane, with dihedral angles <CCCC of 1.1° and 2.1°, respectively. This kind of delocalization of the electron on the carbon atom, leading to additional stability, is absent in Birad (2) and TS1 (2) of the Keto (2) channel, because it

is located on the β carbon atom, resulting in retention of the double character of the ethylenic bond and nonplanarity of the carbon atoms in these structures. The effective activation barrier of the step leading to Enol (1) from Birad (1) is lower with respect to its counterpart in Keto (2) channel, mainly because of more stability of the biradical leading to the enol of VAA and the corresponding transition state, TS1(1), imparted by

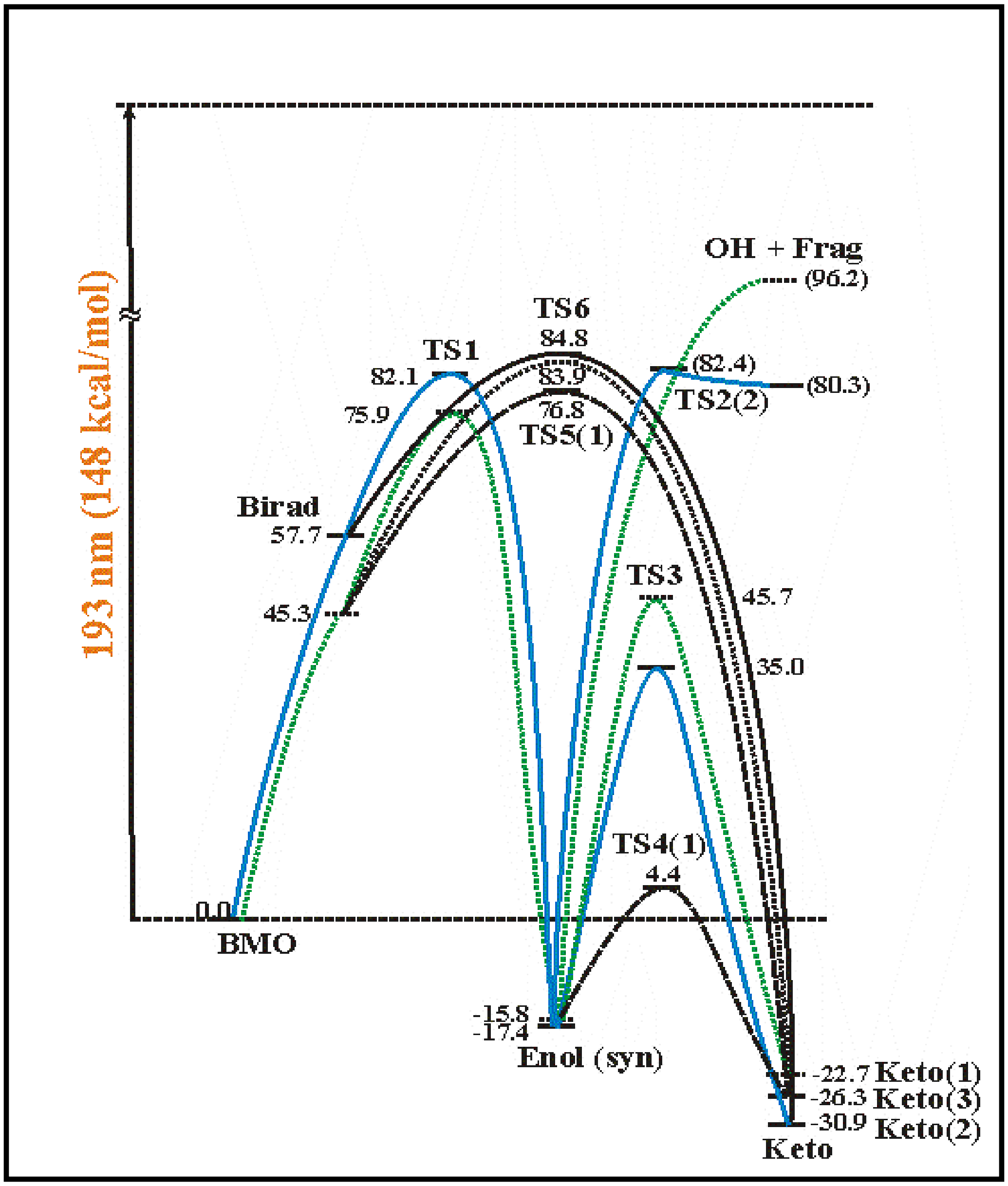

Fig. 5.11: Potential energy diagram for formation of OH from theground electronic state of BMO on excitation at 193 nm.

delocalization of the electron on the α C atom by the ethylenic double bond. The lower energy requirement for formation of the enol of VAA suggested preference for the Aldehyde (1) channel over the Keto (2) channel. With different orientations of HO with respect to the ethylenic double bond, we identified both the syn-(the dihedral angle <HOCC~0°) and anti-(the dihedral angle <HOCC~180°) conformers of these enols, with the former, in both the cases, being lower in energy. The synconformers of enols of VAA and MVK are more stable than the anti form, by 2.1 and 0.7 kcal mol^{-1}, respectively. The calculated energy difference between the two conformers is in good agreement with that in the other enols. The synform of vinyl acetaldehyde is more stable than the anti form by 1.3–2.0 kcal mol^{-1} [120, 121]. For phenyl acetaldehyde and acetophenone, these were calculated to be 2.0 and 0.7 kcal mol^{-1}, respectively. This value for 8-oxabicyclo[5.1.0]octa-2,4-diene (epoxyoxepin) was calculated to be 2.0 kcal mol^{-1} [117]. As for the structures of syn- and antiforms of Enol (1), the antiform has all C and O atoms in a plane with the dihedral angle HOCC(C=C) of 180.0°, whereas the synform, with dihedral angle HOCC(C=C) of 5.6°, has planar OCCC but nonplanar CCCC backbone, with dihedral angles of 0.4° and 34.5°, respectively. In the case of Enol (2), both the anti- and synforms have all the C and O atoms in a plane, but the values of the dihedral angle HOCC(C=C) are different, 180.0° and 23.3°, respectively.

Step 3: Formation of OH

In addition to the tautomerization pathway, the energized enols formed, after molecular rearrangement of the biradicals, produced on excitation of BMO at 193 nm, can undergo the C—OH bond cleavage generating the observed OH radical. This OH channel can involve either simple C—OH bond cleavage, or a transition state, implying presence of an exit barrier for the latter case. The corresponding TS, shown as TS2 (2) in Fig. 5.10, could be located from only Enol (2), and not from Enol (1). It implies that the enol of MVK generated OH, with a barrier, whereas that of VAA undergoes simple C—OH bond rupture, generating OH, without any exit barrier. However, the relative contributions to the OH channel from these two channels were difficult to ascertain from our studies. We assigned the OH formation from Enol (1) and Enol (2) channels. Theoretically, formation of the keto products is feasible directly via the biradicals, without going through enols. These keto products would be in equilibrium with their respective enol forms, which, on excitation at 193 nm, might lead to OH formation. To investigate this additional possibility of OH formation, we excited the keto products separately at 193 nm and observed no detectable amount of the OH radical being formed. This suggests that under present experimental conditions, the ketones/aldehydes, through their enolic forms, can not produce OH radical directly. Hence, we attribute all the observed OH to the energized enols formed in the course of the reaction.

Step 4: Formation of Keto Structures

The enols produced on photoexcitation of BMO undergo mainly tautomerization to produce keto products, VAA and MVK, shown as Keto (1) and Keto (2), respectively, in Fig. 4.10, which could be detected as stable products, using GC. These keto tautomers are expected to be more stable than their corresponding enols[117, 119, 120]. Our calculations show that VAA and MVK are more stable with respect to the most stable conformer of the corresponding enol, by 6.9 and 13.5 kcal mol^{-1}, respectively, in good agreement with literature values[109, 119-122]. In the vinylalcohol-acetaldehyde pair, considered to be the prototype of keto-enol pair, acetaldehyde is more stable than vinyl alcohol by 10.4–12.9

kcal mol^{-1} [117, 120]. The four-centered TS structures, TS3 (1) and TS3 (2) in Fig. 5.10, for tautomerization were optimized, and the activation barriers for enol to keto conversion were estimated to be 61.5 and 52.4 kcal mol^{-1}, respectively, for the formation of VAA and MVK. There exist an alternative pathway for keto products, directly from the biradical. The corresponding transition state structures for VAA and MVK were optimized, with activation barriers of 83.9 and 84.8 kcal mol^{-1}, respectively, given as TS6 in Fig. 5.11. Thus, theoretical studies reveal that there are more than one route by which the keto structures can be formed from the parent compound. These products can be formed from the biradicals directly, or via formation of enol structures (shown in Fig. 5.10), with a preference, based on energetics, for the latter. The differences in activation barriers for these pathways, for both Keto (1) and Keto (2), are small, 8.0 and 2.7 kcal mol^{-1}, respectively (shown in Fig. 5.11). Hence, the formation of the observed products by either pathway is feasible, with a preference for the enol route.

Another aldehyde, in a good yield, was observed to be CA, which can originate from the Aldehyde (1) channel. The triplet biradical [Birad (1)] can directly rearrange to CA, shown as Keto (3) in Figs. 5.10 and 5.11, via a transition state, whose structure is labeled as TS5 (1). The activation barriers for this channel and that for conversion of this biradical to enol of VAA are comparable (Fig. 5.11). There exists an alternative pathway for CA formation from Enol (1) via transition state TS4 (1), with an activation barrier of 20.2 kcal mol^{-1}. Among all three stable keto products, this alternative pathway of CA formation is the lowest-energy one. Thus, our calculations support the observation of the highest yield of CA, among three stable keto products. Formation of CA by rearrangement of BMO has been reported to take place in the metabolism process of butadiene[106] inside living bodies, and can also be caused by heterogeneous inorganic catalysis[107, 108], though no study of mechanism has been carried out yet. Similar mechanisms, as proposed in this article may be operative in those cases too.

5.3 Summary

Epoxides are essentially cyclic ethers, with three membered rings. Due to smaller ring size, the strain is much higher in these rings. Study of the dynamics of photodissociation of this class of compounds was carried out, to understand the effect of higher strain energy present in the smaller ring compounds on the energy partitioning and overall dynamics of photodissociation. We have irradiated epoxides, with different susbstituent groups at the 3-memberd rings, like ethylene oxide (EO), propylene oxide (PO), butadiene monoxide (BMO) and styrene oxide (SO) with 193 nm laser[109, 123]. In the case of the first two, there is no OH formation by photodissociation, but in case of the other two, OH radical is obtained. One reason for this observation could be due to the fact that, the absorption cross-section (σ), at 193 nm, for EO (0.44×10^{-20} cm^2) and PO (1.5×10^{-20} cm^2) are much smaller than that for BMO (1.2×10^{-17} cm^2), and SO (5.4×10^{-18} cm^2). The analysis of the products of photolysis of BMO and SO at 193 nm by Gas Chromatography-Mass Spectrometry (GC-MS) revealed the presence of some ketonic products. The OH formation channel in these compounds is found to have multiple branches. Since the three-membered epoxide ring is unsymmetrically substituted, the ring opening could be caused by two different channels, involving HC_{α}—O and/or H_2C_{β}—O bond scission, producing two different triplet biradicals. The energy rich biradicals formed in this way can undergo intramolecular H-atom migration from C atom to O atom, giving rise to the enolic forms of different ketones/ aldehydes. These enols, then, either tautomerise to their more stable keto forms, or undergo another C—O bond scission, producing the OH radical. By theoretical calculations, it has been be seen that the OH formation channel is more energy demanding than all the others, and hence, the quantum yield of this channel is quite low for both the compounds (0.02 for SO, and 0.007 for BMO).

From the proposed reaction mechanism, it is evident that the electronic stabilization of the precursor radical of OH from the phenyl π system of SO, or the conjugated π bonds, in the case of BMO, can have a major influence on the yield of OH. This effect is absent in case of EO or PO, which have saturated aliphatic substituents at the epoxide ring. Thus, the quantum yield of OH formation in EO and PO, if any, must be quite low, as compared to that in SO and BMO. Another indication for the importance of this conjugative effect is the difference in the quantum yield of OH formation in photodissociation of SO and BMO, the latter being only about 35% of the former. The higher stability offered by the conjugative effect of the aromatic benzene ring, in the case of SO, as compared to one single conjugated double bond in BMO, is responsible for this difference.

Chapter 6

Conclusion

The main quest of the present thesis work has been to understand the underlying features of kinetics and dynamics of gas-phase reactions, mainly reactions of atmospherically important molecules with OH radicals and unimolecular photodisociation reactions of molecules with ether linkage. The individual experiments done to fulfill this aim, their results, and supporting theoretical calculations have been elaborated upon in the preceding chapters. This concluding chapter summarizes all the results obtained from these studies, and discusses the relevance of these results in addressing the basic aim of the thesis.

In the first part of this thesis, the kinetics of reaction of OH radical with morpholine and bis- 2,2,2-trifluoro diethyl ether (TFEE), both important from the viewpoint of atmospheric chemistry, has been discussed. The experimental results, in the case of TFEE, have been compared with the existing literature values, and structure activity relationships. In the case of morpholine, which is a secondary amine, as well as a cyclic ether, the experimental results indicate similarity of the kinetics of OH radical reactions with both classes of compounds. The second part of the thesis discusses the dynamic studies of OH formation channel in the laser-induced photodissociation of cyclic ethers and epoxides. The variation in the dissociation dynamics due to difference in the structural features of the cyclic compounds are experimentally and theoretically probed in this part.

Bis-2,2,2 trifluoroethyl ether (TFEE), is a potential chlorofluorocarbon (CFC) alternative. This molecule is a typical representative of the hydrofluoroether group. These compounds have the highly desirable quality of being benign to the ozone layer due to absence of Cl atom in their structure. But, before being used and produced in mass scale, another important aspect of these compounds, which is their atmospheric lifetime, has to be seriously investigated. The global warming potential (GWP), which is a measure of the capacity of any compound to trap heat in the atmosphere, has a direct relationship with its lifetime in it. A compound which has high reactivity with the oxidizing species present in the lower parts of the atmosphere, mainly the troposphere, naturally has lower atmospheric lifetime, and hence, lower global warming potential. Moreover, these highly reactive compounds are less probable to travel very far from their source, and hence have less probability to have long distance, or long term, adverse effects on the atmosphere. Since the hydrofluoroethers contain H-atoms which are readily abstracted by oxidizing species, like the OH radical, these are most likely to be removed, within a comparatively short time, from the troposphere. The reaction of these compounds with OH radical, which is the major removal channel of these compounds, is extremely important for measuring their atmospheric lifetime, and has to be studied in details. In this context, the kinetics of the reactions of various members of the hydrofluoroether family with OH has already been studied, by employing various experimental methods[27-31, 33]. The data obtained from these studies, using different techniques, though fairly consistent for some of the molecules, can vary substantially for others, like in case of TFEE. The difference in the kinetic parameters obtained from these studies may arise due to systematic errors involved in the techniques employed, and in such cases, more independent studies, by different techniques of generation and detection of free radicals in the absolute method, or by using different standards in relative rate method, are required. Laser Photolysis-Laser Induced Fluorescence (LP-LIF) is a standard absolute technique, used in kinetic studies. This method has the advantage of being very sensitive and specific. We have employed this technique, for the first time, to determine the bimolecular rate constant k_2 as well as E_a/R, for the reaction of OH with TFEE. Here, the concentration of OH radicals generated and monitored can be as low as 10^7- 10^{11} molecules cm^{-3}, and hence, any secondary reaction and mutual reactions of OH radicals are avoided. By our method, the bimolecular rate coefficient at 298 K, $k_2(298)$, has been measured to be $(1.47 \pm 0.03) \times 10^{-13}$ $cm^3 molecule^{-1} s^{-1}$, and the temperature dependence of k_2 is determined to be $(4.5 \pm 0.8) \times 10^{-12} \exp[-(1030 \pm 60)/T]$ $cm^3 molecule^{-1} s^{-1}$. The rate coefficient at room temperature is very close to the average of the three previous measurements, whereas the values of E_a/R and A-factor are higher than the two previously reported values. This study gives the atmospheric lifetime of TFEE as 0.35 years, which predicts quite a low GWP for TFEE, as compared to typical CFC molecules (e.g., 6 years for methyl chloroform).

Unlike the ether molecules, morpholine, which is a widely used industrial chemical, is expected to have a complex kinetic behavior, because it is a multifunctional molecule, with an ether linkage, as well as a secondary amine linkage, in its six-membered ring structure. The ether linkage increases the reactivity with OH radical in comparison with the corresponding hydrocarbons. Many ethers[39], diethers[40] and cyclic ethers[41] are known to have very high rate coefficients for their reactions with OH radical. In some of these reactions, the rate constants exhibit slight negative temperature dependence. In the case of secondary amines, experimental studies are fewer in number, but similar trends have been reported. In our study, we have used LP-LIF to measure the kinetic parameters of the reaction of OH radical with morpholine in the gas phase, which is the first study of this kind. From our results, the bimolecular rate coefficient at 298 K, $k_2(298)$, is found to be $(1.47 \pm 0.03)\times10^{-13}$ $cm^3molecule^{-1}s^{-1}$, and the temperature dependence of k_2 is determined to be $(4.5 \pm 0.8) \times 10^{-12}exp[-(1030 \pm 60)/T]$ $cm^3molecule^{-1}s^{-1}$. The experimentally observed pre-exponential factor of morpholine is very close to that for cyclic ethers, like tetrahydrofuran, 1,3 dioxane, 1,3,5 trioxane, oxepane, etc., but the activation energies are found to be more negative. Thus, the presence of an N atom in morpholine probably has a prominent effect on the activation energy. Only two experimental studies on the kinetics of the reaction of OH radical with amines are available[53, 54], and both report high rate constants. The room temperature rate constant of reaction of OH radical with dimethyl amine is reported to be around 6.5 x 10^{-11} cm^3 $molecule^{-1}$ s^{-1}, in both the studies, whereas there is a difference in the rate constant reported for trimethyl amine, 3.5 x 10^{-11} cm^3 $molecule^{-1}$ s^{-1}, by Atkinson et al[53], and 6.1 x 10^{-11} cm^3 $molecule^{-1}$ s^{-1}, by Carl and Crowley[54]. Activation energy is also reported to be negative in the case of CH_3NH_2, $(CH_3)_2NH$, $(CH_3)_3N$ and $C_2H_5NH_2$, in the range of -375 to -500 cal mol^{-1}. The present results on morpholine and the previous calculations on aminoacids[46, 47], suggest that formation of a stable pre-reactive complex can be responsible for the observed negative activation energies in the case of amines also. The pre-exponential factors are 1.02, 2.89, 2.62 and 1.47 x 10^{-11} cm^3 $molecule^{-1}$ s^{-1}, respectively, for the above amines, higher than that observed for morpholine, in the present study. The rate constant observed for morpholine is marginally higher than that observed for these amines, and the activation energy is more negative (-1170 cal mol^{-1}). Thus, it can be seen that formation of pre-reactive complexes, negative activation energy and very high rate constants are the common features of the reactions of OH radical with amines, more prominent than that in the case of oxygen containing compounds. The theoretically computed overall rate constant at room temperature for all possible pathways, in the case of aminoacids, like serine[47], is very close to that observed here for morpholine. *Ab initio* molecular orbital calculations for the H-abstraction pathway from morpholine by OH radical using Gaussian 98 package, indicate the presence of two types of pre-reactive complexes. The H-atom of the OH radical can either get hydrogen bonded to the N-atom, or the O-atom of the morpholine ring. It could be seen that, the N-adduct is slightly more stable than the O-adduct. The energy of the TS, resulting from the former also is negative, as compared to that of the parent, whereas that for the latter is slightly positive. This information, along with the fact that the relative energies of the pre-reactive complex and the transition states computed for the aminoacids are found to be similar to that of morpholine indicates that the OH formation channel, involving the N-adduct, is probably more important than the O-adduct channel, though the latter must also have some contribution.

The second major part of the present thesis, where the dynamics of photodissociation of oxygen containing cyclic compounds is discussed, is divided in two sub-divisions. The first includes five and six-membered cyclic ethers, viz., tetrahydrofuran (THF), tetrahydropyran (THP) and morpholine, and the second includes epoxides, i.e., styrene oxide (SO) and butadiene monoxide (BMO). All these compounds are well-established hazardous chemicals, which, due to their extensive usage in varied fields, get released into the atmosphere, and whence from, in the systems of the living beings. The photochemistry of these molecules needs to be understood from the very basics, to understand their impact on the environment, as well as the living systems. Dynamics studies allow us to look into the chemical reactions, in this cas, unimolecular photodissociation, from the molecular level itself, and therefore, get an insight into the mechanism, as well as the nature of the potential energy surface of these reactions. This knowledge, apart from being instrumental in understanding the photochemistry of related compounds, throws considerable light on the behaviour of these compounds in the upper atmosphere.

For the cyclic ethers, our experimental and theoretical works suggest that the dissociation most likely takes place from the ground state of the molecules. All these compounds are rigid ring type, with no OH functional group present in their structure. Hence, OH must be formed as a secondary product, after some internal rearrangement during photodissociation. The energetic ground state molecule, having excess energy stored in its internal modes, is capable of entering energy expensive reaction channels, producing unusual fragmentation products, such as OH. In most of the cases (THF, THP and triplet channel in morpholine), theoretical studies reveal that, the first step of dissociation is the scission of the ring through C—O bond cleavage, which produces a biradical. This step takes place without any barrier. This biradical, then undergoes intramolecular rearrangement, involving migration of an H-atom from a C-atom in the chain to the O-atom. This step, which involves an energy barrier and a transition state, produces another energetically more stable biradical, which has one OH group at an end. In the next step, OH radical is separated from the rest of the photofragment through another C—O bond cleavage. The experimentally obtained distribution of energy suggests that a major portion of the available energy is partitioned, in all cases, to the relative translational motion of the photoproducts, which, again, indicates the presence of an exit barrier in the potential energy surface. These results are then compared with the different models for energy distribution in unimolecular photodissociation. The two limiting models, namely, the Statistical model, which is applicable for dissociations without barrier, and impulsive model, which is applicable for direct dissociation over a repulsive potential energy surface, fail to explain the experimentally obtained energy distribution. Hence, a hybrid model of energy partitioning, namely, barrier impulsive model, was applied to qualitatively explain the results. This model, predicted a high exit barrier for OH formation channel in the case of THF and THP, about 16 kcal/ mol for THF, and 40 kcal/ mol for THP. A*b initio* molecular orbital calculations, however, revealed very small barrier in both the cases, about 5 kcal/ mol. In the case of morpholine, a very small exit barrier (0.5 kcal/ mol) was seen in the last step. This discrepancy in the size of the actual exit barrier, anyway, should not be taken too seriously, since the effect of the earlier, bigger energy barrier (about 35 kcal/ mol) of the rearrangement step in this multiple-step reaction channel is expected to manifest in the final results. In the case of morpholine, there is an alternative reaction channel (singlet channel), where the reaction proceeds through a concerted step involving C—O bond cleavage and H-atom migration. A stable, alcoholic isomer of morpholine, is produced by this step, which, then dissociates to produce OH radical. In this channel, in the first step, there is an energy barrier, but none in the second step.

In the case of epoxides, it was seen that there is a difference in the results of photodissociation by 193 nm laser, for different compounds. When ethylene oxide (EO), propylene oxide (PO), butadiene monoxide (BMO) and styrene oxide (SO) were irradiated with 193 nm laser[109, 123], the first two did not generate any detectable amount of OH radical, but in the case of the other two, OH radical was obtained. The absorption cross sections of all the four molecules at 193 nm were measured experimentally. The difference in the result of photodisociation of these compounds can be attributed to the fact that the absorption cross-section (σ) at 193 nm for EO (0.44×10^{-20} cm^2) and PO (1.5×10^{-20} cm^2) are much smaller than that for BMO (1.2×10^{-17} cm^2), and SO (5.4×10^{-18} cm^2). Another cause can be the difference in the stability of the biradical produced by epoxide ring cleavage. In the case of SO and BMO, the conjugated double bonds present in the substituent offers reasonable stability to the radical centre produced on the C-atom, which is totally absent in the case of saturated hydrocarbon substituents in case of EO and PO. The analysis by Gas Chromatography-Mass Spectrometry (GC-MS) of the stable product of photolysis of BMO and SO at 193 nm revealed the presence of ketone and aldehyde products. The OH formation channel in these compounds has multiple branches. Since the three-membered epoxide ring is unsymmetrically substituted, the ring opening can be caused by two different channels, involving $HC_\alpha—O$ and/or $H_2C_\beta—O$ bond scission, producing two different triplet biradicals in the first step, the former leading to aldehydes, and the later leading to ketone stable products. The energy-rich biradicals formed in the initial ring opening undergo intramolecular H-atom migration from C-atom to O-atom, giving rise to the enolic forms of different ketones/aldehydes. These enols, then, can either tautomerise to their more stable carbonyl forms or can undergo another C—O bond scission, producing the OH radical. The carbonyl products, however, can be formed from the biradicals directly, or via formation of enol structures, with a preference, based on energetics, for the latter. In both the cases, the aldehyde product is formed in higher yield than the ketone. This could be due to the fact that the radical product of HC_{α}—O bond cleavage is stabilized by the conjugation provided by the susbstituent group, whereas this effect does not work for the radical product of H_2C_{β}—O bond scission. Theoretical calculations showed that the OH formation channel is more energy demanding than all the other channels, and hence, the quantum yield of OH formation channel is quite low, for both the compounds, 0.02 for SO, and 0.007 for BMO. The much higher value of quantum yield on OH formation in the case of SO, as compared to that in BMO, can be due to the better stabilization provided to the radical product of ring cleavage by the aromatic benzene ring in SO, as compared to one single double bond in conjugation in BMO.

The detection of OH radical in the photodissociation of cyclic compounds without having any OH functional group in their structure, is in itself a quite interesting finding. The detailed dynamics study of the OH radical formation channel from bigger, almost strain-free O-atom containing rings, rings containing another heteroatom (N-atom in case of morpholine) and smaller, strained epoxide rings has helped in understanding the general photodissociation dynamics of different kinds of cyclic compounds. With the help of experimental and theoretical investigations, the variation in the features of the potential energy surfaces of the different compounds could be successfully related to the structural properties of the parent molecules. The dynamics studies described in the present thesis have contributed quite substantially into the overall understanding of the relation between the structural features of ring compounds and the dynamics of high-energy channels in their laser induced photodissociation.

References

1. Prinn, R. G.; Huang, J.; Weiss, R. F.; Cunnold, D. M.; Fraser, P. J.; Simmonds, P. G.; McCulloch, A.; Harth, C.; Salameh, P.; ODoherty, S.; Wang, R. H. J.; Porter, L.; Miller, B. R., *Science* **2002,** 292, 1882.
2. Frisch, M. J., *Gaussian 92*. Gaussian Inc.: Pittsburgh, PA, 1992.
3. S.SenGupta; P.Upadhyaya, H.; A.Kumar; D.Naik, P.; N.Bajaj, P., *J. Chem. Phys.* **2005,** 122, 124309.
4. SenGupta, S.; Indulkar, Y.; Dhanya, S.; Naik, P. D., *Int. J. Chem. Kinet.*
5. Naik, P. D.; Upadhyaya, H. P.; Kumar, A.; Sapre, A. V.; Mittal, J. P., *J. Photochem. Photobiol.* **2003,** C 3, 165.
6. Dieke, G. H.; crosswhite, H. M., *J. Quant.Spectrocc. Radiat. Transfer* **1961,** 2, 97.
7. Chidsey, I. L.; Crossley, D. R., *J. Quant. Spectrosc. Radiat.Transfer* **1980,** 23, 187.
8. Dixon, R. N.; Rieley, H., *J. Chem. Phys.* **1989,** 91, 2308.
9. Vasudev, R.; Zare, R. N.; Dixon, R. N., *J. Chem. phys.* **1984,** 80, 4863.
10. Andresen, P.; Ondrey, G. S.; Titze, B.; Rothe, E. W., *J. Chem. Phys.* **1984,** 80, 2548.
11. Tuck, A. F., *J. Chem. Soc. , Faraday Trans. 2* **1977,** 73, 689.
12. Chang, A. H. H.; Hweang, D. W.; Yang, X.-M.; Mebel, A. M.; Liu, S.-H.; Lee, Y.-T., *J. Chem. Phys.* **1999,** 110, 10810.
13. Galloway, D. B.; Meyer, T. G.; Bartz, J. A.; Huey, L. G.; Crim, F. F., *J. Chem. Phys.* **1994,** 100, 1946.
14. Muckerman, J. T., *J. Phys. Chem.* **1989,** 93, 179.

15. North, S. W.; Blank, D. A.; Gazelter, J. D.; Longfellow, C. A.; Lee, Y.-T., *J. Chem. Phys.* **1995,** 102, 4447.

16. Levine, R. D.; Kinsey, J. L., *Atom-Molecular Collision Theory A Guide for the Experimentalist*. Plenum: New York, 1979.

17. Pechukas, P.; Light, J. C., *J. Chem. Phys.* **1965,** 42, 3281.

18. Pechukas, P.; Rankin, C., *J. Chem. Phys.* **1966,** 44, 794.

19. Wittig, C.; Nadler, I.; Reisler, H.; Noble, M.; Catanzarite, J.; Radhakrishnan, G., *J. Chem. Phys.* **1985,** 83, 5581.

20. Levine, R. D.; Bernsteine, R. B., *Acc. Chem. Res.* **1974,** 393.

21. Nadler, I.; Noble, M.; Reisler, H.; Wittig, C., *J. Chem. Phys.* **1985,** 82, 2608.

22. Kim, S. K.; Choi, Y. S.; Pibel, C. D.; Zheng, Q.; Moore, C. B., *J. Chem. Phys.* **1991,** 94, 1954.

23. Hehre, W. J.; Radom, L.; Schleyer, P. V. R.; Pople, J. A., *Ab Initio Molecular Orbital Theory*. John Wiley and Sons: 1986.

24. Hohenberg, P.; Kohn, W., *Phys. Rev.* **1964,** 136.

25. G. Marchionnia; S. Petriccia; P. A. Guardaa; G. Spataroa; Pezzinb, G., *J. Fluorine Chem.* **2004,** 125, 1081.

26. Sekiya, A.; Misaki, S., *J. Fluorine Chem.* **2000,** 101, 215.

27. O'Sullivan, N.; Wenger, J.; Sidebottom, H., In *Proceedings of 7th European commission Symposium on Physicochemical Behaviour of Atmospheric Pollutants*, Venice, Italy, October 1996.

28. Sander, S. P.; Orkin, V. L.; Kurylo, M. J.; Golden, D. M.; Huie, R. E.; Kolb, C. E.; Finlayson-Pitts, B. J.; Molina, M. J.; Friedl, R. R.; Ravishankara, A. R.;

Moortgat, G. K.; Keller-Rudek, H., KINETIC STUDY OF THE GAS-PHASE REACTION OF HYDROXYL RADICAL WITH CF3CH2OCH2CF3 525. *JPL 06-2; NASA-JPL Data*

International Journal of Chemical Kinetics **2006,** DOI 10.1002/kin.

29. Orkin, V. L.; Villinave, E.; Huie, R. E.; Kurylo, M. J., *J. Phys. Chem. A* **1999,** 103, 1999.
30. Tokuhashi, K.; Takahashi, A.; Kaise, M.; Kondo, S.; Sekiya, A.; Yamashita, S.; Ito, H., *J. Phys. Chem. A* **2000,** 104, 1165.
31. Oyaro, N.; Sellevag, S. R.; Nielsen, C. J., *Env. Sci. Technol.* **2004,** 38, 5567.
32. Andersen, M. P. S.; Nielsen, O. J.; Wallington, T. J.; Hurley, M. D.; Demore, W. B., *J. Phys. Chem. A* **2005,** 109, 3926.
33. Wilson, E. W.; Hamilton, W. A.; Mount, H. R.; DeMore, W. B., *J. Phys. Chem. A* **2007,** 111, 1610.
34. DeMore, W. B., *Photochem . Photobiol. A Chem.* **2005,** 176, 129.
35. Urata, S.; Takada, A.; Uchimaru, T.; Chandra, A. K., *Chem. Phys. Lett.* **2003,** 368, 215.
36. Prather, M.; Spivakovsky, C. M. J., *Geophys. Lett.* **1990,** 95, 18723.
37. Kilhorn, J.; Rosner, D. G., Environmental Health Criteria 179, International Programme on chemical Safety. In *United Nations Environment Programme*, International Labour Organisation and World Health Programme: Geneva, 1996.
38. Kwok, E. S. C.; Atkinson, R., *Atmospheric Environment* **1995,** 29, 1685.
39. Melouki, A.; Teton, S.; Lebras, G., *Int. J. Chem. Kinet.* **1995,** 27, 791.

40. Porter, E.; Wenger, J.; Treacy, J.; Sidebottom, H.; Mellouki, A.; Teton, S.; LeBras, G., *J. Phys. Chem. A* **1997,** 101, 5770.

41. Moriarty, J.; Sidebottom, H.; Wenger, J.; Mellouki, A.; LeBras, G., *J. Chem. Phys. A* **2003,** 107, 1499.

42. Dey, G. R.; Kishore, K., *Rad. Phys. Chem.* **2003,** 67, 115.

43. Wayner, D. D. M.; Clark, K. B.; Rauk, A.; Yu, D.; Armstrong, D. A., *J. Am. Chem. Soc.* **1997,** 119, 8925.

44. SenGupta, S.; Kumar, A.; Naik, P. D.; Bajaj, P. N., *Chem. Phys. Lett.* **2008,** 465.

45. El-Nahas, A. m.; Uchimaru, T.; Sugie, M.; Tokuhashi, K.; Sekiya, A., *J. Mol. Struct. (Theochem)* **2005,** 722, 9.

46. Cruz-Torres, A.; Galano, A.; Alvarez-Idaboy, J. R., *Phys. Chem. Chem. Phys.* **2006,** 8, 285.

47. Galano, A.; Alvarez-Idaboy, J. R.; Cruz-Torres, A.; Santoyo, M. E. R.-. *J. Mol. Struct. (Theochem)* **2003,** 629, 165.

48. Laarhoven, L. J. J.; Mulder, P.; Wayner, D. D. M., *Acc. Chem. Res.* **1999,** 32, 342.

49. Lelavee, J.; Allonas, X.; Fouassier, J.-P., *J. Am. Chem. soc.* **2002,** 124, 9613.

50. Hammond, G. S., *J. Am. Chem. soc.* **1955,** 77, 334.

51. Rayez, M. T.; Rayez, J. C.; Sawerysyn, J. P., *J. Phys. Chem.* **1994,** 98, 11342.

52. Aschmann S. M.; Atkinson, R., *Int. J. Chem. Kinet.* **1998,** 30, 533.

53. Atkinson, R.; Perry, R. A.; Pitts, J. N., *J. Chem. phys.* **1978,** 68, 1850.

54. Carl, S. A.; Crowley, J. N., *J. Phys. Chem.* **1998,** 102, 8131.

55. Melnik, D. J.; Gopalakrishnan, S.; Miller, T. A.; Miller, F. C., *J. Phys. Chem.* **2003,** 118, 3589.

56. Cadiolli, B.; Galinella, E.; Columbbeau, C.; Jobic, H.; Berthier, G., *J. Phys. Chem.* **1993,** 97, 7844.

57. Lambert, J. B.; Keske, R. G.; Weary, D. K., *J. Am. Chem. soc.* **1967,** 89, 5921.

58. Flygare, W. H., *Annu. Rev. Phys. Chem.* **1967,** 18, 325.

59. Breed, H. E.; Gundersen, G.; Seip, R., *Acta Chem. scand.* **1979,** Ser. A A33, 225.

60. Pickette, L. W.; Hoeflich, N. J.; Liu, T. C., *J. Am. Chem. soc.* **1951,** 73, 4865.

61. Hernandez, G. J., *J. Phys. Chem.* **1963,** 38, 2233.

62. Rao, V. M.; Kewley, R., *Can. J. Chem.* **1969,** 47, 1289.

63. Pickette, H. M.; Strauss, H. L., *J. Chem. Phys.* **1970,** 11, 376.

64. Cueto, M.; Darias, J.; Rovirosa, J.; Martin, A. S., *J. Nat. Prod.* **1998,** 61, 1466.

65. Koert, U., *J. Prakt. Chem.* **2000,** 342, 325.

66. Namekawa, M.; Ito, K.; Mitsumari, T.; Yoshinobu, M., *Jpn. Kokai Tokkyo Koho* **1997,** A2, 21.

67. Shi, G.; Alfanso, D.; Fatope, M. O.; Zeng, L.; Gu, Z.-M.; Xhao, G.-X.; He, K.; Mc.Dougal, J. M.; Laughlin, L. L., *J. Am. Chem. soc.* **1995,** 117, 10409.

68. Swochka, S. G., *Power* **1988,** 132, 67.

69. Hiratani, T.; Asagi, Y.; Matsaska, A.; Uchida, K.; Yamaguchi, H., *Jpn. J. Antibiot.* **1991,** 44, 993.

70. Gip, L., *Adv. Ther.* **1989,** 6, 26.

71. Dowherty, S.; Guillard, C.; Pichall, P., *J. Chem. Soc., Faraday Trans.* **1995,** 91, 1853.

72. Friedel, R. A.; McKinney, D. S., *J. Am. Chem. Soc.* **1947,** 91, 1853.

73. Indris, O.; Stahl, W.; Kretschmer, U., *J. Mol. Spec.* **1998,** 190, 372.

74. Alekseev, N. V., *J. Struct. Chem.* **1965,** 5, 837.

75. Davidson, R.; Hog, J.; Warsop, P. A.; Whiteside, J. A. B., *J. Chem. Soc. Faraday Transaction 2* **1972,** 68, 1652.

76. Doucet, J.; Sauvageau, P.; Sandorfy, C., *Chem. Phys. Lett.* **1972,** 17, 316.

77. Bremner, L. J.; Curtis, M. G.; Walker, I. C., *J. Chem. Soc., Faraday Transactions* **1991,** 87, 1049.

78. Kramer, J., *J. phys. Chem.* **1982,** 82.

79. Klute, C. H.; Walters, W. D., *J. Am. Chem. soc.* **1946,** 68, 506.

80. Lifshitz, A.; Bidani, M.; Bidani, S., *J. Phys. Chem.* **1986,** 90, 3422.

81. Laptev, V. B.; Ryabov, E. A.; Tumanova, L. M., *Zh. Fiz. Khim.* **1989,** 63, 1892.

82. Kramer, J., *J. Phys. Chem.* **1982,** 86, 26.

83. Roquitte, B. C., *J. Am. Chem. soc.* **1969,** 91, 7664.

84. Roquitte, B. C., *J. Phys. Chem.* **1966,** 70, 1334.

85. Diaz, Z.; Doepker, R. D., *J. Phys. Chem.* **1978,** 82.

86. SenGupta, S.; Upadhyaya, H. P.; Kumar A.; Naik, P. D.; Bajaj, P. N., *J. Chem. Phys.* **2005,** 122, 124309.

87. Watanabe, K.; Nakayama, T.; Mottl, J., "Final Report on Ionization Potential of Molecules by Photoionization Method". *University of Hawaii* **1959**, (unpublished).

88. Plackaert, A. A.; Doucet, J.; Sandorfy, C., *J. Chem. phys.* **1974,** 60, 4846.

89. Gray, G. D.; Warsop, P. A.; Whiteside, J. A. B., *J. Chem. Soc. , Faraday Trans.* **1970,** 66, 2130.

90. Robin, B.; Kuebler, N. a., *J. Electron Spectrosc. Relat. Phenom.* **1972,** 1, 13.

91. Cornish, T. J.; Baer, T.; Pedersen, L. G., *J. Phys. Chem.* **1989,** 93, 6064.

92. Zimina, G. M.; Kosobutski, V. S.; Petrayev, E. P.; Shadyro, O. I., *Khim. Vys. Energ.* **1986,** 20, 225.

93. Kasparov, M. S.; Tromifov, V. I., *Khim. Vys. Energ.* **1978,** 12, 461.

94. Scala, A. A.; Nguyen, D.; Rourke, W.; M. Caputo (Worcester Polytechnic Institute, M., *Progress Report No.(DOE/ER/)03569-Tl(unpublished)*

95. Sorkhabi, O.; Qi, F.; Rizvi, A. H.; Suits, A. G., *j. Chem. Phys.* **1999,** 111, 100.

96. Xu, S.; Tan, X.; Yao, Q.; He, M.; Zhou, Y.; Chen, J., *Proc. SPIE-The Int. Doc. Opt. Eng.* **2001,** 4414, 53, and references therein.

97. Mitchell, D.; Koenig, T. M., *Synth. Commun.* **1995,** 25, 1231.

98. Fulton, D. A.; Gibson, C. L., *Tetrahedron Lett.* **1997,** 38, 2019.

99. Ramanathan, K.; Rogers, K., *Sensor Actuator. B* **2003,** 91, 205.

100. Tezuka, M.; Yajima, T., *Plasma Chem. Plasma Process.* **1996,** 16, 329.

101. Cho, B. T.; Choi, O. K., *Bull. Korean Chem. Soc.* **2001,** 22, 443.

102. Nyquist, R. a.; Fiedler, S., *Vib. Spectrosc.* **1994,** 7, 149.

103. Parker, R. E.; Isaacs, N. E., *Chem. Rev. (Washington D. C.)* **1959,** 59, 737.

104. Meester, C. d.; Poncelet, F.; Roberfroid, M.; Mercier, M., *Biochem. Biophys. Res. Commun.* **1978** 80, 298.

105. Maniglier-Poulet, C.; Xiuaoquin, C.; Ruth, J. A.; Ross, D., *Chem. Biol. Interact.* **1995** *97, 119.*

106. Steltzer, R. R.; Elfarra, A. A., *Carcinogenesis* **1999,** 20, 285.

107. Alper, H.; DesRoches, D.; Durst, T.; Legault, R., *J. Org. Chem.* **1976,** 41, 3611.

108. Monnier, J. R.; Low, J. M., US Patent No. 4,925,987 (15 May 1990).

109. Kumar, A.; SenGupta, S.; Pushpa, K. K.; Naik, P. D.; Bajaj, P. N., *Chem. Phys. Lett.* **2006,** 430, 240.

110. SenGupta, S.; Indulkar, Y.; Kumar, A.; Naik, P. D.; Bajaj, P. N., *J. Chem. Phys.* **2008,** 128, 024309.

111. Kristinsson, H.; Griffin, G. W., *Angew Chem.* **1965,** 77, 859.

112. Kristinsson, H.; Griffin, G. W., *J. Am. Chem. Soc.* **1966,** 88, 1579.

113. Sonawane, H. R.; Sethi, S. C.; Merchant, S. N., *Indian J. Chem* **1984,** B 23, 940.

114. White, R. C.; Wedyck, E. J.; Jr., K. O. L., *J. Photochem. Photobiol.* **1993,** 71, 127.

115. Padwa, A.; Au, A.; Lee, G. A.; Owens, W., *J. Org. Chem.* **1975,** 40, 1142.

116. Linder, S.; White, K.; Palmer, M.; Arney, B.; White, R., *Tetrahedron Lett.* **2002,** 43, 2002.

117. George, P.; Bock, C. W.; Glusker, J. P., *J. Mol. Struct.* **1996,** 376, 425.

118. Liu, C.-C.; Lien, M.-H., *J. Phys. Chem.* **1996,** 100, 594.

119. Rodriguez, A. M., *J. Mol. Struct.* **1999,** 463, 283.

120. Apeloig, Y.; Arad, D.; Rappoport, Z., *J. Am. Chem. soc.* **1990,** 112, 9131.

121. Wilberg, K. B.; Breneman, C. M.; LePage, T. J., *J. Am. Chem. Soc.* **1990,** 112, 61.

122. Wu, C.-C.; Lien, M.-H., *J. Phys. Chem.* **1996,** 100, 594.

123. SenGupta, S.; Indulkar, Y.; Kumar, A.; Dhanya, S.; Naik, P. D.; Bajaj, P. N., *J. Phys. Chem.* **2008,** 112, 12572.

List of Journal Publications included in the present thesis

1. **Kinetic study of the gas-phase reaction of hydroxyl radical with $CF_3CH_2OCH_2CF_3$ using LP-LIF method**

   International Journal of Chemical Kinetics ***42*** *(2010) 519*

   S. SenGupta, Y. Indulkar, A. Kumar, and S. Dhanya

2. **Kinetics of gas phase reaction of OH with morpholine – an experimental and theoretical study**

   The Journal Of Physical chemistry ***114*** *(29) 7709*

   S. SenGupta, Y. Indulkar, A. Kumar, S. Dhanya, P.D. Naik, and P. N. Bajaj

3. **Detection of OH radical in laser induced photodissociation of tetrahydrofuran at 193 nm**

   The Journal Of Chemical Physics ***122*** *(2005) 124309*

   S. SenGupta, H. P. Upadhyaya, A. Kumar, P. D. Naik and P. N. Bajaj

4. **Dynamics of OH radical generation in laser-induced photodissociation of tetrahydropyran at 193 nm**

   The Journal Of Chemical Physics ***124*** *(2006) 024305*

   S. SenGupta, H. P. Upadhyaya, A. Kumar, P. D. Naik and P. N. Bajaj

5. **The dynamics of OH generation by photodissociation of morpholine molecule at 193 nm**

   Chemical Physics Letters ***465*** *(2008) 197–202*

   S. SenGupta, A. Kumar , P.D. Naik, and P.N. Bajaj

6. **Detection of OH on photolysis of styrene oxide at 193 nm in gas phase**

   Chemical Physics Letters ***430*** *(2006) 240–246*

   A. Kumar , **S. SenGupta**, K.K. Pushpa, P.D. Naik, P.N. Bajaj

7. **Studies on photodissociation of butadiene monoxide at 193 nm**

   The Journal Of Chemical Physics ***128*** *(2008) 024309*

   S. SenGupta, Y. Indulkar, A. Kumar*, P.D. Naik, P. N. Bajaj